

AD_____

Award Number: DAMD17-02-1-0124

TITLE: Optimized Hyperthermia Treatment of Prostate Cancer Using a Novel Intracavitary
Ultrasound Array

PRINCIPAL INVESTIGATOR: Nadine Smith, Ph.D.

CONTRACTING ORGANIZATION: The Pennsylvania State University
University Park, PA 16802-7000

REPORT DATE: January 2006

TYPE OF REPORT: Final

PREPARED FOR: U.S. Army Medical Research and Materiel Command
Fort Detrick, Maryland 21702-5012

DISTRIBUTION STATEMENT: Approved for Public Release;
Distribution Unlimited

The views, opinions and/or findings contained in this report are those of the author(s) and should not be construed as an official Department of the Army position, policy or decision unless so designated by other documentation.

REPORT DOCUMENTATION PAGE				Form Approved OMB No. 0704-0188	
Public reporting burden for this collection of information is estimated to average 1 hour per response, including the time for reviewing instructions, searching existing data sources, gathering and maintaining the data needed, and completing and reviewing this collection of information. Send comments regarding this burden estimate or any other aspect of this collection of information, including suggestions for reducing this burden to Department of Defense, Washington Headquarters Services, Directorate for Information Operations and Reports (0704-0188), 1215 Jefferson Davis Highway, Suite 1204, Arlington, VA 22202-4302. Respondents should be aware that notwithstanding any other provision of law, no person shall be subject to any penalty for failing to comply with a collection of information if it does not display a currently valid OMB control number. PLEASE DO NOT RETURN YOUR FORM TO THE ABOVE ADDRESS.					
1. REPORT DATE (DD-MM-YYYY) 01-1-2006		2. REPORT TYPE Final		3. DATES COVERED (From - To) 14 DEC 2001 - 13 DEC 2005	
4. TITLE AND SUBTITLE Optimized Hyperthermia Treatment of Prostate Cancer Using a Novel Intracavitary Ultrasound Array				5a. CONTRACT NUMBER	
				5b. GRANT NUMBER DAMD17-02-1-0124	
				5c. PROGRAM ELEMENT NUMBER	
6. AUTHOR(S) Nadine Smith, Ph.D. E-mail: nbs@engr.psu.edu				5d. PROJECT NUMBER	
				5e. TASK NUMBER	
				5f. WORK UNIT NUMBER	
7. PERFORMING ORGANIZATION NAME(S) AND ADDRESS(ES) The Pennsylvania State University University Park, PA 16802-7000				8. PERFORMING ORGANIZATION REPORT NUMBER	
9. SPONSORING / MONITORING AGENCY NAME(S) AND ADDRESS(ES) U.S. Army Medical Research and Materiel Command Fort Detrick, Maryland 21702-5012				10. SPONSOR/MONITOR'S ACRONYM(S)	
				11. SPONSOR/MONITOR'S REPORT NUMBER(S)	
12. DISTRIBUTION / AVAILABILITY STATEMENT Approved for Public Release; Distribution Unlimited					
13. SUPPLEMENTARY NOTES					
14. ABSTRACT <p>Ultrasound induced hyperthermia is a useful adjuvant to radiation therapy in the treatment of prostate cancer. This requires specific ultrasound phased array design and appropriate thermometry method. Inhomogeneous, acoustical, three-dimensional (3D) prostate models and economical computational methods provide necessary tools to predict the appropriate shape of hyperthermia phased arrays for better focusing and steering. A 3D acoustical prostate model was created depending on photographic data from the Visible Human Project®. The k-space computational method was used on this coarse grid and inhomogeneous tissue model to simulate the steady state pressure wavefield of the designed phased array using the linear acoustic wave equation. To insure the uniformity and spread of the pressure in the length of the array, and the steering and focusing capability in the width of the array, the equally-sized elements of the 80 elements phased array were 1 x 14 mm. Noninvasive MRI thermometry and a feedback controller were used to accomplish ex vivo and in vivo hyperthermia evaluations of the fabricated probe. Both exposimetry and k-space simulation results demonstrated good agreement within 9%. With a desired temperature plateau of 43.0°C, ex vivo and in vivo controlled hyperthermia experiments showed that the MRI temperature at the steady state was 42.9 ± 0.38°C and 43.1 ± 0.80°C, respectively. Noninvasive MRI thermometry validated this optimized hyperthermia transducer design and the feedback controller with in vivo hyperthermia treatment of canine prostate.</p>					
15. SUBJECT TERMS <p>ultrasound, hyperthermia, array, noninvasive, thermometry magnetic resonance imaging, in vitro and in vivo results</p>					
16. SECURITY CLASSIFICATION OF:			17. LIMITATION OF ABSTRACT	18. NUMBER OF PAGES	19a. NAME OF RESPONSIBLE PERSON
a. REPORT	b. ABSTRACT	c. THIS PAGE			USAMRMC
U	U	U	UU	189	19b. TELEPHONE NUMBER (include area code)

Table of Contents

Cover.....	1
SF 298.....	2
Introduction.....	4
Body.....	5
Key Research Accomplishments.....	42
Reportable Outcomes.....	43
Conclusions.....	45
References.....	46
Appendices.....	48

1. INTRODUCTION

The goal of this research was to uniformly heat the full prostate gland to 43°C for 30 to 60 minutes to insure hyperthermia effectiveness in the treatment of prostate cancer. Ultrasound induced hyperthermia is a useful adjuvant to radiation therapy in the treatment of prostate cancer. A uniform thermal dose (43°C for 30 minutes) is required within the targeted cancerous volume for effective therapy. This imposes specific ultrasound transducer design requirements. Although phased arrays have been previously used to overcome the inability of nearfield focusing of large cylindrical piezoelectric transducers, the lack of an acoustically inhomogeneous three dimensional (3D) prostate model and economical computational methods have made it difficult to predict the appropriate shape of the array for better focusing and steering. This research utilizes the *k*-space computational method and a 3D, inhomogeneous, large scale, and coarse grid human prostate model to design an intracavitary probe for hyperthermia treatment of prostate cancer. Magnetic resonance imaging (MRI) thermometry and automatic feedback controlling were also used to accomplish the therapy. To achieve this, a 3D prostate model utilizing imaging data from the Visible Human Project® was used to determine acoustical parameters of glandular, connective, fat, and muscle tissues. The acoustical model, included sound speed, density, and absorption parameters, and was determined depending on optical parameters of each pixel of image layers. The *k*-space computational method used this coarse grid and inhomogeneous tissue model to simulate ultrasound wave propagation to predict the steady state pressure wavefield of the designed phased array. To insure the uniformity and spread of the pressure in the length of the array, and the steering and focusing capability in the width of the array, the equal sized elements of the phased array were 1 x 14 mm. The anatomical measurements of the prostate were used to predict the final phased array specifications (4 x 20 planar array, 1.2 MHz, element size = 1 x 14 mm, array size = 56 x 20 mm). A single input single output, switching, feedback controller was developed to control hyperthermia temperatures from the probe. Good agreement between the exposimetry and the *k*-space computational method results was shown. As an example, the -3 dB distances of the focal volume were 22.0 and 20.0 mm in the propagation direction for *k*-space prostate simulation and exposimetry results, respectively. Temperature simulations indicated that the rectal wall temperature was elevated less than 2°C during hyperthermia treatment. Steering and focusing ability of the designed probe in both azimuth and propagation directions were found to span the whole prostate volume with minimal grating lobes (-10 dB reduction from the main lobe) and minimal heat damage to the rectal wall. *Ex-vivo* controlled hyperthermia experiments showed that the rise time was reduced by a factor of two when doubling the driving power. With a desired temperature plateau of 43.0°C, the MRI temperature results at the steady state were $42.9 \pm 0.38^\circ\text{C}$ and $43.1 \pm 0.80^\circ\text{C}$ for *ex-vivo* and *in-vivo* experiments, respectively. Unlike conventional computational methods, the *k*-space method provides a powerful tool to predict the pressure wavefield and temperature rise in sophisticated, large scale, 3D, inhomogeneous and coarse grid models.

2. BODY:

Ultrasonic hyperthermia is a promising technique for treatment of prostate cancer. When performed in conjunction with chemotherapy or radiotherapy, hyperthermia increases the damage to cancer cells caused by radiation, and prevents subsequent repair of cancerous tumors (1, 2). Intracavitary ultrasound arrays are an ideal tool for hyperthermia treatments because deep localized heating can be achieved with precise power control and without ionizing radiation (3-5).

By accounting for the physical differences between the prostate gland and surrounding tissue structures, it was possible to design a transducer to produce heating within an area closely approximating the size of the prostate, while causing minimal damage to surrounding tissue. A two-dimensional intracavitary array transducer was constructed and has been evaluated using exposimetry techniques and magnetic resonance imaging (MRI) thermometry methods. Summarizing from the original grant application, the overall specific aims from this project were:

Specific Aim:

1. Realistic modeling of ultrasound prostate hyperthermia.
2. Beam design and optimization: Using the new model for ultrasound-prostate interaction, optimal sonications for therapeutic hyperthermia have been determined.
3. Hyperthermia array design and fabrication: A two-dimensional array transducer has been designed for practical realization of the optimal sonication methods.
4. *In vitro* and *in vivo* hyperthermia monitored with MR thermometry.
5. *In vivo* prostate hyperthermia and evaluation: Using the two-dimensional ultrasound array, *in vivo* prostate hyperthermia was evaluated using canine prostate.

Starting from December 2000 and ending in December 2005, the timeline and specific goals for this project were:

A. Tissue Modeling

- Create reference three-dimensional tissue map for the prostate region by segmentation of Visible Man data set. (Months 1-6)
- Implement relaxation absorption, acoustic nonlinearity, and heat transfer effects into k-space method. (Months 1-6)
- Create additional models of the prostate region, using modified geometries based on clinical image data. (Months 6-12)

B. Beam Design

- Simulate hyperthermia treatments in the tissue models and compute as a function of wave and beam parameters. (Months 6-18)
- Optimize wavefield and beam parameters for prostate hyperthermia treatments. (Months 9-18)

C. Transducer Array Design and Fabrication

- Design transducer for realization of ultrasonic beams corresponding to optimal temperature distributions. (Months 8-18)
- Transducer construction and crystal dicing. Machining of transducer body. Cabling and crystal matching to resonance frequency. (Months 10-15)

- Transducer exposimetry and evaluation. (Months 12-18)
- D. *In vitro* and *in vivo* hyperthermia monitored with MR thermometry
- Compare simulated temperature fields with three-dimensional MR temperature maps in phantoms and *in vivo* rabbit muscle using the ultrasound array. (Months 18-24)
 - *In vivo* prostate hyperthermia experiments: dog prostate studies in a 2 Tesla whole body MRI. (Months 24-36)
- E.. Dissemination of Results
- Present results at scientific meetings. (Months 6-36)
 - Publish research results in archival journals. (Months 12-36)

The results herein will describe the final results achieved on this project over the entire project. From the timeline and goals above, the specific goals A – D are described in the following sections.

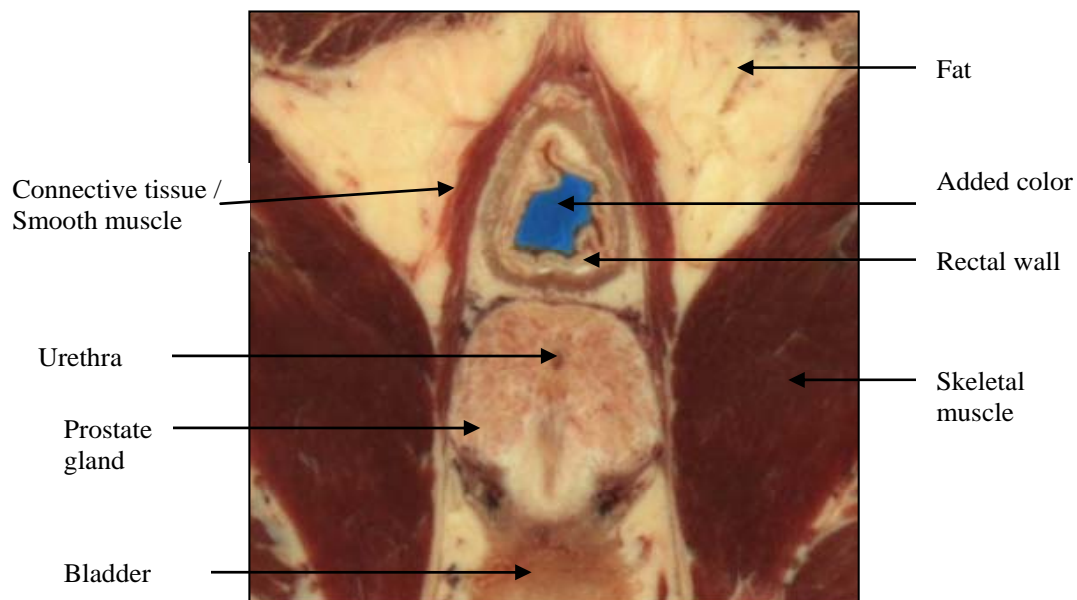


Figure 1. A picture showing one slice of the prostate gland. The gland is surrounded by skeletal and smooth muscles, where the rectum is located above the gland while the bladder is beneath it. The rectum is surrounded by a connective tissue sheet, embedded in a fatty triangular shaped area.

A. Tissue Modeling

To determine whether scattering off of tissue inhomogeneities radically distorts the beam patterns calculated with homogeneous models; an anatomically and acoustically accurate model was constructed using photographic data from the Visible Human Project (6, 7). Figure 1 shows a sample slice of the prostate gland taken from the Visible Human Project library (8). The gland is surrounded by skeletal and smooth muscles, where the rectum and the bladder are located respectively above and beneath it. Forty seven slices, downloaded and cropped to a 257 x 257 point region of interest, appear in Figure 2. The distance between each slice for the male subject is 1.0 mm. This distance is unsuitably coarse for simulation of acoustic propagation in the 1.2-1.8 MHz range. Three extra slices, created between the consecutive 1.0 mm slices by interpolating two adjacent

images to reduce the distance between consecutive images to 0.25 mm (Figure 3),
overcame this problem.

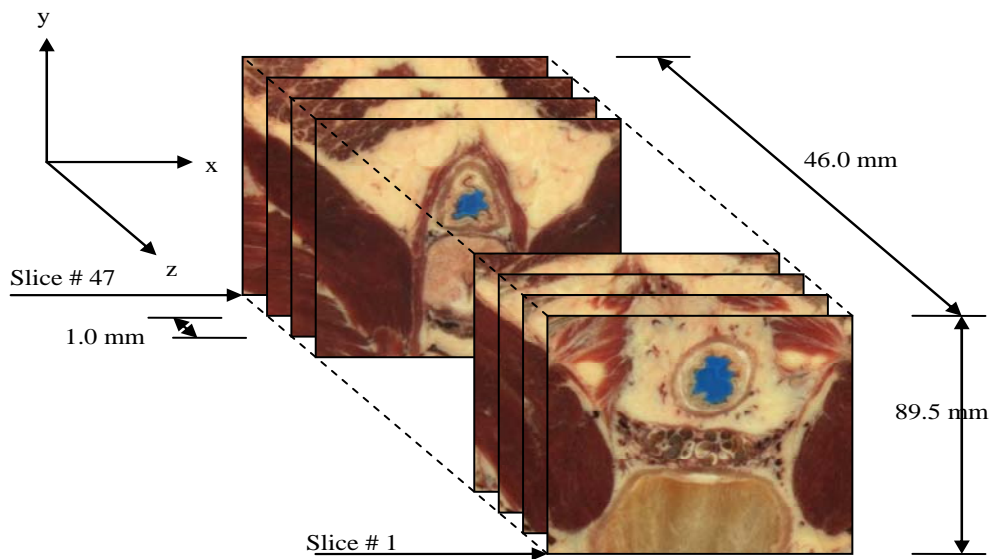


Figure 2: The three-dimensional photograph of the prostate showing 47 slices of $89.5 \times 89.5 \text{ mm}^2$ images with 1.0 mm distance between each slice.

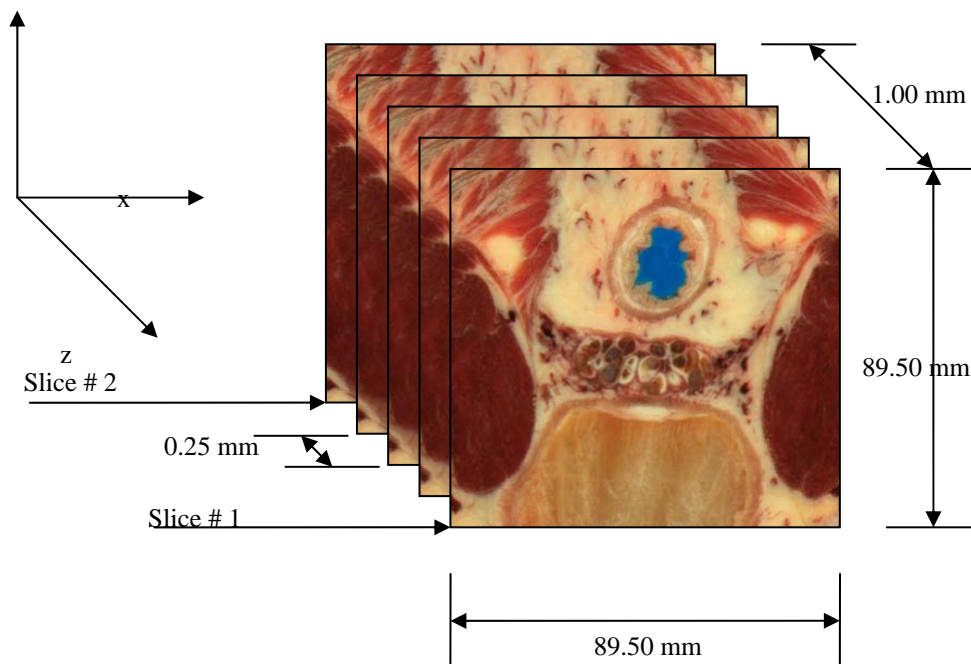


Figure 3. Three averaged slices are shown between slices #1 and 2 to reduce the distance between consecutive slices to 0.25 mm. The centered slice was produced by averaging the outer images, while the other two slices were produced by averaging the centered averaged slice with the outer slices.

This technique produced a centered slice by interpolating the outer images, and produced the other two slices by interpolating the centered slice with the outer slices. This resulted in one hundred eighty five square images to create the 3-D model of the prostate region.

A 3-D acoustical model was created based on the optical parameters of each pixel in the actual and interpolated images. The tissue surrounding the prostate gland consists of fat, muscle, and connective tissues. The prostate gland itself consists of compound tubular-alveolar glands embedded in a mass of smooth muscle and dense connective tissue(9). The 3-D mapped model reads the optical parameters that define the fractional fat, connective, glandular and muscle content of each pixel. Table 1 summarizes averaged acoustical values of these tissues from the literature measured at 37°C.

Table 1. The acoustical parameters (sound speed, density and absorption) of connective tissue, muscle, fat and water at 37°C and 1.2 MHz. The absorption value of connective tissue was projected from an assumed linear relation between sound speed and absorption for muscle and fat extrapolated to connective tissue.

Tissue type	Sound speed (m/s)	Density (kg/m ³)	Absorption @ 1.2 MHz (dB/mm)
Smooth muscle / Connective tissue	1613	1120	0.1030
Skeletal Muscle	1580	1050	0.0890
Fat	1450	950	0.0340
Water	1524	992	0.0003

The 3-D photographic data was used to create three sets of 3-D acoustical data; these are: 1) sound speed variation, 2) density distribution, and 3) absorption parameters. Sound speed of each pixel was estimated depending on the fractional optical constituent of water, muscle, fat and connective tissues. The fractional constituent of water was mapped depending on the hue and value of each pixel, while muscle and connective tissues were mapped depending on a combination of saturation and value parameters (9). Each slice in the original photographic data was converted to a hue, saturation and value (HSV) image in order to calculate the amount of each tissue constituent for each pixel. Mass density values were mapped depending on empirical linear relations between sound speed and mass density of the values shown in Table 1.

The linear relation was to produce three 3-D data sets for sound speed, density variations and absorption parameters depending on an anatomically accurate 3-D photographic image of the prostate and the surrounding tissue. Figure 4 shows the volumetric prostate image as mapped to sound speed, density and absorption. Executing a MATLAB® program generated sound speed, density and absorption depending on the relationships discussed earlier. Figure 4. shows the sound speed mapping of, for example, slice # 1908; the sound speed varies through the soft tissue of that image from about 1400 to 1600 m/s. The skeletal muscle tissue that surrounds the prostate gland has a sound speed of about 1550 m/s. The prostate gland itself is mapped to connective tissue and some fat and muscle tissues. This mapping is apparently consistent with the description of the gland that describes it as tubular and alveolar tissues, imbedded in smooth muscle and connective tissues. The rectal wall translates into muscle and fat tissues as shown in Figure 4. The connective tissue that surrounds the rectum appears to have a sound speed of about 1610 m/s.

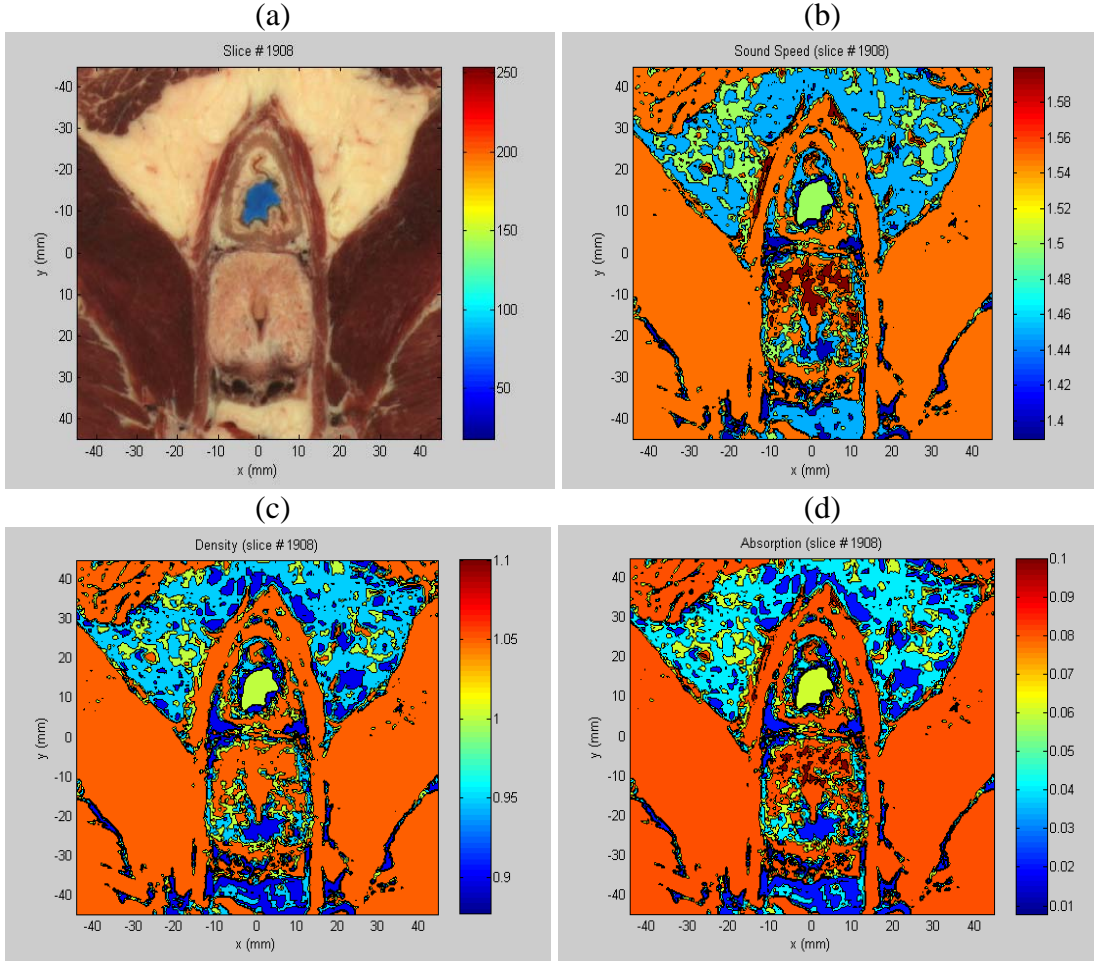


Figure 4. The acoustical mapping of a selected (a) photographic slice to (b) sound speed (mm/μs), (c) density (g/cm³), and (d) absorption (dB/mm).

Figure 4c shows the density variations through slice #1908. The density varies from about 900 to 1100 kg/m³. Compared to the sound speed map, this figure discriminates each soft tissue accurately and has good agreement for skeletal muscle, fat, connective tissue and water. Figure 4d shows the absorption variations of the soft tissue of slice #1908; the absorption varies from 0.01 to 0.1 dB/mm. The absorption parameters of fat, connective and skeletal muscle tissues matches those values summarized in Table 1 when measured at 37°C. Comparing the values of sound speed, density and absorption of various tissues in Figures 4b, 4c and 4d respectively, to the standard values of these soft tissues, positive agreement resulted from this mapping for the whole three-dimensional model.

B. Wave propagation using the *k*-space method

The *k*-space computational method was appropriate for the simulation purposes of wave propagation in inhomogeneous media using coarse grids while maintaining accuracy (10, 11). The linear wave equation, utilizing inhomogeneous medium, was

solved for usage in the k -space computational method and was tested in a 3D human breast model by other researchers. However, this research included the mathematical derivation of this method. First-order coupled propagation equations depending on the mass conservation, momentum conservation and state equations were used (12). These are:

$$\frac{\partial p(\bar{x}, t)}{\partial t} + \rho(\bar{x})c^2(\bar{x})\nabla \cdot v(\bar{x}, t) = -\alpha(\bar{x})p(\bar{x}, t) \quad (1),$$

$$\rho(\bar{x})\frac{\partial v(\bar{x}, t)}{\partial t} + \nabla p(\bar{x}, t) = 0 \quad (2),$$

where $p(\bar{x}, t)$ is the spatially (\bar{x} is representing the 3D Cartesian axis i.e. (x,y,z)) and temporally dependent acoustic perturbation in pressure; $\rho(\bar{x})$ is the spatially dependent density; $c(\bar{x})$ is the spatially dependent sound speed; $v(\bar{x}, t)$ is the particle velocity, and $\alpha(\bar{x})$ is the absorption coefficient that is equivalent to the inverse of a spatially-dependent relaxation time. All absorption effects (viscous losses, heat conduction losses and internal molecular processes losses) are represented by this single relaxation time. From (2), a simplified equation could be written as:

$$\frac{\partial v(\bar{x}, t)}{\partial t} = \frac{-\nabla p(\bar{x}, t)}{\rho(\bar{x})}$$

by differentiating (1) with respect to time and taking the divergences of (2) the resulting equations are:

$$\frac{\partial^2 p(\bar{x}, t)}{\partial t^2} + \rho(\bar{x})c^2(\bar{x})\frac{\partial}{\partial t}\nabla \cdot v(\bar{x}, t) = -\alpha(\bar{x})\frac{\partial p(\bar{x}, t)}{\partial t} \quad (1')$$

$$\rho(\bar{x}, t)\frac{\partial}{\partial t}\nabla \cdot v(\bar{x}, t) + \frac{\partial v(\bar{x}, t)}{\partial t}\nabla \cdot \rho(\bar{x}) + \nabla^2 p(\bar{x}, t) = 0 \quad (2')$$

rearranging (1') produces:

$$\frac{\partial}{\partial t}\nabla \cdot v(\bar{x}, t) = -\left(\frac{\alpha(\bar{x})}{\rho(\bar{x})c^2(\bar{x})}\frac{\partial p(\bar{x}, t)}{\partial t} + \frac{1}{\rho(\bar{x})c^2(\bar{x})}\frac{\partial^2 p(\bar{x}, t)}{\partial t^2}\right)$$

substituting the above equation into (2'), the resulting equation after some algebraic steps is:

$$\frac{-\alpha(\bar{x})}{c^2(\bar{x})}\frac{\partial p(\bar{x}, t)}{\partial t} - \frac{\partial^2 p(\bar{x}, t)}{c^2(\bar{x})\partial t^2} - \frac{1}{\rho(\bar{x})}\nabla p(\bar{x}, t)\nabla \cdot \rho(\bar{x}) + \nabla^2 p(\bar{x}, t) = 0 \quad (3).$$

To write this equation in a form similar to the wave equation requires extra algebraic manipulations. The simplification of the divergence of the gradient of the pressure divided by the density is:

$$\nabla \cdot \left(\frac{\nabla p(\bar{x}, t)}{\rho(\bar{x})}\right) = \frac{\nabla^2 p(\bar{x}, t)}{\rho(\bar{x})} - \frac{\nabla p(\bar{x}, t)\nabla \cdot \rho(\bar{x})}{\rho(\bar{x})^2} \quad (4)$$

Substituting equation (4) into equation (3) the resulting equation is:

$$\nabla \cdot \left(\frac{1}{\rho(\bar{x})}\nabla p(\bar{x}, t)\right) - \frac{1}{\rho(\bar{x})c^2(\bar{x})}\frac{\partial^2 p(\bar{x}, t)}{\partial t^2} = \frac{\alpha(\bar{x})}{\rho(\bar{x})c^2(\bar{x})}\frac{\partial p(\bar{x}, t)}{\partial t} \quad (5)$$

The above equation represents the linear wave equation in an inhomogeneous medium with absorption parameters included as a virtual source that depends on the time

derivative of the pressure, multiplied by a frequency independent absorption factor. In order to use the k -space method to solve for the propagation of sound, simplifying equation (5) separates the spatially dependent sound speed and density parameters from the second order derivatives of the pressure with respect to spatial and temporal variables. The next derivation will neglect the absorption term and include it in the effective source terms, after simplification.

The starting equation is:

$$\nabla \cdot \left(\frac{1}{\rho(x)} \nabla p(\bar{x}, t) \right) - \frac{1}{\rho(x)c^2(x)} \frac{\partial^2 p(\bar{x}, t)}{\partial t^2} = 0 \quad (6)$$

Define the normalized pressure as: $\psi(\bar{x}, t) = \frac{p(\bar{x}, t)}{\sqrt{\rho(x)}}$. By substituting this in equation (6)

the result is:

$$\nabla \cdot \left(\frac{1}{\rho(x)} \nabla \rho^{1/2}(\bar{x}) \psi(\bar{x}, t) \right) = \frac{\rho^{1/2}(\bar{x})}{\rho(x)c^2(x)} \frac{\partial^2 \psi(\bar{x}, t)}{\partial t^2}.$$

This equation simplifies to:

$$\nabla^2 \psi(\bar{x}, t) - \rho^{1/2}(\bar{x}) \psi(\bar{x}, t) \nabla^2 \rho^{-1/2}(\bar{x}) = \frac{1}{c^2(x)} \frac{\partial^2 \psi(\bar{x}, t)}{\partial t^2}.$$

More simplifications produce:

$$\nabla^2 \psi(\bar{x}, t) - \frac{1}{c_0^2} \frac{\partial^2 \psi(\bar{x}, t)}{\partial t^2} = \frac{1}{c_0^2} [c_0^2 \rho^{1/2}(\bar{x}) (\nabla^2 \rho^{-1/2}(\bar{x})) \psi(\bar{x}, t) + \left(\frac{c_0^2}{c^2(x)} - 1 \right) \frac{\partial^2 \psi(\bar{x}, t)}{\partial t^2}].$$

More simplicity arises from defining the effective sources of $q(\bar{x}, t)$ and $v(\bar{x}, t)$ functions as follows:

$$q(\bar{x}, t) = c_0^2 \rho^{1/2}(\bar{x}) \psi(\bar{x}, t) \nabla^2 \rho^{-1/2}(\bar{x})$$

$$v(\bar{x}, t) = \left(\frac{c_0^2}{c^2(x, t)} - 1 \right) \psi(\bar{x}, t).$$

Equation (6) simplifies to:

$$\nabla^2 \psi(\bar{x}, t) - \frac{1}{c_0^2} \frac{\partial^2 \psi(\bar{x}, t)}{\partial t^2} = \frac{1}{c_0^2} \left(q(\bar{x}, t) + \frac{\partial^2 v(\bar{x}, t)}{\partial t^2} \right) \quad (7)$$

The above equation can be transformed to the frequency domain easily by 3D spatial Fourier transformation as follows:

$$k^2 F(k, t) - \frac{1}{c_0^2} \frac{\partial^2 F(k, t)}{\partial t^2} = \frac{1}{c_0^2} \left(Q(k, t) + \frac{\partial^2 V(k, t)}{\partial t^2} \right) \quad (8)$$

where $F(k, t)$, $Q(k, t)$ and $V(k, t)$ are the 3D spatial Fourier transformations of $\psi(\bar{x}, t)$, $q(\bar{x}, t)$ and $v(\bar{x}, t)$ respectively. Equation 7 satisfies the total wavefield, defined as the summation of the incident and the scattered fields ($\psi(\bar{x}, t) = \psi_i(\bar{x}, t) + \psi_s(\bar{x}, t)$), and the scattered wavefield, as well. However, the incident wavefield is satisfied using the wave equation without any sources:

$$\nabla^2 \psi_i(\bar{x}, t) - \frac{1}{c_0^2} \frac{\partial^2 \psi_i(\bar{x}, t)}{\partial t^2} = 0,$$

In order to solve for the inhomogeneous medium (i.e. to include both the incident and the scattered wavefields), required introducing a new auxiliary source, as $w(\bar{x}, t) = \psi_s(\bar{x}, t) + v(\bar{x}, t)$. Substitution of this new term in equation (8) resulted in the following simplified equation:

$$\frac{\partial^2 W(k, t)}{\partial t^2} = k^2 c_0^2 [W(k, t) - V(k, t)] - Q(k, t) \quad (9)$$

where,

$$V(k, t) = \mathbb{F} \left[\left(1 - \frac{c^2(\bar{x})}{c_0^2} \right) (\psi_i(\bar{x}, t) + w(\bar{x}, t)) \right]$$

$$Q(k, t) = c_0^2 \mathbb{F} \left[\sqrt{\rho(\bar{x})} \nabla^2 \rho^{-1/2}(\bar{x}) [\psi_i(\bar{x}, t) + w(\bar{x}, t) - v(\bar{x}, t)] \right],$$

where \mathbb{F} indicates spatial Fourier transform.

A non-standard finite difference approach was used to solve this equation (13); the discretization of the time derivative term gives:

$$W(k, t + \Delta t) - 2W(k, t) + W(k, t - \Delta t) = 4 \sin^2 \left(\frac{c_0 k \Delta t}{2} \right) \left[V(k, t) - W(k, t) - \frac{Q(k, t)}{c_0^2 k^2} \right] \quad (10).$$

This k - t propagator (Equation 10) is the key equation for solving for the propagation in an inhomogeneous medium after setting both the initial and the boundary conditions.

B.1 Nonlinear wave equation and the k-space method

The nonlinear wave equation was proposed by Dr Sparrow for usage in the k -space computational method. This section includes brief description of the mathematical model. The density scaled wave equation including acoustic nonlinearities is:

$$\nabla^2 \psi(\bar{x}, t) - \sqrt{\rho(\bar{x})} \psi(\bar{x}, t) \nabla^2 \frac{1}{\sqrt{\rho(\bar{x})}} - \frac{1}{c^2(\bar{x})} \frac{\partial^2 \psi(\bar{x}, t)}{\partial t^2} = - \frac{\beta(\bar{x})}{\sqrt{\rho_0} c_0^4} \frac{\partial^2 (\psi^2(\bar{x}, t))}{\partial t^2}$$

where the $(\psi^2(\bar{x}, t))$ term is the source of nonlinearity, and $\beta(\bar{x})$ is the coefficient of nonlinearity. The harmonic oscillator equation is:

$$\frac{\partial^2 W 2(\bar{k}, t)}{\partial t^2} = (c_0^2 k^2) (V L N 2(\bar{k}, t) - W 2(\bar{k}, t)) - Q(\bar{k}, t) \quad (11)$$

where $w 2(\bar{x}, t) = \psi_s(\bar{x}, t) + v_{NL2}(\bar{x}, t)$ is an auxiliary field (where the subscript s refers to the scattered part of the acoustic field); $W 2(\bar{k}, t)$ is its spatial Fourier transform.

$$v_{NL2}(\bar{x}, t) = \left(\frac{c_0^2}{c^2(\bar{x})} - 1 \right) \psi(\bar{x}, t) - \frac{\beta(\bar{x})}{\sqrt{\rho_0} c_0^2} \left(\psi_s^2(\bar{x}, t) + 2\psi_s(\bar{x}, t) \psi_i(\bar{x}, t) \right)$$

(where the subscript i refers to the incident part of the acoustic field) with spatial Fourier transform:

$$VNL2(\bar{k}, t) = \mathbb{F} \left\{ \left(\frac{c_0^2}{c^2(\bar{x})} - 1 \right) \left[\psi_i(\bar{x}, t) + w 2(\bar{x}, t) - \frac{\beta(\bar{x})}{\sqrt{\rho_0} c_0^2} \left(\psi_s^2(\bar{x}, t) - 2\psi_s(\bar{x}, t) \psi_i(\bar{x}, t) \right) \right] \right. \\ \left. - \frac{\beta(\bar{x})}{\sqrt{\rho_0} c_0^2} \left(\psi_s^2(\bar{x}, t) - 2\psi_s(\bar{x}, t) \psi_i(\bar{x}, t) \right) \right\}$$

and,

$$Q(\bar{k}, t) = \mathbb{F} \left\{ c_0^2 \sqrt{\rho(\bar{x})} \nabla^2 \left(\frac{1}{\sqrt{\rho(\bar{x})}} \right) [\psi_i(\bar{x}, t) - w_2(\bar{x}, t) - v_{NL2}(\bar{x}, t)] \right\}.$$

The inclusion of the nonlinear terms in the k -space method made it more useful for computing actual heating patterns through inhomogeneous large scale models.

B.3 k -Space Simulation of the Linear Wave Equation in a Prostate Model

Use of FORTRAN 77 allowed calculation and simulation of wave propagation of sound in the 3D inhomogeneous prostate model. A 6.4 x 6.4 x 4.6 cm model that has 257 x 257 x 185 points was prepared for each acoustical parameter (sound speed, density and absorption). These data, read and processed, were compatible with the mathematically derived model. A tapered absorption boundary layer, created in the absorption data set, used 25 points to create the layer that surrounds the actual model.

The Laplacian of the reciprocal square root of density was calculated and stored as a data file to reduce repetitions. A spherical point source that produces spherical waves in the model is placed in the rectum near the absorbing boundary layer to test the model and the numerical simulation method adapted here. This source was produced mathematically as a Gaussian source in both space and time. It was added to the effective sources resulting from earlier derivation and simplification of the k -space method and the addition of the absorption dependent term. An FFTW (Fastest Fourier Transform in the West) library was attached to the Fortran program to calculate the 3D spatial Fourier transform and the inverse Fourier transform, whenever needed.

The log-scale, gray scale image of the wave propagation in the developed human prostate three-dimensional model appears in Figure 5. The incident wave is shown leading the scattered wavefield produced from the propagation in the human prostate inhomogeneous medium. The spherical source is located in the rectum five points away from the absorption boundary layer. The multi-layer image in this figure includes the absorption variations through the central slice of the 3D model as a background. The tapered absorption boundary layer clearly surrounds the whole image. The designed Fortran program, that produces the 2D gray scaled images of the wave propagation, creates an image every 10 milliseconds. Capturing these images as a JPEG file allowed the use of Photoshop or any other photo editor. While calculations were done for the whole model (i.e. 3D calculations), to reduce the storage space, image production came from the middle two-dimensional slice. The shown image in Figure 5 is the middle slice of the model. The scattered, as well as the incident waveforms were shown and labeled. At the boundaries of the prostate, a noticeable, reflected wave appears. Some irregularity of the shape of the wave while crossing the urethra region is evident. This kind of irregularity will complicate the focusing mechanism in such an inhomogeneous medium. However, the intent of this figure is to test the accuracy of the model and the computational method, rather than any focusing issues. The inclusion of the phased array as a sound source into this model allows prediction and optimization of the pressure wavefield for thermal therapy of the prostate.

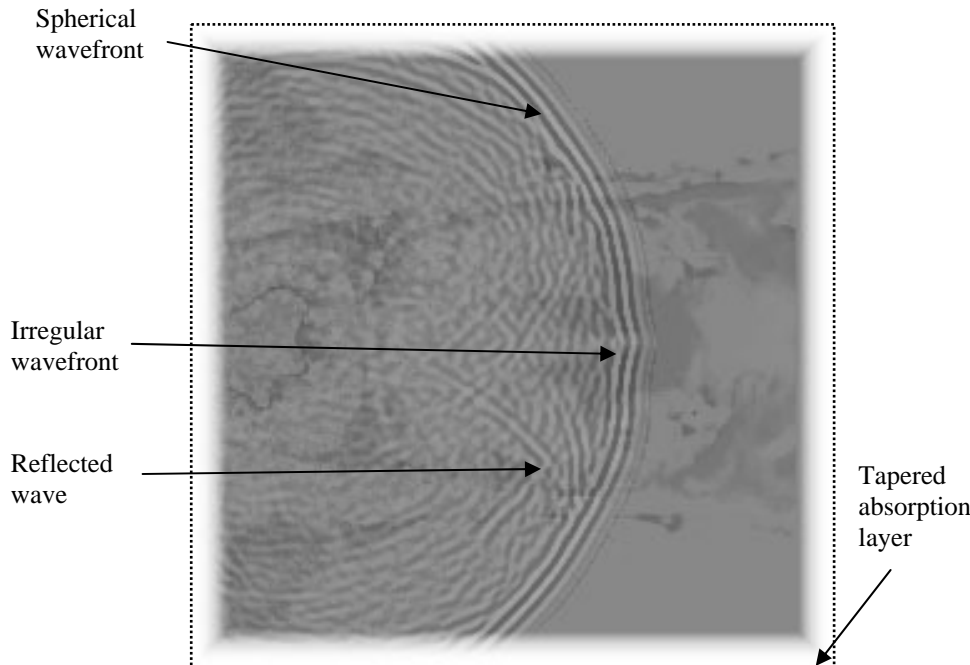


Figure 5. A 2D gray scaled image showing a background layer of the absorption distribution through middle slice of the 3D prostate model. The tapered absorption boundary layer appears at the edges with sharp white color. A black dotted line surrounds the image to distinguish the absorption layer. A spherically propagated wave is shown on top of this background image showing the wave propagation from left to right through the 3D prostate model. The scattered wave is shown following the three cycles wave that has a frequency of 1.2 MHz. Due to sound speed and density changes through this model the wave front is shown with an irregular shape while propagating through the urethra area.

B.4 “Fresnel-lens-like” transducer of incoherent beams

Simulations of our alternative technique for heating the prostate—a “Fresnel-lens-like” transducer that uses incoherent, individually aimed beams of sound to heat the prostate are complete (14). Its design is motivated by several goals for a practical prostate hyperthermia treatment. The first is to heat the entire prostate, if possible, by 6°C for 30-60 minutes, without hot or cold spots. Because the effective thermal dose doubles for every degree above 6°C , and decreases by a factor of four for every degree below 6°C , the maximum range for the temperature rise can be taken to be $\pm 1^{\circ}\text{C}$, although a tolerance of $\pm 0.5^{\circ}\text{C}$ would be considerably better. Finally, the treatment should not take too long, perhaps no more than an hour, because of patient comfort and cost of the treatment. The desirability of a quick overall treatment and the need to heat nearly the entire prostate essentially dictates that all parts of the prostate need to be heated simultaneously in a clinically fielded ultrasonic system.

The frequency of the system should be in the range of 1-2 MHz, as a compromise between the need of the sound to penetrate into the body and reach the prostate, and the competing need for the sound to be substantially absorbed by the prostate. Because of the amount of acoustic power lost on the way to the prostate, the total acoustic power passing through the rectal wall needs to be about double the power that goes through the prostate. Thus the transducer must have an area of about a factor of two larger than the cross sectional area of the prostate to avoid overheating the rectal wall. If, however, such

a large array were made using conventional two-dimensional electronic steering techniques, the requirements on the element size, being a fraction of an acoustic wavelength across, and the need for a large overall array would lead to a two-dimensional array that would have to have thousands of individually wired elements, with as many amplifier channels and wires entering the body. Such an array is likely to be impractical.

During the last reporting period, however, a probe concept was found that is much simpler. The idea is to use fewer, relatively large elements. The elements are several wavelengths across so that each one forms a collimated beam on its own. The beams are geometrically aimed such that each element is responsible for heating a different portion of the prostate. The beams generally converge on the prostate from a range of angles. The general convergence of the beams is used to compensate for the loss of acoustic intensity due to absorption and scattering, such that the intensity, and thus the heating, is made independent of the distance of the tissue from the transducer in the vicinity of the prostate. There is no electronic steering of the array. Instead, incoherence between the beams is maximized by driving neighboring elements with slightly different frequencies. As shown in Figure 6, the present design is to use 44 elements arranged in a honeycomb-like pattern, although newer designs are being simulated with up to 115 elements. The elements are split into three groups—colored red, green and blue in the figure. Each group is driven at a different frequency in the 1-2 MHz band, nominally three frequencies near 1.5 MHz. Each element is 3.2 mm in diameter and sits in a 3.3 mm hole machined into a substrate at the desired angle for that element. In all there are only three small coaxial leads that need to pass into the rectum to power the three groups, contributing to patient comfort and the simplicity of the driving electronics.

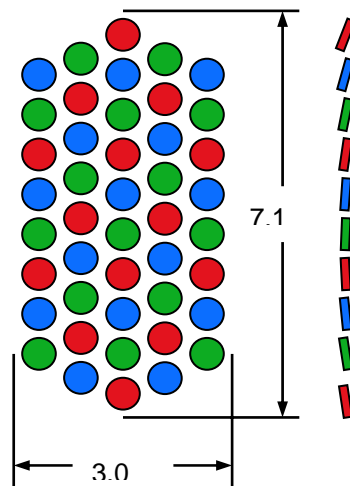


Figure 6. Coronal (front) and sagittal (side) views of a Fresnel-lens-like transducer, showing 44 individually aimed circular elements broken into three interspersed groups.

For each of the three frequency groups of elements, the complex acoustic pressure from the elements of the group are projected into a large three dimensional space and allowed to interfere with each other. Propagation is into an isotropic medium with an

attenuation of 7.5 m^{-1} , which is an average of literature values over tissue types at 1.5 MHz. The real part of the complex pressure for the first group—the “red” elements of Figure 6—is shown in Figure 7. Slices through the center of the prostate, indicated by the circle, in the sagittal, coronal, and axial planes are shown in the figure. This figure can be interpreted as a snap-shot of the sound field for one of the three frequencies, red showing the positive pressure swing and blue showing the negative pressure swing. Similar calculations and plots are made for the other two frequencies as well, although not shown.

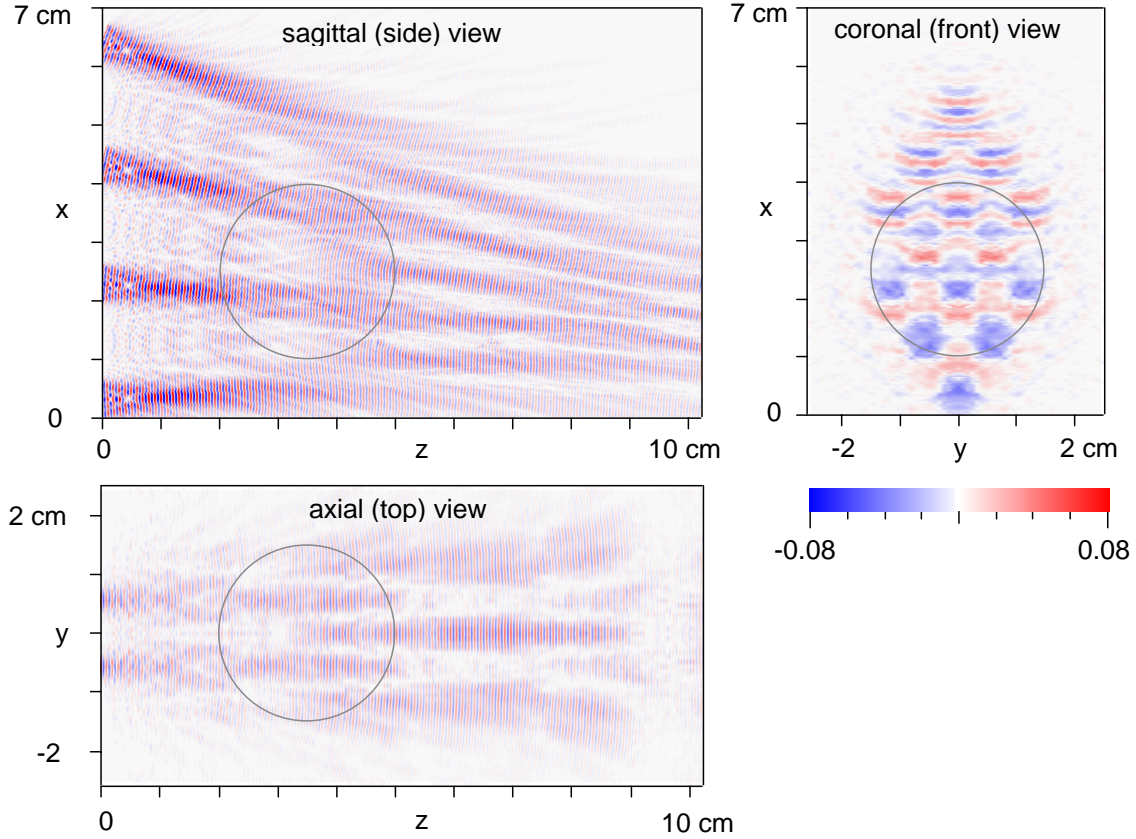


Figure 7. Real part of the complex acoustic pressure from the first group of elements (arbitrary pressure units). The transducer is on the left edge of the sagittal and axial views in the $z = 0$ plane. The prostate is positioned at the circle.

The deposition of heat is assumed to be proportional to the square of the magnitude of the pressure wave. The contribution to the heating for the first group is shown in Figure 8, which is a plot of the square of the magnitude of the complex pressure wave for the first frequency.

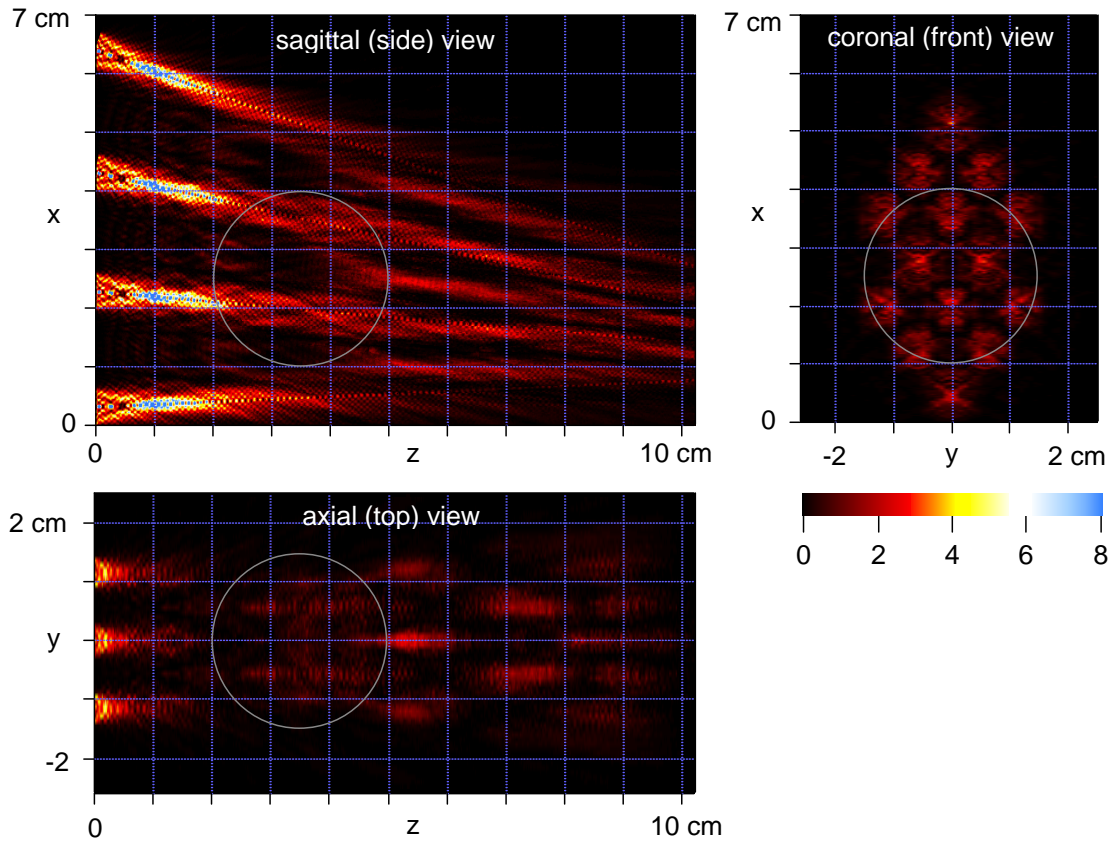


Figure 8. The magnitude squared of the acoustic pressure field, proportional to the heat deposition, of the first group of elements (arbitrary pressure squared units).

The bioheat transfer equation (BHTE) (15-17), was used to calculate the temperature rise from the heat deposition per unit volume. The temperature rise plot is essentially the convolution, or blurring, of the heating plot over a length scale of 5.2 mm, derived using literature values for the thermal conductivity and blood perfusion and heat capacity of typical tissue types. The temperature rise due to each of the three groups of elements in the center of the prostate is seen in the coronal slices of Figure 9. The beams are aimed to minimize interference within one group of elements of the same frequency, while being aimed such that the heating and temperature rise from each of the three groups compliments the others, filling in the spaces within the prostate that the others miss.

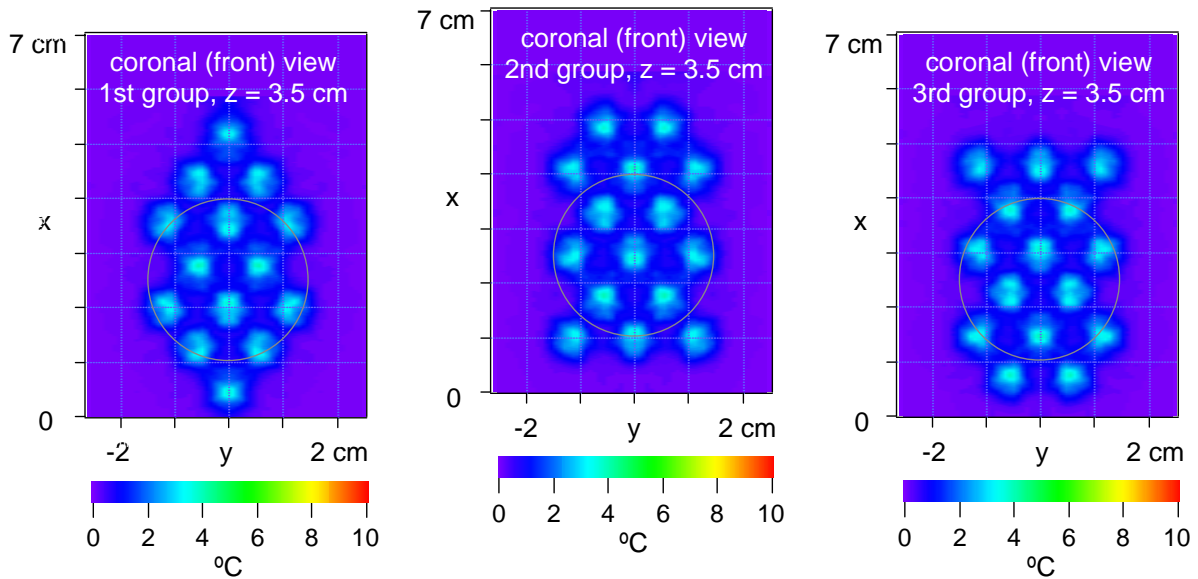


Figure 9. The temperature rise at the prostate due to each of the three groups of elements.

The total temperature rise from all three groups is the sum of the temperature rises due to each group, and is shown in Figure 10. The sum of the three groups of Figure 9 is shown in the upper right panel of Figure 10, and can be seen to be relatively uniform in the x - y plane. Despite the depletion of sound that occurs from attenuation and beam spreading, uniformity is also achieved in z direction, at least in the region of the prostate between $z = 2$ cm to 5 cm, by the converging of the beams toward the far side of the prostate (away from the rectum). More elements point toward the far side of prostate to make sure that it is heated as much as the near side, giving relatively uniform heating in all three dimensions in the region of the prostate.

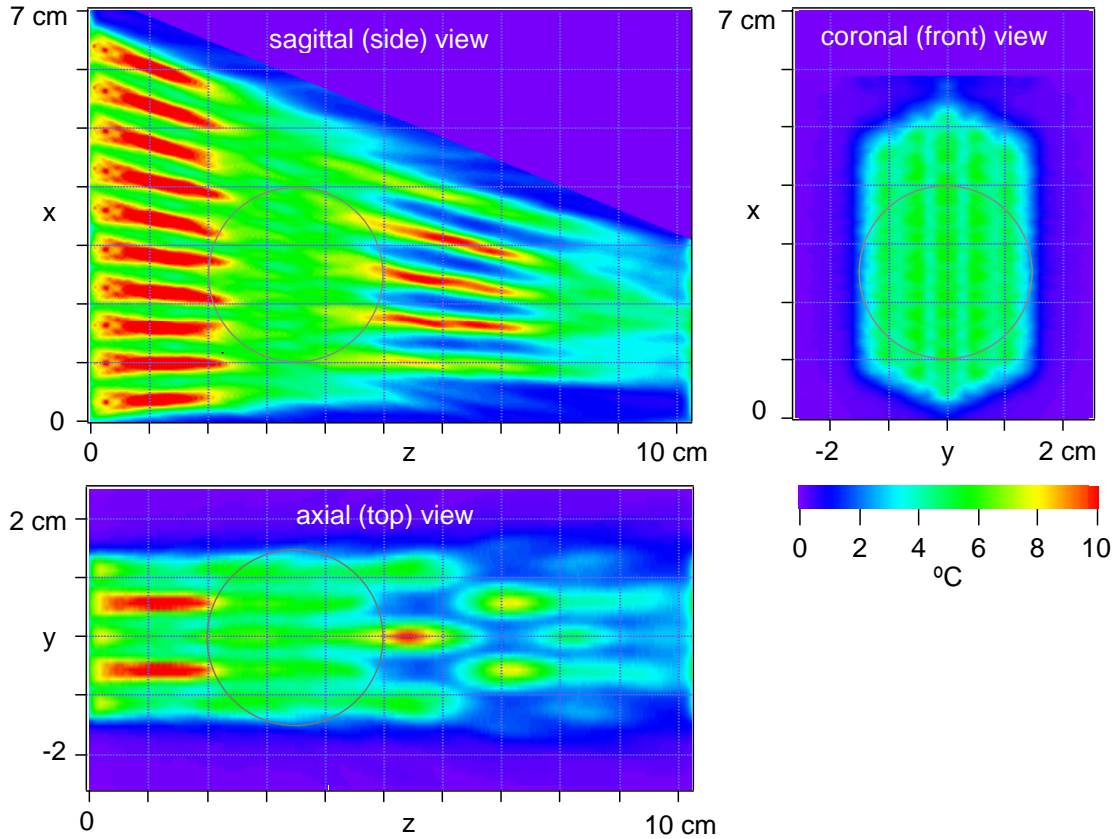


Figure 10. The temperature rise due to heating from all the elements. There is a relatively uniform temperature rise in the region of the prostate, but there are bad hotspots before and after the prostate.

However, there are serious hot spots both before and after the prostate. The hot spots on the far side of the prostate are caused by interference between the beams of sound from the elements within a single group of the same frequency. Back in Figures 6 and 7, the beams of the first group can be seen to start to overlap at about $z = 4$ cm. These overlapping beams cause moire patterns of constructive and destructive interference that are quite pronounced at $z = 6$ cm. For some reason that is not yet understood, it turns out that the places of constructive interference of each of the three groups happen to land right on top of each other, as can be seen in the coronal sections of Figure 11, taken at $z = 6.0$ cm. The interference between the beams within each of the three frequency groups give bright spots in the temperature rise that unfortunately occur at the same x - y coordinates, leading to very serious hot spots behind the prostate that would denature tissue.

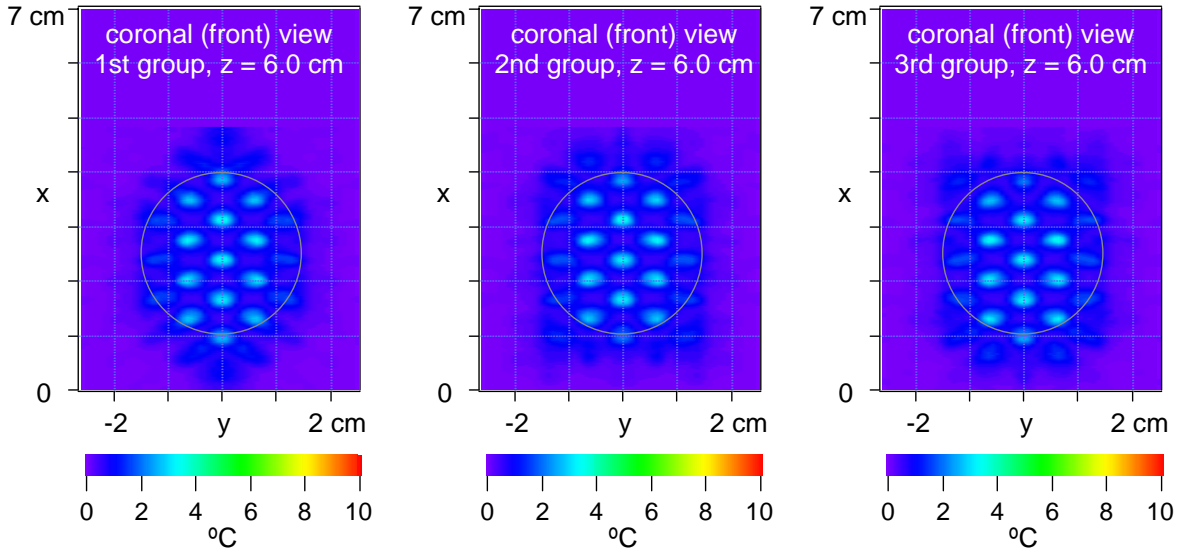


Figure 11. Hot spots due to constructive interference between overlapping parts of beams at each of the three frequencies, that unfortunately occur at the same positions for each frequency.

Three possible ways around this problem were considered. However, a better, simple, and effective way to remedy the problem was found and simulated this reporting period. Since the hot spots are caused by interference between the beams, the spots can be steered by phase shifting the beams. The phase shift is applied by physically shifting element positions in the z direction by a fraction of a wavelength (z shifts are in the range of $\pm 1\text{ mm}$) without changing the direction that the elements point, as suggested by Figure 12. By shifting the lower elements of the first group (red) forward and the upper elements backward, the hot spots of the first group are made to shift upward. Similarly, the hot spots due the second and third groups (green and blue in the figure) are made to move downward and to either the right or the left. Figure 13 shows the result of this geometrical phase shifting. The hot spots for the three groups have moved slightly to new positions and no longer substantially overlap. Thus, the hot spots behind the prostate are mitigated, as can be seen in the total temperature rise plot of Figure 14. By not changing the angle with which the elements point, the heating of the prostate remains uniform in the region where the beams do not overlap.

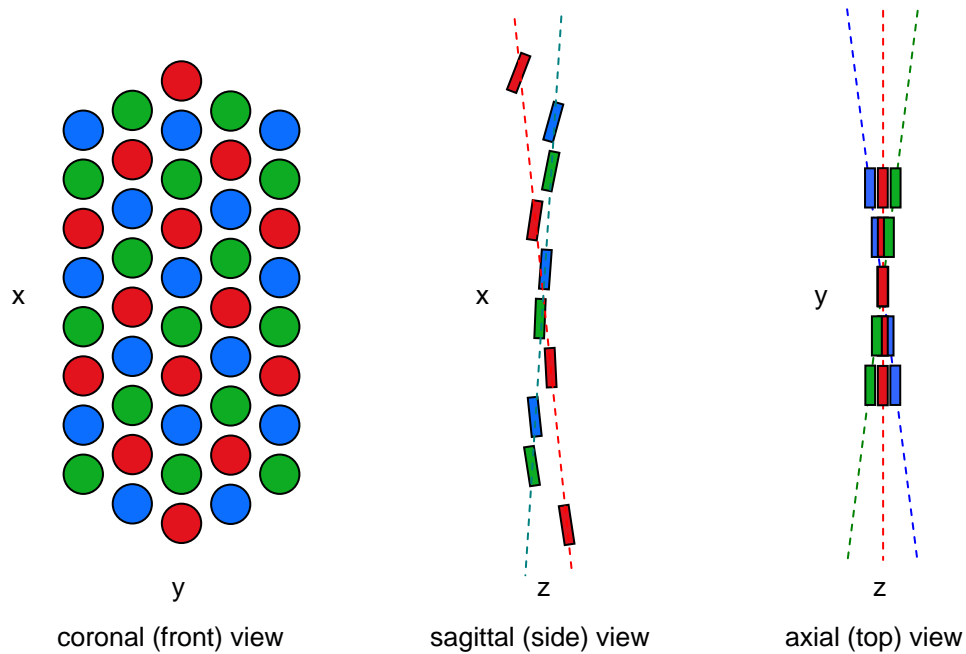


Figure 12. Geometric phase shifting and steering of the elements to move the hotspots on the far side of the prostate, without affecting the beam angles that give uniform heating within the prostate. Elements are moved in the z direction by a fraction of a wavelength; the amount shown is greatly exaggerated for clarity.

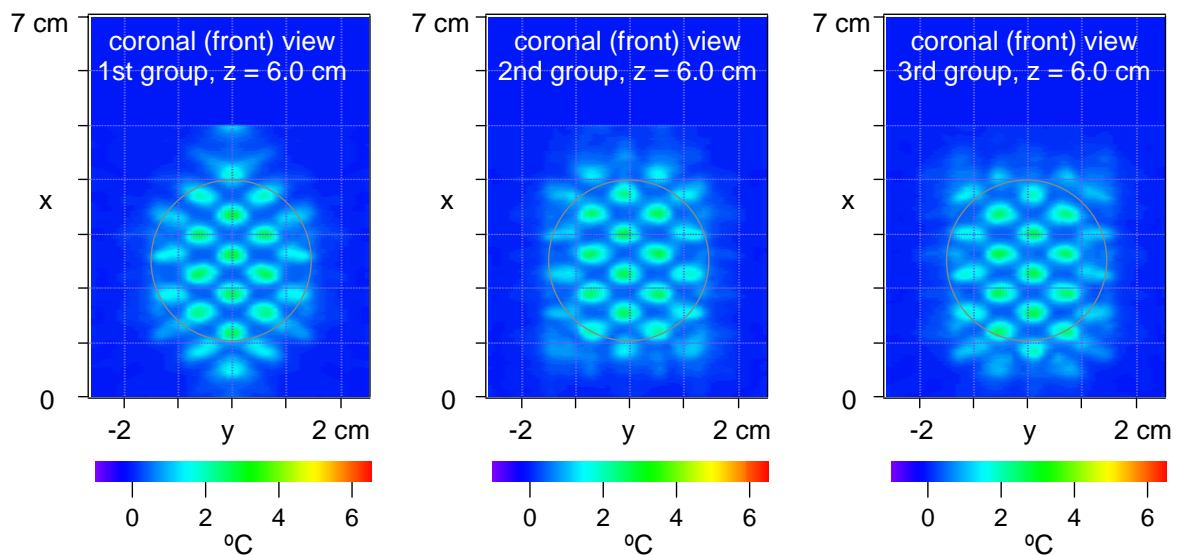


Figure 13. Shifting of the hot spots behind the prostate through geometric steering of beam interference. Please note the change of temperature scale from previous plots. Hot spots no longer occur at the same x - y positions for the three frequency groups of elements.

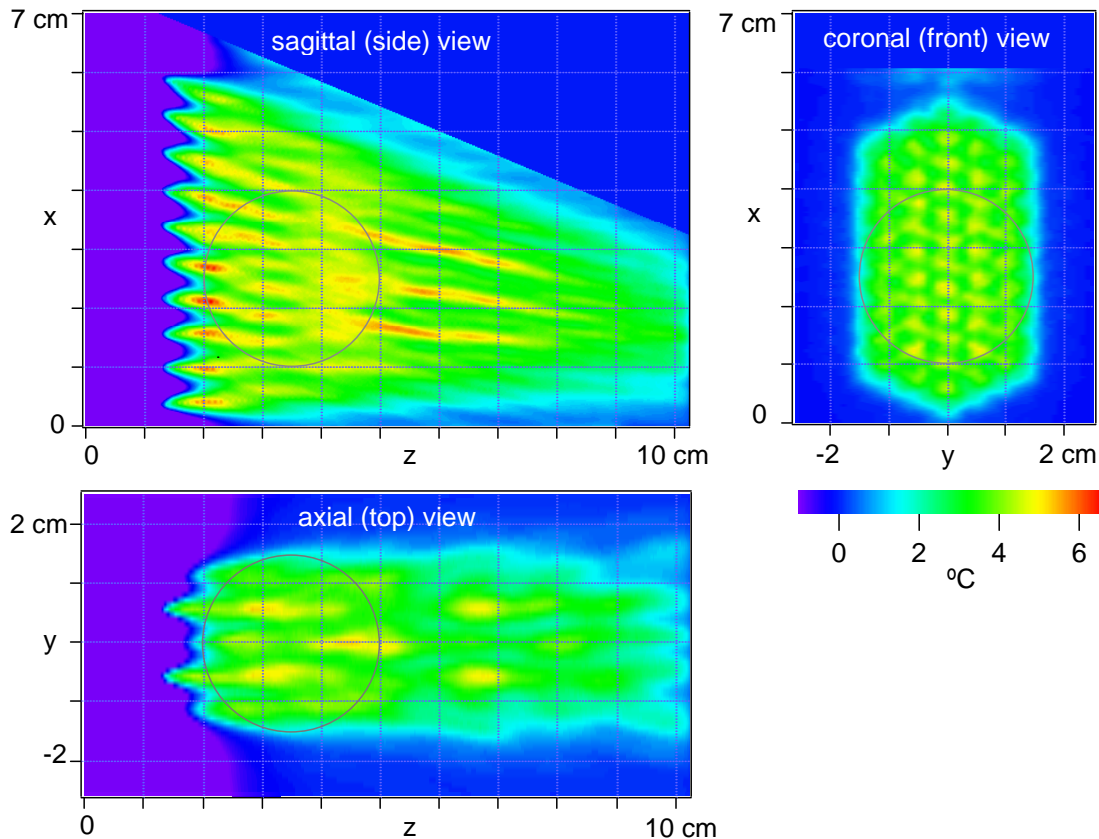


Figure 14. Total temperature rise after mediating against hot spots in the near and far sides of the prostate. Please note the more sensitive temperature scale (color bar) as compared to most of the previous figures.

The hot spots between the transducer and the prostate seen in Figure 10 are caused by the contraction of an acoustic beam in the near field of a circular source. The problem is not as bad as it might seem, however, because the first centimeter or two of propagation from the transducer face will be through chilled water, held in a condom in the rectum, rather than in tissue. This effect has been included in the simulation of Figure 14, where the chilled water is taken to be 12°C below body temperature (nearly room temperature) in the region between $z = 0$ to $z = 1.2$ cm. The chilled water also protects the rectal wall and tissue that is about 5 mm deep into the body.

Simulations were made using a reduced element size, with an increased number of elements. This shortens the near field regime in front of the elements and should bring the hot spots safely into region under the influence of the chilled water. This alternative method of heating the prostate, relying as it does on incoherent, individually aimed beams of sound, appears to be a practical and simple approach to hyperthermia therapy however the transducer construction would have been, at the time, too difficult.

C. Transducer Array Design and Fabrication

Ultrasound phased arrays are suitable for thermal applications since they can focus and steer the ultrasound beam in the targeted volume. The limitations of the dimensions of the array are the physiological measurements of the prostate gland and the rectum.

C1. One-dimensional phased array

Initially, a one-dimensional (1D) ultrasound phased array was used to simulate the pressure field in a homogenous (i.e. water) and an inhomogeneous media. Figure 15 shows the proposed design of a 1D linear phased array that consists of 20 elements, each having 1 x 14 mm dimensions. This linear phased array enables focusing and steering the pressure beam in the elevation direction by changing the phase of each element. However, in the lateral dimension, the intention is that the focal point will spread in the volume that faces the length of the array (i.e. 14 mm). Figure 15 shows the steering and focusing mechanisms of the phased array. The distance from the center of each element to the focal point is represented by distances d_1 to d_{20} . In order to compensate for the differences of each path (i.e. d_1 to d_{20}) to the focal point, the phase of the driving source that translates this difference into time delay or shifts is calculated as follows:

$$\phi_i = 2\pi \frac{(d_i - d_o)}{\lambda},$$

where d_i is the distance from element # i to the focal point (mm); d_o is the distance from the center of the array to the focal point (mm); λ is the wavelength of the sound wave (mm), and ϕ_i is the phase of element # i (rad).

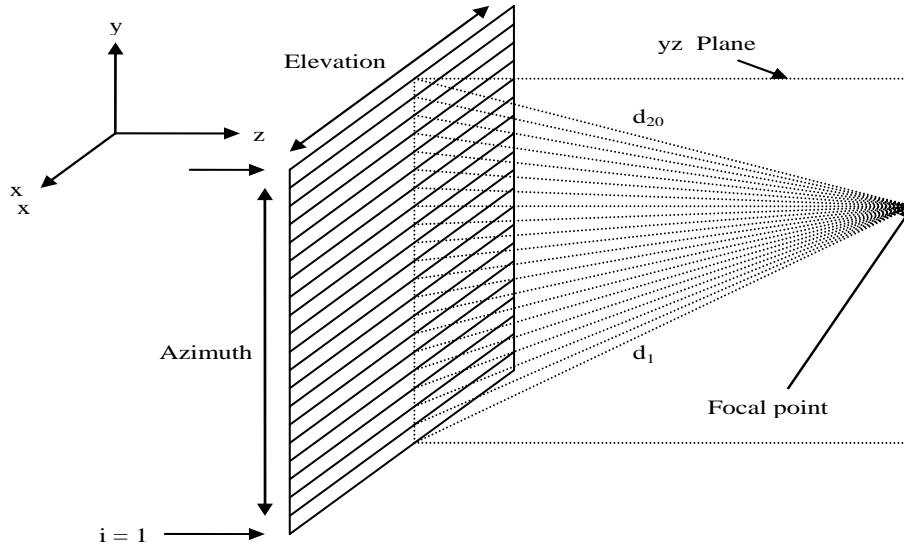


Figure 15. The focusing mechanism is shown for the twenty-element linear phased array. The distances from the center of each element to the focal point (d_1 to d_{20}) are used to calculate the phase and time delays for each element to compensate each driving signal in order to have all the propagated sound waves in phase at the focal point and to add their amplitudes at that point specifically.

The design took into consideration the anatomical measurements of the prostate and the rectal. Four 1D arrays, arranged in a cascade fashion, creates a 56 x 22 mm dimension for the total array including the inactive elements. The chosen frequency of the array is 1.2 MHz, a compromise between a frequency low enough to minimize the acoustic absorption to allow substantial acoustic energy deposition in the prostate a few centimeters away from the probe, and yet high enough that the width of each element, compared to the wavelength of the sound wave, allows for better focusing and steering mechanisms, and for ease of fabrication and soldering. Variation of the amount of power in each of the four arrays provides some control over the amount of heating in the vertical direction. The elements are many wavelengths long in the vertical direction and thus, the acoustic beam from each array ensonifies tissue within a fixed horizontal slab, directly in front of the array, of nominally the same vertical, 14 mm, height of the elements. Electronic phasing of the 20 elements that make up each array allows for steering the beam in the horizontal direction and adjusting the depth of focus in the longitudinal direction. This steering and focusing may be used to vary the heating in the transverse and longitudinal directions to achieve a uniform lateral temperature rise. The size of the array is a compromise between patient comfort and being able to put an adequate amount of acoustic energy on the prostate without overheating the rectal wall. The focal point of each single one-dimensional array can be controlled separately, while the driving power of each sub-element can be controlled independently. In addition to varying the position of the focal point, other parameters that may be optimized include amplitude, duty cycle and power changes for each single element, as well as phase and time of operation for each individual one-dimensional array.

C.2 Pressure Simulation

Simulation of the acoustic pressure field for a 1D phased array has been performed with the *k*-space method applied to an inhomogeneous 3-D human prostate model. A 64 x 64 x 46 mm water model was created to test the focusing mechanism of the designed 1-D phased array using the *k*-space method. As discussed earlier, the phased array represents a continuous source field with phase variations to each sub-element. The kerf width, represented by the lowest dimension between any two consecutive points in the model, is 0.25 mm. This representation will reduce computer memory requirements for such a large scale model. Included in the simulation are twenty elements with 1 x 14 mm² dimensions. Each element was driven temporally in a sinusoidal fashion with 1.2 MHz frequency and a unique phase shift that delays the produced wave to compensate for its path to the focal point compared to other elements. Spatially, a Gaussian approach shades each element due to the clamping boundary condition of each element which was applied using the baffled simple source calculations. The results appear in Figure 16, which shows the pressure squared 2D gray image for the middle slice in both yz (Figure 16a) and xz (Figure 16b) directions. The focal area spreads for about 30 mm in the z-direction while in y-direction it spans about 10 mm.

Figure 16 shows the results of propagating the ultrasound sound wave through the 3-D human prostate model. Selecting the central planes of the model allow plotting the pressure squared distribution in (Figure 17a and b) the yz-plane. While Figure 17a shows the central slice of the model in the yz-plane, the two-layered image in Figure 17b shows

the gray-scaled absorption distribution of the central slice as a background and the pressure squared distribution appears on top of that background.

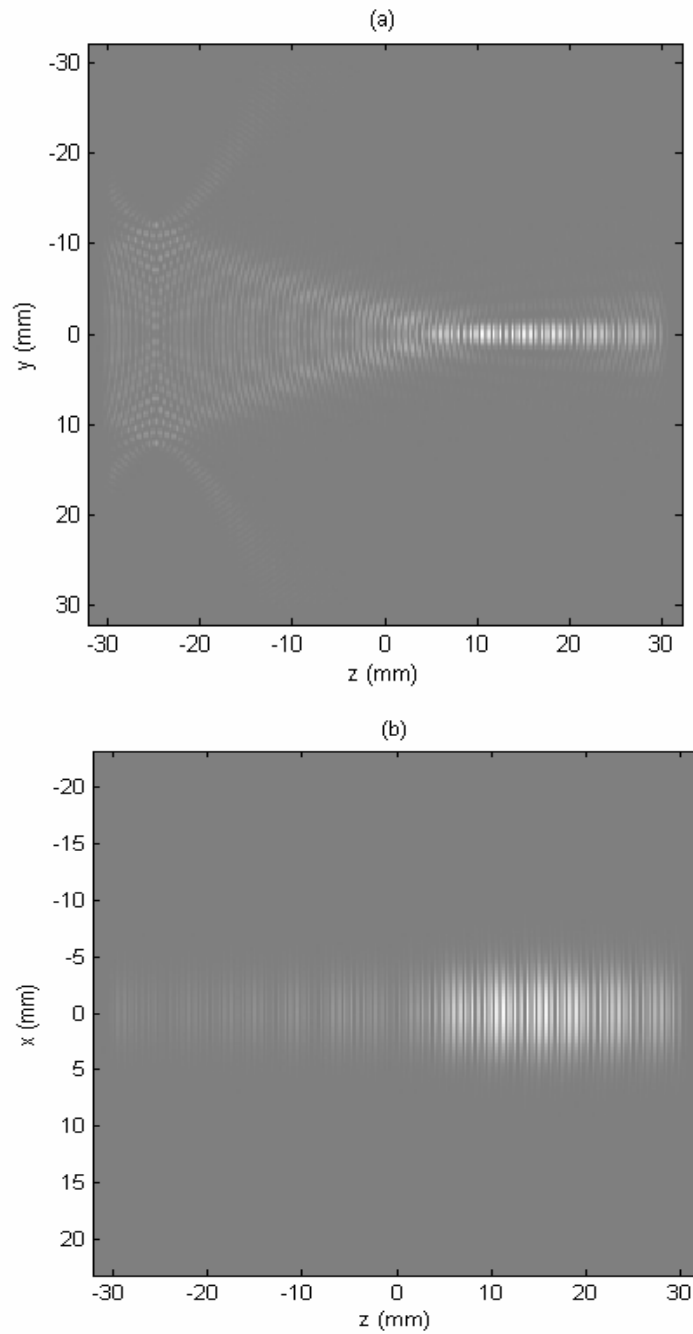
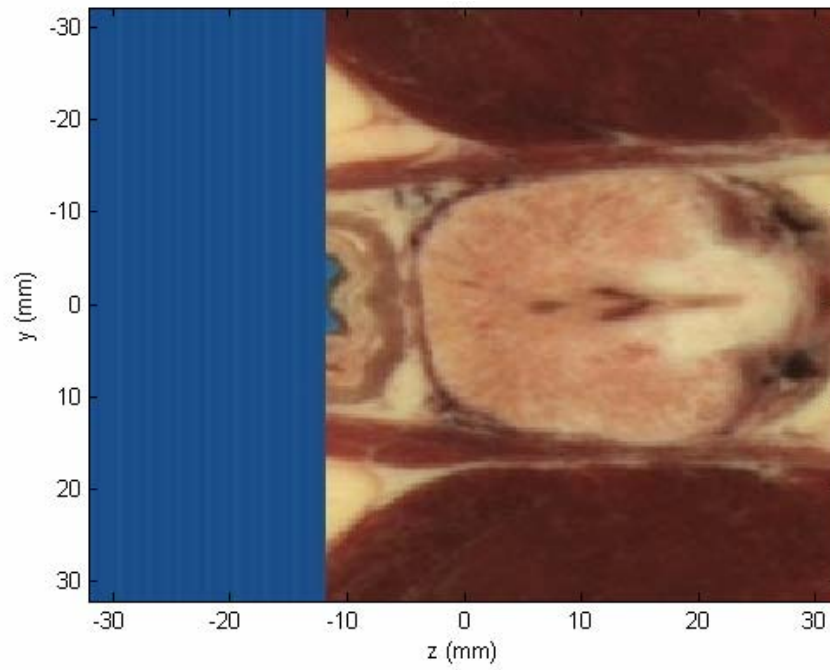


Figure 16 The normalized pressure squared distribution for the central planes of the 3-D water model showing (a) yz -plane and (b) xz -plane. The distributed focal area is about 30 mm in the z -direction while in the x -direction the focal area spans about 10 mm.

(a)



(b)

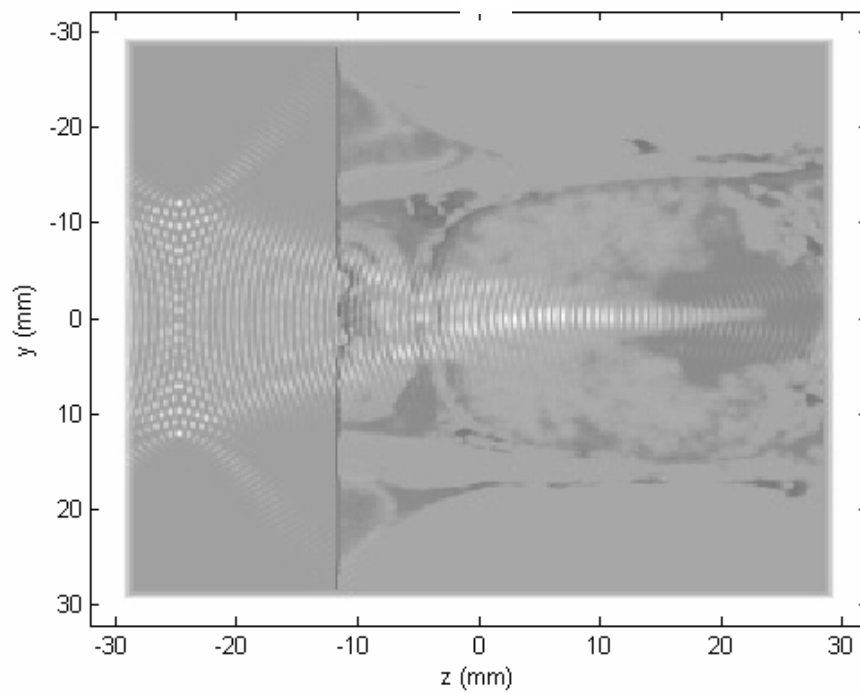


Figure 17. The normalized pressure squared distribution for the central planes of the 3-D human prostate model showing (a) yz-plane central image, (b) two-layered image with the absorption gray-scaled image (yz-plane) as a background and the pressure squared distribution shown on top of the background image.

The nearfield region is defined as the portion of sound field which is characterized by interference phenomena or Fresnel diffraction region. However, the farfield region is characterized by an interference-free sound field or Fraunhofer diffraction region. Previous researchers have studied beam behavior within the nearfield of a vibrating piston. Numerical investigation of the exact equation defining the sound speed field of a circular transducer has revealed that beam spot size is smaller than the size of the transducer. The -3 dB beam size in the nearfield is one-half the transducer size, for $a / \lambda \approx 5.6$, measured axially at a distance of $a^2 / 2\lambda$ (18). Rectangular shaped vibrators, on the other hand, are considered similar to circular radiators. The largest dimension of the rectangular shape is used instead of piston diameter. To apply these ideas to k -space simulation, the pressure distribution should follow the previously explained distribution. However, uniform spatial driving of each sub-element of the phased array produces pure plane wave with negligible spatial interference in the nearfield region. To overcome this problem, a spatial Gaussian shade (SGS) function is suggested as follows:

$$SGS = e^{\left(\frac{-0.5*a^2}{16}\right)},$$

where, a is a set of values representing distances from the center of each element to its length with 0.25 mm step size. SGS values at 3.5 mm away from each element center are 0.707 which satisfied the -3 dB power requirements. This method is considered reasonable for pressure evaluation beyond the $a^2 / 2\lambda$ distance. However, interference-free plane wave distribution, between the face of each active element and the $a^2 / 2\lambda$ distance, is deviated from the actual case. Division of each sub element into distinct simple sources, as conventionally represented earlier, will solve this problem. In this case, a coarse grid of 0.25 mm will not be a wise choice. Conventional simulation of distinct simple sources required 14,000 simple sources in each sub element. Simulation of each simple source radius requires at least 3 points. Previous simulation of a single simple source was achieved using 4 points radius. This requirement contradicts with our goal of utilizing a coarse grid model. For this reason, Gaussian shade was essential in this study to save memory and at the same time to accurately simulate the pressure distribution.

C3. Transducer Fabrication

An MRI compatible transrectal applicator housing for the array was built using Delrin® material. This cylindrical housing had dimensions to fit the designed ultrasound phased array. Figure 18 shows the housing design and its actual dimensions. The intention was that the housing would hold the ultrasound phased array in a rectangular bed as shown in the figure. It also provided an appropriate rear access for the electrical wiring of each element via its lumen. The design also included embedded specialized air and water circulation systems. Two pairs of brass tubes, included in the housing, accomplished air cooling for the back of the phased array and water coupling for the face of the array. The circulated water is held in front of the phased array using a latex membrane, which is fixed in place with o-rings in pre-made grooves as shown in the figure. The latex membrane formed a bolus of water surrounding the array. The description of both the air and water circulation systems will be discussed later. The

Delrin housing was fabricated in-house (Engineering workshop, Penn State, University Park).

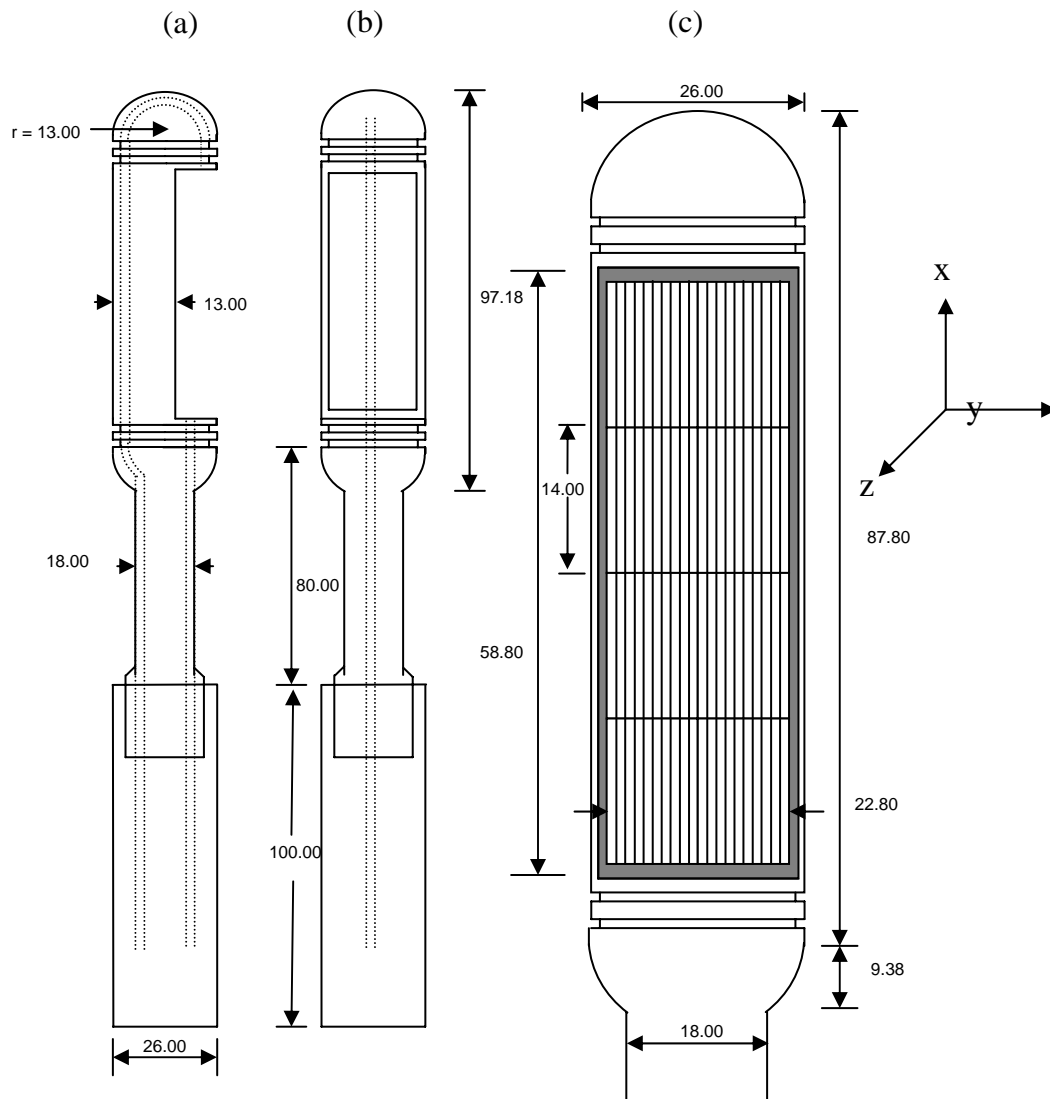


Figure 18. A sketch showing the transrectal intracavitary ultrasound probe in (a) Sagittal (b) coronal, and (c) expanded coronal. Dimensions are in mm.

Two prototypes were fabricated; both were constructed using lead zirconate titanate (PZT-8) (TRS Ceramic, State College, PA, USA). This kind of PZT is capable of withstanding higher driving electrical powers as compared to other materials such as PZT-5a and PZT-4. Two acoustical, matching layers were built on top of the PZT ceramic piece. These layers tended to increase the transmitted acoustical energy efficiency while delivering sound energy from high acoustical impedance (acoustical impedance of PZT-8 equals 36 Mrayl) (Z_p) to low acoustical impedance of water or soft tissue (acoustical impedance of water is 1.5 Mrayl) (Z_t). The choice of these matching

layers was dependent on pre-derived equations that calculate the impedance of quarter wavelength thickness layers as follows:

$$Z_1 = Z_p^{4/7} Z_t^{3/7}$$

$$Z_2 = Z_p^{1/7} Z_t^{6/7}$$

where, Z_1 , Z_2 , Z_p and Z_t are the acoustical impedances of the first layer, second layer, piezoelectric material and surrounding tissue or medium, respectively (19). The calculated acoustic impedance for the first and second layers, assuming water-coupling medium, were found to be 9.2 and 2.4 Mrayl respectively.

To construct the double matching layers, parafilm affixed an appropriate dimension PZT-8 piece to a glass plate with an adhesive primer poured onto the surface of the transducer face. The silver-conducting, first matching layer (acoustical impedance is 7.3 Mrayl) was poured onto the transducer surface, which was prepared using a 2:1 epoxy-to-silver mixture of Insulcast 501 (Insulcast, Roseland, NJ, USA) and 2-3 micron silver epoxy (Aldrich, Milwaukee, WI, USA). The whole assembly was centrifuged for 10 minutes and cured overnight; then the surface of the matching layer was sanded and lapped to the designed quarter wavelength thickness. Preparation of the second matching layer (acoustic impedance is 3.0 Mrayl) followed in a similar fashion but without any centrifuging mechanism. EPO-TEK 301 part A and part B (Epoxy technology, Billerica MA), mixed using a 20:5 mixing ratio created a clear uncured viscous fluid. Another piece of glass was used to spread this mixture on top of the first conductive layer and fixed using appropriate fixtures while curing overnight. The fixture and the second glass piece were removed. Another sanding and lapping process reduced the thickness of this layer to the required quarter wavelength thickness. The PZT-8 piece with its two acoustical matching layers was removed from the glass after heating the wax that bonded both of them. Dicing into 80 elements formed the complete array. The cuts were done by dicing the PZT-8 material 100% through its thickness using a dicing saw (Model 780, K & S-Kulick and Soffa Industries, Willow Grove, PA) at the Ultrasound Therapeutic Application Laboratory facilities (University Park, PA). The kerf width of 0.12 mm represents the thickness of the cutting blade. One major fabrication difference between prototype #1 and prototype #2 was the usage of a special kind of primer (CHEMLUK, AP-131, Lord Corp., Erie, PA) on top of the cleaned PZT piece before pouring the first conductive layer. This enhanced the bonding between these two materials. Only prototype #2 had this fabrication enhancement.

Figure 19 shows phased array #1 after building the matching layers and dicing the ceramic piece. The electrical wiring of the prototype array #1 involved 60 elements while wiring prototype array #2 involved 40 elements. The inner 2 one-dimensional arrays of prototype #1 were connected electrically in parallel (i.e. each two adjacent elements were soldered together as a one element). The outer 2 one-dimensional arrays of this prototype were connected separately. Ultimately, for prototype #1, 60 elements were soldered to 60 coaxial cables. On the other hand, for prototype #2, 20 wires were used to solder the first two one-dimensional arrays in parallel, while soldering the remaining two adjacent arrays together in parallel. Therefore, prototype #2 had 40 independently controlled elements.

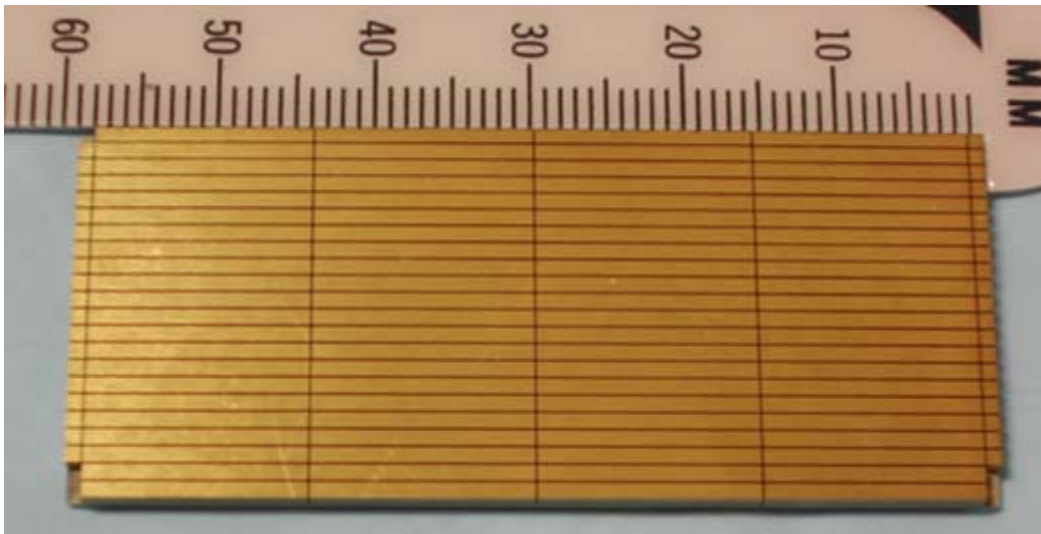


Figure 19. Photo showing the front view of the 20 x 4 element array.

Sixty, magnetic resonance imaging (MRI) compatible, 28 AWG, 32 ohm miniature coaxial cables, each 10.5 meters long (Belden Inc., St. Louis, Missouri), bundled together, formed the connection between the elements of the prototype arrays and the amplifier system. A micro-tip soldering pin was used to solder the core of each coaxial cable to its designated element. For this process, the soldering temperature was kept below 500°F (less than the Curie temperature of PZT-8) to prevent any damage to the piezoelectric ceramic. Figure 20 shows the soldered transducer. Four ground wires were soldered to four different points on the conductive matching layer. These wires, joined together and soldered to the ground points of each coaxial cable, formed one ground connection for the whole array. Figures 21 and 22 shows the final product of the transrectal applicator (prototype #2).

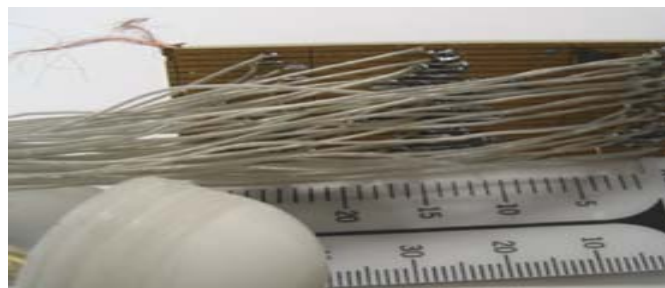


Figure 20: The soldering of the prototype array #1. Sixty miniature coaxial cables were soldered to the sixty element phased array. Four points were connected to different points of the conductive matching layer to be soldered to the shield connection of each coaxial cable.

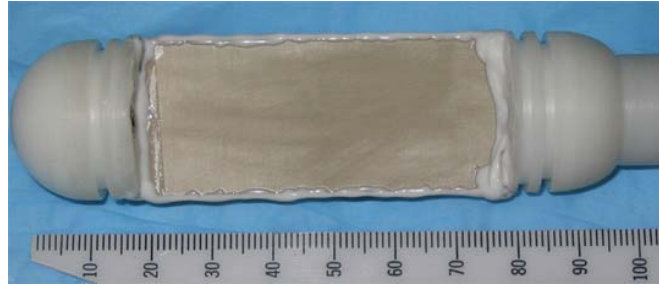


Figure 21: A photograph showing the transrectal probe utilizing prototype array #2, after assembling the soldered array and the appropriate brass tubes into the MRI compatible housing.

(a)



(b)



Figure 22: A photograph showing (a) the inflated water bolus of the transrectal probe and (b) the probe with its 10.5 m electrical cables and air and water circulation hoses.

In order to drive the 60 element phased array efficiently, the 60 coaxial cables were connected to a D1 male connector that connects directly to the 64 channel Amplifier system (UDS 2050PA, Advanced Surgical Systems, Inc., Tucson, Arizona) (Figure 23). The original amplifier was designed including an RS232 serial port for computer control software. It has 16 slots for amplifier cards and another 16 slots for electrical matching circuit boards. Each matching board card contains four electric matching circuits for individual elements. The purpose of these matching circuits is to match each element with its coaxial cable to the output impedance of the amplifier, which is a pure resistance of 50 ohms. This matching will enable the maximum power transfer from the amplifier to

the piezoelectric element and prevent any power reflection between the amplifier and the coaxial cable. This circuit is essential to increase the efficiency of the transducer and to eliminate any power dissipation between the amplifier and the array. The matching circuits were built using an electrical circuit using the Network Analyzer. While submerging the whole array in a large beaker filled with water, the network analyzer reads the electrical impedance at the designed frequency (1.2 MHz). The number of turns for the serial inductor helps reduce or increase the magnitude of the impedance. While parallel capacitance plays an important role in fixing the phase parameter, any change in the capacitance or the inductance will change both the magnitude and phase of the electrical impedance. For this reason a series of attempts were made for each electrical matching circuit to get both inductance and capacitance values to match the whole electrical parameters to 50 ohms at zero phase.



Figure 23. The 64 channels power amplifier system (Advanced Surgical Systems, Tucson, AZ).

Testing of the phased array prototypes used a constructed automated exosimetry system (20). A personal computer was connected to a four-motor positioning system (Velmex Inc, Bloomfield, NY) via an RS232 serial port controlled the exosimetry system. The computer also interfaced with a digital oscilloscope (Agilent 54622A, Agilent Technologies, Palo Alto, CA) through a general purpose interface bus (GPIB) card. The phased array was connected to a 64 channel amplifier with LC (inductive-capacitive) electrical matching circuits for each channel. Another computer controlled the parameters of each channel of the power amplifier: frequency, power, and phase. The receiving hydrophone was connected via a pre-amplifier to the digital oscilloscope.

The collected linear exosimetry scan of a single 1D phased array in the x, y, and z directions (Figure 24) were compared to the linear simulated results for the simple source, *k*-space in the watery model, and *k*-space in the prostate model simulations. Figure 15a shows linear cross section of the focal point in the z-direction. The focal point is shifted to $z = 0$ mm for all different linear results. The -3 dB distances in the z-direction are 28.0, 20.0, 20.0, 22.0 mm for the simple source simulation, exosimetry actual result, *k*-space simulation in the watery model, and *k*-space simulation in the prostate model, respectively. In the nearfield, the pressure squared level is maintained below -6 dB value for the simple source simulation, exosimetry results, and *k*-space simulation in the watery model. However, an elevated value of the pressure squared level is apparent for the *k*-space simulation in the prostate model; the value is kept below -4 dB. Figure 24b shows a linear cross section of the focal point in the x-direction. The focal

point is shifted to $x = 0$ mm. The -3 dB distances are 8.25, 4.75, 5.25, and 5.25 mm for the simple source simulation, exposimetry results, k -space simulation in the watery model, and k -space simulation in the prostate model, respectively. The -3 dB distances for the four methods was determined to be 2 mm.

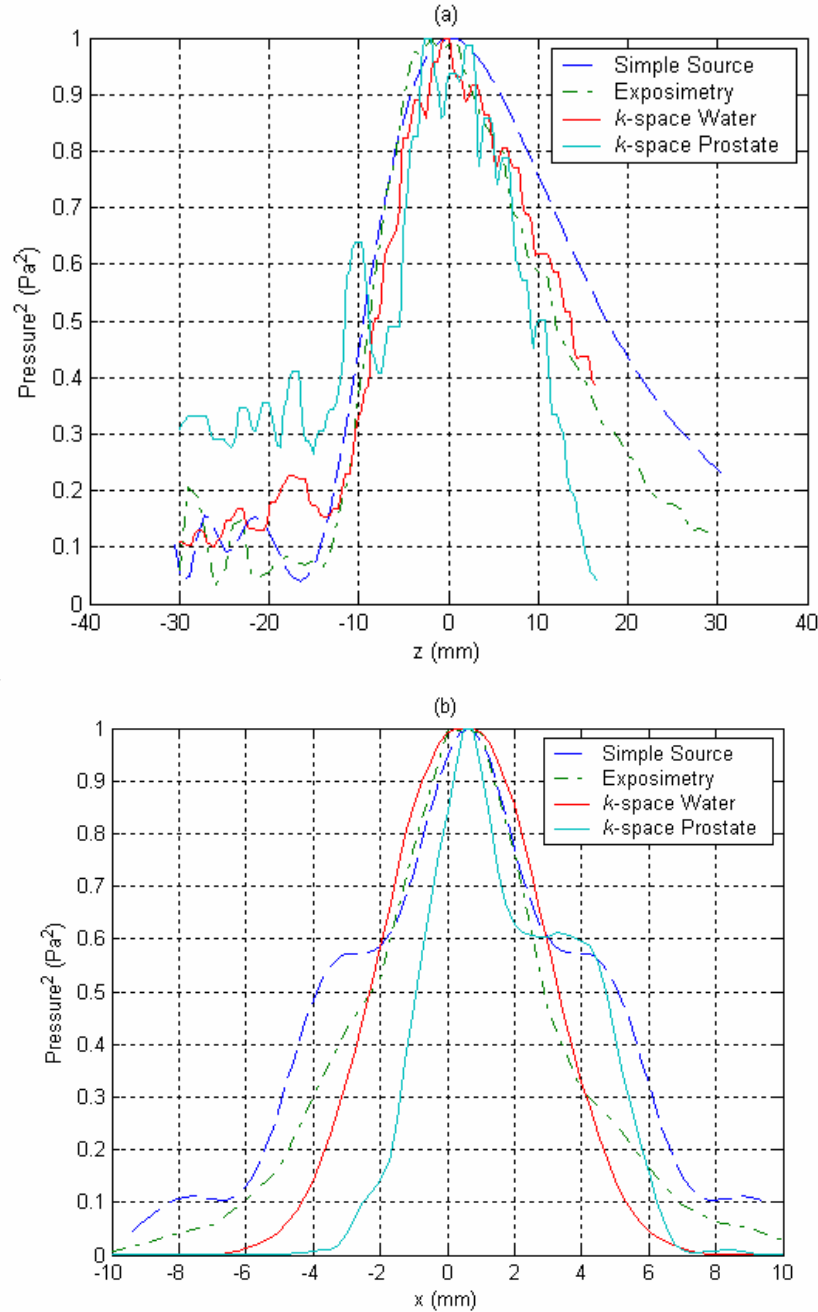


Figure 24 A comparison between normalized pressure squared for baffled simple source simulation, k -space simulation in homogeneous medium (water) and inhomogeneous medium (human prostate model) and exposimetry results while crossing through the focal point in the (a) z -direction and (b) x -direction

Temperature simulations were achieved using the bioheat transfer equation (21):

$$\rho c_t \frac{\partial T(x,t)}{\partial t} = k \left(\frac{\partial^2 T(x,t)}{\partial x^2} \right) - w c_b (T(x,t) - T_a) + q(x)$$

where, $T(x,t)$ is tissue temperature ($^{\circ}\text{C}$); c_t is the specific heat of the tissue ($3770 \text{ J/kg}^{\circ}\text{C}$); c_b is the specific heat of the blood ($3770 \text{ J/kg}^{\circ}\text{C}$); ρ is the density (998 kg/m^3); k is the thermal conductivity ($0.5 \text{ W/m}^{\circ}\text{C}$); T_a is the arterial blood temperature (37°C); w is the tissue perfusion ($8.33 \times 10^{-9} \text{ kg/m}^3\text{s}$); $q(x)$ is the power deposited locally in the tissue (Wm^{-3}). The deposited power was extracted from three perpendicular lines that crossed the focal volume of simulated and measured acoustical pressure variations. Two minutes of temperature rise was simulated for the extracted lines. Initially, the temperature was set to 37°C ; the temperature of the focal point was allowed to increase to 43°C . The results are shown in Figure 25. The temperature was allowed to increase from 37°C to 43°C at the maximum point of the focal volume. A watery medium was selected with a starting temperature of 37°C . Two minutes of heating was simulated to reach the steady state temperature of 43°C .

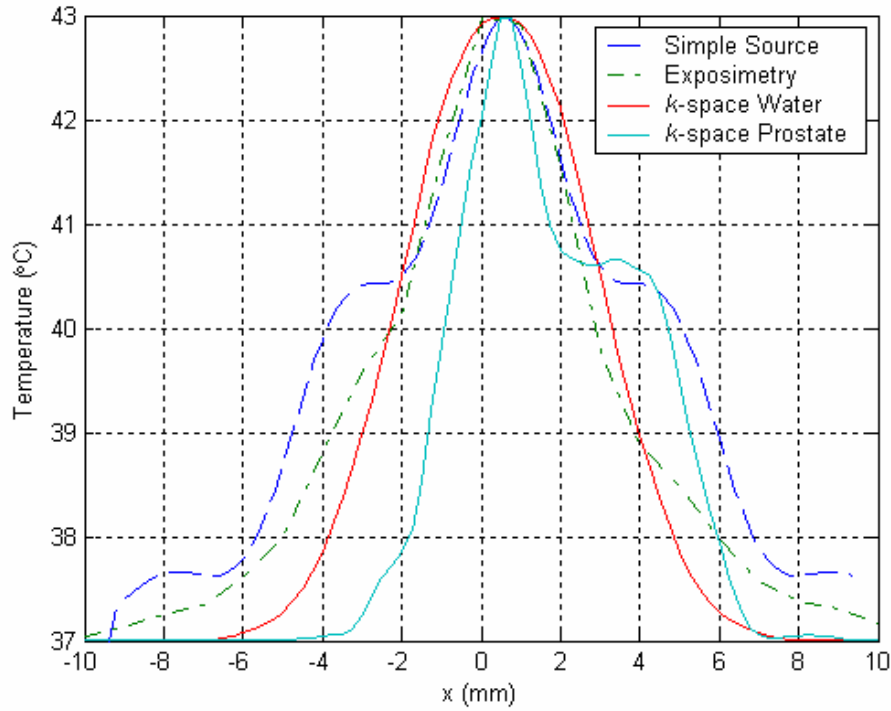


Figure 25. A comparison between temperature distribution in a water medium for baffled simple source simulation, k -space simulation in a homogeneous medium (water) and an inhomogeneous medium (human prostate model), and exposimetry results while crossing through the focal point in the x -direction.

D. *In vitro* and *in vivo* hyperthermia monitored with MR thermometry

Previous researchers have successfully demonstrated the application of temperature feedback control for thermal treatment of disease using MR thermometry. Using the temperature-dependent proton resonance frequency (PRF) shift, ultrasound heating for hyperthermia to a target organ (such as the prostate) can be tightly controlled. However, using fixed gain controllers, the response of the target to ultrasound heating varies with type, size, location, shape, stage of growth, and proximity to other vulnerable organs. To adjust for clinical variables, feedback self-tuning regulator (STR) and model reference adaptive control (MRAC) methods have been designed and implemented utilizing real-time, on-line MR thermometry by adjusting the output power to an ultrasound array to quickly reach the hyperthermia target temperatures. The use of fast adaptive controllers in this application is advantageous, because adaptive controllers do not require *a priori* knowledge of the initial tissue properties and blood perfusion and can quickly reach the steady state target temperature in the presence of dynamic tissue properties (e.g. thermal conductivity, blood perfusion). This research was conducted to rapidly achieve and manage therapeutic temperatures from the ultrasound array utilizing novel MRI-guided adaptive closed-loop controllers in both *in vivo* (rabbit & canine) experiments (22, 23).

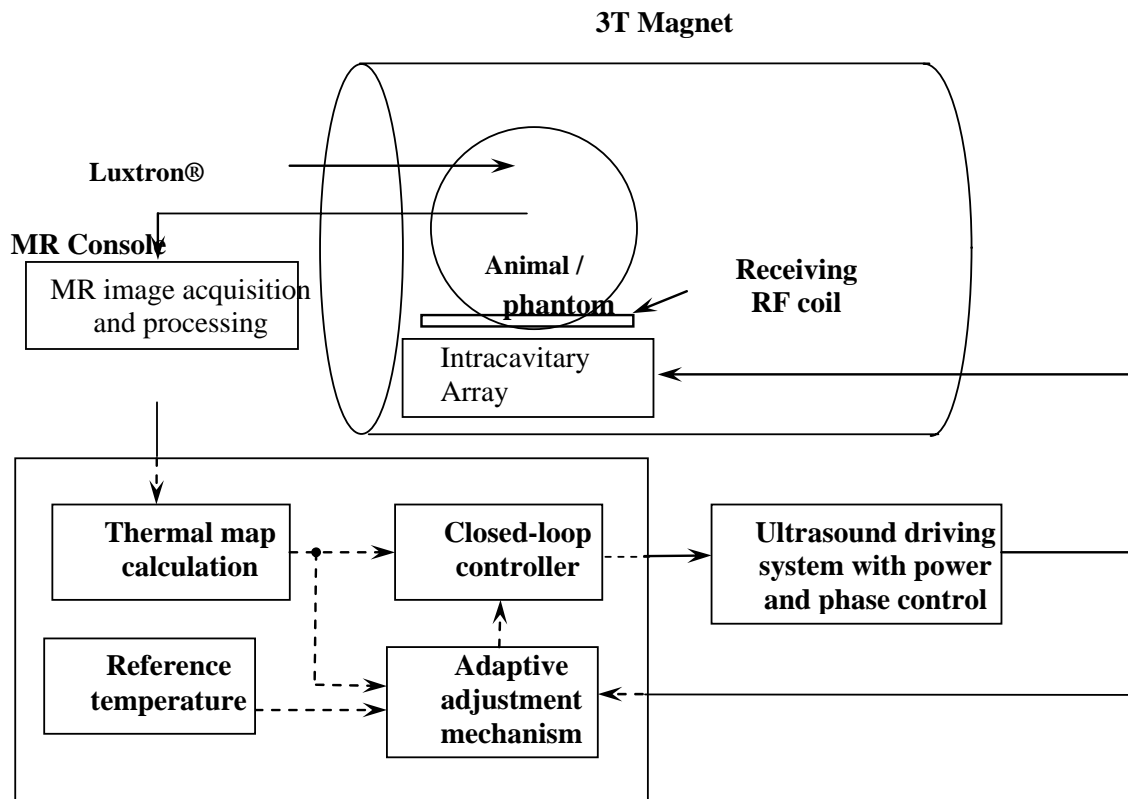


Figure 26. Block diagram of the ultrasound hyperthermia system using MRI thermometry as thermal feedback. The intracavity ultrasound array is placed inside the MR scanner for hyperthermia treatment together with the animal/phantom.

The block diagram shown in Figure 26 displays the entire system used to conduct the ultrasound hyperthermia control experiments using MR thermometry. In the figure, an intracavitary ultrasound array was designed for transrectal prostate cancer hyperthermia. The electrical driving signal (phase and amplitude) to the array was amplified by a 64-channel programmable ultrasound driving system with a maximum output power of 60 W per channel. The ultrasound array and animals were placed inside a birdcage coil to receive/transmit the radio frequency (RF) signal for MRI measurement. Temperature maps constructed from MRI data using proton resonance frequency (PRF) shift were acquired and compared to a desired reference temperature (24). The adaptive feedback controllers programmed in the PC used this information in adjusting the amount of power applied to produce the desired temperature response.

Fast gradient sequence was used to acquire thermal images for feedback control of the hyperthermia experiments. The MEDSPEC S300 3 Tesla magnet in the Center for NMR Research at the Penn State Hershey Medical Center was used for these experiments. To test the system, a simple experiment was carried out to monitor the temperature elevation in bovine tissue. The unfocused transducer was used for this test. A special apparatus held the transducer and its bolus close to the bovine tissue, and the whole apparatus was inserted in the RF head coil which was placed in the uniform field of the static magnetic field and the gradient coils. Three MRI slices were produced to locate appropriate volume inside the bovine tissue for temperature monitoring. A base line image was produced using the fast gradient echo sequence to produce an image using these parameters (ET = 150, RT = 200, flip angle = 30, FOV = 14 x 14 cm², matrix size = 128 x 64, and acquisition time = 6.4 s). The transducer was excited for 5 minutes before acquiring another image.

Seven New Zealand white rabbits (4~5 kg, males) were used for 24 separate control hyperthermia experiments. All animal experiments were conducted with procedures approved by the Penn State Institutional Animal Care and Use Committee (IACUC). The experimental setup for the rabbits test was similar to the *ex vivo* phantom experiment. Rabbits were anaesthetized with an intramuscular injection of ketamine (40 mg/kg, Fort Dodge Animal Health, Fort Dodge, IA) and xylazine (10 mg/kg, Phoenix Scientific, Inc., St. Joseph, MO). After shaving the thigh, depilatory agent was applied to the skin to eliminate any remaining hair. The rabbits were laid down on the platform on their lateral position and their shaved thigh was just above the ultrasound transducer through the acoustic window. To make effective acoustic contact, ultrasound gel were applied between the water bolus membrane and the rabbit thighs. The rabbit controlled heating experiments were performed in a similar manner as the *ex vivo* experiments except the control variables used a time constant for the reference temperature at $4\tau = 8$ minutes and the ultrasound exposure time was 25 minutes.

Using rabbit thigh muscle, *in vivo* animal experiments were conducted using a similar procedure as the bovine muscles phantom experiments with the animal anesthetized by the combination of ketamine (40 mg/kg) and xylazine (10 mg/kg). Figure 27 is an axial view of the MR temperature map, showing the rabbit thigh muscle above the ultrasound array surrounded by its water filled bolus. Both the animal and phantom experiments used head-sized birdcage coil with a length of 29 cm and inner diameter of 26 cm. For rapid hyperthermia heating, the time constant of the target temperature was

selected to be less than 2 minutes for a total experimental time of 25 minutes. A region of interest (ROI) was pre-selected for the control area.

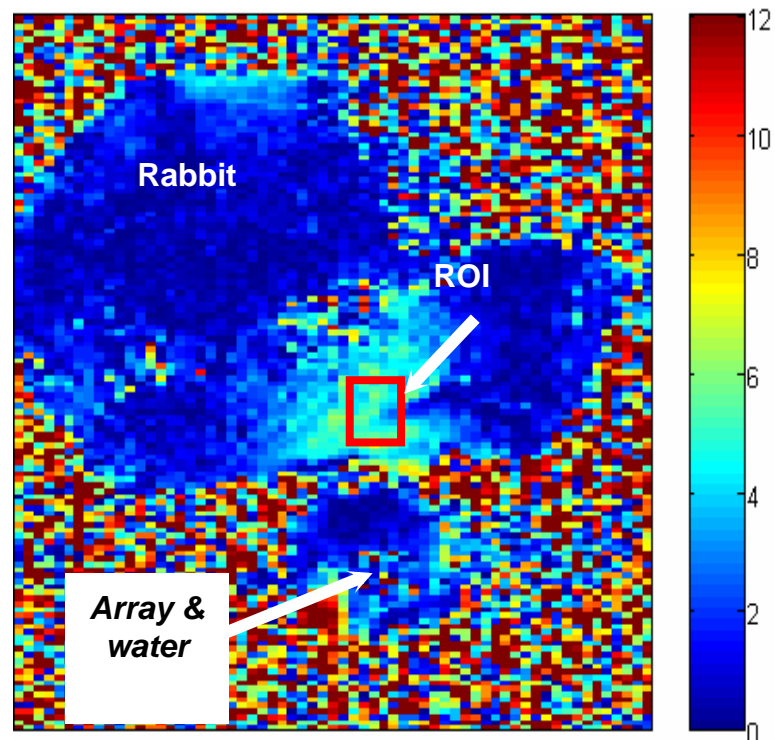


Figure 27. The temperature map (temperature change indicated by the color bar on the right of the figure in °C) of the axial view of the MRI-guided *in vivo* ultrasound hyperthermia experiments setup.

Ultrasound hyperthermia results have been demonstrated for both the *in vitro* and *in vivo* experiments. Figure 28(a) shows the results of the nine *in vitro* experiments, plotting the target temperature (solid line) and the MR temperatures with a steady state temperature of 38°C. Starting at an initial phantom temperature of 28°C, the temperature reaches the steady state within 6.0 minutes; deviation from the target profile was no greater than $\pm 1.37^\circ\text{C}$. Similar to the *in vitro* results, *in vivo* temperature change can be seen in Figure 28(b) where the rabbit thigh muscle was heated initially from 36.5°C for 25 minutes. For this experiment the target temperature was 44.5°C and was achieved in 8.0 minutes. The maximum variation from the desired temperature profile was -3.9°C ; after reaching steady state, tissue temperature was maintained at $44.5^\circ\text{C} \pm 1.2^\circ\text{C}$.

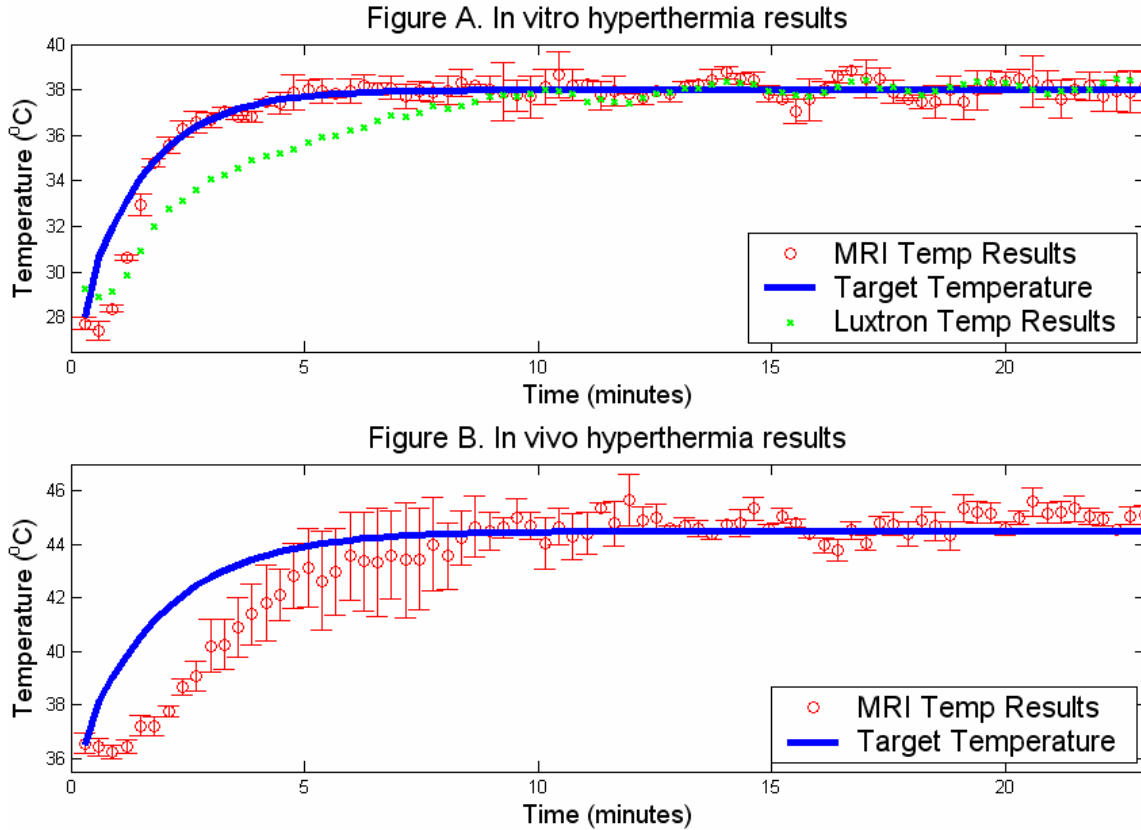


Figure 28. Example (a) *in vitro* and (b) *in vivo* ultrasound hyperthermia experiment temperature rise results in an MRI. The (a) temperature elevation and reference temperature profile is plotted for 25 minutes of ultrasound exposure using bovine muscle as a tissue phantom. An example (b) *in vivo* rabbit hyperthermia temperature profile is also shown.

Temperature regulation using the control methods and MRI thermal feedback demonstrates the stability and robustness during the ex vivo and in vivo ultrasound hyperthermia experiments. To optimize the controller's performance, several parameters have been tested such as time constants of reference temperature, adaptation gains, and initial values of the control variable. The parameters were tested in such a way that one of them was varied, while the others were held constantly. Then the controller's response of rise time, overshoot temperature, and steady state errors were analyzed and summarized in Table 2 under the column of "Experimental result summary".

From Table 2, examining the controller results from experiment #1, it is indicated that with small time constant ($4\tau = 3$ min) the controller is able to reach the therapeutic level faster (3 ± 0.5 min $<$ 8 ± 0.5 min) than with large time constant ($4\tau = 8$ min), however, it caused larger overshoot ($1.9 \pm 0.6^\circ\text{C} > 1.3 \pm 0.3^\circ\text{C}$) and greater oscillations ($1.8 \pm 0.5^\circ\text{C} > 1.5 \pm 0.6^\circ\text{C}$). Based on the allowable overshoot and oscillations, in this research, 4τ was limited to times greater than 5 minutes in order to ensure animal safety. From the results of experiment #2 in Table 2, with smaller adaptation gain, the adaptive controller updated the control parameters in a slower way so that it took longer (8.1 ± 0.5 min $>$ 7.85 ± 0.5 min) for the control variables to reach the optimal values than with the larger gain,. Not surprisingly, the conservative manner also resulted in smaller overshoot

$(1.3 \pm 0.3^{\circ}\text{C} < 1.5 \pm 0.4^{\circ}\text{C})$ and perhaps smaller steady state error although not shown in this research.

Since the acquisition of a slice of MRI temperature image took longer time (7.4 seconds per measurement) than the fiber optic thermometer (up to 0.25 second per measurement), it took a much longer time for the controllers to reach the optimal values starting from zero initial values. To improve this, the initial values optimized from simulations and previous experiments were applied. Table 2 also shows that with optimized initial parameters values, the performance of the control system was significantly improved, yielding smaller rise time ($6 \pm 0.5 \text{ min} < 12 \pm 0.5 \text{ min}$), less overshoot ($1.1 \pm 0.3^{\circ}\text{C} < 5.2 \pm 0.6^{\circ}\text{C}$), and lower steady state oscillations ($1.5 \pm 0.6^{\circ}\text{C} < 3.5 \pm 0.5^{\circ}\text{C}$).

Table 2. The experimental results of rise time, overshoot, and steady state errors by examining the variation of one MRAC control variable at a time for adaptive MRI thermal feedback control of ultrasound hyperthermia. For each experiment (i.e. 1, 2 or 3), the control parameter under investigation is marked as bold.

Exp. #	Control parameters			Experimental results summary		
	Time constant (min)	Adaptation gain	Initial values	Rise time (min)	Over-shoot ($^{\circ}\text{C}$)	Steady-state error ($^{\circ}\text{C}$)
1	$4\tau = 3$	0.005	optimized value	3 ± 0.5	1.9 ± 0.6	1.8 ± 0.5
	$4\tau = 8$	0.005	optimized value	8 ± 0.5	1.3 ± 0.3	1.5 ± 0.6
2	$4\tau = 7.8$	0.005	optimized value	8.1 ± 0.5	1.3 ± 0.3	1.5 ± 0.5
	$4\tau = 7.8$	0.015	optimized value	7.85 ± 0.5	1.5 ± 0.4	1.5 ± 0.5
3	$4\tau = 6$	0.005	zero	12 ± 0.5	5.2 ± 0.6	3.5 ± 0.5
	$4\tau = 6$	0.005	optimized value	6 ± 0.5	1.1 ± 0.3	1.5 ± 0.6

One important issue during MR thermometry is motion. Temperature measurement using MR is actually based on the subtraction of current image with respect to the initial one. Motion during the experiment can result in measurement errors or mistaken measurements, which can typically cause the controller to oscillate or even become unstable. In this research, the temperature was acquired by averaging a region of MR measurement ($4 \times 3 \text{ mm}^2$). This can effectively compensate for small motion such as breath. Results from the in vivo experiments showed the controller worked well under small motion. Large motion such as animal kick was also observed during the experiments typically followed by experiment failure. To minimize the animal movement, anesthetized drug should be paid special attention to avoid movement as much as possible.

Canine (six, ~15 kg mongrel, male) were used for the prostate hyperthermia experiment with the MR thermometry and adaptive temperature controller. Dogs were anaesthetized with Telazol (100 mg/ml, reconstituted with Tiletamine hydrochloric acid and Zolazepam hydrochloric acid, Fort Dodge Animal Health, Fort Dodge, IA). The rectum of the dogs were and filled with degassed acoustic coupling gel. After placing the dogs on the MRI table, the array was inserted. Good contact was verified by MRI images before baseline temperature sensitive MRI images were collected. The temperature from a pre-defined region in the canine prostate was selected as the feedback to the controller. The target temperature was set to 43°C , the time constant of the reference was $4\tau = 6$ minutes, and the exposure time was chosen to be 10 minutes.

Figure 29(a) shows an axial view of the experimental setup (typical results) indicating the ultrasound array coupled to a canine prostate through the water bolus inside the rectum. The region of interest (ROI) was chosen in the middle of the prostate. Average MR measurement in the ROI was sent to the controller as thermal feedback. The plot in Figure 20(b) shows within 6.5 ± 0.5 minutes the canine prostate temperature reached the $43 \pm 2.0^{\circ}\text{C}$ for a total of 5 experiments. The target temperature was set to be 43°C with exponential time constant $4\tau = 6$ minutes. To save the animal for as many experiments as possible, each experiment was stopped one minute after the steady-state temperature was reached.

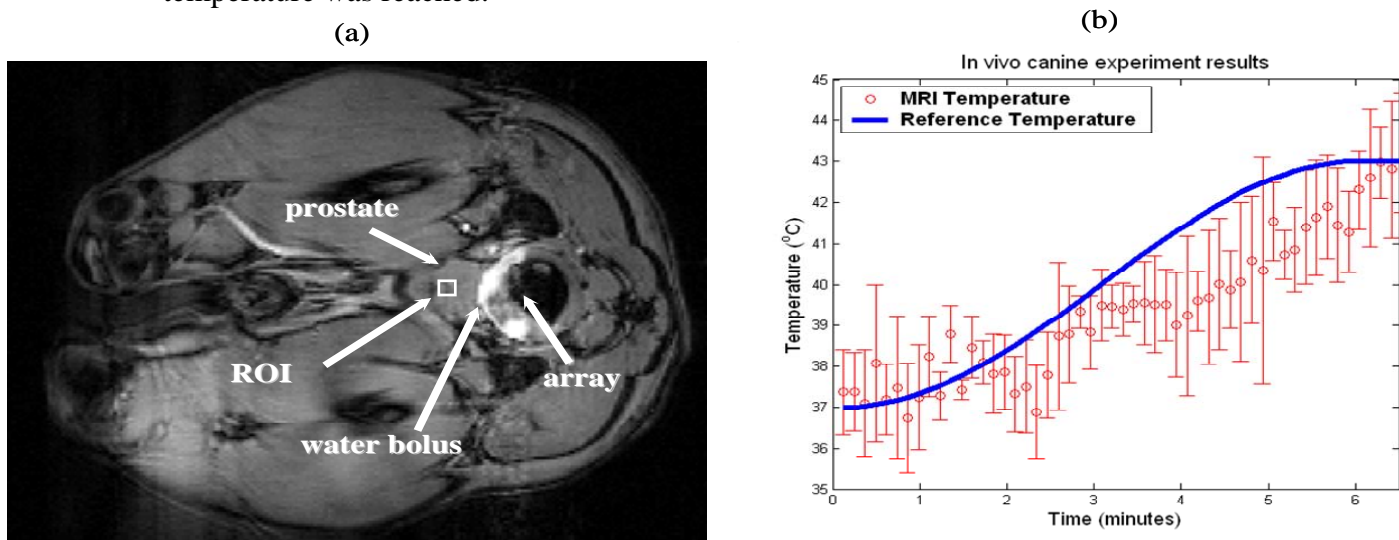
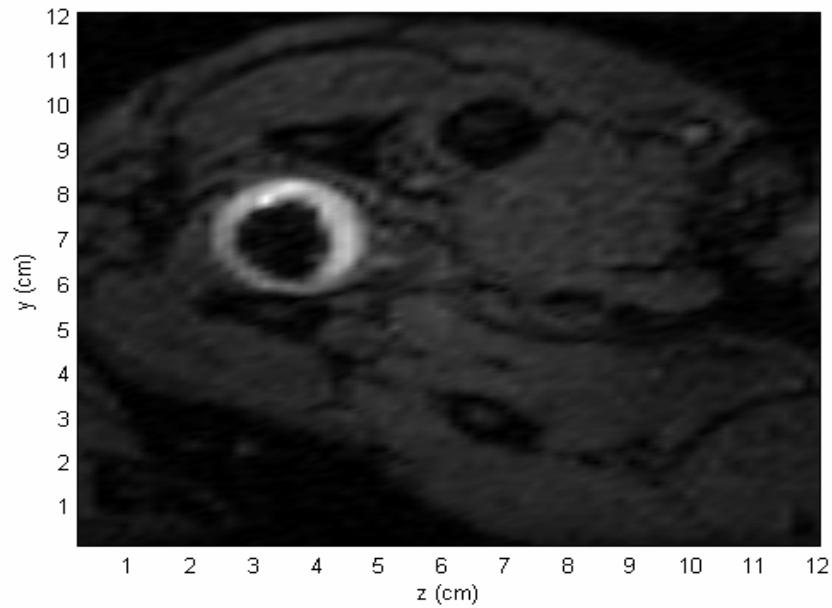


Figure 29 (a) MR image of the axial view of the canine prostate, showing the location of the ultrasound array, canine prostate and water bolus. (b) In the preliminary canine prostate hyperthermia experiments, the agreement of MR temperature measurements and the reference indicates the potential of intracavitary ultrasound hyperthermia treatment for human prostate cancer.

From another canine experiment, Figure 30a shows an MRI magnitude image of a selected cross sectional slice through a canine prostate gland. The hyperthermia transrectal probe (black-colored) is shown surrounded by a bolus of water (bright white-colored). The prostate gland is shown facing the bolus. A complex structure of muscle and fat tissues are surrounding the prostate gland and the water bolus. Figure 30b shows

a thermal distribution image after five minutes of driving the transducer. Heat is distributed through the prostate gland that faces the water bolus. Relative temperature values are varied in these areas from 6°C to 9°C. Figure 31 shows controlled temperature of the prostate gland for periods of twenty minutes. For the hyperthermia transducer, the rise time is 6.9 ± 1.74 min and the steady state temperature is 5.8 ± 1.44 °C for a 20 minute treatment.



(b)

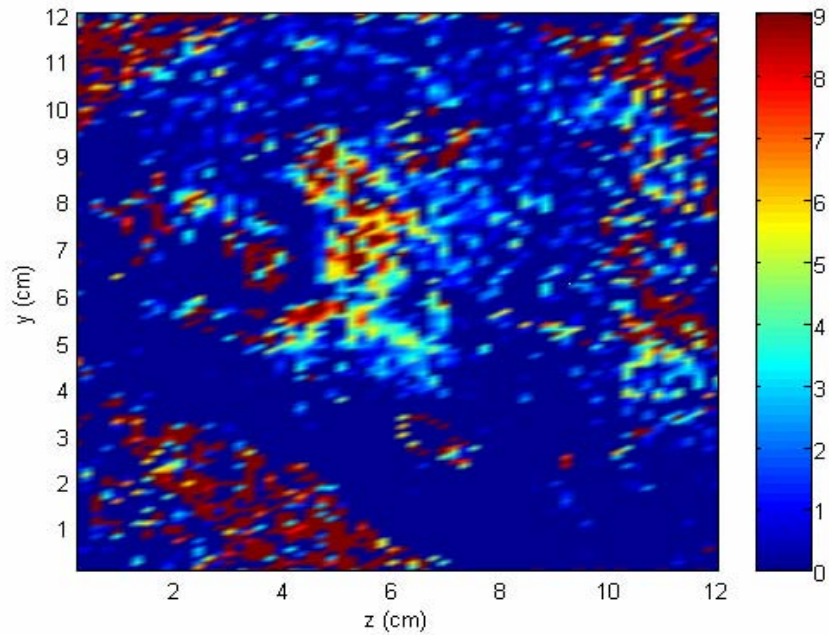


Figure 30 (a) MRI magnitude image of a selected canine slice showing the unfocused transducer cross sectional view facing the prostate gland. (b) Thermal distribution (color bar) image after driving the unfocused transducer for five minutes.

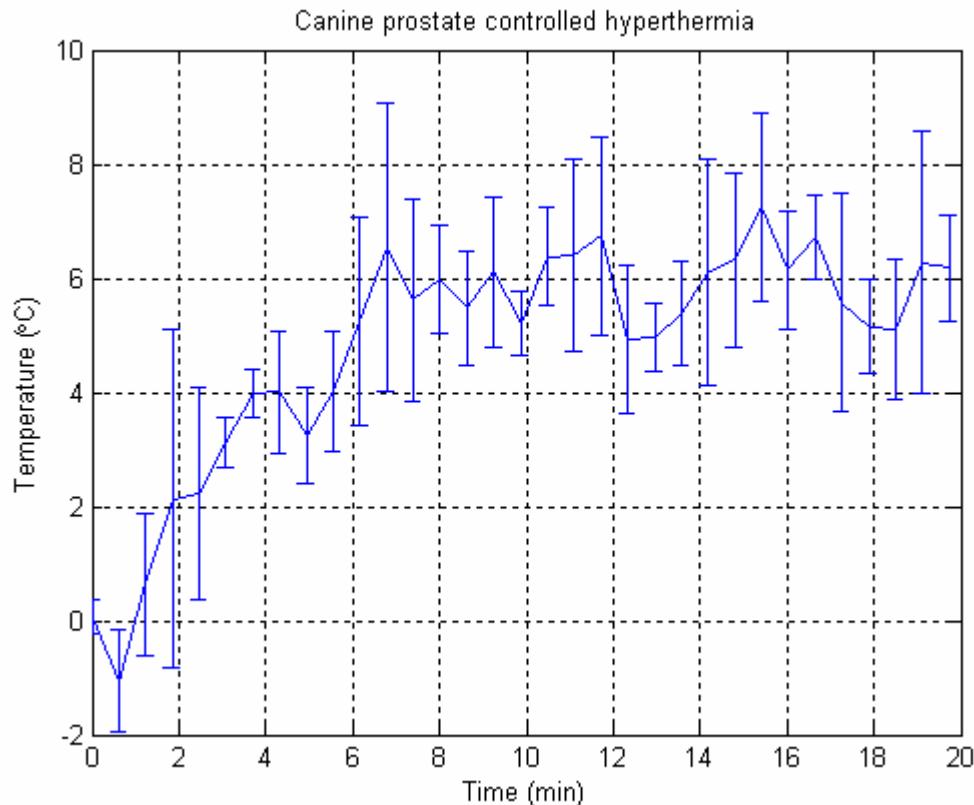


Figure 31. *In-vivo* controlled hyperthermia results using MRI thermometry and switching controller for the hyperthermia array on canine prostate.

The 2D phased array using MRI-guided adaptive closed loop controller system *in vivo* in both canine prostate and rabbit thigh experiments worked well for up to 40 minutes. For the examples shown, (i.e. Figure 31) only the transient temperature versus time region is shown since there was little change in the temperature at steady state. Generally, as before, animal motion is a problem for long experiments. Nevertheless, MRI provides an accurate and noninvasive thermometry method to monitor, to guide and to control the ultrasound hyperthermia treatment.

3. KEY RESEARCH ACCOMPLISHMENTS:

- Visible Human Project data used for determination of three-dimensional tissue map for the prostate region by segmentation.
- Optimization of the array design strategy through modeling the tissue characteristics using:
 - Nonlinear acoustic propagation
 - “Fresnel-lens-like” Transducer with aimed, incoherent beams of sound
 - Wave propagation using the k -space method
- Implement relaxation absorption, acoustic nonlinearity, and heat transfer effects using k -space method (Method can be applied for other tissue types such as breast tissue or liver tissue).

- Constructed and implemented a hyperthermia transducer with clinical applicator body design with a working multielement array
- Ultrasound exosimetry of hyperthermia array with good agreement between model (computational k-space method and experimental results).
- MRI thermometry results using the hyperthermia ultrasound array with controlled feedback. Experimental results *in vitro* and *in vivo* (rabbits and canines).

4. REPORTABLE OUTCOMES:

Funding from this award has been used to produce a published manuscript, submitted manuscripts, conference proceeding and has been cited in several invited talks. In all publications and invited talks using the data resulting from this grant, the Department of Defense Congressionally Directed Medical Prostate Cancer Research Program has been gratefully acknowledged. Copies of the manuscripts, proceedings and presentations are included in the appendix.

Publications

- Saleh, K. and Smith, N.B., Two Dimensional Array Design for Tissue Ablation for Treatment of Benign Prosthetic Hyperplasia, *International Journal of Hyperthermia*, 20:1, February 2004, 7-31.
- Saleh, K. and N.B. Smith, Design and evaluation of a 3 x 21 element 1.75 dimensional tapered ultrasound phased array for the treatment of prostate disease, *Materials Research Innovation*, 8, (2) 2004, pp 121-124.
- Sun L., Collins C. M, Schiano, J. and Smith, N.B "Adaptive control for MRI-guided ultrasound hyperthermia treatment for prostate disease: *in vivo* and *ex vivo* results" *Mag Res Engineering*, Vol. 27B, Issue 1, Oct 2005, Pages: 51-63.
- Saleh, K. and N.B. Smith, "A 63 element 1.75 dimensional ultrasound phased array for the treatment of benign prostatic hyperplasia", *BioMedical Engineering On-Line*, 4:39, 2005.
- Al-Bataineh, O., Mast, T., Keolian, R., Sparrow, V., Park, E., and Smith, N, "Utilization of the k-space method in the design of a hyperthermia phased array" *submitted to Ferroelectrics Special Issue: Piezoelectric Composites and Other Related Areas*, 2005.
- Al-Bataineh, O., Collins C. M, Park, E., Lee, H. and Smith, N.B, "MR thermometry verification of a hyperthermia ultrasound array designed using the k-space computational method" *submitted to BioMedical Engineering On-Line*, 2005.

Abstracts

- Saleh, K. and Smith, N.B., Two Dimensional Array Design for Tissue Ablation for Treatment of Benign Prosthetic Hyperplasia, *International Society of Magnetic Resonance in Medicine (ISMRM) Workshop on MRI-Guided Focused Ultrasound Surgery*, 19-21 June 2002, Cambridge, MA. pp 63-66.
- Al-Bataineh. O.M., Keolian, R., Sparrow, V., Smith, N.B., Optimized Hyperthermia Treatment of Prostate Cancer using a Novel Intracavitary Ultrasound Array, 146th Meeting of the Acoustical Society of America, 10-14 November 2003, Austin, Texas.

- Keolian, R., V. Sparrow, Harpster, L., and N.B. Smith. 2003. A "Fresnel-Transducer" for Prostate Hyperthermia Treatment *Acoustical Society of America*, 146th Meeting of the Acoustical Society of America, 10-14 November 2003, Austin, Texas.
- Saleh, K. and Smith, N.B., " Design and evaluation of a 63 element 1.75-dimensional ultrasound phased array for treating benign prostatic hyperplasia," *Acoustical Society of America*, 146th Meeting of the Acoustical Society of America, 10-14 November 2003, Austin, Texas.
- Sun, L., Schiano, J. and Smith, N.B " Novel Adaptive Control Methods for Ultrasound Thermal Treatment with a Two-Dimensional Tapered Array," *Proceedings of the IEEE 2003 Ultrasonics Symposium*, Honolulu, Hawaii, 8-11 October 2003, pp. 1274-1277.
- Sun L., Al-Bataineh O., Collins C., Smith M.B., and Smith, N.B. Fast adaptive control for MRI-guided ultrasound hyperthermia treatment for prostate disease: in vitro and in vivo results, International Society of Magnetic Resonance in Medicine (ISMRM) Twelfth Scientific Meeting & Exhibition, Kyoto, Japan, 15-21, May 2004.
- L. Sun, J.L. Schiano and N.B. Smith, PID and Adaptive Controller Design for Ultrasound Thermal Treatment of Prostate Diseases, International Association of Science and Technology for Development (IASTED) International Conference, Applied Modeling and Simulation (AMS 2002) November 4-6, 2002 MIT, Cambridge, USA pp 347-352.
- Smith, N.B. "Therapeutic Applications of Ultrasound: Treatment of Prostate Disease", Invited seminars to:
- Case Western Reserve University- Department of Biomedical Engineering, 14 March 2002.
 - University of Illinois Urbana Champaign, Bioacoustics Research Laboratory Seminar Series, March 4, 2003
 - University of Illinois Chicago – Department of Bioengineering, May 2, 2003
 - University of Virginia - Department of Biomedical Engineering, Nov. 7, 2003
 - Penn State University, College of Medicine Hershey, Nov. 11, 2003.
 - University of Illinois Urbana Champaign, Department of Clinical Veterinarian Medicine, 20 August 2004
 - Penn State University, Department of Electrical Engineering, 23 September 2004

5. CONCLUSIONS:

Uniform heating of the prostate to 43°C for 30 minutes is essential to satisfy thermal dose requirements in hyperthermia treatment of prostate cancer. Intracavitary ultrasound applicators offer non-invasive and non-ionizing methods to accomplish hyperthermia therapy necessities against prostate cancer with reduced side effects compared to competing modalities. To achieve thermal uniformity through such a complex physiological organ utilizing ultrasound technology, two different designs were investigated depending on computer modeling and different computational methods. A two dimensional phased array was constructed and tested *in vivo* to assess the significance of this applicator in prostate cancer hyperthermia therapy.

The first effort of this research project focused on the initial design of the array based on computer simulations of the ultrasound energy interactions with the prostate and surrounding tissue. In accordance with the initial aims and timetable, the areas were: (a) elucidation of the ultrasound interaction with the prostate tissue (tissue modeling) (b) beam design and optimization, and (c) hyperthermia array design and fabrication. Previously, much research in this area has treated the prostate and surrounding tissue as homogeneous media. For our design, the simulations take into account the inhomogeneity of the prostate to produce a uniform heating pattern using k-space propagation and application of the non-linear bioheat transfer equation to determine the optimal thermal treatment. In contrast to clinical imaging transducers, much novel research was required for transducer construction in applications of high powered ultrasound hyperthermia given of constraints as an intracavitary device.

The next major stage of this research project was focused on the construction of the array based on results of computer simulations of the ultrasound energy interactions with the prostate. In accordance with the aims our effort went toward: (a) transducer construction (b) optimization of the transducer array design for easy modifications, and (c) MRI thermometry experiments (*in vitro* and *in vivo*) using the hyperthermia ultrasound array. For the constructed applicator, supplementary simulations were used to refine our array pattern and were easily and quickly implemented in the applicator based on our MRI thermometry results. The final array took into account the inhomogeneity of the prostate to produce a uniform heating pattern using k-space propagation and application of the non-linear bioheat transfer equation to determine the optimal thermal treatment.

Using the intracavitary array transducer, noninvasive magnetic resonance imaging thermometry methods were used to determine the spatial and temporal temperature field pattern from the ultrasound using initially bovine tissue as a phantom and *in vivo* rabbit thigh muscle. The final area used the optimized array to heat the prostate of a canine while the temperature change is monitored using MRI to determine the clinical efficacy of this device. Noninvasive temperature monitoring using MRI was used to control thermal deposition in an *in vivo* canine prostate hyperthermia experiments. Several New Zealand rabbits and six canines were used to evaluate the fabricated 2D phased array using MRI-guided adaptive closed loop controller system. The controller was able to elevate the temperature of specified region of interest from 37°C to 43°C in 6 minutes and keep that temperature for about 30 minutes or more. These experiments proved the ability of ultrasound transducers to uniformly heat the whole prostate to the required thermal dose regardless of the physiological activities that counteracts any local

temperature elevation. Moreover, MRI images provide an accurate and safe method of controlling heat deposition within the required region of interest. The only timeline deviation was to ask for a "no-cost" extension in the final year to complete three-four canine experiments otherwise there were no deviations from the original research plan and this research progressed on schedule.

So what is the impact of this research? Ultimately, the knowledge gained from this research can further be applied to noninvasive treatment of other cancers such as breast cancer or cancers of the liver or kidney. Linear and nonlinear wave propagation investigations using k -space computational algorithm are important tools not only for medical applications but also for many acoustical branches. The novel idea of incoherent beams is helpful in reducing the complexity of the driving electronic equipments with less control parameters to insure the uniformity and stability of the treatment. Additionally, previous clinical studies of hyperthermia using intracavitary ultrasound arrays have shown promising results for the clinical treatment of prostate cancer (2). With the increasing aging population within the US, there are increasing incidents of prostate cancer. With an estimated 37,000 deaths per year, prostate cancer is the second leading cause of cancer death in men. Although age is perhaps the most important risk factor, the incidence and mortality rate is twice as high for African-American men as for Caucasian men (25-28). Moreover, the knowledge gained from this research can further be applied to noninvasive treatment of other cancers such as breast cancer or cancers of the liver or kidney.

List of all Personal receiving pay from research effort

Nadine Smith, PhD Assistant Professor of Acoustics and Bioengineering

Lewis E. Harpster, MD Assistant Professor of Surgery-Urology

Robert M. Keolian, PhD Associate Professor of Acoustics

Victor Sparrow, PhD, Associate Professor of Acoustics

O. Al-Bataineh, Graduate Research Assistant (received PhD December 2005)

K. Saleh, Graduate Research Assistant (received PhD May 2004)

6. REFERENCES (*Science* format)

Reference List

1. M. D. Hurwitz, I. D. Kaplan, G. K. Svensson, K. H. Hynynen, J. L. Hanson, 1999), p. 21.
2. M. D. Hurwitz, I. Kaplan, G. K. Svensson, J. Hansen, K. H. Hynynen. Feasibility and patient tolerance of a novel transrectal ultrasound hyperthermia system for treatment of prostate cancer. *International Journal of Hyperthermia* 17(1), 31-37. 2001.
3. T. Christopher, *IEEE Trans. Ultrason. Ferroelectr. Freq. Control* 52, 1523 (2005).
4. M. D. Hurwitz *et al.*, *Int. J. Hyperthermia* 21, 649 (2005).
5. C. J. Diederich *et al.*, *Int. J. Hyperthermia* 20, 739 (2004).
6. O. M. Al-Bataineh, R. Keolian, V. W. Sparrow, N. B. Smith, 2003. 146th Meeting of the Acoustical Society of America, 10-14 November 2003, Austin, Texas.
7. O. M. Al-Bataineh *et al.* Utilization of the k -space method in the design of a hyperthermia phased array. *Ferroelectrics Special Issue: Piezoelectric Composites and*

Other Related Areas 2006 (*submitted*).

8. National Library of Medicine (US) Board of Regents. Electronic Imaging: Report of the Board of Regents. NIH Publication , 90-2197. 1990.
9. T. D. Mast. Empirical relationships between acoustic parameters in human soft tissues. *Acoustics Research Letters Online* 1(2), 37-42. 2000.
10. T. D. Mast *et al.* A k-space method for large-scale models of wave propagation in tissue. *IEEE Trans. Ultrason., Ferroelect., Freq. Contr.* 48(2), 341-354. 2001.
11. M. Tabei, T. D. Mast, R. C. Waag. A new k-space method for coupled first-order acoustic propagation equations. *Journal of the Acoustical Society of America* (*submitted*). 2001.
12. T. D. Mast, L. M. Hinkelman, L. A. Metlay, M. J. Orr, R. C. Waag, *J. Acoust. Soc. Am.* 106, 3665 (1999).
13. T. D. Mast *et al.*, *IEEE Trans. Ultrason. Ferroelectr. Freq. Control* 48, 341 (2001).
14. R. Keolian, V. W. Sparrow, L. Harpster, N. B. Smith, 146th Meeting of the Acoustical Society of America, 10-14 November 2003, Austin, Texas.
15. H. H. Pennes, *Journal of Applied Physiology* 1, 93 (1948).
16. W. L. Nyborg, *Phys. Med. Biol.* 33, 785 (1988).
17. L. Curiel *et al.*, *Med. Biol. Eng Comput.* 42, 44 (2004).
18. J. Zemanek, *J Acoust Soc Am* 49, 181 (1971).
19. L. E. Kinsler, A. R. Frey, A. B. Coppens, J. V. Sanders, *Fundamentals of Acoustics* (John Wiley & Sons, New York, ed. 3rd, 1982).
20. P. Lewin, M. Ziskin, *Ultrasonic Exposimetry* (CRC Press, Boca Raton, FL, 1992).
21. H. H. Pennes, *Journal of Applied Physiology* 1, 93 (1948).
22. L. Sun, C. Collins, J. Schiano, N. B. Smith. Adaptive control for MRI-guided ultrasound hyperthermia treatment for prostate disease: *in vivo* and *ex vivo* results. *Magnetic Resonance in Engineering* 27B(1), 51-63. 2005.
23. O. M. Al-Bataineh, C. Collins, E. J. Park, H. Lee, N. B. Smith. MR thermometry verification of a hyperthermia ultrasound array designed using the k-space computational method, *BioMedical Engineering OnLine*. 2006. (*submitted*).
24. A. H. Chung, K. H. Hynynen, H. E. Cline, F. A. Jolesz. Quantification of thermal exposure using proton resonance frequency shift. *Proc.SMR 4th Meeting*, ISSN 1065-9889 3, 1751. 1996.
25. L. A. G. Reis, C. L. Kosary, B. F. Hankey, B. A. Miller, "Cancer Statistics Review, 1973-1994: Tables and Graphs" (NIH Publication No. 97-2789, (National Cancer Institute, Bethesda, MD, 1997).
26. P. A. Wingo, S. Landis, L. A. Ries, *Cancer* 80, 1810 (1997).
27. R. T. Greenlee, T. Murray, S. Bolden, P. A. Wingo, *CA Cancer J. Clin.* 50, 7 (2000).
28. P. A. Wingo, L. A. Ries, S. L. Parker, C. W. Heath, *Cancer Epidemiol. Biomarkers Prev.* 7, 271 (1998).

7. APPENDICES (in order as each appears in the appendix)

Publications

- Saleh, K. and Smith, N.B., Two Dimensional Array Design for Tissue Ablation for Treatment of Benign Prosthetic Hyperplasia, *International Journal of Hyperthermia*, 20:1, February 2004, 7-31.
- Saleh, K. and N.B. Smith, Design and evaluation of a 3 x 21 element 1.75 dimensional tapered ultrasound phased array for the treatment of prostate disease, *Materials Research Innovation*, 8, (2) 2004, pp 121-124.
- Sun L., Collins C. M, Schiano, J. and Smith, N.B "Adaptive control for MRI-guided ultrasound hyperthermia treatment for prostate disease: *in vivo* and *ex vivo* results" *Mag Res Engineering*, Vol. 27B, Issue 1, Oct 2005, Pages: 51-63.
- Saleh, K. and N.B. Smith, "A 63 element 1.75 dimensional ultrasound phased array for the treatment of benign prostatic hyperplasia", *BioMedical Engineering On-Line*, 4:39, 2005.
- Al-Bataineh, O., Mast, T., Keolian, R., Sparrow, V., Park, E., and Smith, N, "Utilization of the k-space method in the design of a hyperthermia phased array" *submitted to Ferroelectrics Special Issue: Piezoelectric Composites and Other Related Areas*, 2005.
- Sun L., Collins C. M, Park, E., Lee, H. and Smith, N.B, "MR thermometry verification of a hyperthermia ultrasound array designed using the k-space computational method" *submitted to BioMedical Engineering On-Line*, 2005.

Abstracts

- Saleh, K. and Smith, N.B., Two Dimensional Array Design for Tissue Ablation for Treatment of Benign Prosthetic Hyperplasia, *International Society of Magnetic Resonance in Medicine (ISMRM) Workshop on MRI-Guided Focused Ultrasound Surgery*, 19-21 June 2002, Cambridge, MA. pp 63-66.
- Al-Bataineh. O.M., Keolian, R., Sparrow, V., Smith, N.B., Optimized Hyperthermia Treatment of Prostate Cancer using a Novel Intracavitary Ultrasound Array, 146th Meeting of the Acoustical Society of America, 10-14 November 2003, Austin, Texas.
- Keolian, R., V. Sparrow, Harpster, L., and N.B. Smith. 2003. A "Fresnel-Transducer" for Prostate Hyperthermia Treatment *Acoustical Society of America*, 146th Meeting of the Acoustical Society of America, 10-14 November 2003, Austin, Texas.
- Saleh, K. and Smith, N.B., " Design and evaluation of a 63 element 1.75-dimensional ultrasound phased array for treating benign prostatic hyperplasia," *Acoustical Society of America*, 146th Meeting of the Acoustical Society of America, 10-14 November 2003, Austin, Texas.
- Sun, L., Schiano, J. and Smith, N.B " Novel Adaptive Control Methods for Ultrasound Thermal Treatment with a Two-Dimensional Tapered Array," *Proceedings of the IEEE 2003 Ultrasonics Symposium*, Honolulu, Hawaii, 8-11 October 2003, pp. 1274-1277.
- Sun L., Al-Bataineh O., Collins C., Smith M.B., and Smith, N.B. Fast adaptive control for MRI-guided ultrasound hyperthermia treatment for prostate disease: *in vitro* and *in vivo* results, *International Society of Magnetic Resonance in Medicine (ISMRM) Twelfth Scientific Meeting & Exhibition*, Kyoto, Japan, 15-21, May 2004.
- L. Sun, J.L. Schiano and N.B. Smith, PID and Adaptive Controller Design for Ultrasound Thermal Treatment of Prostate Diseases, *International Association of Science and*

Technology for Development (IASTED) International Conference, Applied Modeling and Simulation (AMS 2002) November 4-6, 2002 MIT, Cambridge, USA pp 347-352.

Two-dimensional ultrasound phased array design for tissue ablation for treatment of benign prostatic hyperplasia

K. Y. SALEH†* and N. B. SMITH†‡

† Department of Bioengineering; ‡ Graduate Program in Acoustics, College of Engineering, The Pennsylvania State University, 206 Hallowell Building, University Park, PA 16802, USA

(Received 11 October 2002; revised 16 April 2003; accepted 11 May 2003)

This paper describes the design, construction and evaluation of a two-dimensional ultrasound phased array to be used in the treatment of benign prostatic hyperplasia. With two-dimensional phased arrays, the focal point position can be controlled by changing the electrical power and phase to the individual elements for focusing and electronically steering in a three-dimensional volume. The array was designed with a steering angle of $\pm 14^\circ$ in both transverse and longitudinal directions. A piezoelectric ceramic (PZT-8) was used as the material of the transducer, since it can handle the high power needed for tissue ablation and a matching layer was used for maximum acoustic power transmission to tissue. Analysis of the transducer ceramic and cable impedance has been designed for high power transfer with minimal capacitance and diameter. For this initial prototype, the final construction used magnet compatible housing and cabling for future application in a clinical magnetic resonance imaging system for temperature mapping of the focused ultrasound. To verify the capability of the transducer for focusing and steering, exposimetry was performed and the results correlated well with the calculated field. *Ex vivo* experiments were performed and indicated the capability of the transducer to ablate tissue using short sonications. For sonications with exposure time of 10, 15 and 20 s, the lesion size was roughly 1.8, 3.0 and 4.3 mm in diameter, respectively, which indicates the feasibility of this device.

Key words: Ultrasound transducer, two-dimensional array, focusing, matching layer, necrosis.

1. Introduction

Focused ultrasound surgery (FUS) or high intensity focused ultrasound (HIFU) is a clinical method for treating benign prostatic hyperplasia (BPH), a benign growth of prostatic cells that is not life threatening but can cause blockage to the urine flow as a result of the prostate pushing against the urethra and the bladder¹. With FUS, tissue is non-invasively necrosed by elevating the temperature at the focal point above 60°C using short sonications (10–30 s) and deep FUS has been reported to successfully ablate prostate tissue without inducing damage to the rectal wall^{2–5}. The goal of prostate ablation is mainly to remove a non-desirable growth of the prostate. This can be achieved using FUS that can necrose the target volume by focusing the ultrasound beam at a certain position, and then steer the focus to cover the whole enlarged volume. Since the size of the enlargement is usually much bigger than the size of the ultrasound focus, either a single focus is electronically steered in consecutive sonications or multiple focal points can be used at the same time to generate multiple lesions.

* To whom correspondence should be addressed. e-mail: kysbio@engr.psu.edu

Existing techniques for treating BPH include hyperthermia, focused ultrasound, transurethral resection, prostatectomy and surgery. Although preferable, surgical techniques have numerous complications that appear in about one in four cases which include impotence, incontinence, urinary tract infections and often require a lengthy hospitalization⁶. With FUS, the ultrasound beam is focused at a specific location in the target volume to be necrosed. Since the tissue volume to be necrosed is larger than the geometric focus of the array, the transducer needs to be physically moved repeatedly to destroy the desired volume and unnecessarily extend the treatment time. Phased arrays overcome this problem by electrically steering the focal point from one location to another by changing the phase and power to the individual elements of the array.

Previous effective prostate ultrasound devices include both mechanically and electrically steered designs. One example of a commercial design is a focused, single element transducer which was mechanically manoeuvred to ablate tissue (SonablateTM 500, Focus Surgery Inc., Indianapolis, IN, USA). Electrically steered include an experimental design which used a one-dimensional (1-D) 57×1 aperiodic, linear array ($87 \times 15 \text{ mm}^2$) which reduced grating lobes and could steer the focus in the radial and longitudinal but not the transverse direction⁷. Another experimental design was a 60×1 linear array ($75 \times 15 \text{ mm}^2$) with a mechanical translation that could electrically steer the focus in the radial and longitudinal but not the transverse direction⁸. The drawbacks behind these designs are that they can only steer the focus in the radial and longitudinal directions or require complex mechanisms to move the focus. Improvements over 1-D arrays for the treatment of localized prostatic cancer can be achieved. A new spherically curved 1.5-D phased array that used high intensity electronically focused ultrasound to steer a beam along two axes was designed and tested, allowing enough depth to be reached to treat large prostates and eliminating two degrees of mechanical movement⁹. The advantage with a 2-D phased array is that it can electrically focus and steer in the radial, longitudinal and transverse directions, which means that it has the capability of focusing and steering in a 3-D volume without the need to physically move the array.

Issues regarding the construction of an array used for FUS of the prostate initially deal with the frequency and size of the ceramic to be diced into an array. The resonance frequency should be greater than 500 kHz ¹⁰, while the size of the transducer needs to be large enough to be able to deliver high power but small enough to be an intra-cavitary device. Before construction, computer simulations can be performed to determine the acoustic field. Pressure wave and temperature simulations indicated that a tapered array design reduced grating lobes significantly compared to equal element size arrays. Based on the computer model, a tapered array that satisfied grating lobes, frequency, and size limitations was designed. Lead zirconate titanate (PZT) was chosen as the ceramic material of the array, since it has the capability of handling the high electrical powers used in focused ultrasound. To maximize the acoustical power transmission from the elements and improve the structural integrity of the array face, a conductive matching layer was designed and fabricated. Issues regarding the cabling and electrical matching of the elements were also considered. Exposimetry of the acoustic field from the array was performed to compare experimental and calculated theoretical results. *Ex vivo* experiments using porcine kidney were also performed to demonstrate the feasibility of the array to necrose tissue. This research describes the design, construction and

evaluation of a 2-D ultrasound phased array that is capable of focusing and steering in a 3-D volume to be used in the treatment of BPH.

2. Materials and methods

2.1. Simulations

Computer simulation programs were written to determine the number and the size of the phased array elements in addition to determining the pressure and temperature field from the device. The array was modelled (figure 1) as a 2-D square array in order to have focusing and steering capabilities in both x - and y -directions (x =transverse, y =longitudinal and z =radial). The phase of each element was determined such that signals from individual elements were coherent at the shifting focal point. Measuring the difference in path length between each element to the focus in comparison to the path from the centre of the array to the focus determined the element phase calculation. The phase, ϕ_i , (degrees) of element i was given by:

$$\phi_i = \frac{360^\circ}{\lambda} (d_i - d_o) - 360^\circ n \quad (1)$$

where λ is the wavelength (m), d_i is the distance (m) from the centre of element i to the focal point, d_o is the distance (m) from the centre of the array to the focus and n is an integer to keep $0 = \phi_i = 360^\circ$. Huygen's principle was used to model the pressure field as a summation of simple sources¹¹. Thus, the total acoustic pressure at any point in the field can be calculated using:

$$p(x, y, z) = \sum_{i=1}^n \sqrt{\frac{2P\rho}{cA}} \left(\frac{fS}{d_i} \right) \exp \left[j \left(\phi_i - \frac{2\pi d_i}{\lambda} \right) - d_i \alpha \right] \quad (2)$$

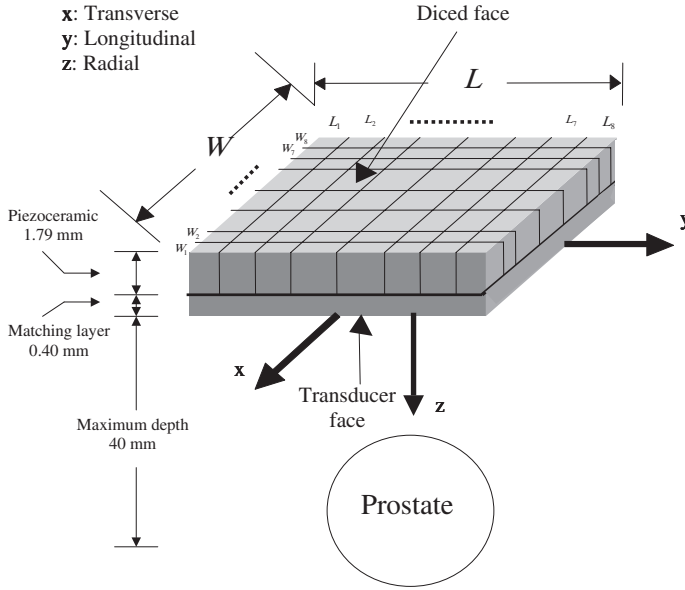


Figure 1. Based on the simulations, a diagram of the 2-D 64 element (8×8) tapered array with total size of $20 \times 20 \text{ mm}^2$ with the proportions of the ceramic and matching layer illustrated. The diced face of the ceramic was cut 70% through and each individual element was attached to the electrical cabling using low temperature soldering material.

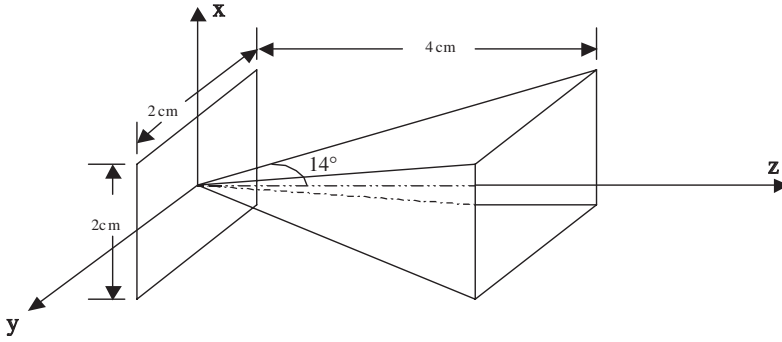


Figure 2. Within the volume shown in front of the transducer ($2 \times 2 \text{ cm}^2$), the array was designed to focus and steer with an acceptable grating lobe level.

where p is the total acoustic pressure in Pascals (Pa), P is the total acoustic power emitted by the array in watts (W), ρ is the density of the medium (998 kg m^{-3}), c is the speed of sound in the water (1500 m s^{-1}), A is the total surface area of the array (m^2), f is the resonance frequency (1.2 MHz), S is the area of the corresponding element (m^2) and α is the attenuation in soft tissue ($10 \text{ Np m}^{-1} \text{ MHz}^{-1}$).

This array was capable of focusing and steering with a steering angle of 14° with a maximum focal depth of 4 cm. Figure 2 shows the volume in which the focal point can be focused and steered. Attempting to focus at a point that is out of this angle will result in a significant increase in grating lobes.

Off-axis focusing and the grating lobe level are directly related to each other, since increasing the steering angle causes a non-linear increase in the grating lobe level. For a focal point aimed at 0, 0, 30 mm, the results, which were plotted as a mesh (figure 3(a)) or contour (figure 3(b)), have shown to give a normalized intensity with a grating lobe level at $\sim -20 \text{ dB}$. Steering the focal point in the x -direction by focusing at 3, 0, 30 mm caused the grating lobe level to become -14 dB . The result is shown as a mesh (figure 3(c)) or contour (figure 3(d)). Further increase of the steering angle increased the grating lobe level. For a focus at 6, 0, 30 mm, the grating lobe level was -10 dB , as shown in the mesh (figure 3(e)) or contour (figure 3(f)) plots. Attempting to focus at a point that is outside the steering volume shown in figure 2 resulted in a significant increase of the grating lobe level. A focus at 9, 0, 30 mm (steering angle = $17^\circ > 14^\circ$) resulted in an unacceptable grating lobe level of -1.5 dB , which is shown in the mesh (figure 3(g)) or contour (figure 3(h)) plots. In figures 3(b), (d), (f) and (h), the contour levels were plotted at 90, 80, 70, 60, 50, 40, 30, 20 and 10% of the maximum intensity.

Reduction of the treatment time can be achieved by generating multi-focal points simultaneously. Four focal points can be generated by dividing the array into four parts, each of which is responsible for generating a single focal point. Figure 4(a) shows a mesh plot for the normalized intensity as a function of x and y with four focal points being generated at the locations $(x, y, z) = (\pm 2, \pm 2, 30) \text{ mm}$. Reducing the distance between the focal points made them overlap. Focusing at $(x, y, z) = (\pm 1.5, \pm 1.5, 30) \text{ mm}$ resulted in a partial overlapping as shown in the mesh plot (figure 4(b)) for the normalized intensity. A complete overlap between the four focal points was observed when focusing at $(x, y, z) = (\pm 1, \pm 1, 30) \text{ mm}$, as shown in the normalized intensity mesh plot (figure 4(c)).

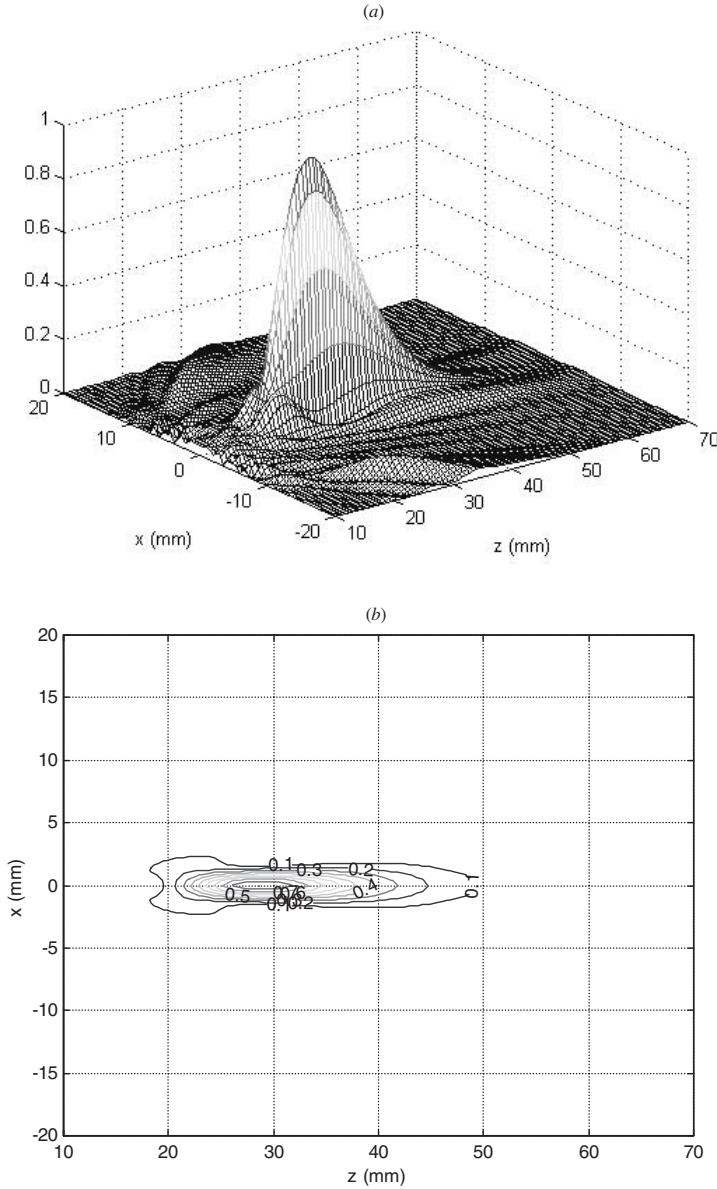


Figure 3. Off-axis focusing has a direct impact on the grating lobe level. Increasing the steering angle caused an increase in the grating lobe level. Shown is (a) a mesh or (b) a contour plot for the normalized intensity in the x - and z -directions with a focal point aimed at $(x, y, z) = (0, 0, 30)$ mm that resulted in a grating lobe level of -20 dB. A focus at $(x, y, z) = (3, 0, 30)$ mm resulted in a grating lobe level of -14 dB, as shown when plotting the normalized intensity as a (c) mesh or (d) contour. Further increase in the steering angle caused a further increase in the grating lobe level. Focusing at $(x, y, z) = (6, 0, 30)$ mm caused the grating lobe level to be -10 dB, which is shown in the normalized intensity (e) mesh or (f) contour plot. Attempting to focus outside the volume shown in figure 2 resulted in undesirable grating lobe values. Aiming the focus at $(x, y, z) = (9, 0, 30)$ mm resulted in a grating lobe level of -1.5 dB. The normalized intensity for this case is shown as a (g) mesh or (h) contour. In (b), (d), (f) and (h), the contour values were taken at 90, 80, 70, 60, 50, 40, 30, 20 and 10% of the normalized intensity.

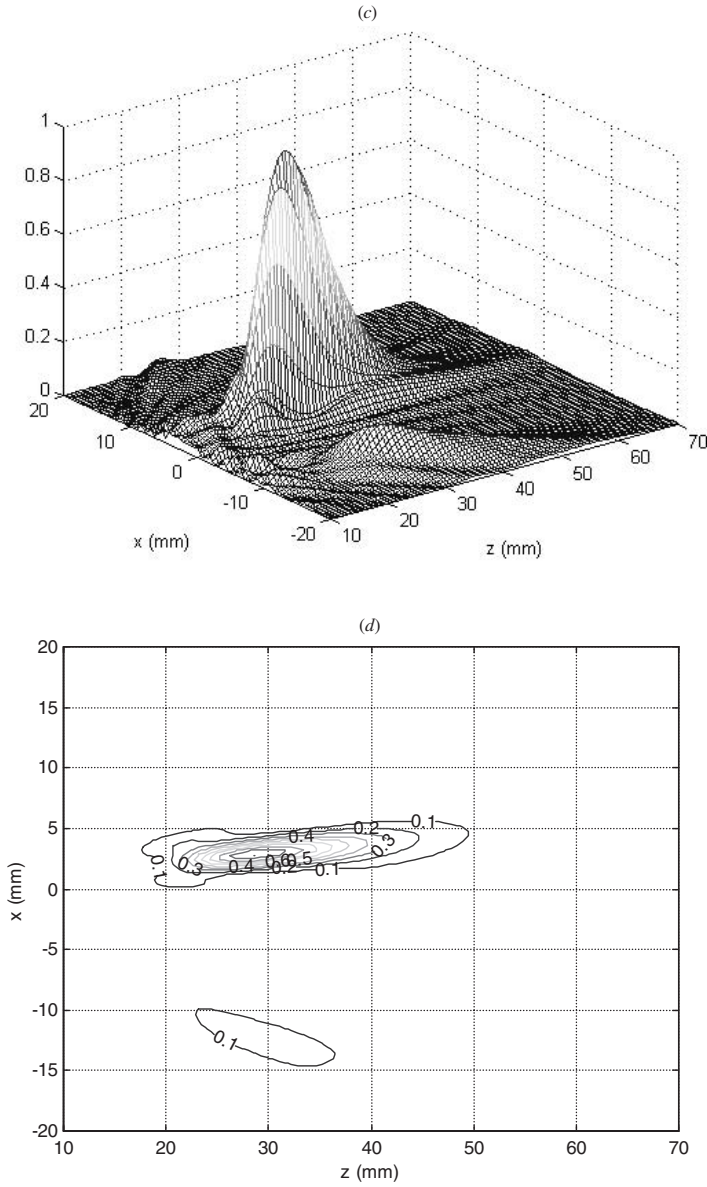


Figure 3. Continued.

From the pressure field of the simulated array, the temperature distribution in the tissue was modelled using the Pennes' bioheat transfer equation (BHTE)¹²:

$$\rho C_t \frac{\partial T}{\partial t} = K \left(\frac{\partial^2 T}{\partial x^2} + \frac{\partial^2 T}{\partial y^2} + \frac{\partial^2 T}{\partial z^2} \right) - w C_b (T - T_a) + q(x, y, z) \quad (3)$$

where C_t is the specific heat of the tissue ($3770 \text{ J kg}^{-1} \text{ }^\circ\text{C}^{-1}$), K is the thermal conductivity ($0.5 \text{ W m}^{-1} \text{ }^\circ\text{C}^{-1}$), T is the temperature at time t at the point x, y, z in $^\circ\text{C}$, T_a is the arterial blood temperature (37°C), w is the perfusion in the tissue ($5 \text{ kg m}^{-3} \text{ s}^{-1}$),

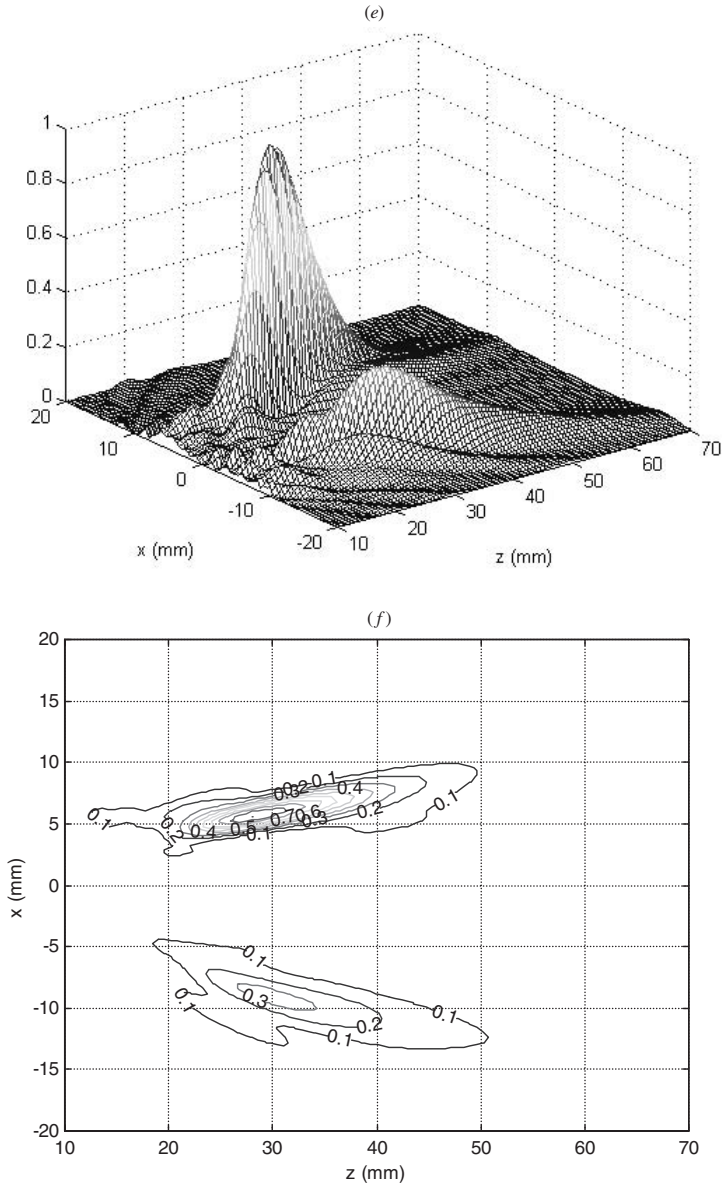


Figure 3. Continued.

C_b is the specific heat of the blood ($3770 \text{ J kg}^{-1} \text{ } ^\circ\text{C}^{-1}$) and $q(x, y, z)$ is the power deposited at the point x, y, z . The power was calculated from the pressure field of the array design while the BHTE was determined using a numerical finite difference method with the boundary conditions set at 37°C . The total intensity at point (x, y, z) was also calculated from the pressure field of the simulated array and is given by¹³:

$$I(x, y, z) = \frac{p^2(x, y, z)}{2\rho c} \quad (4)$$

where $I(x, y, z)$ is the intensity at point x, y, z in W m^{-2} .

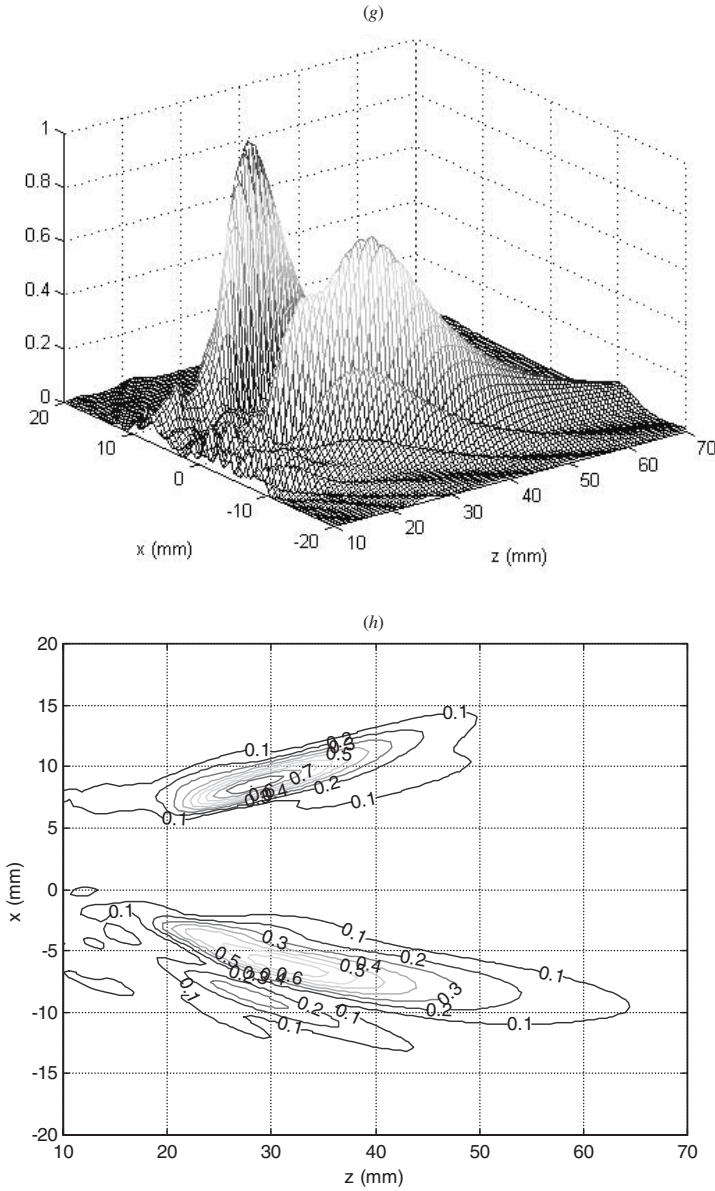


Figure 3. Continued.

Based on previous studies of transrectal probes, the width of the ceramic should be roughly no wider than 23 mm¹⁴. Initially, the simulated design used equal size elements of $2.5 \times 2.5 \text{ mm}^2$ and, although it was capable of focusing and steering, it suffered from large grating lobes outside the focus. For example, at a focus of $(x, y, z) = (5, 0, 30) \text{ mm}$ (i.e. the 0, 0, 0 position is at the centre of the transducer face in figure 1), the grating lobe level was -3.47 dB , which was not desirable since this high level can cause an increase in tissue temperature outside the focus. Removing the periodicity of the array or tapering it has been shown to reduce the grating lobe level¹⁵. Both dimensions of the array were chosen to be identical in order to

have same focusing and steering capabilities in both x and y directions. The maximum possible steering angle was calculated to be $\tan^{-1}(1.0/4.0) = 14^\circ$, with maximal focal depth of 40 mm. The improved tapered array design started with a $20 \times 20 \text{ mm}^2$ piece cut into an 8×8 pattern with 64 individual elements with lengths (L) and

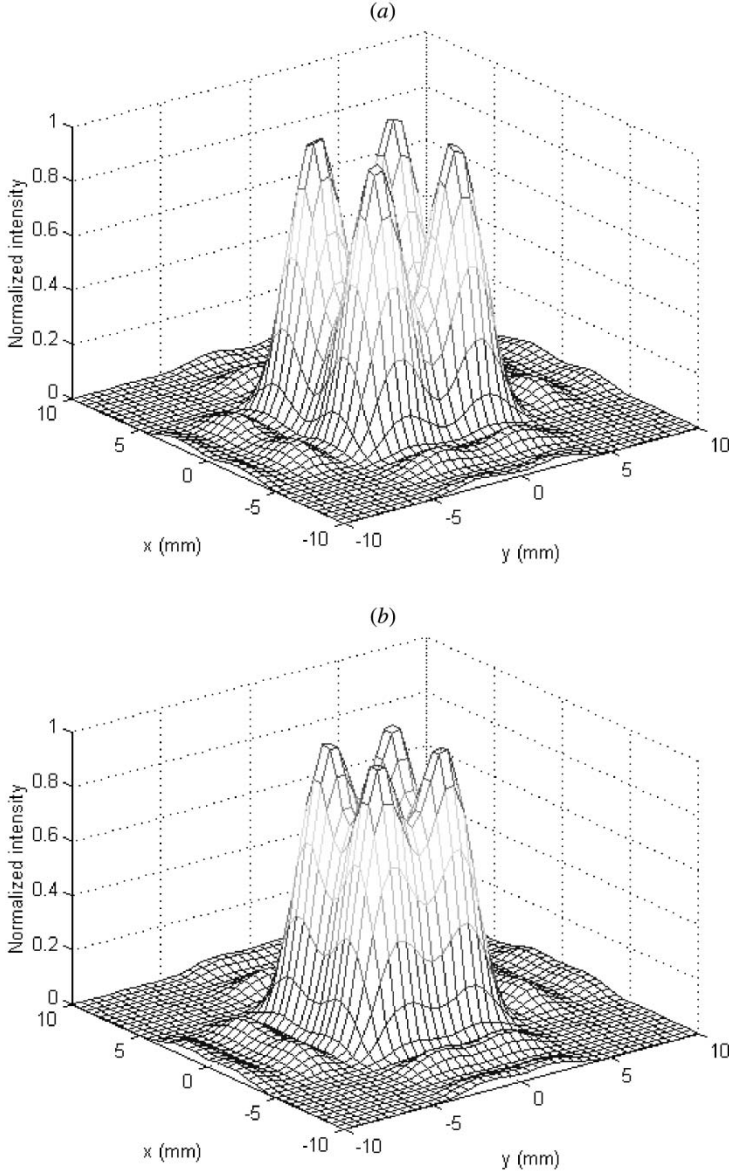


Figure 4. Pressure field simulations were performed to verify the capability of the array in generating four focal points by driving four parts of the array separately. Shown is the normalized intensity in the x - and y -directions for four focal points aimed at the locations $(x, y, z) = (\pm 2, \pm 2, 30) \text{ mm}$ plotted as (a) a mesh. Partial overlapping between the four focal points occurred when focusing at $(x, y, z) = (\pm 1.5, \pm 1.5, 30) \text{ mm}$, as shown in the (b) mesh plot of the normalized intensity, while complete overlapping occurred when focusing at $(x, y, z) = (\pm 1, \pm 1, 30) \text{ mm}$, which is shown in (c).

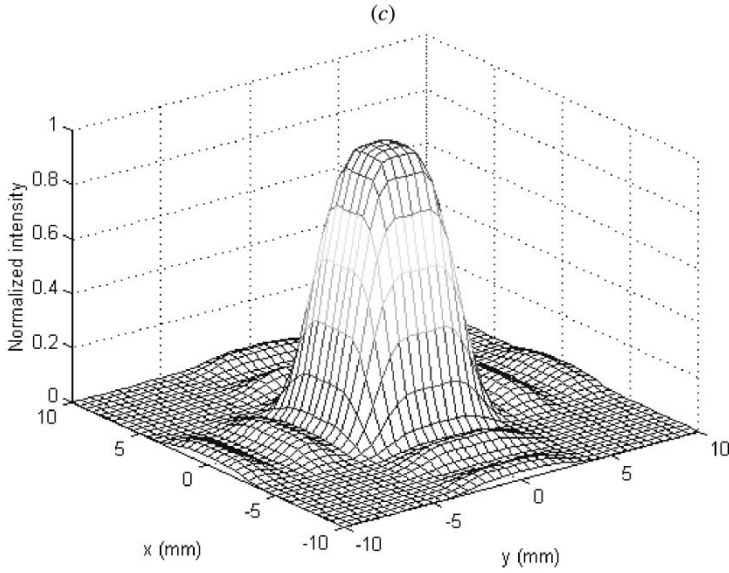


Figure 4. Continued.

widths (W) of 2.00, 2.33, 2.66, 3.00, 3.00, 2.66, 2.33, 2.00 mm for elements $i=1-8$, respectively (figure 1). Simulations have shown that the grating lobe level of the tapered design has decreased to -8.24 dB at a similar focus location of 5, 0, 30 mm. Figure 5(a) shows a mesh plot for the normalized intensity as function of x and z , while figure 5(b) is the corresponding contour plot with contour levels at 90, 70, 50, 30 and 10% of the maximum intensity. From the simulations, a grating lobe level of 15% of the maximum value was observed which decreased at smaller steering angles. One of the techniques that can be used to reduce the grating lobes is based on the use of sub-sets of elements and de-activation of several elements in the array¹⁶. Although with this technique the grating lobes could be suppressed as a result of the non-periodicity resulted from activating some elements and de-activating others (usually chosen in random), for an array with a small number of elements a trade-off has to be made between using less elements and the need to drive those elements with higher power to generate the same lesion size with the same time. Temperature simulations were also used to verify the potential to increase the tissue temperature to 60°C with short sonications. Figure 5(c) shows the temperature distribution corresponding to the pressures for figure 5(a) and an increase in temperature was observed at the intended location of $(x, z) = (5, 30)$ mm.

As indicated, off-axis focusing has a direct impact on the grating lobe level and, thus, the temperature. Increasing the steering angle leads to increasing the grating lobe level and, thus, causing an undesirable temperature increase at the grating lobe position. Figures 6(a–d) corresponded to the simulated pressure field generated in figures 3(a), (c), (e) and (g), respectively. For a focal point aimed at 0, 0, 30 mm, the temperature distribution plotted as a function of x and z (figure 6(a)) shows a 60°C focus at the intended location with a temperature value of almost 37°C elsewhere. Off-axis focusing caused a temperature increase at the location of the grating lobe. For a focus at 3, 0, 30 mm, the temperature at the grating lobe location was found to be 40°C , as shown in figure 6(b). Increasing the steering angle increased the

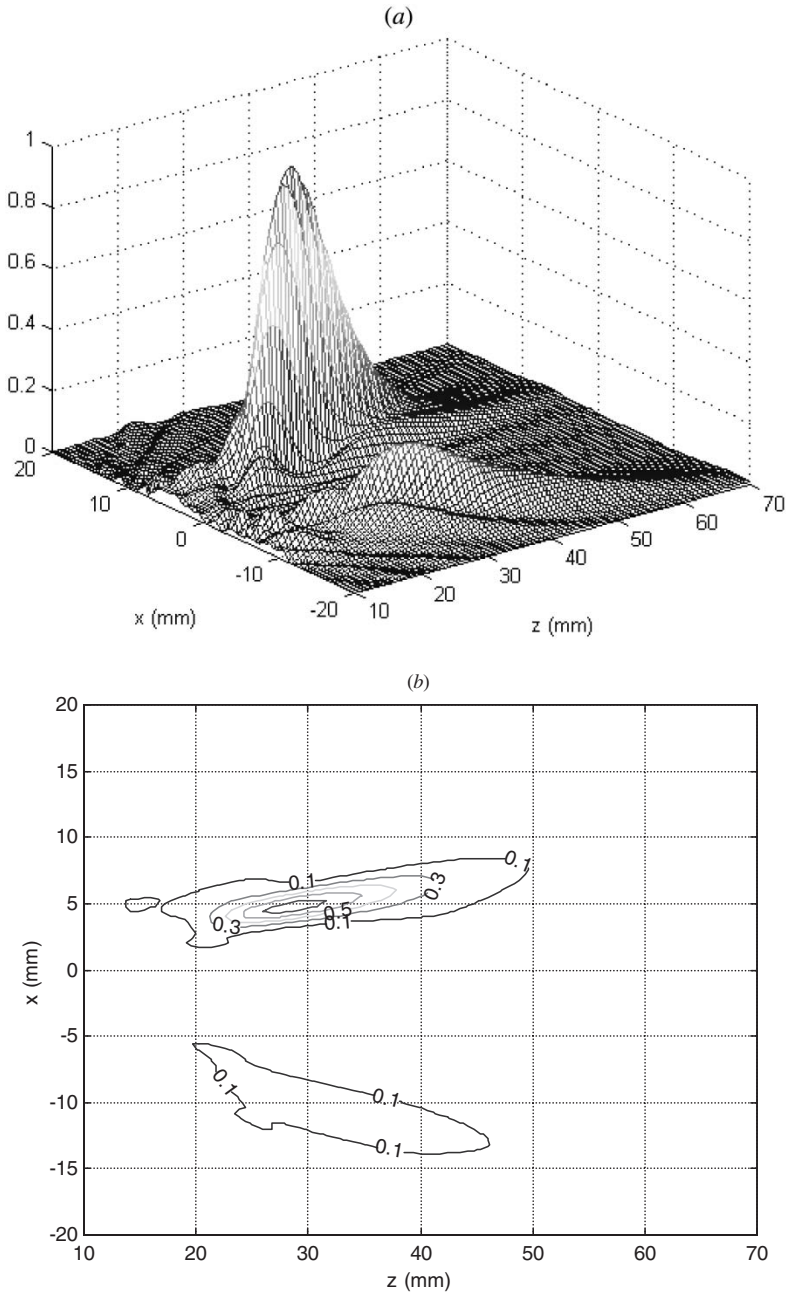


Figure 5. Before the construction of the array, simulations of the acoustic field were performed to evaluate the focusing of the elements and reduce potential grating lobes. Shown is the normalized intensity (a) in the x - and z -directions for a focal point at $(x, y, z) = (5, 0, 30)$ mm along with (b) contour plot values taken at 90, 70, 50, 30, 10% of the normalized intensity with a grating lobe level of 15% of the maximum intensity. A temperature map (c) corresponding to the pressures generated in (a) was numerically solved using the bioheat transfer equation. This simulated figure shows an increase in tissue temperature to the target of 60°C at the focal point using 10s sonication, while outside the target region the temperatures were normal, as indicated from the temperature colour bar.

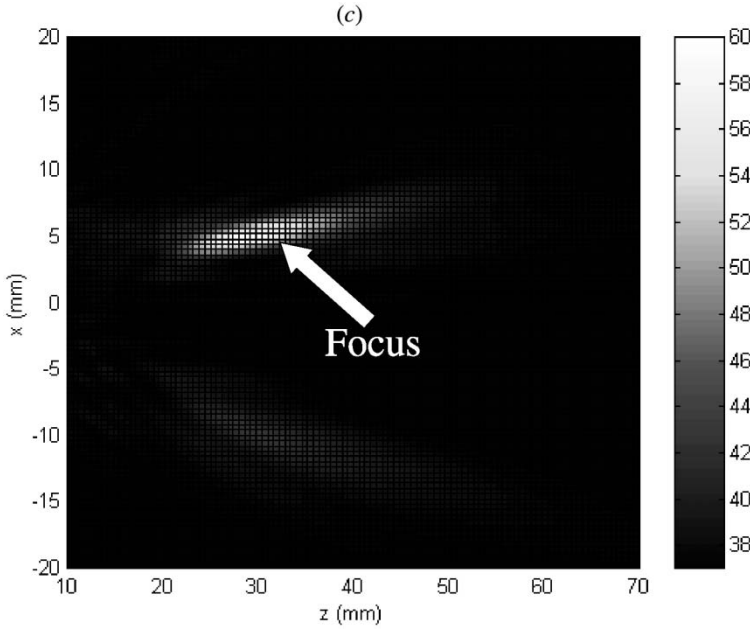


Figure 5. Continued.

grating lobe level and, thus, the undesirable temperature. A temperature of 43°C was observed at the grating lobe location when aiming the focus at 6, 0, 30 mm, as shown in figure 4(c). Trying to steer the focus outside the volume shown in figure 2 resulted in an unacceptable temperature value resulting from the grating lobe. A focus at 9, 0, 30 mm resulted in a grating lobe temperature of 58°C , as shown in figure 6(d).

2.2. Transducer construction

Choosing an appropriate piezoceramic material to be used in this application is essential, since it affects both electrical and acoustical properties of the array. Appropriate PZT that can be used include PZT-4, PZT-5H and PZT-8. For ultrasound imaging arrays, PZT-5H has a better performance when compared to the others, from a capacitance point of view, which is due to the fact that it has a large permittivity value, but at the same time it cannot handle the large electrical power that is used in focused ultrasound. With respect to power, PZT-4 and PZT-8 are good candidates with an advantage for PZT-8 over PZT-4, since it has an extremely high mechanical quality and extremely low loss factor. Thus, PZT-8 material (TRS Ceramics, State College, PA, USA) was chosen and diced, in house, into 64 elements forming the complete array. The cuts were made by dicing the material 70% through its thickness with a kerf width of $96\mu\text{m}$ using a dicing saw (Model 780, K & S-Kulick and Soffa Industries, Willow Grove, PA, USA) at the National Institute of Health (NIH) Medical Ultrasonic Transducer Technology Resource Centre located on The Pennsylvania State University campus (University Park, PA, USA).

For maximum acoustical power transfer from the individual elements to the tissue, a conductive matching layer was designed and fabricated. The thickness and material selection of the matching layer were designed based on the solution

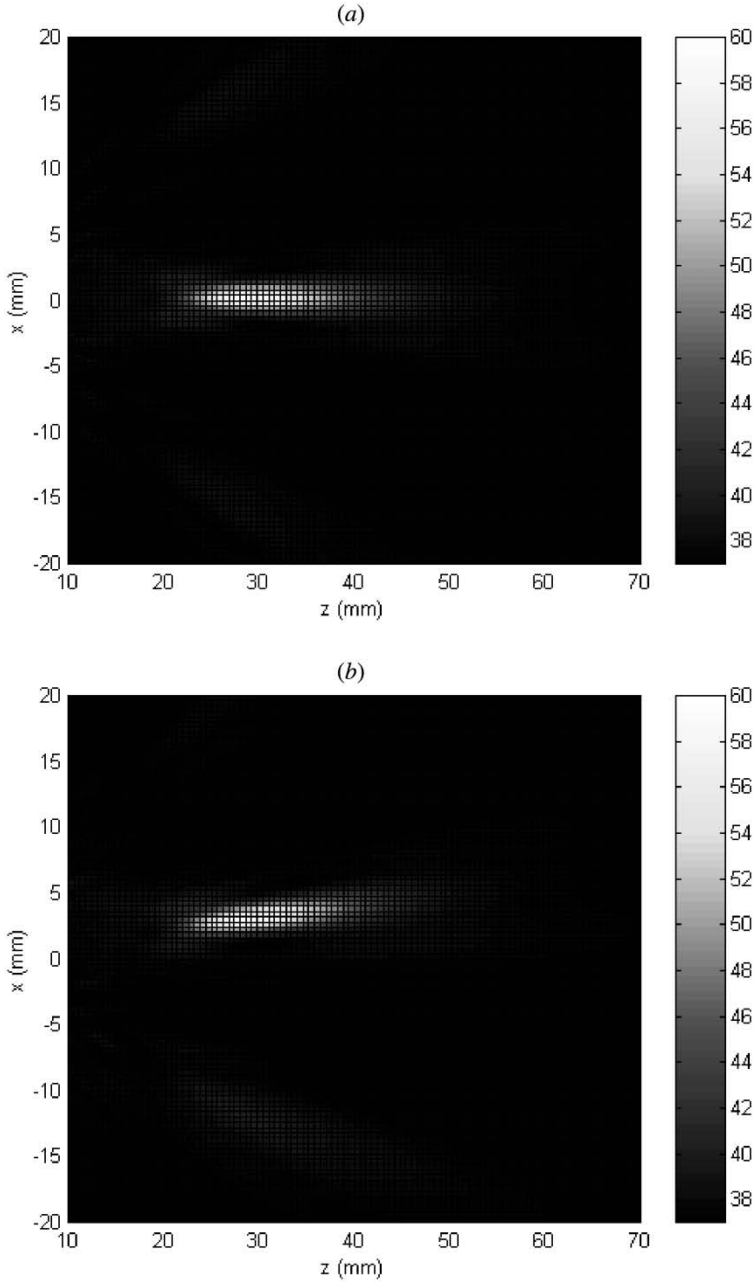


Figure 6. Corresponding to the pressures generated in figures 3(a), (c), (e) and (g), numerical temperature simulations were done using the bioheat transfer equation to plot the temperature maps (a), (b), (c) and (d), respectively. Those temperature maps show the effect of off-axis focusing on the temperature generated by the grating lobes. The temperature at the grating lobe location was found to be 38, 40, 43 and 58°C as a result of aiming the focus at $(x, y, z) = (0, 0, 30)$, $(3, 0, 30)$, $(6, 0, 30)$ and $(9, 0, 30)$ mm, respectively, as shown in (a), (b), (c) and (d), respectively.

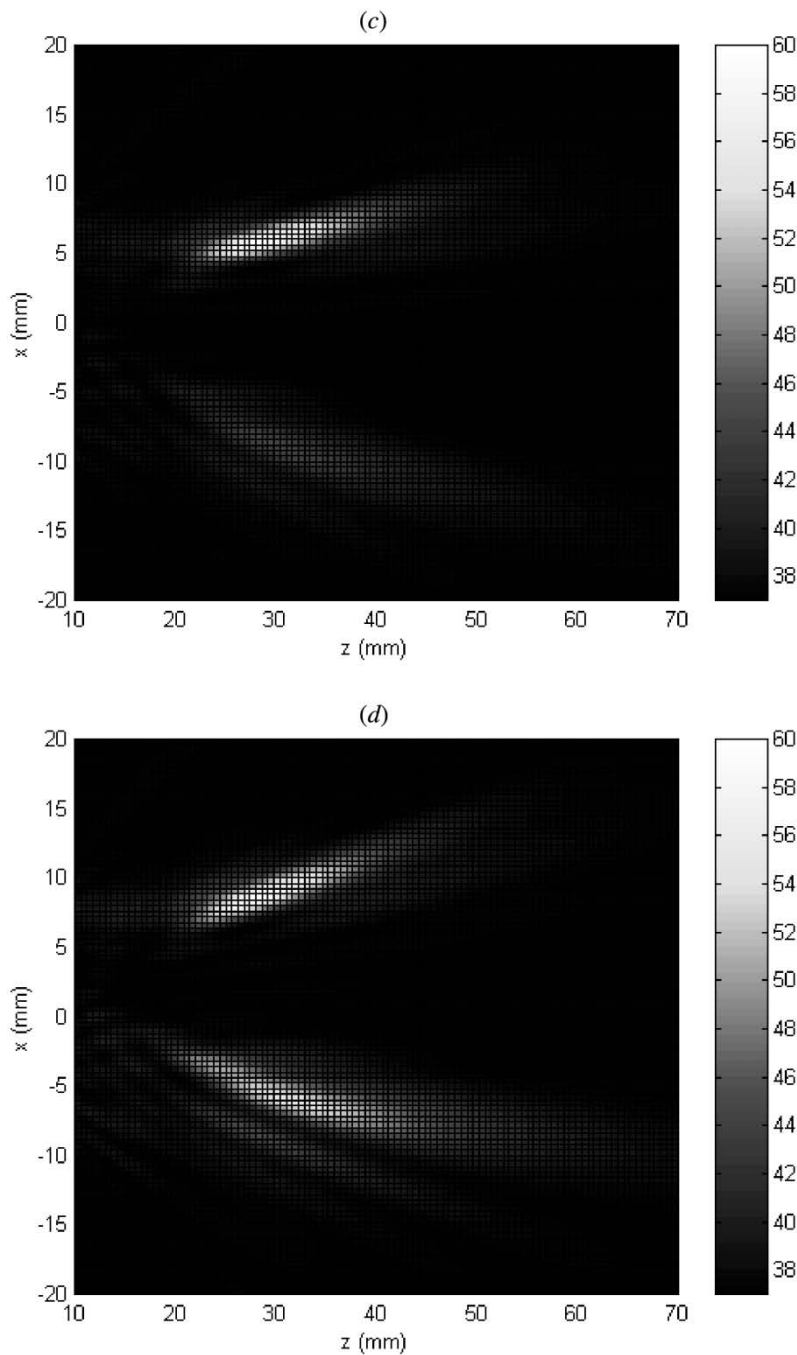


Figure 6. Continued.

to a three layer problem (transducer, matching layer and tissue), which ensured the required maximum power transfer. The PZT-8 material chosen for this design had an acoustic impedance of $\sim 33 \text{ Mpa s m}^{-1}$ and the human tissue has an acoustic impedance of $\sim 1.48 \text{ Mpa s m}^{-1}$ ^{17,18}. Since the input and the load impedances are not

the same, the intermediate matching layer was used between the piezoelectric material and the human tissue. Analysing a three layer problem indicated that the maximum power transmission occurs when the characteristic impedance of the matching layer equals the geometric mean of the piezoelectric characteristic impedance and the tissue characteristic impedance. With the longitudinal velocity in the matching layer material of $v_L = 1900 \text{ m s}^{-1}$ and since the resonance frequency of the array (f_o) was 1.2 MHz, the thickness of the matching layer was determined to be:

$$L = \frac{\lambda}{4} = \frac{1}{4} \left(\frac{v_L}{f_o} \right) = \frac{1}{4} \left(\frac{1900 \text{ m s}^{-1}}{1.2 \times 10^6 \text{ s}^{-1}} \right) = 0.396 \text{ mm}. \quad (5)$$

To construct the matching layer, parafilm was used to affix the piezoceramic to a glass plate with an adhesive primer poured onto the surface of the transducer face. The transducer was surrounded with a rubber dam and the silver conducting matching layer was poured onto the transducer surface. The matching layer, mixed in-house, was a 2:1, epoxy-to-silver mixture of Insulcast 501 (Insulcast, Roseland, NJ, USA) and 2–3 micron silver epoxy (Aldrich, Milwaukee, WI, USA). The whole assembly was centrifuged for 10 min and cured overnight. After the rubber assembly was removed, the surface was sanded and lapped to the designed thickness. For the initial prototype, the specially machined, waterproof applicator housing ($90 \times 60 \times 60 \text{ mm}^3$) was made from magnet compatible acrylic.

The capacitance of each element in the array depends primarily on the thickness, permittivity and the surface area. Since the element surface area is small, the capacitance will be small and, therefore, the element impedance will be large which makes it necessary to find a suitable cable that has a relatively low capacitance per unit length and, thus, high electrical impedance. For wiring the array, a low capacitance cable (75Ω , 15 pF/ft and 42 AWG) was used. The choice of such a cable was made based on the difficulty to electrically match small array elements to 50Ω using high capacitance cables. Figure 7 shows a photograph of the final array.



Figure 7. Photograph of the constructed, waterproof array machined from acrylic with 2.3 m low capacitance cable which connected to the amplifier system.

The connector between the cable and the amplifier used loose crimp contacts (PEI Genesis, Philadelphia, PA, USA), while the soldering between the cable and the 64 individual array elements used Indalloy #1E (Indium Corporation of America, Utica, NY, USA). This low temperature soldering material ensured that the temperature during soldering did not exceed the curie temperature for PZT-8 material. To drive the array, a specially built amplifier driving system (Advanced Surgical Systems Inc., Tucson, AZ, USA) was used¹⁹. Briefly, this amplifier system was a multi-channel high power, ultrasound phased-array transducer driver for 64 elements, which is capable of delivering 60 W per channel with $\pm 1^\circ$ phase resolution each. To match the impedance of the elements to the amplifier, individual LC (L = inductor and C = capacitor) circuits were built for each of the 64 elements to match each one to the common value of $50\ \Omega \angle 0^\circ$.

2.3. *Exposimetry*

To determine the acoustic field generated by the array, an automated computer controlled positioning system, which could translate an hydrophone throughout the acoustic field of the array placed in a water tank, was used. The transducer was submerged in water (room temperature, $\sim 20^\circ\text{C}$) in a tank ($120 \times 50 \times 52\text{ cm}^3$) made almost anechoic with sound absorbing rubber. A custom-made degasser, built in-house, was used to reduce the dissolved oxygen content of the distilled water to 1–2 ppm to reduce cavitation. The system was controlled using a personal computer connected to a four-motor positioning system (Velmex Inc., Bloomfield, NY, USA) via the RS232 serial port and also connected, via the general purpose interface bus (GPIB), to a digital oscilloscope (Agilent 54622A, Agilent Technologies, Palo Alto, CA, USA), which recorded the voltage amplitudes detected by the hydrophone. Custom written, Quick Basic (Microsoft Corporation, Redmond, WA, USA) programs were used for automated control of the motors and data acquisition from the oscilloscope. Initially, multiple on-axis (i.e. where the focus is along the major z -axis, z_f) exposimetry experiments were performed. With the focus set to 0, 0, z_f mm, z_f was varied from 10–40 mm, with a step size of 2 mm. To determine the repeatability of the focusing, 5–10 experiments were performed at each location. For off-axis studies (i.e. where the focus was not on z but aimed toward the x or y axis, x_f or y_f , respectively), the focus was located at x_f , y_f , 30 mm, while the steering angle was adjusted to the desired value by choosing appropriate values for x_f and y_f . The steering angle was varied from -14° to $+14^\circ$ with a step size of 2° in both x and y directions with multiple experiments (5–10) performed at each angle. In both the on-axis and off-axis experiments, the scanning step size was 0.5 mm, while the scanning area was $20 \times 20\text{ mm}^2$. The hydrophone voltage recordings were used to calculate the normalized intensities based on the pressures that were plotted as the mean and standard deviation of the results ($\bar{x} \pm \text{SD}$) and compared against the calculated values^{20,21}.

2.4. *Ex vivo experiments*

To test the feasibility of the array to ablate tissue, the array was submerged 3 cm in the tank aimed perpendicular to the surface of the water. Fresh porcine kidney was obtained, placed in the tank and held in front of the transducer face using metal clamps to ensure that it did not move during the experiments. A distance of 1 cm was maintained between the face of the array and the kidney to mimic the distance of a water bolus used in clinical treatments²². Sonication experiments drove

each element at an average electrical power of 8 W for 10 s for both on- and off-axis focusing. For the off-axis focusing, the steering angle was at 5.7° in the x -direction and 13.1° in the y -direction. To examine the effects of sonication time, subsequent sonications used exposures of 15 and 20 s. At the end of the sonications, the kidney was carefully removed and sliced with a scalpel to evaluate the ablated areas. Lesions were recorded several times for size using a digital caliper and digitally photographed.

3. Results

To test the correlation between experimental and theoretical results, exposimetry experiments were performed. As an example of a typical result at the location $(x, y, z) = (0, 3, 30)$ mm, figure 8(a) shows a comparison plot along the x -axis of the calculated and experimental normalized intensities. Figure 8(b) plots similar theoretical and experimental data but along the y -axis for the same focus. For both plots, the theoretical intensity data correlated well with the experimental results. From multiple experiments to evaluate the feasibility of the array to steer the focus, a typical 3-D normalized intensity result from a focal point was aimed at $-2, -0.7, 30$ mm. The results were plotted as a mesh (figure 9(a)) or contour (figure 9(b)), with contour levels at 90, 70, 50, 30 and 10% of the maximum intensity and the grating lobe levels at ~ -7.0 dB or less.

Ex vivo experiments were also performed to verify the feasibility of the array to generate foci that are capable of ablating tissue. In the first sonication experiment, the elements were driven at an average power of 8 W for 10 s for on-axis focusing. In the plane that was 30 mm deep in tissue and parallel to the face of the array, a cigar shaped lesion with a length of 4.5 mm, along the z -axis, and a diameter of

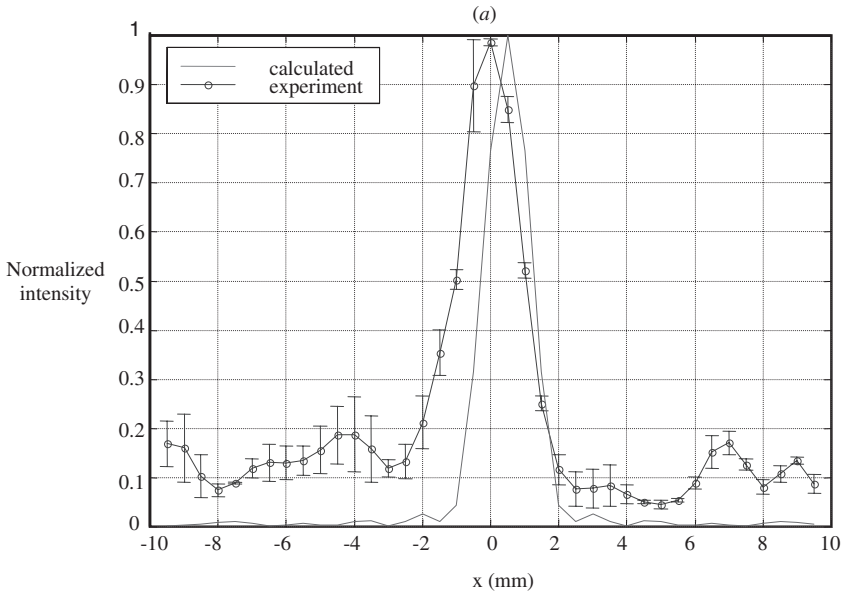


Figure 8. Comparison of calculated and experimental normalized intensities for a focus at 0, 3, 30 mm plotted along the (a) x -axis and (b) y -axis.

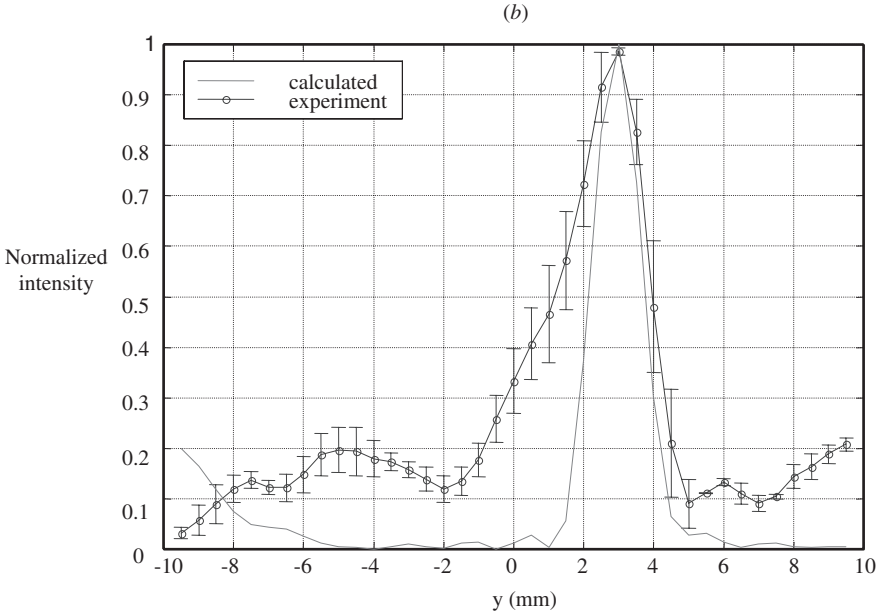


Figure 8. Continued.

2 mm was observed (figure 10(a)). Evaluation of the off-axis steering also used an average power of 8 W for 10 s to generate three separate lesions at locations $(x, y, z) = (-3, -7, 30)$, $(0, 0, 30)$ and $(3, 7, 30)$ mm. Figure 10(b) shows a digital photograph of three lesions, each ~ 2 mm in diameter, which corresponded to the intended locations. To determine the effects of sonication time, the location and exposure time was focused at 0, 0, 30 mm for 10 s, 0, 0, 34 mm for 15 s and 0, 0, 39 mm for 20 s at 8 W per element. Three lesions were observed with a diameter of 2, 2.9 and 4 mm that corresponded to the sonication times of 10, 15 and 20 s, respectively (figure 10(c)).

Further *ex vivo* experiments were performed to verify the capability of the array in generating off-axis lesions. A single 10 s sonication was performed with the elements of the array driven at an average power of 8 W to generate a single off-axis lesion at the location 5, 0, 30 mm. Figure 11(a) is a cross-section that was made in the plane that was 9.5° ($\tan^{-1}(5/30) = 9.5^\circ$) away from the z -axis, which shows a lesion with ~ 4 mm length along that axis. A cross-section in the plane that was 30 mm deep in tissue and parallel to the face of the transducer shows the shape and size of the lesion in the x - y plane, which was observed to be 2 mm in diameter, as shown in figure 11(b).

As shown in the simulations from figure 4(c), the array was theoretically capable of generating a single large focal point that resulted from the overlapping of four focal points generated separately at the locations $\pm 1, \pm 1, 30$ mm. To verify this, the average power was kept at 8 W and the sonication time was increased to 25 s to compensate for the reduction in the overall power per focus. A cross-section was made in a plane that was 30 mm deep in tissue and parallel to the x - y plane. A large lesion with a diameter of 4 mm was observed (figure 12) using this focal overlapping technique.

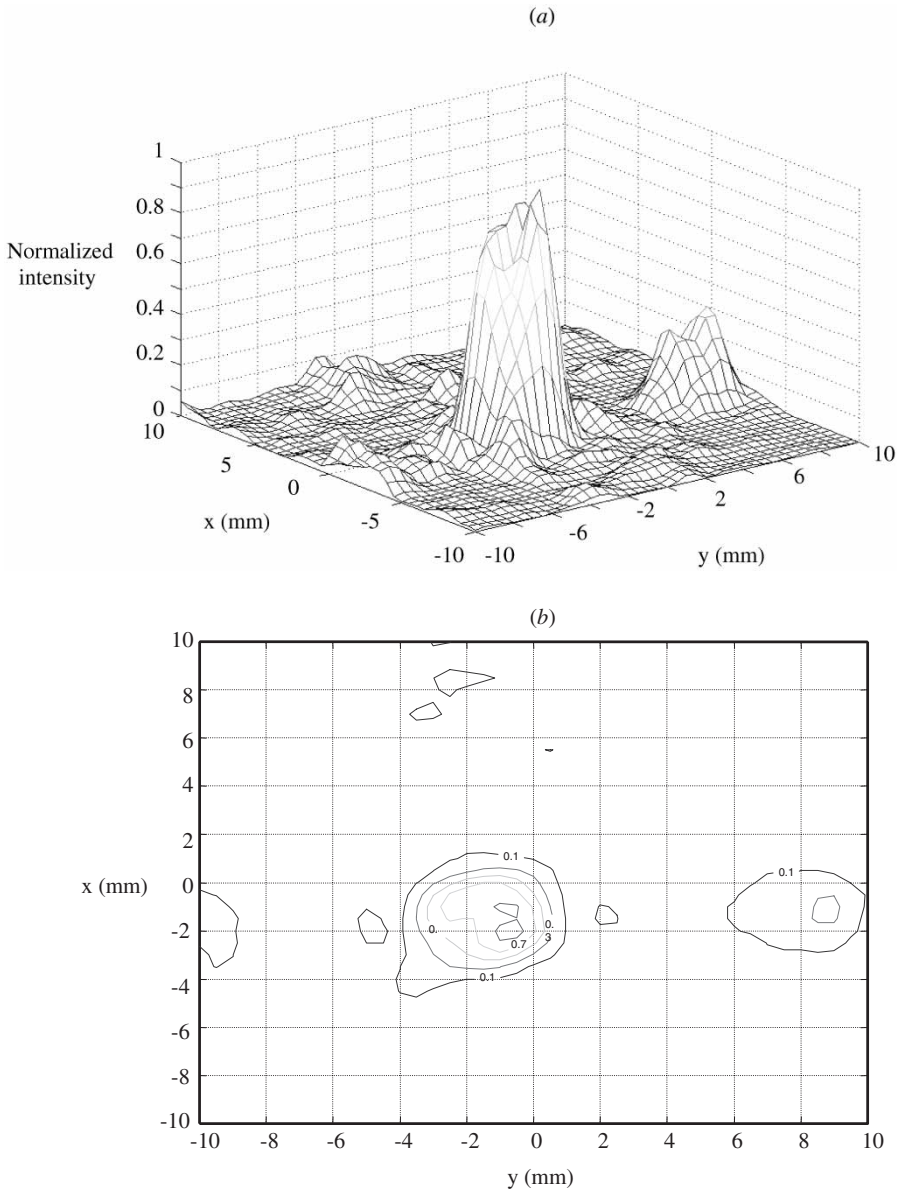


Figure 9. Exposimetry results of the normalized intensity for off-axis focusing with the focal point aimed at $-2, -0.7, 30$ mm plotted as (a) a mesh or (b) a contour with levels indicated at 90, 70, 50, 30, 10%. These results indicate acceptable grating lobes of less than -7.0 dB.

4. Discussion

Intra-cavitary ultrasound offers an attractive means of focused ultrasound treatment for benign prostatic hyperplasia with significant advantages over other treatment methods due to the relatively short treatment time, its non-invasive nature and reduced complications. One compelling reason for using an intra-cavitary device with focused ultrasound is that the prostate is easily accessible via transrectal applicators, which allow for heating of the target volume in the prostate with

minimal heating of normal tissue. Using phased arrays to electrically focusing the ultrasound beam provides a controlled localized power deposition into tissue and reduces significantly the treatment time since the focus is electronically scanned instead of manually.

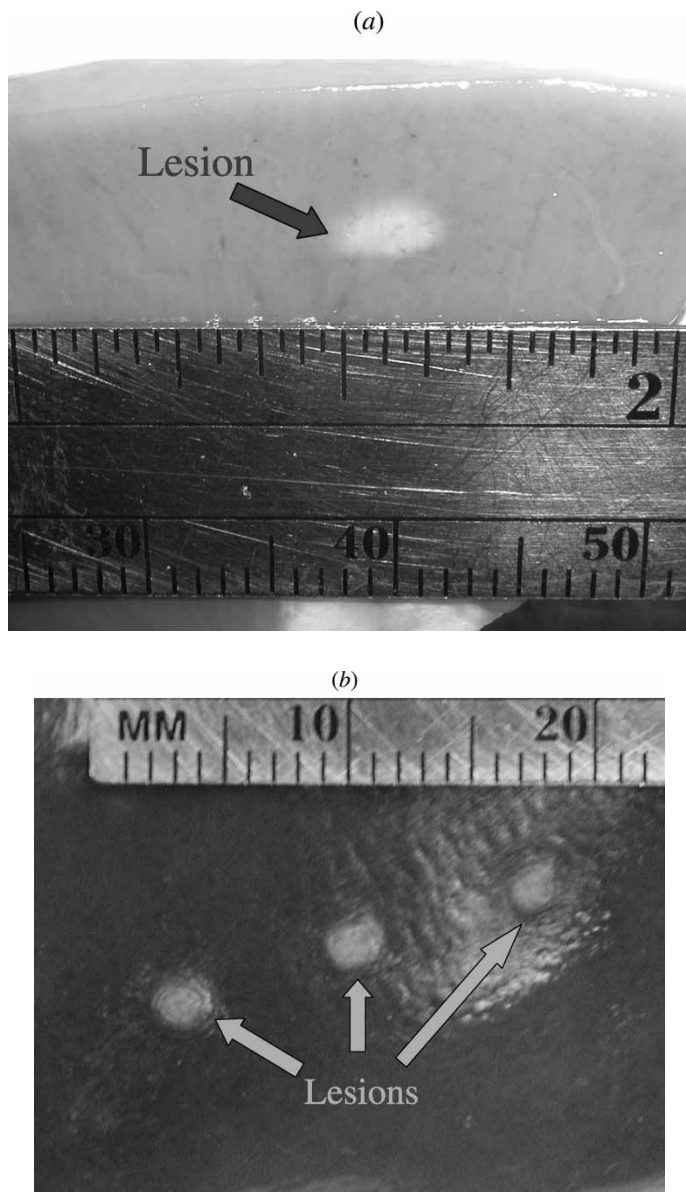


Figure 10. *Ex vivo* experimental results of lesions created with on and off-axis focusing with the array driven at an average of 8 W per element for various sonication times. (a) Focusing 30 mm into the tissue, a cigar shaped lesion was created from a 10 s sonication. (b) Evaluation of the electrical steering at $(x, y, z) = (-3, -7, 30)$, $(0, 0, 30)$ and $(3, 7, 30)$ mm created 2 mm diameter lesions. (c) Effects of the sonication time variation are illustrated from exposure times of 10, 15 and 20 s.

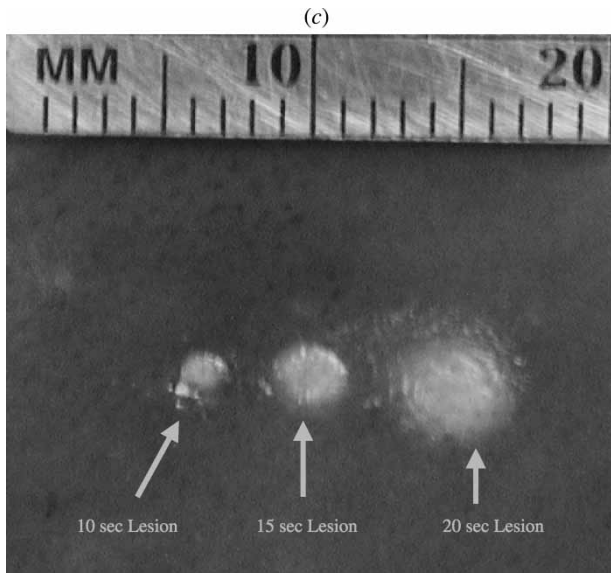


Figure 10. Continued.

Previous focused ultrasound array designs were problematic, since they required complex methods to move the focus, or had linear (1-D) designs that were only capable of focusing along one axis. These drawbacks were the motivation to design a new array that can be used in FUS and, at the same time, be systematically controlled to reposition the focus throughout a specific volume with an acceptable level of grating lobes. Care was taken with this new 64 element, 8×8 array to account for capacitance issues between the ceramic and cables by modelling the system and impedance testing with various cables. Further improvement over this array design seems to be feasible due to recent developments in building focused transducers using piezocomposite technology²³. Using piezocomposites removes the concern of low width to thickness ratios, which was an issue in this array design. A three layer PZT-8 material may also be used to increase the capacitance and, thus, make it easier to electrically match the small elements.

In designing this array, several issues were taken into account to address its application for BPH treatment. The dimensions of the array were designed for an intra-cavitary rectal device. With appropriate housing, a dimension of 2×2 cm array is suitable. Although the housing used here does not satisfy this condition, this design was used to evaluate the feasibility of the steering. Another issue concerning this design was the grating lobe level, which was reduced significantly by tapering the elements widths and lengths of the array.

To treat the prostate, this array was aimed toward the intended target volume and the elements were driven at a calculated amplitude and phase to generate either a single focal point with electrical steering or generate multiple focal points simultaneously to increase the necrosed volume per sonication. To generate multiple focal points, the total area of the array was divided into several sub-areas (four, for example), the array was driven in such a way that each one of these sub-areas was responsible for generating a single focal point. Although this reduces

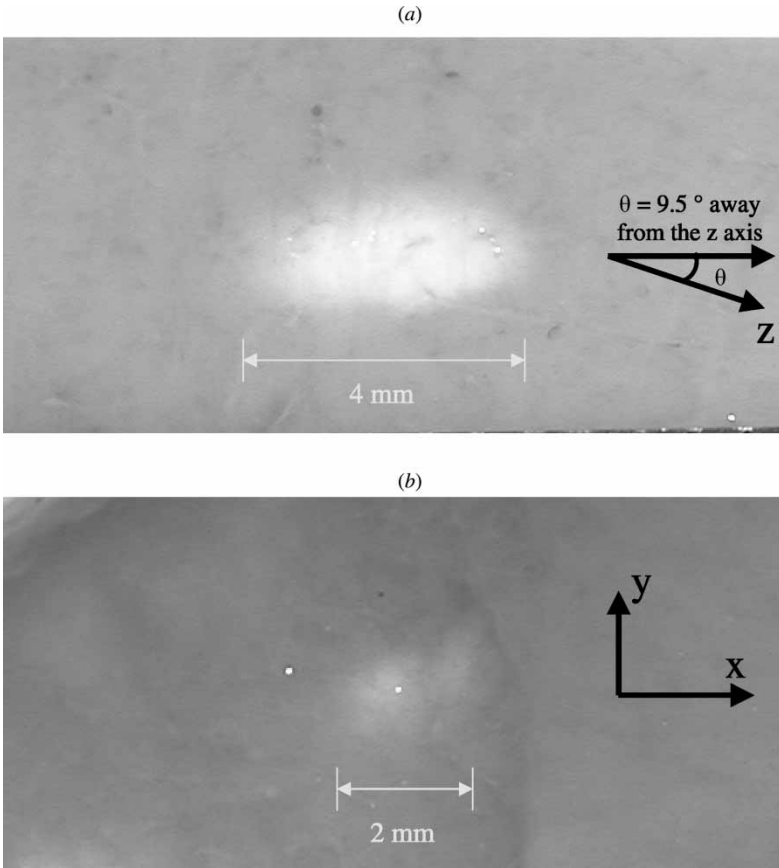


Figure 11. An *ex vivo* experimental result showing orthogonal paired cross-sections of a lesion generated by focusing at 5, 0, 30 mm (steering angle = 9.5° away from the z-axis). Shown is (a) a cross-section made along the focusing plane (9.5° away from the z-axis) that indicates a 4 mm long cigar shaped lesion and (b) a cross-section made parallel to the x-y plane and 30 mm deep in tissue, showing the size of the lesion in that plane, which was found to be a 2 mm diameter lesion.

the sonication time, it requires more driving power since each sub-area needs to generate a single focal point.

This array is not designed to ablate the whole prostate, although that can be achieved by mechanically moving the array several times depending on the prostate size. As was previously shown in figure 2, this array can necrose a volume that lies in its steering volume. Assuming that the centre of the volume to be necrosed is 3 cm deep, this array is capable of necrosing a volume of at least $1 \times 1 \times 2 \text{ cm}^3$ without mechanically moving the array. Taking this ($1 \times 1 \times 2 \text{ cm}^3$) as the target volume, two techniques can be used to necrose it; the first one is using a single focal point regime in which the target volume is divided into small volumes. The size of these small volumes is chosen based on the size of the lesion and the sonication time. For a 10 s sonication, the lesion was found to be a 4 mm long cigar shape with 2 mm diameter. Therefore, dividing the $1 \times 1 \times 2 \text{ cm}^3$ volume into $5 \times 5 \times 5$ points indicates that 125 sonications are needed to necrose the target based on a single 10 s sonication that is electronically steered between the 125 positions. Starting at the centre of the

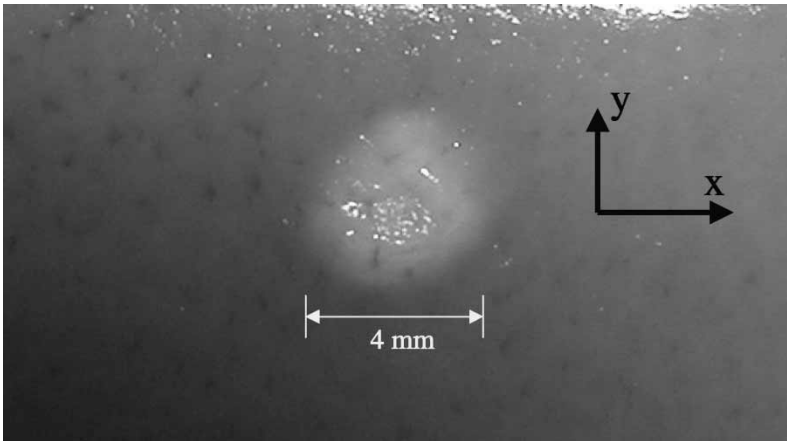


Figure 12. To verify the feasibility of generating a large lesion as a result of four overlapped small lesions, the array was driven at an average power of 8 W for 25 s, with four focal points aimed at $\pm 1, \pm 1, 30$ mm. A cross-section made parallel to the x - y plane and 30 mm deep in tissue shows the generation of a single large lesion with a diameter of 4 mm.

target volume, a single focal point is generated there and then electronically steered 125 times to cover the whole volume. To avoid uncontrolled heat buildup and pre-focal heating, the switching between the focal points is done in a way that any two focal points consecutive in time are far away from each other in distance. By doing that, enough time is given to the pre-focal positions to cool down. A second technique to necrose a large volume is by generating multi-focal points at the same time. Dividing the array into four areas, each responsible for generating a single focal point, will result in reducing the overall treatment time by a factor of four. This technique is time efficient, but the drawback behind it is that the driving electrical power per unit area should be increased.

Since the maximum possible steering angle for this array is 14° in both transverse and longitudinal directions, attempting to focus outside this volume will add a significant amount of grating lobes which will cause an unwanted heating. This puts a limitation for this array if the target volume extends beyond the 14° limit. Trying to focus 2 cm deep is feasible, however the maximum off-axis steering at 2 cm deep is 0.5 cm, which adds another limitation if a 1 cm off-axis steering is required to ablate anterolateral prostate tissue.

When coupled with MR temperature mapping, FUS provides an efficient way to treat BPH and at the same time gives a quick feedback about the temperature distribution inside the prostate⁸. Although ultrasound imaging for the prostate has shown to give good results^{24,25}, the array described here was designed to be accompanied by an MRI.

Similar to prostate cancer treatment with focused ultrasound, benign fibroadenomas in the breast are currently treated clinically using multiple sonication from a single element transducer which is mechanically scanned²⁶. In conjunction, magnetic resonance imaging (MRI) for guidance of thermotherapy of the procedure²⁷. Although the treatment has been shown to be effective, the process includes an unnecessary delay due to the mechanical scanning protocol. When closely spaced locations are targeted with focused ultrasound, thermal build-up results from the accumulation of neighbouring sonications and the near field heating. As a result,

a lengthy delay between sonications (cooling time) is required to reduce thermal build-up. Investigators have shown that a cooling time of 50–60 s was necessary to reduce the heat from the near neighbour sonications²⁸; however, this can add considerable time to the procedure and initiate inaccuracies to the MR thermometry through patient motion. With phased arrays, a focal pattern can be arranged such that there is enough time for the heat to dissipate by sonicating non-neighbouring regions within the tumour²⁹. A treatment planning routine can be plotted over the entire tumour region such that the volume is ablated through distant and non-adjacent ablations to avoid thermal build-up yet destroy the volume in the least amount of time. This research demonstrates the feasibility of an electrically steered array, which can be used to ablate tissue for the intended treatment of benign prostatic hyperplasia. Future plans will advance this design to a clinical model to be used for *in vivo* studies.

Acknowledgements

This work was supported by the Whitaker Foundation (RG-00-0042) and the Department of Defense Congressionally Directed Medical Prostate Cancer Research Program (DAMD17-0201-0124).

References

1. Stephens F. *All about prostate cancer*. South Melbourne, Australia; New York: Oxford University Press, 2000.
2. Tan JS, Frizzell LA, Sanghvi NT, Seip R, Wu JS, Kouzmanoff JT. Design of focused ultrasound phased arrays for prostate treatment. *IEEE Ultrason Symp* 2000; 1247–51.
3. Seip R, Sanghvi NT. Comparison of split-beam transducer geometries and excitation configuration for transrectal prostate HIFU treatments. *IEEE Ultrason Symp* 2001; 1343–46.
4. Ebbini ES, Bischof JC, Coad JE. Lesion formation and visualization using dual-mode ultrasound phased arrays. *IEEE Ultrason Symp* 2001; 1351–54.
5. Yao H, Phukpattaranont P, Ebbini ES. Enhanced lesion visualization in image-guided noninvasive surgery with ultrasound phased arrays. *23rd Annual EMBS international conference, IEEE* 2001; 2492–95.
6. Barrett DM. *Mayo Clinic on prostate health*, 1st edn. Rochester, MN; New York: Mayo Clinic, 2000.
7. Hutchinson EB, Hynynen K. Intracavitary phased arrays for non-invasive prostate surgery. *IEEE Trans Ultrason Ferroelectr Freq Control* 1996; 43: 1032–42.
8. Sokka S, Hynynen K. The feasibility of MRI guided whole prostate ablation with a linear aperiodic intracavitary ultrasound phased array. *Phys Med Biol* 2000; 45: 3373–83.
9. Curiel L, Chavrier F, Souchon R, Birer A, Chapelon JY. 1.5-D high intensity focused ultrasound array for non-invasive prostate cancer surgery. *IEEE Trans Ultrason Ferroelectr Freq Control* 2002; 49: 231–42.
10. Buchanan MT, Hynynen K. Design and experimental evaluation of intracavitary ultrasound phased array system for hyperthermia. *IEEE Trans Biomed Eng* 1994; 41: 1178–87.
11. Zemanek J. Beam behavior within the nearfield of a vibrating piston. *J Acoust Soc Am* 1971; 49: 181–91.
12. Pennes HH. Analysis of tissue and arterial blood temperatures in the resting human forearm. *J Appl Physiol* 1948; 1: 93–122.
13. Nyborg WL. Heat generation by ultrasound in a relaxing medium. *J Acoust Soc Am* 1981; 70: 310–12.
14. Smith NB, Buchanan MT, Hynynen K. Transrectal ultrasound applicator for prostate heating monitored using MRI thermometry. *Int J Radiat Oncol Biol Phys* 1999; 43: 217–25.
15. Hutchinson EB, Buchanan MT, Hynynen K. Evaluation of an aperiodic phased array for prostate thermal therapies. *IEEE Ultrasonics Symp* 1995; 1601–04.

16. Gavrilov LR, Hand JW, Abel P, Cain CA. A method of reducing grating lobes associated with an ultrasound linear phased array intended for transrectal thermotherapy. *IEEE Trans Ultrason Ferroelectr Freq Control* 1997; 44: 1010–7.
17. Goss SA, Johnston RL, Dunn F. Comprehensive compilation of empirical ultrasonic properties of mammalian tissues. *J Acoust Soc Am* 1978; 64: 423–57.
18. Goss SA, Frizzell LA, Dunn F. Ultrasonic absorption and attenuation in mammalian tissues. II. *J Acoust Soc Am* 1980; 68: 93–108.
19. Daum DR. A large scale phased array ultrasound system for non-invasive surgery of deep stated tissue. PhD dissertation, Massachusetts Institute of Technology, Cambridge, MA, 1998.
20. AIUM. *Acoustic output labeling standard for diagnostic ultrasound equipment*. Laurel, MD: Author, 1998.
21. IEEE. *Guide for medical ultrasound field parameter measurements*. New York: Author, 1990.
22. Hurwitz MD, Kaplan I, Svensson GK, Hansen J, Hynynen K. Feasibility and patient tolerance of a novel transrectal ultrasound hyperthermia system for treatment of prostate cancer. *Int J Hyperthermia* 2001; 17: 31–7.
23. Fleury G, Berriet R, Le Baron O, Huguenin B. New piezocomposite transducers for therapeutic ultrasound. *Workshop on MRI-guided Focused Ultrasound Surgery* 2002: 39.
24. Sanghvi NT, Foster RS, Bihle R, Casey R, Uchida T, Phillips MH, Syrus J, Zaitsev AV, Marich KW, Fry FJ. Noninvasive surgery of prostate tissue by high intensity focused ultrasound: an updated report. *Eur J Ultrasound* 1999; 9: 19–29.
25. Chapelon JY, Ribault M, Birer A, Vernier F, Souchon R, Gelet A. Treatment of localised prostate cancer with transrectal high intensity focused ultrasound. *Eur J Ultrasound* 1999; 9: 31–8.
26. Hynynen K, Pomeroy O, Smith DN, Huber PE, McDannold NJ, Kettenbach J, Baum J, Singer S, Jolesz FA. MR imaging-guided focused ultrasound surgery of fibroadenomas in the breast: a feasibility study. *Radiology* 2001; 219: 176–85.
27. Quesson B, de Zwart JA, Moonen CT. Magnetic resonance temperature imaging for guidance of thermotherapy. *J Magn Reson Imaging* 2000; 4: 525–33.
28. McDannold NJ, Jolesz FA, Hynynen KH. Determination of the optimal delay between sonications during focused ultrasound surgery in rabbits by using MR imaging to monitor thermal buildup in vivo. *Radiology* 1999; 211: 419–26.
29. Daum DR, Hynynen K. Thermal dose optimization via temporal switching in ultrasound surgery. *IEEE Trans Ultrason Ferroelectr Freq Control* 1998; 45: 208–15.

Materials Research Innovations

Volume 8 - Number 2 - June 2004

Reactivity Of Tosylhydrazones Under Microwave Irradiation In Solvent-Free Environment

Romano Grandi, Anna Corradi, Christina Leonelli, Christina Siligardi, Paolo Veronesi.

1.06 μm Laser Characteristics Of $\text{Nd}^{3+}:\text{KLa}(\text{WO}_4)_2$ Crystal

Xiumei Han, Lizhen Zhang, Minwang Qiu, Guofu Wang.

Improved Design Of Waveguide Slot Array Applicators For Microwave Heating

Vittorio Castrillo, Guglielmo D'Ambrosio, Rita Massa, Francesco Chiadini, Vincenzo Fiumara, Antonio Scaglione, Gaetano Panariello, Innocenzo M. Pinto.

Microwave Synthesis Of MgB_2 Superconductor

Angelo Agostino, Paolo Volpe, Mario Castiglioni, Marco Truccato.

Feasibility Of Miniature High-Frequency Piezoelectric Ceramic Hollow Spheres For Exposimetry And Tissue Ablation

Osama M. Al-Bataineh, Douglas C. Markley, Richard J. Meyer Jr., Robert E. Newnham, Nadine Barrie Smith.

Preparation And Corrosion Studies Of Self-Healing Multi-Layered Nano Coatings Of Silica And Swelling Clay

Akio Hikasa, Tohru Sekino, Yamato Hayashi, Ramaseshan Rajagopalan, Koichi Niihara.

Characterization And Synthesis Of Some Alternating Terpolymers Of Maleic Anhydride

Ali Boztuğ, Satýlýmyş Basan, Oktay Elcin Ekberov

Void Free Friction Stir Weld Zone Of The Dissimilar 6061 Aluminum And Copper Joint By Shifting The Tool Insertion Location

Won-Bae Lee, Seung-Boo Jung.

Preparation Of Tic Free Ti_3SiC_2 With Improved Oxidation Resistance By Substitution Of Si With Al

Yanchun Zhou, Haibin Zhang, Mingyue Liu, Jingyang Wang, Yiwang Bao.

Revealing The Concept Of Polyarylsilaneimide Quasi Nanocomposite Formation: Correlation With Macroscopic Properties And Electrical Parameters

Atul Tiwari, Kailash Nath Pandey, Gyanesh Narain Mathur, Suresh Kumar Nema.

Effects Of Fine Alumina Dispersion On Ionic Conductivity And Mechanical Properties Of Ytterbia Stabilized Cubic Zirconia

Masashi Wada, Tohru Sekino, Takafumi Kusunose, Tadachika Nakayama, Yong-Ho Choa, Koichi Niihara.

Design And Evaluation Of A 3 X 21 Element 1.75 Dimensional Tapered Ultrasound Phased Array For The Treatment Of Prostate Disease

Khaldon Y. Saleh, Nadine Barrie Smith.

Due to an editorial production error, our research presented herein was erroneously attributed to the wrong research group on the following page but correctly listed on the front cover (previously page) and on page 124. *Materials Research Innovations* will be printing a corrected version of this paper in a subsequent issue.

Masashi Wada, Tohru Sekino, Takafumi Kusunose, Tadachika Nakayama, Yong-Ho Choa, Koich Niihara

Design And Evaluation Of A 3 x 21 Element 1.75 Dimensional Tapered Ultrasound Phased Array For The Treatment Of Prostate Disease

Received: 29 September 2003 / Revised: 22 March 2004 / Accepted: 30 September 2003

Abstract

This paper describes the design, construction, and evaluation of a 1.75 dimensional (1.75-D) tapered ultrasound phased array to be used in the treatment of benign prostatic hyperplasia and prostate cancer. The array was designed to be able to focus and steer in a three dimensional volume with a maximum steering angle of $\pm 13.5^\circ$ in the transverse direction and a maximum depth of penetration of 11 cm, which allows the treatment of large prostates. A piezoelectric ceramic (PZT-8) at a frequency of 1.2 MHz was used as the material of the transducer since it can handle the high power needed for tissue ablation and two matching layers were used for maximum acoustic power transmission to tissue. To verify the capability of the transducer for focusing and steering, exposimetry was performed and the results correlated well with the calculated field.

Keywords *Transducer 1.75-D array Focusing Matching layer Necrosis*

Introduction

Focused ultrasound surgery (FUS) has been shown to give promising results in treating benign prostatic hyperplasia (BPH) [1, 2, 3, 4]. Although BPH is not life threatening, treating it is necessary since normal urine flow and function can be disrupted as a result of the prostate pushing against the urethra and the bladder. The goal of this research was to construct, computationally and experimentally, a 1.75-D tapered phased array suitable for tissue ablation in the prostate. Part of the design criteria was that a specific region in a target volume will be ablated by focusing the ultrasound beam at that region using short, high temperature sonications. Additionally, for magnetic resonance imaging (MRI) monitoring and temperature guidance, a magnet compatible ultrasound phased array was designed for the treatment of BPH [5].

Previous one dimensional (1-D) prostate array transducer geometries include a 64 x 1 aperiodic linear array which reduced grating lobes and could electrically adjust the focus at distal and proximal locations along the urethra, and a 60 x 1 linear array with a mechanical rotation which could electrically steer the focus along the urethra and mechanically steer left and

right of the mid-sagittal urethra [6, 7]. A design which had better focusing capabilities than a 1-D array was a 64 x 4 spherically curved 1.5 dimensional (1.5-D) array that could, but had restrictions to the focusing volume, focus and steer in the three directions [8]. The drawbacks behind these prostate arrays are that they can only focus at distal or proximal locations along the urethra or complex mechanics which move the focus. The advantage with a 1.75-D array is that it can electrically focus at distal and proximal locations along the urethra and left and right of the mid-sagittal line by changing the phase to the elements. One difficulty with designing a 1.75-D array is in dicing the ceramic 100% through its thickness while maintaining a common grounding for all of the elements. To overcome this problem, two matching layers (the first one being conductive) were designed and constructed. The two matching layers not only help make a common ground, but they also increase, to a large extent, the acoustical power efficiency, and facilitate in maintaining the structural integrity of the array. This research presents a 3 x 21 element 1.75-D tapered ultrasound array designed to ablate tissue while overcoming many problems involved with transducer fabrication.

Materials and Methods

Simulations

Computer simulation programs were written to determine the number and the size of the phased array elements in addition to determining the pressure and temperature field from the device. The array was modeled (Fig. 1) as a 1.75-D tapered array in order to have focusing and steering capabilities in both x and z directions (x = transverse, y = longitudinal and z = radial). Focusing in the y direction is done in a different way; the array is divided into three identical rows, each one represents a single linear array. If the focus is required at y = 0, the middle row should be used. A focus at y = -0.9 mm requires driving the lower row, while a focus at y = +0.9 mm requires the operation of the upper row. Although the degree of freedom in the y direction is not perfect, the size of the lesion generated by a single sonication compensates for that, since the focus length is about 9 mm in the y direction. The driving phase of each element was determined such that signals from individual elements were all

in phase only at the focal point. Huygen's principle was used to model the pressure field as a summation of simple sources [9]. With these requirements, this array was capable of focusing and steering with a steering angle of $\pm 13.5^\circ$ with maximum focal depth of 11 cm.

Off-axis focusing and the grating lobe level are directly related to each other since increasing the steering angle causes a nonlinear increase in the grating lobe level. Another factor that affects the grating lobe level is the periodicity of the elements widths (tapered versus equal size). Tapered or aperiodic element arrays have been shown to reduce significantly the grating lobe level [10, 11]. Figure 2 shows a comparison of the grating lobe levels for both tapered and equal size arrays as a function of off-axis focal point position x_f . At zero steering angle ($x_f = 0$), the tapered array has 6% less grating lobes than the equal size array. Although this is not a great improvement, at large steering angles, this improvement becomes more significant. The grating lobe for the tapered array was reduced (compared to the equal size array) by about 8, 14, 14, 16 and 14% for $x_f = 2, 4, 6, 8$ and 10 mm, respectively.

Initially the simulated design for the intensity used equal size elements of $9 \times 2.1 \text{ mm}^2$, and although it was capable of focusing and steering, it suffered from large grating lobes outside the focus. For example, at a focus of $(x, y, z) = (2, 0, 50) \text{ mm}$ (i.e. the 0, 0, 0 position is at the center of the transducer face in Fig. 1), the grating lobe level was -4.95 dB which was not desirable since this high level can cause an increase in tissue temperature outside the focus. Removing the periodicity of the array or tapering it has been shown to reduce the grating lobe level. The maximum possible steering angle was calculated to be $\tan^{-1}(1.2/5.0) = 13.5^\circ$ with maximal focal depth of 11 cm. Improvements to the tapered array design started with a $27 \times 53 \text{ mm}^2$ solid piezoceramic cut into a 3×21 pattern with 63 individual elements with lengths (L_i) of 1.68, 1.73, 1.81, 1.91, 2.02, 2.14, 2.26, 2.36, 2.43, 2.48, 2.50, 2.48, 2.43, 2.36, 2.26, 2.14, 2.02, 1.91, 1.81, 1.73, 1.68 mm for elements $i = 1$ through 21, respectively, and widths (W) of 9.0 mm for all elements $i = 1$ through 3, respectively (Fig. 1). Simulations have shown that the grating lobe level of the tapered design has decreased to -6.20 dB at a similar focus location of 2, 0, 50 mm. Temperature simulations were also used to verify the potential to increase the tissue temperature to 60°C with short sonications [12]. Figure 3 shows an example of the temperature distribution as a function of x and z corresponding to an intended focal point position of (2, 0, 50) mm.

Transducer construction

Choosing an appropriate piezoceramic material to be used in this application is essential since it affects both electrical and acoustical properties of the array. Lead zirconate-titanate (PZT-8) can handle the large electrical power needed for tissue ablation and has an extremely high mechanical quality and extremely low loss factor. Thus PZT-8 material (TRS Ceramics, State College, PA, USA) was chosen at a frequency of 1.2 MHz and

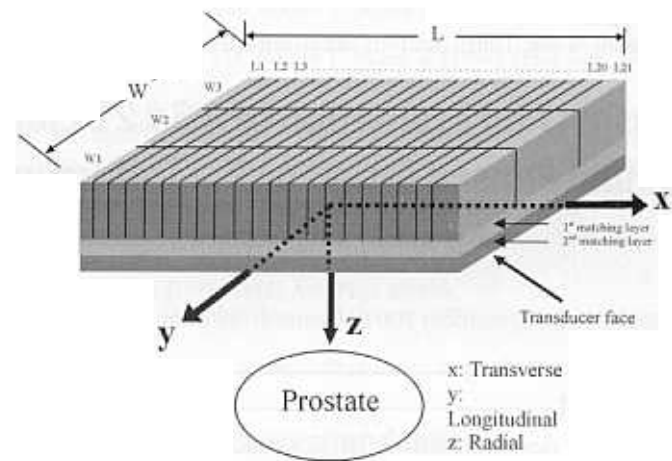


Fig. 1. Based on the simulations, a diagram of the 1.75-D 63 element (3×21) tapered array with total size of $27 \times 53 \text{ mm}^2$ with the proportions of the ceramic and matching layer illustrated. The diced face of the ceramic was cut 100% through and each individual element was attached to the electrical cabling using low temperature soldering material

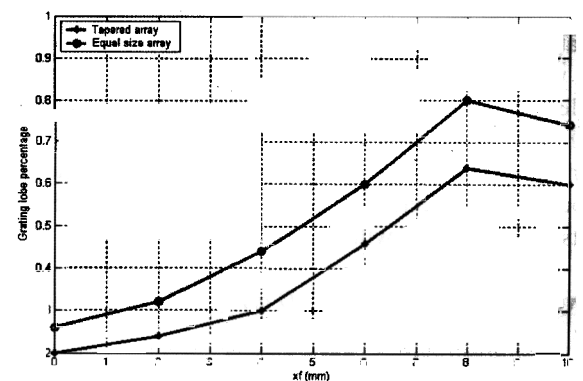


Fig. 2. Simulation results showing the relationship between element size and the grating lobe level as a function of off-axis focal point position x_f and thus the steering angle. Plotted for both tapered and equal size arrays, the grating lobe level was decreased by a percentage of 6, 8, 14, 14, 16 and 14 % for $x_f = 0, 2, 4, 6, 8$ and 10 mm, respectively, when compared to an equal size array

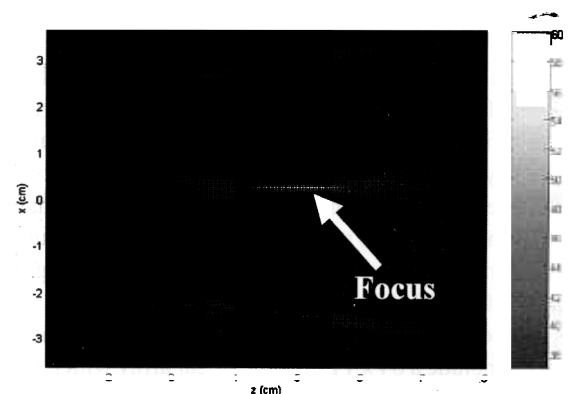


Fig. 3. A temperature map for a focal point at $(x, y, z) = (2, 0, 50) \text{ mm}$ was numerically solved using the bioheat transfer equation. This simulated figure shows an increase in tissue temperature to the target of 60°C at the focal point using a 10 sec sonication while outside the target region the temperatures were normal as indicated from the temperature color bar

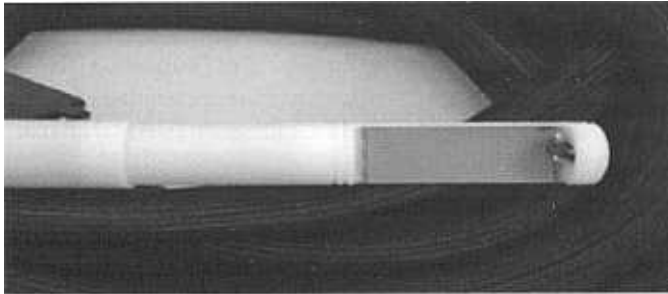


Fig. 4. Photograph of the constructed, waterproof array machined from Delrin® with 8.3 m low capacitance cable that connected to the amplifier system

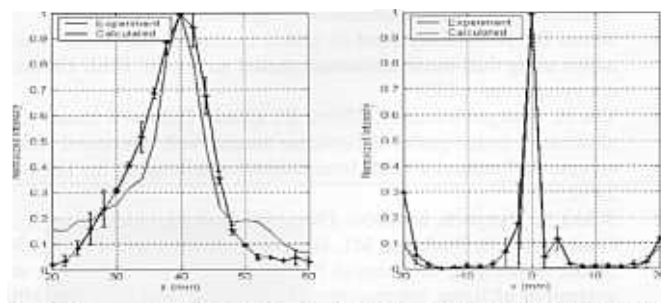


Fig. 5. Comparison of calculated and experimental normalized intensities for a focus at 0, 0, 40 mm plotted along the (a) z axis and (b) x axis

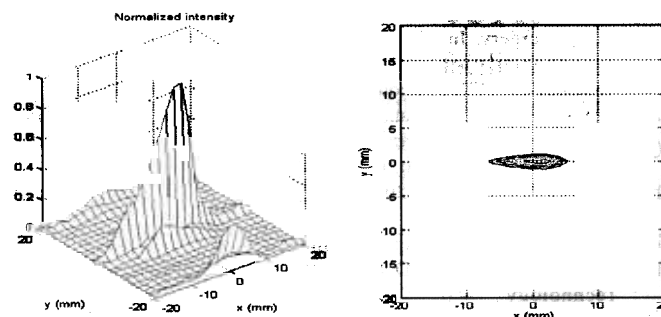


Fig. 6. Exposimetry results of the normalized intensity for off-axis focusing with the focal point aimed at 0, 0, 40 mm plotted as a (a) mesh or (b) contour with levels indicated at 90, 70, 50, 30, 10%. These results indicate acceptable grating lobes of less than -7.0 dB

diced, in house, into 3×21 elements forming the complete array. The cuts were made by dicing the material 100% through its thickness with a kerf width of $300 \mu\text{m}$ using a dicing saw (Model 780, K & S-Kulick and Soffa Industries, Willow Grove, PA, USA) in our lab. For maximum acoustical power transfer from the individual elements to the tissue, two matching layers were designed and constructed. The thickness and material selection of the matching layers were designed based on the solution to a four layer problem (transducer, first matching layer, second matching layer, and tissue), which ensured the required maximum power transfer. Each of the two matching layers was designed for a quarter wavelength thickness. Accordingly, the thickness of the first and second matching layers was determined to be 0.396 and 0.429 mm, respectively [11]. The first matching layer, mixed in-house, was a 2:1 epoxy to silver mix-

ture of Insulcast 501 (Insulcast, Roseland, NJ, USA) and 2-3 micron silver epoxy (Aldrich, Milwaukee, WI, USA), while the second matching layer was a SPURR (Spi Supplies, West Chester, PA, USA) four-part low viscosity material. For this array design (Fig. 4), the specially machined, waterproof cylindrical applicator housing (30 mm diameter) was made from magnet compatible Delrin® (Dupont, Wilmington, DE, USA) at the Penn State engineering shop.

To drive the array, a specially built amplifier driving system (Advanced Surgical Systems Inc., Tucson, AZ, USA) was used [13]. Briefly, this amplifier system was a multi-channel high power, ultrasound phased-array transducer driver for 64 elements which is capable of delivering 60 W per channel with $\pm 1^\circ$ phase resolution each. To match the impedance of the elements to the amplifier, individual LC (L = inductor and C = capacitor) circuits were built for each of the 63 elements to match each one to the common value of $50 \angle 0^\circ$.

Exposimetry

Initially, multiple on-axis (i.e. where the focus is along the major z axis, z_f) exposimetry experiments were performed. With the focus set to $0, 0, z_f$ mm, z_f was varied from 10 mm to 110 mm with a step size of 5 mm. To determine the repeatability or standard deviation of the focusing, 5–10 experiments were performed at each location. For off-axis studies (i.e. where the focus was not on z but aimed toward the x axis, x_f), the focus was located at $x_f, 0, 60$ mm while the steering angle was adjusted to the desired value by choosing appropriate values for x_f . The steering angle was varied from -13° to $+13^\circ$ with a step size of 2° in both x and y directions with multiple experiments (5–10) performed at each angle. In both the on-axis and off-axis experiments, the scanning step size was 0.5 mm while the scanning area was 20×20 mm². The hydrophone voltage recordings were used to calculate the normalized intensities based on the pressures that were plotted as the mean and standard deviation of the results ($\bar{x} \pm \text{s.d.}$) and compared against the calculated values [14, 15].

Results

To test the correlation between experimental and theoretical results, numerous exposimetry experiments were performed throughout the desired ablation volume to determine the focusing capability of the array. As an example of a typical exposimetry result at the location $(x, y, z) = (0, 0, 40)$ mm, Fig. 5a shows a comparison plot along the z axis of the calculated and experimental normalized intensities. Figure 5b plots similar theoretical and experimental data, but instead, along the x axis for the same focus $(0, 0, 40)$ mm. As can be seen for both plots, the theoretical intensity data correlated well with the experimental results.

To evaluate the feasibility of the array to steer the focus, a typical three dimensional normalized intensity result from a focal point was directed at $0, 0, 40$ mm. The results were plotted as a mesh (Fig. 6a) and contour (Fig. 6b) with contour levels at

90, 70, 50, 30 and 10% of the maximum intensity with the grating lobe levels at about -7.0 dB or less.

Discussion

Intracavitary ultrasound offers an attractive means of focused ultrasound treatment for benign prostatic hyperplasia with significant advantages over other treatment methods due to the relatively short treatment time, its noninvasive nature and reduced complications. One compelling reason for using an intracavitary device with focused ultrasound is that the prostate is easily accessible via transrectal applicators, which allow for heating of the target volume in the prostate with minimal heating of normal tissue. Using phased arrays to electrically focusing the ultrasound beam provides a controlled localized power deposition into tissue and reduces significantly the treatment time since the focus is electronically scanned instead of manually.

Previous focused ultrasound array designs were problematic since they required complex methods to move the focus, or had linear (one dimensional) designs that were only capable of focusing along one axis. These drawbacks were the motivation to design a new array that can be used in FUS and at the same time be systematically controlled to reposition the focus throughout a specific volume with an acceptable level of grating lobes. Care was taken with this new 63 element, 3 x 21 array, to account for capacitance issues between the ceramic and cables by modeling the system and impedance testing with various cables.

In designing this array, several issues were taken into account to address its application for BPH treatment. The dimensions of the array were designed for an intracavitary rectal device. With appropriate housing, a dimension of 2.7 cm x 5.3 cm array is suitable. Another issue concerning this design was the grating lobe level, which was significantly reduced by tapering the elements widths of the array.

To treat the prostate, this array was aimed toward the intended target volume, and the elements were driven at a calculated amplitude and phase to generate either a single focal point with electrical steering, or generate multiple focal points simultaneously to increase the necrosed volume per sonication. With phased arrays a focal pattern can be arranged such that there is enough time for the heat to dissipate by sonicating non-neighboring regions within the tumor [16]. A treatment planning routine can be plotted over the entire tumor region such that the volume is ablated through distant and non-adjacent ablations to avoid thermal build-up yet destroy the volume in the least amount of time. This research demonstrates the feasibility of an electrically steered array which can be used to ablate tissue for the intended treatment of benign prostatic hyperplasia. Future plans will apply this design for potential clinical evaluation with animal *in vivo* studies.

Acknowledgements

This work was supported by the Whitaker Foundation (RG-00-0042) and the Department of Defense Congressionally Directed Medical Prostate Cancer Research Program (DAMD17-0201-0124).

References

1. Tan JS, Frizzell LA, Sanghvi NT, Seip R, Wu JS, Kouzmanoff JT (2000) Design of focused ultrasound phased arrays for prostate treatment. In: IEEE Ultrasonics symposium, p 1247
2. Seip R, Sanghvi NT (2001) Comparison of split-beam transducer geometries and excitation configuration for transrectal prostate HIFU treatments. In: IEEE Ultrasonics symposium, p1343
3. Ebbini ES, Bischof JC, Coad JE (2001) Lesion formation and visualization using dual-mode ultrasound phased arrays. In: IEEE Ultrasonics symposium p1351
4. Yao H, Phukpattaranont P, Ebbini ES (2001) Enhanced lesion visualization in image-guided noninvasive surgery with ultrasound phased arrays. 23rd annual EMBS international conference, In: IEEE p 2492
5. Sokka S, Hynynen, K (2000) Phys Med Biol 45:3373
6. Hutchinson EB, Buchanan MT, Hynynen K (1996) Med Phys 23:767
7. Sokka S, King R, McDannold NJ, Hynynen K (1999) Design and evaluation of linear intercavitary ultrasound phased array for MRI-guided prostate ablative therapies. In: IEEE Ultrasonics Symposium p 1435
8. Curiel L, Chavrier F, Souchon R, Birer A, Chapelon J (2002) 1.5-D high intensity focused ultrasound array for non-invasive prostate cancer surgery. In: IEEE Trans Ultrason Ferroelectr Freq Control 49:231
9. Zemanek J (1971) J Acoust Soc Am 49:181
10. Hutchinson EB, Buchanan MT, Hynynen K (1995) Evaluation of an aperiodic phased array for prostate thermal therapies. In: IEEE Ultrasonics symposium, p 1601
11. Saleh KY, Smith NB (2004) International Journal of Hyperthermia 20:7
12. Pennes HH (1948) J Appl Physiol 1:93
13. Daum DR (1998) PhD dissertation, Massachusetts Institute of Technology
14. AIUM (1998) Acoustic output labeling standard for diagnostic ultrasound equipment, Laurel, MD: American Institute of Ultrasound in Medicine
15. IEEE Guide for Medical Ultrasound Field Parameter Measurements (1990) New York: Institute of Electrical and Electronics Engineers, Inc.
16. Daum DR, Hynynen K (1998) IEEE Trans Ultrason Ferroelectr Freq Control 45:208

Addresses For Correspondence

N. B. Smith, K. Y. Saleh (✉) (E-mail: kysbio@engr.psu.edu)
Department of Bioengineering, The Pennsylvania State University,
206 Hallowell Building, University Park, PA 16802, USA

N. B. Smith, Graduate Program in Acoustics, The Pennsylvania State University, 206 Hallowell Building, University Park, PA 16802, USA

Adaptive Real-Time Closed-Loop Temperature Control for Ultrasound Hyperthermia Using Magnetic Resonance Thermometry

L. SUN,¹ C.M. COLLINS,² J.L. SCHIANO,³ M.B. SMITH,² N.B. SMITH^{1,4}

¹ Department of Bioengineering, College of Engineering, The Pennsylvania State University, University Park, PA 16802

² Center for NMR Research, Department of Radiology, College of Medicine, The Pennsylvania State University, Hershey, Pennsylvania 17033

³ Department of Electrical Engineering, College of Engineering, The Pennsylvania State University, University Park, Pennsylvania 16802

⁴ Graduate Program in Acoustics, College of Engineering, The Pennsylvania State University, University Park, Pennsylvania 16802

ABSTRACT: Previous researchers have successfully demonstrated the application of temperature feedback control for thermal treatment of disease using MR thermometry. Using the temperature-dependent proton resonance frequency (PRF) shift, ultrasound heating for hyperthermia to a target organ (such as the prostate) can be tightly controlled. However, using fixed gain controllers, the response of the target to ultrasound heating varies with type, size, location, shape, stage of growth, and proximity to other vulnerable organs. To adjust for clinical variables, feedback self-tuning regulator (STR) and model reference adaptive control (MRAC) methods have been designed and implemented using real-time, online MR thermometry by adjusting the output power to an ultrasound array to quickly reach the hyperthermia target temperatures. The use of fast adaptive controllers in this application is advantageous because adaptive controllers do not require a priori knowledge of the initial tissue properties and blood perfusion and can quickly reach the steady-state target temperature in the presence of dynamic tissue properties (e.g., thermal conductivity, blood perfusion). This research was conducted to rapidly achieve and manage therapeutic temperatures from an ultrasound array using novel MRI-guided adaptive closed-loop controllers both in ex vivo and in vivo experiments. The ex vivo phantom experiments with bovine muscle ($n = 5$) show that within 6 ± 0.2 minutes, the tissue temperature increased by $8 \pm 1.37^\circ\text{C}$. Using rabbits' ($n = 5$) thigh muscle, the in vivo experiments demonstrated the target temperature reached $44.5^\circ\text{C} \pm 1.2^\circ\text{C}$ in 8.0 ± 0.5 minutes. The preliminary in vivo experiment with canine prostate hyperthermia achieved $43 \pm 2^\circ\text{C}$ in 6.5 ± 0.5 minutes. These results demonstrate that the adaptive controllers with MR thermometry are able to effectively track the target temperature with dynamic tissue properties. © 2005 Wiley Periodicals, Inc. Concepts Magn Reson Part B (Magn Reson Engineering) 27B: 51–63, 2005

Received 17 January 2005; revised 27 May 2005;
accepted 30 May 2005

Correspondence to: Dr. Lei Sun; E-mail: sunlei@usc.edu

Concepts in Magnetic Resonance Part B (Magnetic Resonance Engineering), Vol. 27B(1) 51–63 (2005)

Published online in Wiley InterScience (www.interscience.wiley.com). DOI 10.1002/cmr.b.20046

© 2005 Wiley Periodicals, Inc.

KEY WORDS: MR thermometry; adaptive temperature control; closed loop; ultrasound hyperthermia

INTRODUCTION

Recent developments in clinical treatments using thermal effects have expanded the treatment options for certain oncology patients (1). Cancer associated with the prostate gland draws special attention because it is the second leading cause of cancer-related death in men reported by American Cancer Society. By applying heat to the local tissues, hyperthermic cytotoxicity and two different types of interaction, thermal radiosensitization and thermal chemosensitization, are induced to provide effective local treatment of isolated disease. Local hyperthermia elevating the target tissue temperature to 43–45°C can kill cancer cells either alone or in conjunction with radiotherapy or chemotherapy with minimal damage to the surrounding and intervening normal tissues (2–8).

Magnetic resonance (MR) thermometry has been used in vivo for noninvasive robust monitoring and control of hyperthermia therapies (9–15). MR thermometry using the temperature-dependent proton resonance frequency (PRF) shift has been shown to provide accurate spatial localization, adequate temperature sensitivity, and tissue contrast for precise two-dimensional (2D) temperature measurement as well as tissue identification (16, 17).

Previous research has successfully demonstrated the application of temperature feedback control for hyperthermia treatment of disease using MR thermometry (9, 10, 18–22). However, regulation of the target tissue temperature within a narrow therapeutic range to minimize the damage to normal tissues presents many challenges. Tumors vary in type, size, location, and stage of growth, and have dynamic properties such as blood perfusion. To avoid large overshoots, the controllers with fixed gains required prolonged rise times (9, 18). In applying a physical model of heat conduction, some control methods neglect the effects of blood perfusion and assume the absorption and diffusion of heat to be independent of space and time, which limited the stability and tolerance for spatial deviations (10, 19, 22). With the assumption that tissue parameters are time invariant, other controllers had less ability to track the system variations during the long period of hyperthermia (21). These results motivate the use of an adaptive controller whose gains are automatically adjusted to

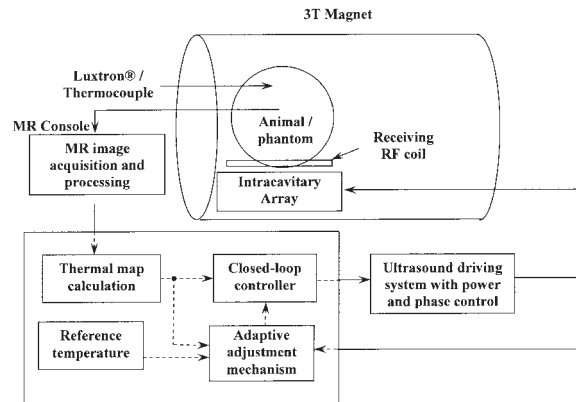


Figure 1 Block diagram of the ultrasound hyperthermia system using MRI thermometry as thermal feedback. The intracavitary ultrasound array is placed inside the MR scanner for hyperthermia treatment together with the animal/phantom. Online thermal feedback is acquired by processing the MR images and transferring to the closed-loop adaptive controller, which determines the proper amount of power outputting from the amplifier to generate optimal temperature rise trajectory in the target tissue.

provide desired steady-state and transient characteristics even among various patients.

The goal of this research was to design and evaluate three adaptive temperature control methods using MR thermometry for thermal feedback in ultrasound hyperthermia. The controllers were required to achieve and maintain a target temperature for a sustained period with minimal overshoots, rapid rising time, and small oscillations. Simulations were used to determine the proper initial parameters for the adaptive controllers. In vivo and ex vivo experiments using MR thermometry demonstrated the performance and effectiveness of the noninvasive robust and adaptive feedback temperature control system.

MATERIALS AND METHODS

The block diagram shown in Fig. 1 displays the entire system used to conduct the ultrasound hyperthermia control experiments using MR thermometry. In the figure, an intracavitary ultrasound array with 16 elements was designed for transrectal prostate cancer hyperthermia. The electrical driving signal (phase and amplitude) to the array was amplified by a 64-channel

programmable ultrasound driving system with a maximum output power of 60 W per channel. The ultrasound array and animal (or phantom) were placed inside a birdcage coil to receive/transmit the radio frequency (RF) signal for MRI measurement. Temperature maps constructed from MRI data using PRF shift were acquired and compared with a desired reference temperature. The adaptive feedback controllers programmed in the PC used this information in adjusting the amount of power applied to produce the desired temperature response. Detailed descriptions of each individual system follow.

Adaptive Control Algorithms

System Identification. As a starting point, a dynamic model of the hyperthermia process using batch least-squares system identification was first obtained (23). To identify the hyperthermia system, the electrical power to the ultrasound transducer and the measured tissue temperatures were taken as the input and output of the system, respectively. With reasonable assumption that the system satisfied an auto regressive moving average (ARMA) model, the system was expressed in the following difference equation:

$$y(k) + \alpha_1 y(k-1) + \alpha_2 y(k-2) + \dots + \alpha_n y(k-n) = \beta_1 u(k-1) + \beta_2 u(k-2) + \dots + \beta_m u(k-m), \quad [1]$$

where $y(k)$ is the tissue temperature at time k , $u(k)$ is the electrical power applied to the transducer, n and m are unknown integers representing the number of poles and zeros, respectively, $\alpha_1, \alpha_2, \dots, \alpha_n$, and $\beta_1, \beta_2, \dots, \beta_m$ are unknown real-valued coefficients of the system. Equation [1] has the compact form

$$A(q)y(k) = B(q)u(k), \quad [2]$$

where A and B are polynomials in the forward shift operator q , e.g., $q^n u(k) = u(k+n)$.

The unknown parameters in Eq. [2] are estimated from experimental data using batch least-squares identification. Pole-zero maps are used to show the effect of experimental excitations on the estimated model. The poles of a system are the roots to equation $A(q) = 0$, whereas the zeros are the roots to equation $B(q) = 0$. The location of the poles and zeros determine the transient response characteristics of the hyperthermia process. In Fig. 2, the horizontal and vertical axes show the real and imaginary parts of the poles and zeros, respectively. Small crosses indicate poles; small circles indicate zeros. The dotted circles

of radius 1 represent the stability boundary; poles located outside the circle indicate a dynamically unstable system. Poles located near the inside boundary of the circle or on the negative real axis indicate an oscillatory transient response. Complex valued poles and zeros must be accompanied with their complex conjugates because the system polynomials A and B have real-valued coefficients.

Four identification experiments were conducted on the phantom system with four different excitations: the square-wave excitations with periods of 3 and 10 s and power levels of 0.5 and 5 W respectively. For a linear time-invariant system, the coefficients of the system polynomials A and B are constant, and so the pole and zero locations should not vary with power level or the shape of the excitation waveform.

Figure 2(a–d) demonstrates the locations of poles and zeros of the system with four different square-wave excitations: (a) period of 10 s and power level from 5 to 20W, (b) period of 10 s and power level from 0.5 to 50W, (c) period of 3 s power 5 to 20W, and (d) period of 3 s power 0.5 to 50W. The locations of the poles and zeros are significantly changed at different power levels and shapes of the excitation waveforms.

The variation of the locations of the poles and zeros due to different excitations shows that the hyperthermia system is not a time-invariant system. As a result, a fixed gain controller is unlikely to provide adequate transient response characteristics and steady-state tracking accuracy. For this reason, we designed a series of adaptive control systems to regulate the temperature of the time-varying system like the ultrasound hyperthermia system.

Adaptive Control Designs. In comparison with fixed-gain controllers, adaptive control systems automatically tune the control gains to compensate for temporal variations in the system model (23). Adaptive control systems consist of two feedback loops: a fast, inner loop that implements feedback control between the process output and input, and a slow, outer loop that tunes the control parameters. Because the system model for the hyperthermia process is affected by the excitation input, it is expected that the adaptive controller will provide better performance than a fixed-gain controller.

There are two broad categories of adaptive controllers, self-tuning regulators (STR) and model reference adaptive control (MRAC) systems. In STR adaptive controllers, an online system identification scheme is used to continually update a process model, which is then used to select control gains that meet desired performance specifications. In MRAC sys-

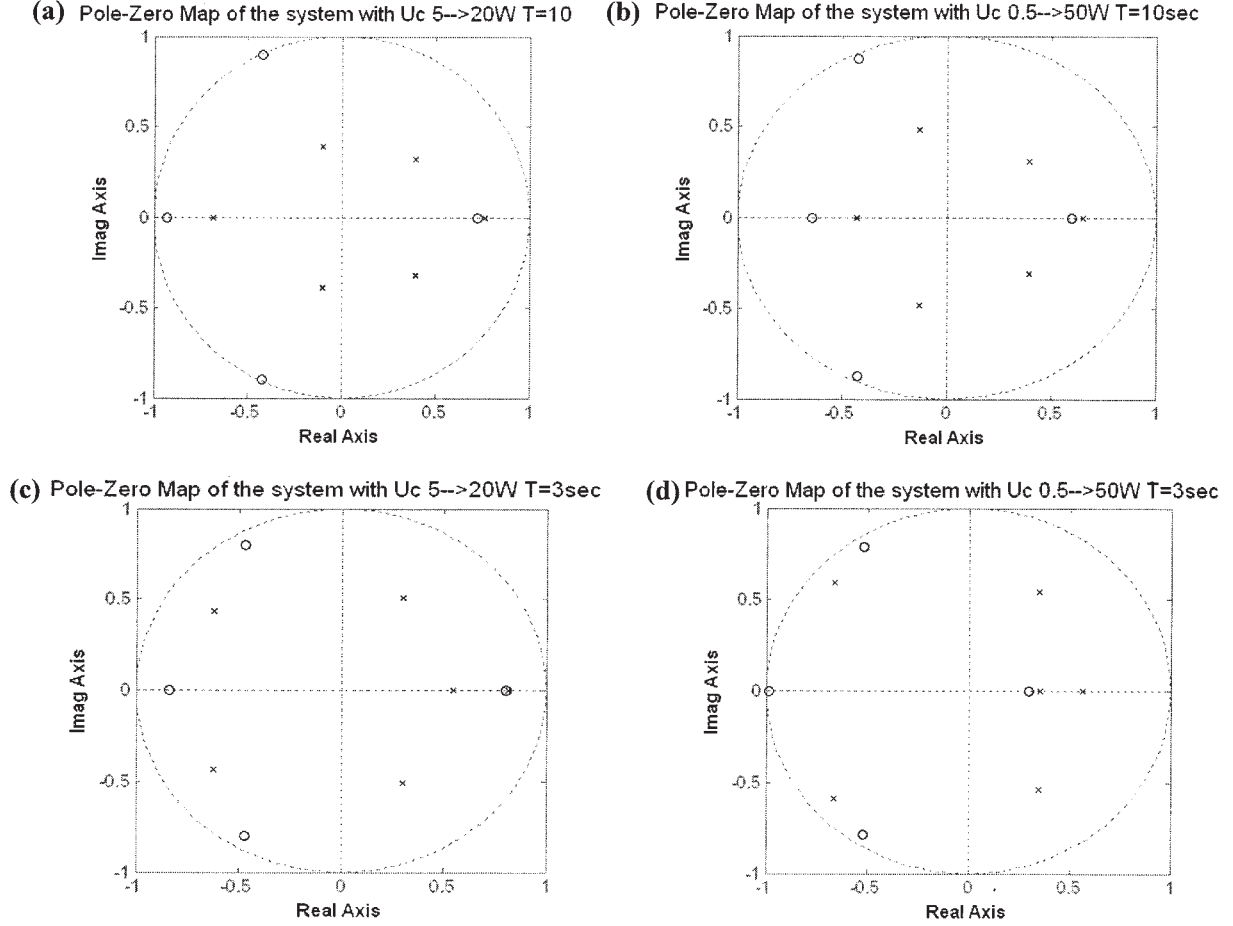


Figure 2 Pole-zero maps plot the locations of poles and zeros of the same hyperthermia system with different square wave input excitations: the input square-wave with (a) a period of 10 s and a power level of 5 to 20 W; (b) a period of 10 s and a power level of 0.5 to 50 W; (c) a period of 3 s and a power level of 5 to 20 W; (d) a period of 3 s and a power level of 0.5 to 50 W.

tems, the difference between the closed-loop output of the process and a reference model exhibiting desired performance characteristics is used to adjust the gain parameters. An MRAC system does not explicitly estimate the process model, and, because it forces the process output to follow that of a reference model, is less sensitive to errors in estimating the process dynamics.

A fixed-gain proportional-plus-integral-plus-derivative (PID) controller was also studied in this research as a reference to evaluate the performance of the adaptive controllers. The results obtained using a PID controller with fixed gains were compared with the adaptive methods in simulations and experiments to demonstrate the advantages of adaptive control.

Self-Tuning Regulator (STR). The STR uses a polynomial feedback law of the form

$$Ru(k) = Tu_c(k) - Sy(k), \quad [3]$$

where R , S , and T are polynomials. This feedback law can be used to implement a PID controller, or a more advanced designs based on observer feedback systems (23). Figure 3 shows a block diagram of the controller. The transfer function from the command input $u_c(k)$ to the process output

$$y(t) = \frac{BT}{AR + BS} u_c(t). \quad [4]$$

The roots of the closed-loop characteristic polynomial A_c ,

$$AR + BS = A_c, \quad [5]$$

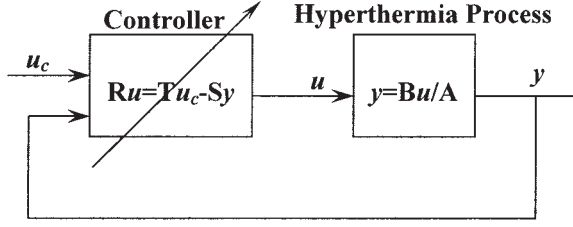


Figure 3 A general linear adaptive controller with two degrees of freedom and adjustable control parameters. B/A is the transfer function of the process. A and B are relative prime and A is also assumed monic (23). R , S , and T are control polynomials to achieve desired performance of the closed-loop system.

determine the transient response characteristics of the closed-loop systems. The roots are chosen by the designer, and Eq. [5] is used to solve for the controller polynomials R and S . The polynomial T is chosen so that the closed-loop system in Eq. [5] has desired zero locations.

Model Reference Adaptive Control (MRAC). The diagram of a MRAC system is shown in Fig. 4. This system has an inner feedback loop composed of the process and the controller, and an outer feedback loop for adjusting controller parameters. The parameters were changed on the basis of the error between the output of the system, T_{actual} , and the output of the desired model, $T_{desired}$. We consider two separate parameter adjustment mechanisms (23). The first mechanism is based on Lyapunov stability theory and yields an adjustment mechanism that guarantees stability of the closed-loop adaptive system. The second mechanism uses a gradient method, known as the MIT rule, for adjusting the controller parameters.

To design the MRAC, we represent the hyperthermia process using the state-space model

$$x(k+1) = Ax(k) + Bu(k), \quad [6]$$

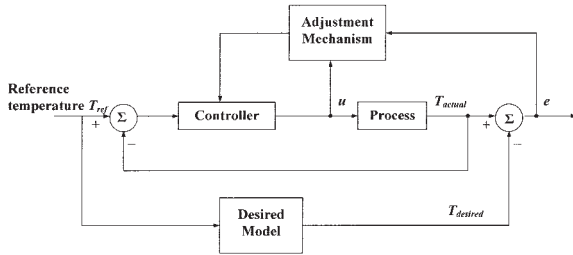


Figure 4 Block diagram of a model reference adaptive control (MRAC) system. The controller is adjusted based on the error between the actual output T_{actual} and the model output $T_{desired}$ and input u .

where $x(k)$ is an $n \times 1$ state vector, which represents the temperatures; $u(k)$ is $m \times 1$ vector defining the powers to the amplifier; A is an $n \times n$ system matrix, which incorporates both conduction and perfusion terms; and B is an $n \times m$ system input matrix, which represents the effects of the m power patterns. It is desired that the closed-loop response $x(k)$ of the hyperthermia process match the response $x_m(k)$ of a reference model

$$x_m(k+1) = A_m x_m(k) + B_m u_c(k), \quad [7]$$

where $x_m(k)$ is the state vector representing the temperatures of the model and $u_c(k)$ is the input vector defining the command inputs to the model. The polynomials A_m and B_m are the state matrix and input matrix of the model, respectively, and are chosen by the designer.

The inner loop of the MRAC system uses the general linear control

$$u(k) = M(\theta)u_c(k) - L(\theta)x(k), \quad [8]$$

where M and L are control gain matrices with adjustable parameters θ . Combining Eqs. [6–8] yields a dynamic model for the inner loop of the MRAC system

$$\begin{aligned} x(k+1) &= (A - BL(\theta))x(k) + BM(\theta)u_c(k) \\ &= A_c(\theta)x(k) + B_c(\theta)u_c(k). \end{aligned} \quad [9]$$

Let e be the error between the output y of the closed-loop system and the output y_m of the model. To minimize the error e , the parameters θ were adjusted in such a way that the loss function

$$J(\theta) = \frac{1}{2} e^2 \quad [10]$$

was minimized. As mentioned earlier, there are two techniques for adjusting θ . We first consider the MIT rule, where we move the parameters in the direction of the negative gradient of J , that is,

$$\frac{d\theta}{dt} = -\gamma \frac{\partial J}{\partial \theta} = -\gamma e \frac{\partial e}{\partial \theta}, \quad [11]$$

where γ is the adaptation gain.

Approximating the dynamics of the hyperthermia process as a second-order system and applying the MIT rule yields the parameter adjustment law

$$\begin{aligned}
\theta_1(k+1) &= \theta_1(k) \\
&\quad - \gamma \left(\frac{q}{q^2 + a_{m1}q + a_{m2}} U_c \right) e(k+1) \\
\theta_2(k+1) &= \theta_2(k) \\
&\quad - \gamma \left(\frac{1}{q^2 + a_{m1}q + a_{m2}} U_c \right) e(k+1) \\
\theta_3(k+1) &= \theta_3(k) \\
&\quad - \gamma \left(\frac{q}{q^2 + a_{m1}q + a_{m2}} Y \right) e(k+1) \\
\theta_4(k+1) &= \theta_4(k) \\
&\quad - \gamma \left(\frac{q}{q^2 + a_{m1}q + a_{m2}} Y \right) e(k+1). \quad [12]
\end{aligned}$$

The selection of adaptation gain is critical because there is no guarantee that an adaptive controller based on the MIT rule will give a stable closed-loop system.

To guarantee closed-loop stability, we consider a second adjustment that is based on Lyapunov stability theory. By choosing the parameter adjustment law chosen as

$$\Theta(k+1) = \Theta(k) - \gamma \Psi^T P e(k), \quad [13]$$

where $e(k) = x(k) - x_m(k)$, $\gamma > 0$ is the adaptation gain; P is a positive definite matrix; Ψ is a matrix containing A_c , B_c , A_m , and B_m , it can be shown that the closed-loop system is stable. In the Results section, simulation and experimental results for the three adaptive as well as fixed-gain control systems considered in this section are shown: STR adaptive control, MRAC using the MIT rule, MRAC using Lyapunov stability theory, and PID control.

Transrectal Intracavitary Array and Amplifier System

An ultrasound array was designed for transrectal intracavitary use to heat the entire prostate with little harm to other organs from the limited confines of the rectum (24, 25). Resonating at 1.5 MHz, the applicator was constructed of PZT-8 (lead zirconate-titanate, EDO, Salt Lake City, UT) material using one-third cylinder sections cut from 25-mm O.D., 15-mm-long full cylinders. The cylindrical sections were subdivided by scoring the inner electrode surface and were arranged along the primary axis of the applicator body. The array has 16 elements arranged in a 4×4

pattern. Each element can be powered individually or in any combination by the amplifier system.

The applicator was powered by a 64-channel high-power ultrasound phased-array driving amplifier (Advanced Surgical System Inc., Tucson, AZ). Designed to operate between 1 and 2 MHz and to deliver 60 W per channel, the amplifiers had externally mounted electrical matching circuits that transformed the transducer impedance to 50Ω , matching the output impedance of the amplifiers (26).

Water circulator (Model 75211-21 and 75211-22, Cole-Parmer Instrument Company, Vernon Hills, IL) and air-flow systems (A-850 Maxima air pump, Rolf Hagen Corp., Mansfield, MA) were connected to the applicator and used to inflate and control the temperature of a latex water bolus (PROcovers®, ATL Supplies, Reedsville, PA), which provided acoustic coupling between the array and the rectum. All components of the array and circulation system were made from nonmagnetic materials.

MR Thermometry

The proton resonance frequency (PRF) has been shown to be linearly dependant on temperature (16). Temperature-induced PRF shifts can be estimated with MRI by measuring changes in the phase of the MR signal and dividing by 2π multiplied by the time in which the phase developed. A reference phase image was acquired before the delivery of ultrasound. Subsequent images were acquired at 7.4-s intervals to measure the phase change over time. Exploration of the temperature-dependant PRF has been shown to have an accuracy of $\pm 0.5^\circ\text{C}$ (16). From a recent study using the PRF shift for noninvasive temperature monitoring, heating from focused ultrasound was monitored in vivo with an accuracy of 0.37°C and a time resolution of 438 ms (27).

The PRF shift was evaluated by using a spoiled gradient echo (SPGR) sequence with the following imaging parameters: repetition time, $\text{TR} = 100$ ms, echo time, $\text{TE} = 15$ ms, flip angle $= 30^\circ$, data matrix 64×64 , field of view (FOV) $= 16 \times 16$ cm, slice thickness $= 8$ mm, and bandwidth $= 61.7$ kHz. These parameters were chosen to maximize the temperature-dependent phase shift while maintaining a high temporal resolution. The temperature elevation was obtained using the temperature dependence for muscle $\alpha(t) = -0.00909$ ppm/ $^\circ\text{C}$ (17). A birdcage coil with a length of 29 cm and inner diameter of 26 cm was used to acquire the MRI RF signals. The magnet scanner was a 3 Tesla system (MEDSPEC S300, Bruker BioSpin, Ettlingen, Germany).

The MRI-derived average temperature of a 4×3 pixel region was used as input to the adaptive controller. This region was chosen to be near an optical temperature probe (Model 3100, Luxtron® Corp., Mountain View, CA). The temperature probe was shielded in a brass catheter to avoid direct ultrasound heating (28) and for the localization in the MR images.

Computer Simulation of Ultrasound Hyperthermia Process

Simulations were initially performed before experiments to compare different control methods and to determine the initial control variables. The acoustical pressure of an 8×8 two-dimensional array (29) was calculated by modeling every element of the array as an independent simple source and the net pressure due to all the elements was determined by summing the effects of each simple source (30). The deposited power contributing to the temperature elevation at some depth into the tissue was calculated by considering attenuation appropriately in the model (31).

The nature of heat transfer in tissue from the ultrasound field was determined by applying Pennes' bioheat transfer equation (32, 33), which combines the convective effects of the blood flow and the conductive properties of soft tissues, providing a simplified model for heat transfer in biological systems (34). In simulation, the bioheat transfer equation was implemented in a space of $40 \times 40 \times 20 \text{ mm}^3$ with digitized spatial and temporal cubic grid of $1 \times 1 \times 1 \text{ mm}^3$ and 1 s period, respectively, and realized using a finite difference method. The focus was located 40 mm away from the surface of the transducer. Boundary condition as well as the initial condition of the block was set at 37°C with the blood temperature constantly at 37°C . Other simulation parameters are tissue density of 998 kg/m^3 , specific heat of both tissue and blood $3770 \text{ J/(kg}^\circ\text{C)}$, and thermal conductivity of $0.5 \text{ W/(m}^\circ\text{C)}$.

To conduct computer simulations with different controllers, the distribution of the deposited power in a 3D tissue volume was calculated with initial electrical power of 0.1 W, subsequently the thermal response of the tissue was estimated using the bioheat transfer equation. The temperature at predefined location as well as history data points were analyzed by the adaptive controller to predict the proper amount of power for the next cycle of heating.

To evaluate the performance of the adaptive control and PID control methods, blood perfusion rate was set to linearly increase from 2.0 to $10.0 \text{ kg/m}^3\text{s}$

during the 30-minute heating period. Using STR, the first 20 s of the hyperthermia treatment was used to estimate the initial STR control parameters. For the MRAC methods the initial value of the control parameters Θ was set to zero with proper value of adaptation gains. The reference temperature for all controllers was an exponential signal with a time constant of $4\tau = 5$ minutes.

Ex Vivo Phantom Experiments

Nine ex vivo phantom experiments with bovine muscle tissue were conducted within the MRI scanner using the intracavitary applicator. The ultrasound array was fastened to a platform made of plexiglas, which has an elliptical hole ($8 \times 15 \text{ cm}$) as an acoustic window, allowing the ultrasonic energy to be transmitted to the target. Phantoms were placed right above the window with solid contact to the inflated water bolus using ultrasound gel (Sonotech Inc., Bellingham, WA). The degassed water was circulated through the bolus at room temperature to allow the constant boundary condition. MR temperatures in a region of interest (ROI) selected from the tissue from predefined images were used as feedback to the controller. For comparison to the MRI-derived temperature measurement, the ROI was selected adjacent to an optical temperature probe embedded in the tissue.

A desired increase of 8°C above initial temperature was set to simulate the temperature rise for hyperthermia treatment. Exponential function with time constant of $4\tau = 6$ minutes was applied as reference input. The adaptation gains ($\gamma = 0.005\sim 0.015$) and initial control variables were carefully chosen to generate minimal overshoots, small oscillation, and fast settling time. The sonication time was 30 minutes, with the initial electrical power of 0.1 W. The tissue was allowed to return to room temperature before subsequent experiments.

In Vivo Animal Experiments

Rabbit Experiments. Five New Zealand white rabbits (4–5 kg, males) were used for 24 separate control experiments. All animal experiments were conducted with procedures approved by the Penn State Institutional Animal Care and Use Committee (IACUC). The experimental setup for the rabbits test was similar to the ex vivo phantom experiment. Rabbits were anaesthetized with an intramuscular injection of ketamine (40 mg/kg, Fort Dodge Animal Health, Fort Dodge, IA) and xylazine (10 mg/kg, Phoenix Scientific, Inc., St. Joseph, MO). After

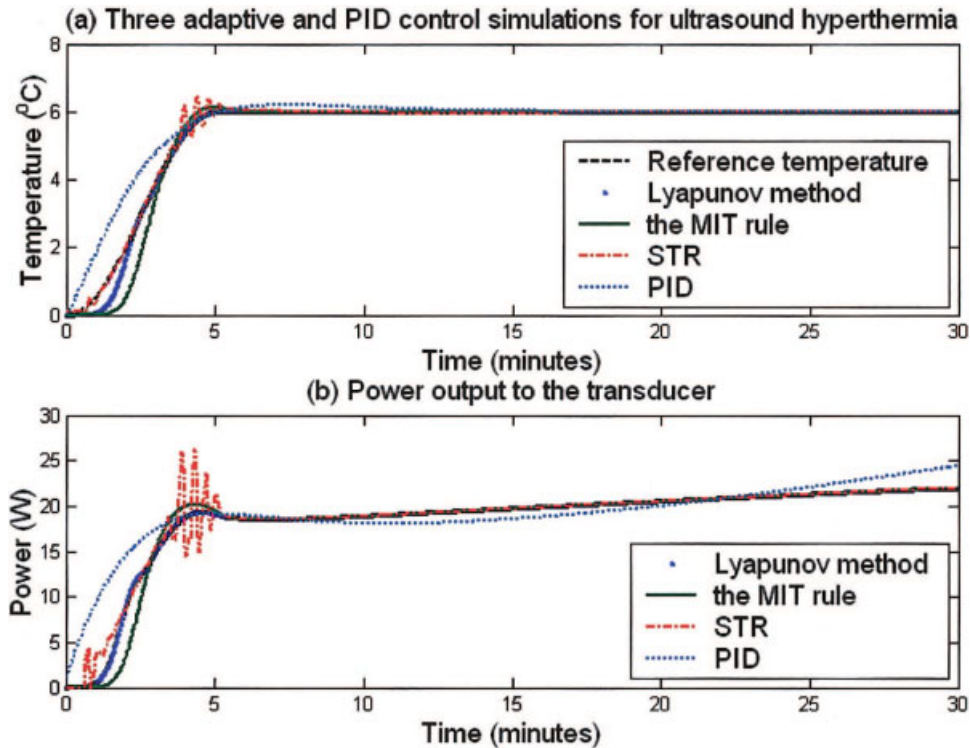


Figure 5 Computer simulation results of three adaptive and PID controllers with a blood perfusion rate from $2.0 \text{ kg/m}^3\text{s}$ to $10.0 \text{ kg/m}^3\text{s}$ during the simulated hyperthermia process. (a) Temperature elevation and reference temperature trajectory. Detailed results of rise time, overshoot temperatures, and steady-state errors are listed in Table 2. (b) Electrical power transmitted from the amplifier as a function of time for the Lyapunov-based MRAC, MIT rule-based MRAC, STR, and PID control methods. [Color figure can be viewed in the online issue, which is available at www.interscience.wiley.com.]

shaving the thigh, depilatory agent was applied to the skin to eliminate any remaining hair. The rabbits were laid down on the platform on their lateral position and their shaved thigh was just above the ultrasound transducer through the acoustic window. To make effective acoustic contact, ultrasound gel was applied between the water bolus membrane and the rabbit thighs. The rabbit controlled heating experiments were performed in a similar manner as the ex vivo experiments except the control variables used a time constant for the reference temperature at $4\tau = 8$ minutes, and the ultrasound exposure time was 25 minutes.

Canine Experiment. Two canines (~ 15 kg mongrel, male) were used for the prostate hyperthermia experiment with the MR thermometry and adaptive temperature controller. These dogs were anaesthetized with Telazol (100 mg/ml, reconstituted with Tiletamine hydrochloric acid and Zolazepam hydrochloric acid, Fort Dodge Animal Health, Fort Dodge, IA). The rectums of the canines were cleaned and filled with degassed acoustic coupling gel. After placing the

dogs on the MRI table, the array was inserted. Good contact was verified by MRI images before baseline temperature sensitive MRI images were collected. The temperature from a predefined region in the canine prostate was selected as the feedback to the controller. The target temperature was set to 43°C , the time constant of the reference was $4\tau = 6$ minutes, and the exposure time was chosen to be around 8 minutes.

RESULTS

Simulation Results

Figure 5(a) shows the reference temperature and the temperature elevations from the adaptive and PID controllers while the power trajectories to the amplifier as directed by each controllers are plotted in Fig. 5(b). The controllers had a desired target temperature of 43°C and rise time of 5 minutes with the blood perfusion linearly increased from 2.0 to $10.0 \text{ kg/m}^3\text{s}$ during the 30-minute hyperthermia simulation. Re-

Table 1 Overall Rise Time, Overshoots, and Steady-State Errors Summarized from the Temperature Elevations of the Three Adaptive and PID Controllers Computer Simulations

Methods	Rise Time (Min)	Overshoot (°C)	Steady-State Error (°C)
PID	4.7	0.2	0.4
STR	4.8	1.4	0.3
MRAC (MIT rule)	4.9	0.3	0.1
MRAC (Lyapunov)	5.0	0.2	0.1

Figure 5(a) plots the temperature elevation of each controller as a function of time.

sults of rise time, overshoots, and steady-state errors from Fig. 5(a) are listed in Table 1. All three methods reached the steady state temperature within 5 ± 0.2 minutes and maintained the target temperature with errors less than 0.3°C . It is noted that two MRAC methods had smaller overshoots (0.3°C) than the STR controller (1.4°C).

Ex Vivo Phantom Results

Nine ex vivo experiments were conducted with Lyapunov-based MRAC method using five bovine muscle phantoms. MR temperatures in an ROI adjacent to an optical temperature probe were used as thermal feedback to the controller. The target temperature of 10°C above the ambient temperature (28°C) was desired for 25 minutes of hyperthermia. The time constant of the exponential reference was $4\tau = 6$ minutes. The adaptation gain of the MRAC method was set to 0.001.

As a typical result, Fig. 6 plots the exponential reference temperature (solid line), the temperature elevation from the fiber optic probe (dots), and the MR measurement within the ROI (open circles, mean \pm SD). Starting at an initial phantom temperature of 28°C , the controller achieved the steady-state temperature of 38°C within 6.0 ± 0.2 minutes. The deviation of the MR measurement to the steady-state temperature was no greater than $\pm 1.37^\circ\text{C}$. After the first 10 minutes, the MR measurement agreed with the probe temperature measurement to within $\pm 0.89^\circ\text{C}$.

In Vivo Animal Results

Rabbit Results. An MR image of an axial view of the rabbit thigh and the transducer orientation is shown in Fig. 7. As indicated in the figure, the array is adjacent to the rabbit thigh along with the ROI in which the temperature was determined for the input to the controller. For rapid hyperthermia heating without caus-

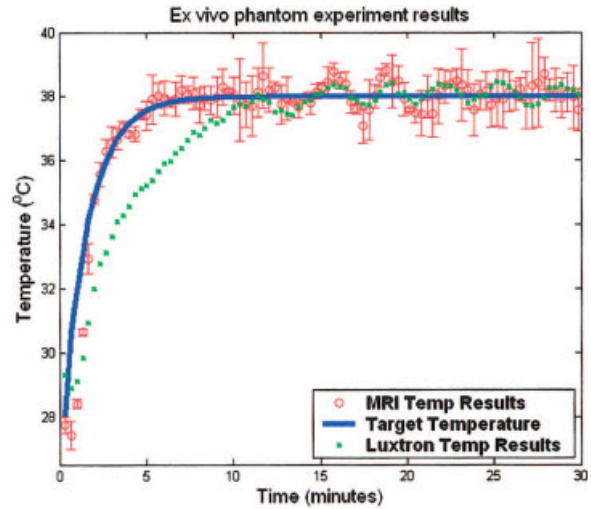


Figure 6 A typical plot of the result from ex vivo bovine muscle hyperthermia experiments using MRAC adaptive temperature control and MR thermometry. Shown are temperature elevation acquired by MR (circles with error bars) inside the ROI, measurements made by fiber optic probe (small squares) neighboring the ROI, together with reference temperature (line). [Color figure can be viewed in the online issue, which is available at www.interscience.wiley.com.]

ing skin burn, it is desired to reach 44.3°C with the time constant of $4\tau = 8$ minutes for a total of 25 minutes hyperthermia.

Figure 8 plots a representative result with the reference temperature and MR temperature elevations. The rabbit thigh muscle was heated from 36.8°C to 44.3°C in 8.0 ± 0.5 minutes. The maximum variation

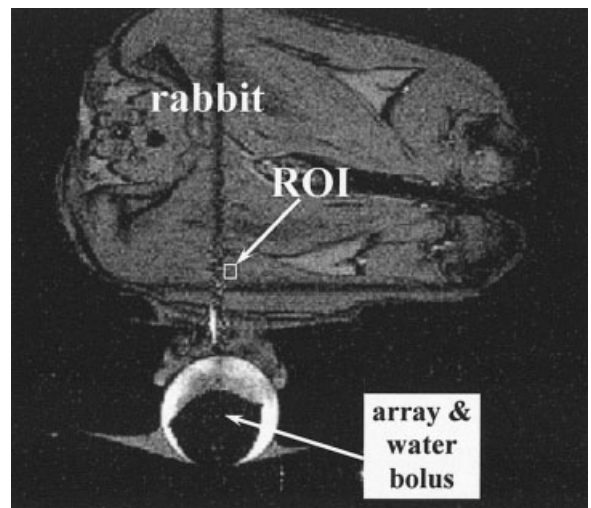


Figure 7 MR image showing the axial view of the rabbit thigh, displaying the location of the array and water bolus with respect to the ROI.

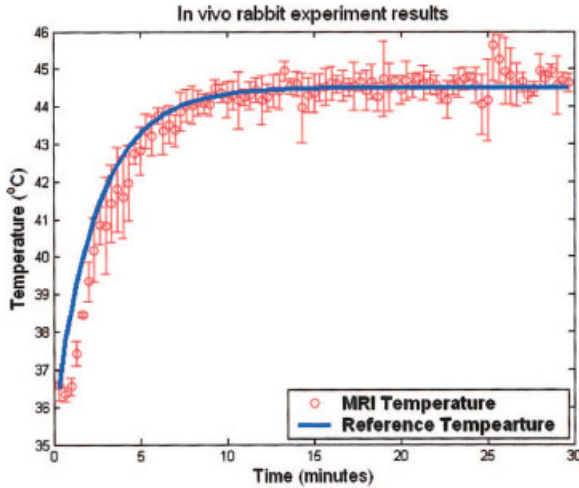


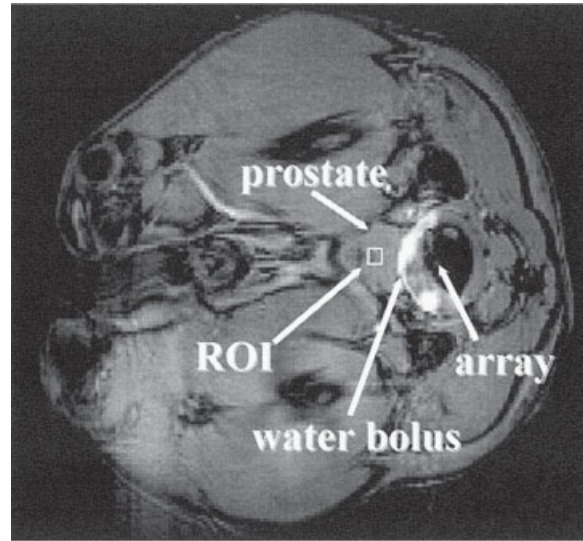
Figure 8 MRAC adaptive feedback temperature elevation from the average of the in vivo rabbit thigh muscle hyperthermia using the control variables as $4\tau = 8$ min, adaptation gain = 0.005, and optimized initial value. MR measurement (circles) and reference (line) are plotted versus the time. [Color figure can be viewed in the online issue, which is available at www.interscience.wiley.com.]

from the desired temperature profile was 2.2°C . After reaching steady state, tissue temperature was maintained at 44.3°C with average variation of 1.45°C .

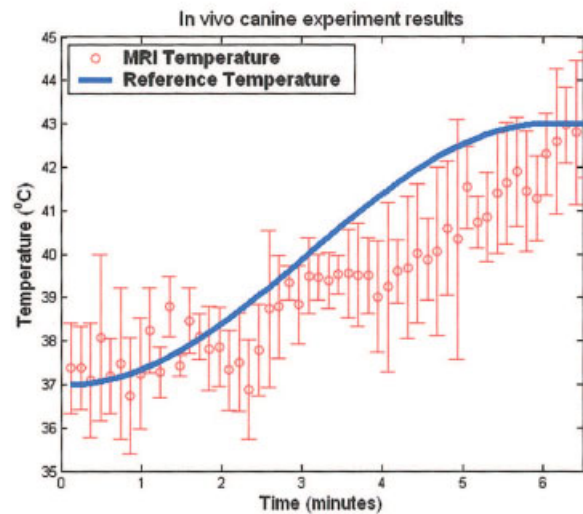
Canine Results. Figure 9(a) shows an axial view of the experimental setup, indicating the ultrasound array solidly coupled to the canine prostate through the water bolus inside the rectum. ROI was chosen in the middle of the prostate as shown in Fig. 9(a) with 4×3 pixels. Average MR measurement in the ROI was sent to the Lyapunov-base MRAC controller as thermal feedback. The plot in Fig. 9(b) shows within 6.5 ± 0.5 minutes the canine prostate temperature reached the $43 \pm 2.0^{\circ}\text{C}$ for a total of 10 experiments for two canines. The target temperature was set to be 43°C with exponential time constant $4\tau = 6$ minutes. To save the animal for as many experiments as possible, each experiment was stopped 1 minute after the steady-state temperature was reached. However, the full 25 minutes heating using rabbits has been shown previously to demonstrate the effectiveness of the controller.

DISCUSSIONS AND CONCLUSIONS

In computer simulation, although each control method kept a stable steady-state temperature, the power levels linearly increased as a function of time. This could be explained by the increase in blood perfusion, tak-



(a)



(b)

Figure 9 (a) MR image of the axial view of the canine prostate, showing the location of the ultrasound array, canine prostate, and water bolus. (b) In the preliminary canine prostate hyperthermia experiments, the agreement of MR temperature measurements and the reference indicates the potential of intracavitary ultrasound hyperthermia treatment for human prostate cancer. [Color figure can be viewed in the online issue, which is available at www.interscience.wiley.com.]

ing more heat away from the target tissue and resulting in more input energy required to maintain the steady-state temperature. The mean overshoot by STR was substantially higher than that using MRAC and PID methods, which was also demonstrated in the ex vivo experiments using fiber optic probes (Table 2) (35, 36). The main cause of the large vibrations using

Table 2 Mean Performance of the ex vivo Experiments with Bovine Muscles Using the Conventional PID and the Three Adaptive Controllers

Methods	Rise Time (Min)	Overshoot (°C)	Steady-State Error (°C)
PID	6.5	0.8	1.0
STR	6	1.8	1.5
MRAC (MIT rule)	6	0.1	0.2
MRAC (Lyapunov)	6	0.1	0.2

STR controller was due to the involvement of explicit system identification step. The measurement resolution of the fiber optic thermometer ($\sim 0.01^\circ\text{C}$) is significant compared with the temperature increase per measurement ($\sim 0.04^\circ\text{C}$). Therefore, the estimated system parameters had low accuracy and long convergence period, which resulted in the temperature oscillations in both simulations and ex vivo experiments. Although PID control with fixed gains showed good performance in simulations, its experimental results displayed large overshoot and large steady-state errors. Moreover, one optimal combination of control gains works only for limited hyperthermia systems, any component change (e.g., different transducer or different patient) will need another gain set. Finding the optimal gain is time and effort intense.

MRAC, on the other hand, does not require prior knowledge of the hyperthermia system showing fast rise time, small overshoot, small steady-state oscillations in simulations and ex vivo and in vivo experiments (see Table 2). One important advantage of using MRAC is that the rise time is significant decreased compared with nonadaptive control methods. In previous research using a PID controller with constant gains by Smith et al. (9), about 7–24 minutes was required for 7°C temperature increase, whereas

with this MRAC control method, only 6–8 minutes was needed for the same 7°C temperature increase.

Temperature regulation using the MRAC methods and MRI thermal feedback demonstrates the stability and robustness during the ex vivo and in vivo ultrasound hyperthermia experiments. To optimize the controller's performance, several parameters have been tested, such as time constants of reference temperature, adaptation gains, and initial values of the control variable Θ . The parameters were tested in such a way that one of them was varied, while the others were held constantly. Then the controller's response of rise time, overshoot temperature, and steady-state errors were analyzed and summarized in Table 3 in the experimental result summary column.

From Table 3, examining the controller results from experiment 1, it is indicated that with small time constant ($4\tau = 3$ min) the controller is able to reach the therapeutic level faster (3 ± 0.5 min $< 8 \pm 0.5$ min) than with large time constant ($4\tau = 8$ min); however, it caused larger overshoot ($1.9 \pm 0.6^\circ\text{C} > 1.3 \pm 0.3^\circ\text{C}$) and greater oscillations ($1.8 \pm 0.5^\circ\text{C} > 1.5 \pm 0.6^\circ\text{C}$). Based on the allowable overshoot and oscillations, in this research, 4τ was limited to times greater than 5 minutes to ensure animal safety.

From the results of experiment 2 in Table 3, with smaller adaptation gain ($\gamma = 0.005$), the adaptive controller updated the control parameters in a slower way so that it took longer (8.1 ± 0.5 min $> 7.85 \pm 0.5$ min) for the control variables to reach the optimal values than with the larger gain ($\gamma = 0.015$). Not surprisingly, the conservative manner ($\gamma = 0.005$) also resulted in smaller overshoot ($1.3 \pm 0.3^\circ\text{C} < 1.5 \pm 0.4^\circ\text{C}$) and perhaps smaller steady-state error, although not shown in this research.

Finally, since the acquisition of a slice of MRI temperature image took longer time (7.4 s per measurement) than the fiber optic thermometer (up to

Table 3 The Experimental Results of Rise Time, Overshoot, and Steady-State Errors by Examining the Variation of One MRAC Control Variable at a Time for Adaptive MRI Thermal Feedback Control of Ultrasound Hyperthermia

Exp. No.	Control Parameters		Initial Values	Experimental Results Summary		
	Time Constant (Min)	Adaptation Gain		Rise Time (Min)	Overshoot (°C)	Steady-State Error (°C)
1	$4\tau = 3$	0.005	Optimized value	3 ± 0.5	1.9 ± 0.6	1.8 ± 0.5
	$4\tau = 8$	0.005	Optimized value	8 ± 0.5	1.3 ± 0.3	1.5 ± 0.6
2	$4\tau = 7.8$	0.005	Optimized value	8.1 ± 0.5	1.3 ± 0.3	1.5 ± 0.5
	$4\tau = 7.8$	0.015	Optimized value	7.85 ± 0.5	1.5 ± 0.4	1.5 ± 0.5
3	$4\tau = 6$	0.005	Zero	12 ± 0.5	5.2 ± 0.6	3.5 ± 0.5
	$4\tau = 6$	0.005	Optimized value	6 ± 0.5	1.1 ± 0.3	1.5 ± 0.6

For each experiment (i.e., 1, 2, or 3), the control parameter under investigation is marked as bold.

0.25 s per measurement), it took a much longer time for the controllers to reach the optimal values starting from zero initial values. To improve this, the initial values optimized from simulations and previous experiments were applied. Table 3 also shows that with optimized initial parameters values, the performance of the control system was significantly improved, yielding smaller rise time ($6 \pm 0.5 \text{ min} < 12 \pm 0.5 \text{ min}$), less overshoot ($1.1 \pm 0.3^\circ\text{C} < 5.2 \pm 0.6^\circ\text{C}$), and lower steady-state oscillations ($1.5 \pm 0.6^\circ\text{C} < 3.5 \pm 0.5^\circ\text{C}$).

One important issue during MR thermometry is motion. Temperature measurement using MR is actually based on the subtraction of current image with respect to the initial one. Motion during the experiment can result in measurement errors or mistaken measurements, which can typically cause the controller to oscillate or even become unstable. In this research, the temperature was acquired by averaging a region of MR measurement ($4 \times 3 \text{ mm}^2$). This can effectively compensate for small motion, such as breath. Results from the in vivo experiments showed the MRAC controller worked well under small motion. Large motion, such as animal kick, was also observed during the experiments typically followed by experiment failure. To minimize the animal movement, anesthetized drug should be paid special attention to avoid movement as much as possible.

In summary, to accomplish the noninvasive ultrasound hyperthermia treatment, self-tuning regulator (STR) and model reference adaptive control (MRAC) methods with MR thermometry were proposed and applied to an intracavitary ultrasound hyperthermia system. Computer simulations as well as ex vivo phantom and in vivo animal experiments displayed that these methods did not require a priori knowledge of the tissue properties and adaptively adjusted the amplitudes of the array's driving signal according to the blood perfusion and other dynamic tissue properties to achieve controlled, effective ultrasound hyperthermia.

ACKNOWLEDGEMENTS

This work was supported by the Whitaker Foundation (RG-00-0042) and the Department of Defense Congressionally Directed Medical Prostate Cancer Research Program (DAMD17-0201-0124).

REFERENCES

1. Overgaard J, Gonzalez GD, Hulshof MC, Arcangeli G, Dahl O, Mella O, et al. 1995. Randomised trial of

- hyperthermia as adjuvant to radiotherapy for recurrent or metastatic malignant melanoma. *European Society for Hyperthermic Oncology. Lancet* 345(8949):540–543.
2. Overgaard J. 1989. The current and potential role of hyperthermia in radiotherapy. *Int J Radiat Oncol Biol Phys* 16:535–549.
3. Overgaard J, Overgaard M. 1987. Hyperthermia as an adjuvant to radiotherapy in the treatment of malignant melanoma. *Int J Hyperthermia* 3(6):483–501.
4. Dewey WC, Hopwood LE, Sapareto SA, Gerweck LE. 1977. Cellular response to combination of hyperthermia and radiation. *Radiology* 123:463–474.
5. Sneed PK, Phillips TL. 1991. Combining hyperthermia and radiation: How beneficial? *Oncology* 5(3):99–112.
6. Falk MH, Issels RD. 2001. Hyperthermia in oncology. *Int J Hyperthermia* 17(1):1–18.
7. Hildebrandt B, Wust P, Ahlers O, Dieing A, Sreenivasa G, Kerner T, et al. 2002. The cellular and molecular basis of hyperthermia. *Crit Rev Oncol Hematol* 43:33–56.
8. Wust P, Hildebrandt B, Sreenivasa G, Rau B, Gellermann J, Riess H, et al. 2002. Hyperthermia in combined treatment of cancer. *Lancet Oncol* 3:487–497.
9. Smith NB, Merrilees NK, Dahleh M, Hynynen K. 2001. Control system for an MRI compatible intracavitary ultrasound array for thermal treatment of prostate disease. *Int J Hyperthermia* 17(3):271–282.
10. Salomir R, Vimeux FC, de Zwart JA, Grenier N, Moonen CT. 2000. Hyperthermia by MR-guided focused ultrasound: accurate temperature control based on fast MRI and a physical model of local energy deposition and heat conduction. *Magn Reson Med* 43(3):342–347.
11. Hazle JD, Diederich CJ, Kangasniemi M, Price RE, Olsson LE, Stafford RJ. 2002. MRI-guided thermal therapy of transplanted tumors in the canine prostate using a directional transurethral ultrasound applicator. *J Magn Reson Imaging* 15:409–417.
12. McNichols RJ, Kangasniemi M, Gowda A, Bankson JA, Price RE, Hazle JD. 2004. Technical developments for cerebral thermal treatment: Water-cooled diffusing laser fibre tips and temperature-sensitive MRI using intersecting image planes. *Int J Hyperthermia* 20:45–56.
13. Weidensteiner C, Quesson B, Caire-Gana B, Kerioui N, Rullier A, Trillaud H, et al. 2003. Real-time MR temperature mapping of rabbit liver in vivo during thermal ablation. *Magn Reson Med* 50:322–330.
14. Wust P, Gellermann J, Seebass M, Fahling H, Turner P, Włodarczyk W, et al. 2004. Part-body hyperthermia with a radiofrequency multi-antenna applicator under online control in a 1.5 T MR-tomograph. *Rofo* 176:363–374.
15. Guilhon E, Quesson B, Moraud-Gaudry F, de Verneuil H, Canioni P, Salomir R, et al. 2003. Image-guided control of transgene expression based on local hyperthermia. *Mol Imaging* 2:11–17.

16. Ishihara Y, Calderon A, Watanabe H, Okamoto K, Suzuki Y, Kuroda K, et al. 1995. A precise and fast temperature mapping using water proton chemical shift. *Magn Reson Med* 34(6):814–823.
17. Kuroda K, Chung A, Hynynen K, Jolesz F. 1998. Calibration of water proton chemical shift with temperature for noninvasive temperature imaging during focused ultrasound surgery. *J Magn Reson Imaging* 8(1): 175–181.
18. Behnia B, Suther M, Webb AG. 2002. Closed-loop feedback control of phased-array microwave heating using thermal measurements from magnetic resonance imaging. *Magn Reson Eng* 15(1):101110.
19. Quesson B, Vimeux F, Salomir R, de Zwart JA, Moonen CT. 2002. Automatic control of hyperthermic therapy based on real-time Fourier analysis of MR temperature maps. *Magn Reson Med* 47(6):1065–1072.
20. Hutchinson E, Dahleh M, Hynynen K. 1998. The feasibility of MRI feedback control for intracavitary phased array hyperthermia treatments. *Int J Hyperthermia* 14(1):39–56.
21. Vanne A, Hynynen K. 2003. MRI feedback temperature control for focused ultrasound surgery. *Phys Med Biol* 48(1):31–43.
22. Mougnot C, Salomir R, Palussiere J, Grenier N, Moonen CT. 2004. Automatic spatial and temporal temperature control for MR-guided focused ultrasound using fast 3D MR thermometry and multispiral trajectory of the focal point. *Magn Reson Med* 52:1005–1015.
23. Astrom KJ, Wittenmark B. 1995. Adaptive control. Boston: Addison-Wesley.
24. Diederich CJ, Hynynen K. 1991. The feasibility of using electrically focused ultrasound arrays to induce deep hyperthermia via body cavities. *IEEE Trans Ultrason Ferroelectr Freq Control* 38(3):207–219.
25. Smith NB, Buchanan M, Hynynen K. 1998. Transrectal ultrasound applicator for prostate heating monitored using MRI thermometry. *Int J Radiat Oncol Biol Phys* 43(1):217–225.
26. Daum DR, Buchanan MT, Fjield T, Hynynen K. 1998. Design and evaluation of a feedback based phased array system for ultrasound surgery. *IEEE Trans Ultrason Ferroelectr Freq Control* 45(2):431–438.
27. de Zwart JA, Vimeux FC, Delalande C, Canioni P, Moonen CT. 1999. Fast lipid-suppressed MR temperature mapping with echo-shifted gradient-echo imaging and spectral-spatial excitation. *Magn Reson Med* 42: 53–59.
28. Hynynen K, Edwards DK. 1989. Temperature measurements during ultrasound hyperthermia. *Med Phys* 16(4):618–626.
29. Saleh K, Smith NB. 2004. Two dimensional array design for tissue ablation for treatment of benign prostatic hyperplasia. *Int J Hyperthermia* 20(1):7–31.
30. Goodman JW. 1968. Introduction to Fourier optics. New York: McGraw-Hill.
31. Nyborg W. 1981. Heat generation by ultrasound in a relaxing medium. *J Acoust Soc Am* 70:310–312.
32. Pennes HH. 1948. Analysis of tissue and arterial blood temperatures in the resting human forearm. *J Appl Physiol* 1:93–122.
33. Sapareto SA, Dewey WC. 1984. Thermal dose determination in cancer therapy. *Int J Radiat Oncol Biol Phys* 10:787–800.
34. Strohbehn JW. 1994. Hyperthermia equipment evaluation. *Int J Hyperthermia* 10(3):429–432.
35. Sun L, Schiano JL, Smith NB. 2002. An adaptive control method for ultrasound prostate hyperthermia. *Proc IASTED Int Conf AMS*, November 4–6, Cambridge, MA, pp 347–352.
36. Sun L, Schiano JL, Smith NB. 2003. Novel adaptive control methods for ultrasound thermal treatment with a two-dimensional tapered array. *Proc IEEE Ultrasonics Symposium*, October 8–11, Honolulu, HI, pp 1274–1277.

Research

Open Access

A 63 element 1.75 dimensional ultrasound phased array for the treatment of benign prostatic hyperplasia

Khaldon Y Saleh*¹ and Nadine Barrie Smith^{1,2}

Address: ¹Department of Bioengineering Graduate Program in Acoustics College of Engineering The Pennsylvania State University 206 Hallowell Building University Park, PA 16802, USA and ²Graduate Program in Acoustics College of Engineering The Pennsylvania State University 206 Hallowell Building University Park, PA 16802, USA

Email: Khaldon Y Saleh* - kysbio@engr.psu.edu; Nadine Barrie Smith - nbs@engr.psu.edu

* Corresponding author

Published: 17 June 2005

Received: 16 December 2004

BioMedical Engineering OnLine 2005, 4:39 doi:10.1186/1475-925X-4-39

Accepted: 17 June 2005

This article is available from: <http://www.biomedical-engineering-online.com/content/4/1/39>

© 2005 Saleh and Smith; licensee BioMed Central Ltd.

This is an Open Access article distributed under the terms of the Creative Commons Attribution License (<http://creativecommons.org/licenses/by/2.0>), which permits unrestricted use, distribution, and reproduction in any medium, provided the original work is properly cited.

Abstract

Background: Prostate cancer and benign prostatic hyperplasia are very common diseases in older American men, thus having a reliable treatment modality for both diseases is of great importance. The currently used treating options, mainly surgical ones, have numerous complications, which include the many side effects that accompany such procedures, besides the invasive nature of such techniques. Focused ultrasound is a relatively new treating modality that is showing promising results in treating prostate cancer and benign prostatic hyperplasia. Thus this technique is gaining more attention in the past decade as a non-invasive method to treat both diseases.

Methods: In this paper, the design, construction and evaluation of a 1.75 dimensional ultrasound phased array to be used for treating prostate cancer and benign prostatic hyperplasia is presented. With this array, the position of the focus can be controlled by changing the electrical power and phase to the individual elements for electronically focusing and steering in a three dimensional volume. The array was designed with a maximum steering angle of $\pm 13.5^\circ$ in the transverse direction and a maximum depth of penetration of 11 cm, which allows the treatment of large prostates. The transducer piezoelectric ceramic, matching layers and cable impedance have been designed for maximum power transfer to tissue.

Results: To verify the capability of the transducer for focusing and steering, exposimetry was performed and the results correlated well with the calculated field. *Ex vivo* experiments using bovine tissue were performed with various lesion sizes and indicated the capability of the transducer to ablate tissue using short sonications.

Conclusion: A 1.75 dimensional array, that overcame the drawbacks associated with one-dimensional arrays, has been designed, built and successfully tested. Design issues, such as cable and ceramic capacitances, were taken into account when designing this array. The final prototype overcame also the problem of generating grating lobes at unwanted locations by tapering the array elements.

1. Background

Treating prostate diseases such as prostate cancer and benign prostatic hyperplasia (BPH) is of great importance. In the United States, most of the new diagnosed prostate cancer cases appear in men who are over the age of 55 while most of the BPH cases appear after the age of 60. According to the National Cancer Institute, 50 percent of men between the ages of 60 and 70, and 90 percent of men between the ages of 70 and 90, have BPH symptoms. Prostate cancer is a life threatening disease while BPH is a benign growth that needs to be treated since normal urine flow can be blocked as a result of the prostate pushing against the urethra and the bladder (National Cancer Institute 1999).

Existing techniques for treating such diseases include hyperthermia, focus surgery, radiotherapy, chemotherapy and surgery. Currently, surgical techniques are widely used over the other modalities; that is due to the inefficiency and the unpleasant side effects those modalities have. However surgical techniques have numerous complications that appear in about one in four cases, which include impotence, incontinence, and urinary tract infections and often require lengthy hospitalization [1,2].

Due to its noninvasiveness, focus surgery is gaining more attention than the other modalities in the past decade [3]. With focus surgery, ultrasound or microwave devices are used to generate a focused beam at a certain location in the prostate, which kills the cells at that location by raising their temperature to 60°C for about ten seconds. Attention is given more to ultrasound rather than microwave. That is because microwave has either a shallow penetration depth (when high frequencies are used) or a lack of the ability to generate a significant focus (when low frequencies are used) [4].

With focused ultrasound (FUS), tissue is noninvasively ablated by elevating the temperature at the focal point above 60°C using short sonications (10–30 seconds). In this kind of treatment, the target volume can be ablated by focusing the ultrasound beam at a certain position, and then steering the focus to cover the whole enlarged volume. Thus FUS can be used for prostate ablation to remove a non-desirable growth of the prostate [5-7]. Since the tissue volume to be ablated is larger than the geometric focus of the array, the transducer needs to be moved repeatedly to destroy the desired volume and unnecessarily extend the treatment time. Phased arrays overcome this problem by electrically steering the focal point from one location to another by changing the phase and power to the individual elements of the array. Previous effective prostate ultrasound devices include both mechanically and electrically steered designs. Electrically steered include a one-dimensional (1-D) 120 × 1 aperiodic, linear

array design (90 × 15 mm²) which reduced grating lobes and could steer the focus in the radial and transverse but not the longitudinal direction [8]. Another experimental design was a 62 × 1, linear array (75 × 15 mm²) with a mechanical translation that could electrically steer the focus in the radial and transverse but not the longitudinal direction [9]. The drawbacks behind these designs are that they can only steer the focus in the radial and transverse directions or require complex mechanisms to move the focus. Improvements over 1-D arrays for the treatment of localized prostatic cancer can be achieved. Many multi-dimensional ultrasound phased arrays have been designed and built for the treatment of prostate diseases; that includes a 1.5-dimensional (1.5-D) phased array [10] (a 1.5-D array consists of three individual linear array that can be driven individually or connected together to form a single linear array), a 1.75-dimensional (1.75-D) phased array [11] (a 1.75-D array consists of many individual linear arrays that are driven separately), and a two-dimensional (2-D) phased array [12]. The advantage with a multi-dimensional phased array is that it has the capability of focusing and steering in a 3-dimensional (3-D) representation of the prostate without the need to physically move the array.

Issues regarding the construction of an array used for FUS of the prostate initially deal with the frequency and size of the ceramic to be diced into an array. The resonant frequency should be greater than 500 kHz [13] while the size of the transducer needs to be large enough to be able to deliver high power but small enough to be an intracavitary device. Before construction, computer simulations can be performed to determine the acoustic field. Pressure wave and temperature simulations indicated that a tapered array design reduced grating lobes significantly compared to equal element size arrays. Based on the computer model, a tapered array that satisfied grating lobes, frequency, and size limitations was designed. Lead zirconate titanate (PZT- 8) was chosen as the ceramic material of the array since it has the capability of handling the high electrical powers used in focused ultrasound. To maximize the acoustical power transmission from the elements and improve the structural integrity of the array face, two matching layers were designed and fabricated. Issues regarding the cabling and electrical matching of the elements were also considered. Exposimetry of the acoustic field from the array was performed to compare experimental and calculated theoretical results. *Ex vivo* experiments using bovine tissue were also performed to demonstrate the feasibility of the array to ablate tissue. This paper describes the design, construction and evaluation of a 1.75-D ultrasound phased array that is capable of focusing and steering in a 3-D volume to be used in the treatment of BPH.

2. Methods

2.1 Simulations

2.1.1 Acoustic pressure field simulations

MATLAB computer simulation programs were written to determine the number and the size of the phased array elements in addition to determining the pressure and temperature fields from the device. The array was modeled (Figure 1) as a 1.75-D tapered array in order to have focusing and steering capabilities in both x and z directions (x = transverse, y = longitudinal and z = radial). Focusing in the y direction is done in a different way; the array is divided into three identical rows, each one represents a single linear array. If the focus is required at $y = 0$, the middle row should be used. A focus at $y = -0.9$ cm requires driving the lower row, while a focus at $y = +0.9$ cm requires the operation of the upper row. Although the degree of freedom in the y direction is not perfect, the size of the lesion generated by a single sonication compensates for that, since the focus length is about 9 mm in the y direction. With these requirements, this array was capable of focusing and steering with a steering angle of $\pm 13.5^\circ$ with maximum focal depth of 11 cm. The phase of each element was determined such that signals from individual elements were coherent at the focal point. Measuring the difference in path length between each element to the focus in comparison to the path from the center of the array to the focus determined the element phase calculation. The phase, ϕ_i , (degrees) of element i was given by:

$$\phi_i = \frac{360^\circ}{\lambda} (d_i - d_o) - 360^\circ n \quad (1)$$

Where λ is the wavelength (m), d_i is the distance (m) from the centre of element i to the focal point, d_o is the distance (m) from the centre of the array to the focus and n is an integer to keep $0 \leq \phi_i \leq 360^\circ$. Huygen's principle was used to model the pressure field as a summation of simple sources [14] and the total acoustic pressure at any point in the field was calculated using the discrete approximation of the Rayleigh- Sommerfeld equation:

$$p(x, y, z) = \sum_{i=1}^n \sqrt{\frac{2P\rho}{cA}} \left(\frac{fS}{d_i} \right) \exp \left[j \left(\phi_i - \frac{2\pi d_i}{\lambda} \right) - d_i \alpha \right] \quad (2)$$

Where p is the total acoustic pressure in Pascals (Pa), P is the total acoustic power emitted by the array in watts (W), ρ is the density of the medium ($998 \text{ kg} \cdot \text{m}^{-3}$), c is the speed of sound ($\text{m} \cdot \text{s}^{-1}$), A is the total surface area of the array (m^2), f is the resonant frequency (1.2 MHz), S is the area of the corresponding element (m^2) and α is the attenuation in soft tissue ($10 \text{ Np} \cdot \text{m}^{-1} \cdot \text{MHz}^{-1}$).

The acoustic pressure field simulations started with a 1-D model that was used to simulate different tapering techniques to see their effect on the grating lobe values. Equal,

linear, Hanning and Hamming tapering techniques were simulated. Improvements to the tapered array design started with a $27 \times 53 \text{ mm}^2$ solid piezoceramic cut into a 3×21 pattern with 63 individual elements with lengths (L_i) of 1.68, 1.73, 1.81, 1.91, 2.02, 2.14, 2.26, 2.36, 2.43, 2.48, 2.50, 2.48, 2.43, 2.36, 2.26, 2.14, 2.02, 1.91, 1.81, 1.73, 1.68 mm for elements $i = 1$ through 21, respectively, and widths (W_i) of 9.0 mm for all elements $i = 1$ through 3, respectively (Figure 1). The maximum possible steering angle was calculated to be $\tan^{-1}(1.2/5.0) = 13.5^\circ$ with maximal focal depth of 11 cm. Off-axis focusing and the grating lobe level are directly related to each other since increasing the steering angle causes a nonlinear increase in the grating lobe level. However, the designed array described in this paper kept a good grating lobe level when aiming the focus at a point that was 5 mm away from the z direction. When focusing at (0.2, 0, 5) and (0.5, 0, 5) cm, the grating lobe level was kept around -12 dB, as can be seen in Figures 2(a) and 2(b), respectively.

2.1.2 Temperature distribution simulations

From the pressure field of the simulated array, the temperature distribution in the tissue was modeled using the Pennes' bioheat transfer equation (BHTE) [15]:

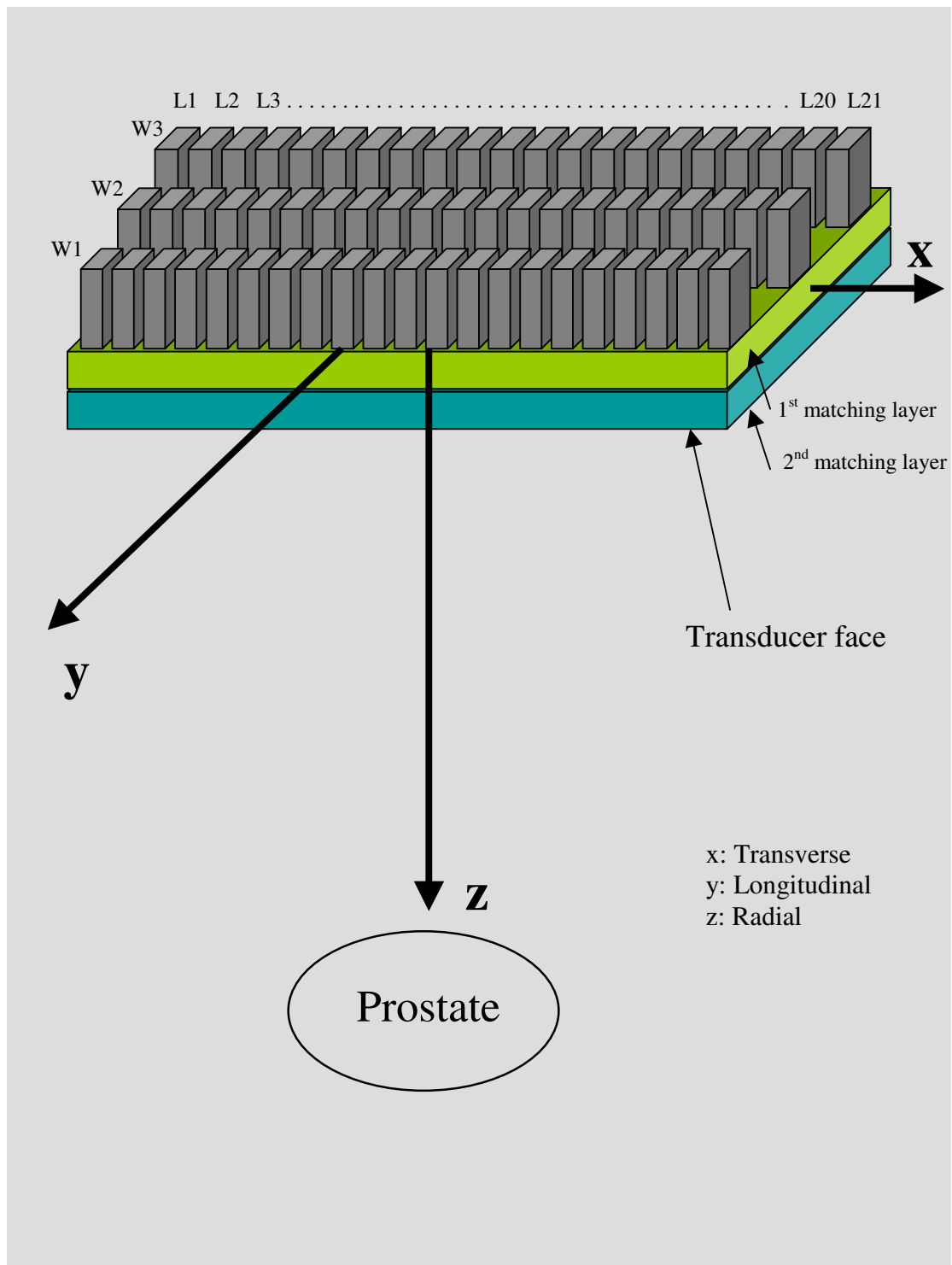
$$\rho C_t \frac{\partial T}{\partial t} = K \left(\frac{\partial^2 T}{\partial x^2} + \frac{\partial^2 T}{\partial y^2} + \frac{\partial^2 T}{\partial z^2} \right) - w C_b (T - T_a) + q(x, y, z) \quad (3)$$

Where C_t is the specific heat of the tissue ($3770 \text{ J} \cdot \text{kg}^{-1} \cdot ^\circ\text{C}^{-1}$), K is the thermal conductivity ($0.5 \text{ W} \cdot \text{m}^{-1} \cdot ^\circ\text{C}^{-1}$), T is the temperature at time t at the point x, y, z in $^\circ\text{C}$, T_a is the arterial blood temperature (37°C), w is the perfusion in the tissue in $\text{kg} \cdot \text{m}^{-3} \cdot \text{s}^{-1}$, C_b is the specific heat of the blood ($3770 \text{ J} \cdot \text{kg}^{-1} \cdot ^\circ\text{C}^{-1}$) and $q(x, y, z)$ is the power deposited at the point x, y, z . The power was calculated from the pressure field of the array design while the BHTE was determined using a numerical finite difference method with the boundary conditions set at 37°C . The total intensity at point (x, y, z) was also calculated from the pressure field of the simulated array and is given by [16]:

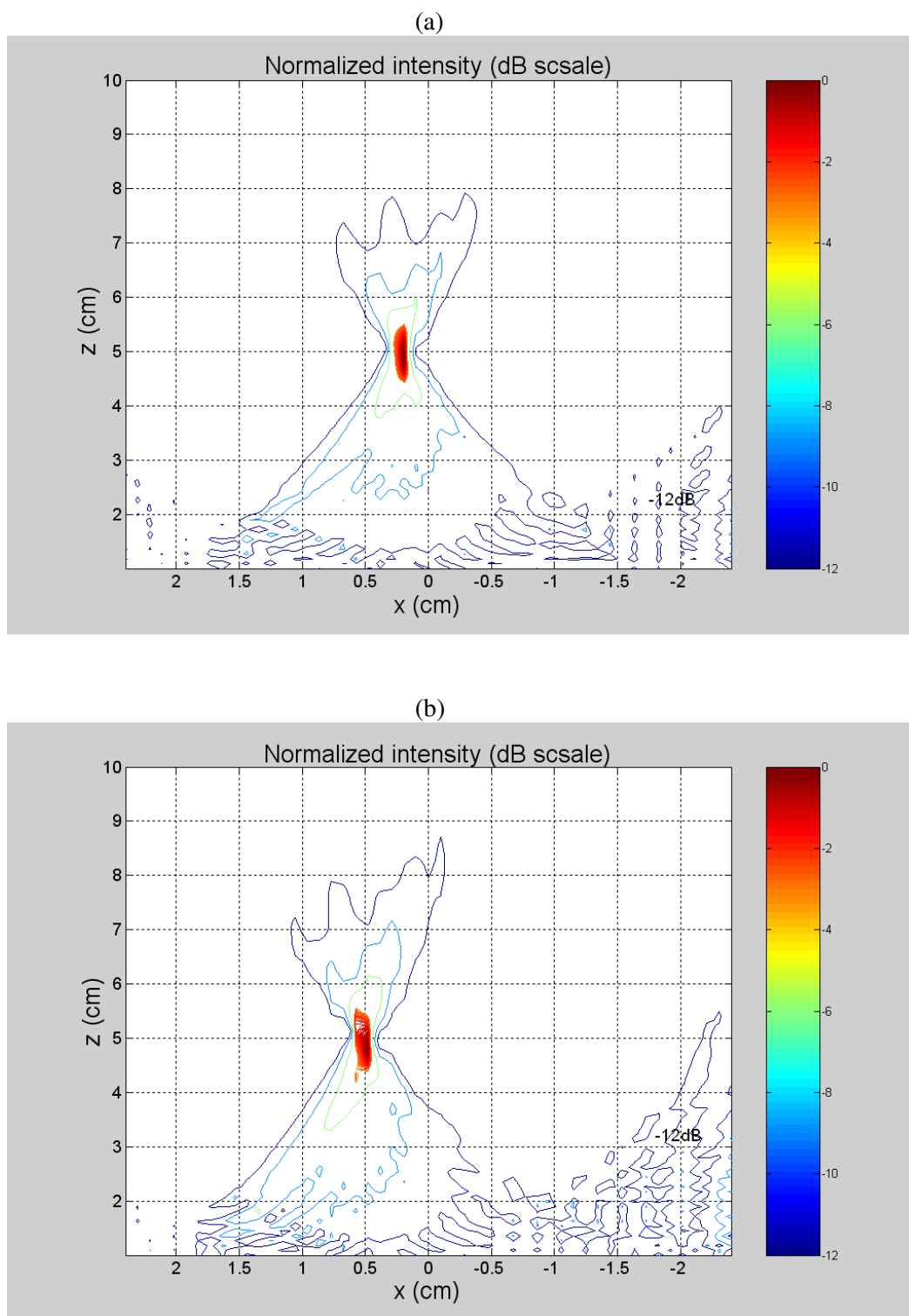
$$I(x, y, z) = \frac{p^2(x, y, z)}{2\rho c} \quad (4)$$

Where $I(x, y, z)$ is the intensity at point (x, y, z) in $\text{W} \cdot \text{m}^{-2}$.

Temperature simulations were used to verify the potential to increase the tissue temperature to about 60°C with short sonications. Both on- and off-axis simulations were performed to see what impact they have on grating lobe values. The effect of off-axis focusing on the temperature distributions becomes more evident at high steering angles. For the case where the steering angle was set to 4.75° , i.e., focus at (5, 0, 60) mm, the temperature distribution was calculated and plotted in Figures 3(a-c) as a

**Figure 1**

Based on the simulations, a diagram of the 1.75-D 63 element (3×21) tapered array with total size of $27 \times 53 \text{ mm}^2$ with the proportions of the ceramic and matching layer illustrated. The diced face of the ceramic was cut 100% through and each individual element was attached to the electrical cabling using low temperature soldering material.

**Figure 2**

Off-axis focusing has a direct impact on the grating lobe level. Increasing the steering angle by changing the focal point position in the x direction increases the grating lobe level. For a focus aimed at (0.2, 0, 5) and (0.5, 0, 5) cm, a fair grating lobe level of about -12dB was observed, as seen in (a) and (b), respectively.

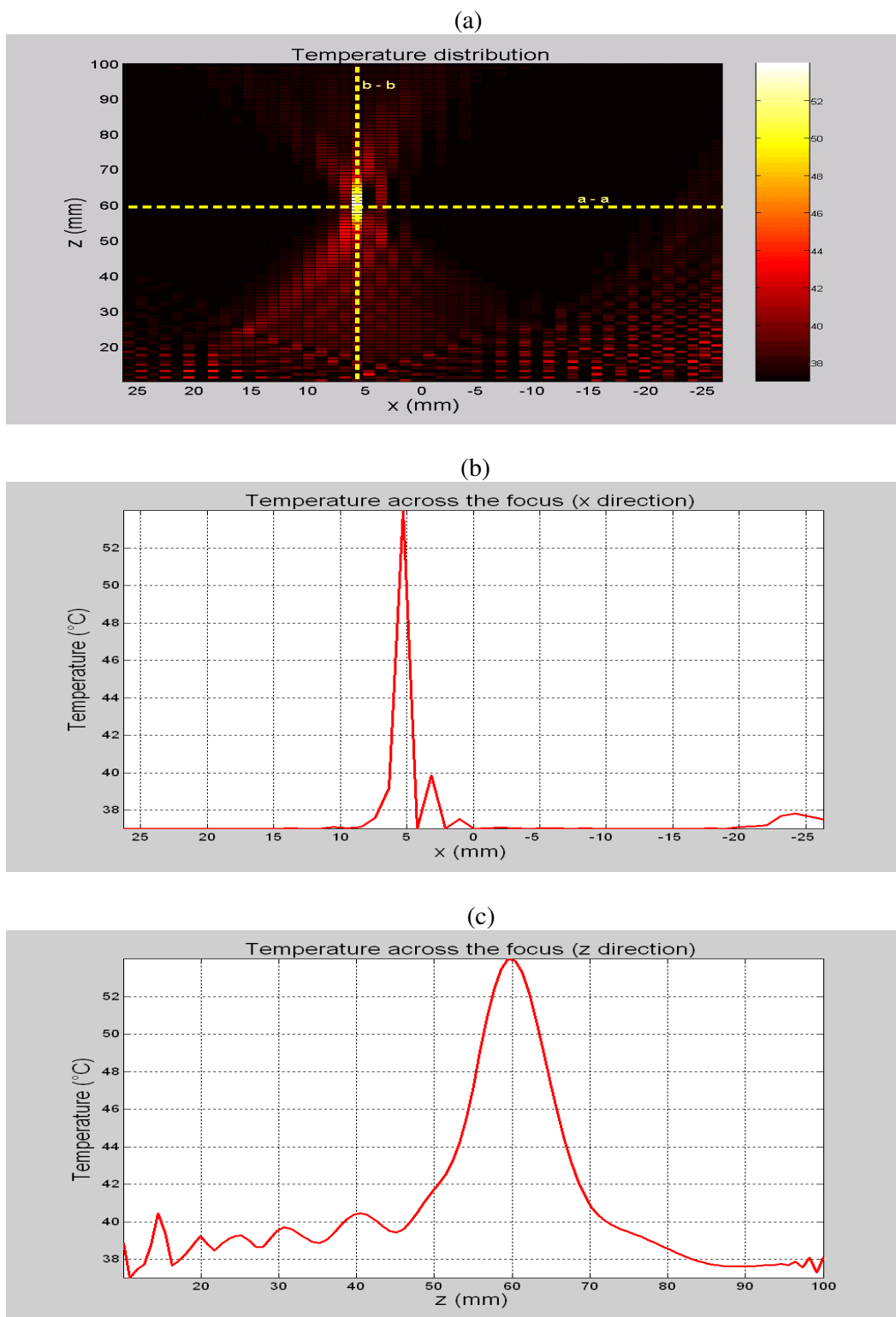


Figure 3

A temperature map (a) for a focus aimed at (5, 0, 60) mm and cross section temperatures (b) and (c) across the lines a-a and b-b, respectively, as a function of distances x and z, respectively.

distribution at the plane of interest, a cross section along the line a-a and a cross section along the line b-b, respectively. Those three figures show that the simulated temperature at the focal point was about 54°C, while the temperature elsewhere was kept below 41°C.

2.2 Transducer construction

The 1.75-D array described in this chapter vibrates in the thickness mode, which means that ϵ_{33} is the permittivity value of interest. Although Lead zirconate-titanate (PZT-5H) has a higher permittivity, which would lead to a higher capacitance, it cannot handle the large power that is used in FUS. PZT-4 and PZT-8 are good candidates concerning power, with an advantage for PZT-8 over PZT-4. The capacitance of a certain element in the array depends on the thickness (which is constant for all elements), the permittivity (which is a material characteristic) and the surface area of that element. Since the areas of the elements of the array are small, this will result in a small capacitance and thus large element impedance.

PZT-8 can handle the large electrical power needed for tissue ablation, has an extremely high mechanical quality factor and extremely low loss factor. Thus PZT-8 material (TRS Ceramics, State College, PA, USA) was chosen at a frequency of 1.2 MHz and diced, in house, into 3×21 elements forming the complete array. The cuts were made by dicing the material 100% through its thickness with a kerf width of 300 μm using a dicing saw (Model 780, K & S-Kulick and Soffa Industries, Willow Grove, PA, USA) in our lab. For maximum acoustical power transfer from the individual elements to the tissue, two matching layers were designed and constructed. The thickness and material selection of the matching layers were designed based on the solution to a four-layer problem (transducer, first matching layer, second matching layer, and tissue), which ensured the required maximum power transfer. The acoustic impedance of the two matching layers (Z_1 and Z_2) was calculated using a criterion determined by Fraser:

$$Z_1 = (Z_{\text{piezo}})^{4/7} (Z_{\text{tissue}})^{3/7} \quad (5)$$

$$Z_2 = (Z_{\text{piezo}})^{1/7} (Z_{\text{tissue}})^{6/7} \quad (6)$$

Each of the two matching layers was designed for a quarter wavelength thickness. Accordingly, the thickness of the first and second matching layers was determined to be 0.396 and 0.429 mm, respectively. The first matching layer, mixed in-house, was a 2:1, epoxy to silver mixture of Insulcast 501 (Insulcast, Roseland, NJ, USA) and 2–3 micron silver epoxy (Aldrich, Milwaukee, WI, USA), while the second matching layer was a SPURR (Spi Supplies, West Chester, PA, USA) four-part low viscosity material. For this array design (Figure 4), the specially machined, waterproof cylindrical applicator housing (30 mm diam-

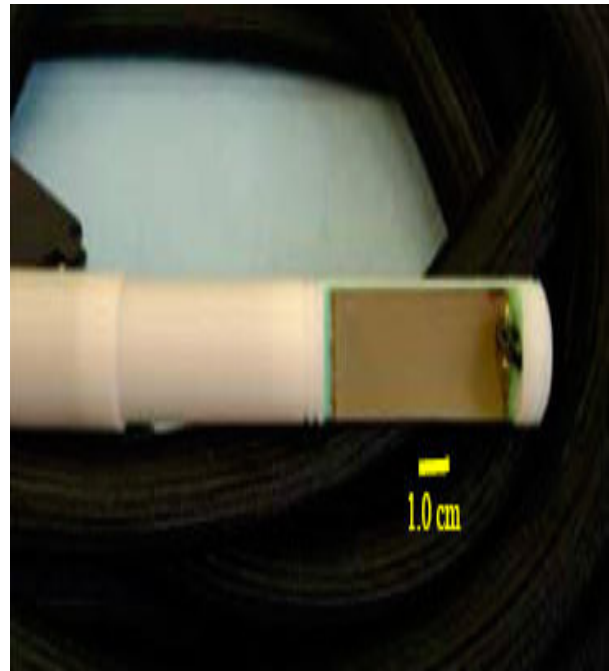


Figure 4

Photograph of the constructed, waterproof array with 7.0 m low capacitance cable that connected to the amplifier system.

eter) was made from magnet compatible Delrin® (Dupont, Wilmington, DE, USA) at the Penn State engineering shop.

Transmission line theory applies to the coaxial cables used in ultrasound applications. The simplest approximation for the transmission line is a lumped capacitance, where the total cable capacitance can be measured by multiplying the cable capacitance per meter, C_m , by the length of the cable L in meters. Since the load impedance (element impedance) is high, the cable has to be a low capacitance cable, which effectively means high cable impedance. A cable with a characteristic impedance of 75 Ω was found to be suitable

The 1.75-D array contains 63 elements. Since those elements are of different size, each one of them will have different electrical impedance depending on the surface area of that element which determines the capacitance of that element and thus the electrical impedance. The target is to match each one of these impedances to the common value of $50\Omega \pm 0^\circ$. A simple LC (L = inductor, C = capacitor) impedance matching circuit was built for each of the 63 elements.

2.3 Exposimetry

To determine the acoustic field generated by the array, an automated computer controlled positioning system, which could translate a hydrophone (needle one with 0.5 mm diameter, Precision Acoustics, UK) throughout the acoustic field of the array placed in a water tank, was used. The transducer was submerged in water (room temperature, approximately 20°C) in a tank (120 × 50 × 52 cm³) made almost anechoic with sound absorbing rubber. A custom made degasser, built in-house, was used to reduce the dissolved oxygen content of the distilled water to 1–2 ppm to reduce cavitation. The system was controlled using a personal computer connected to a four-motor positioning system (Velmex Inc., Bloomfield, NY, USA) via the RS232 serial port and also connected, via the general purpose interface bus (GPIB), to a digital oscilloscope (Agilent 54622A, Agilent Technologies, Palo Alto, CA, USA) which recorded the voltage amplitudes detected by the hydrophone. Custom written, Quick Basic (Microsoft Corporation, Redmond, WA, USA) programs were used for automated control of the motors and data acquisition from the oscilloscope. Initially, multiple on-axis (i.e. where the focus is along the major z axis, *zf*) exposimetry experiments were performed. With the focus set to 0, 0, *zf* mm, *zf* was varied from 10 mm to 110 mm with a step size of 5 mm. To determine the repeatability or standard deviation of the focusing, 5–10 experiments were performed at each location. For off-axis studies (i.e., where the focus was not on z but aimed toward the x axis, *xf*), the focus was located at (*xf*, 0, 60) mm while the steering angle was adjusted to the desired value by choosing appropriate values for *xf*. The steering angle was varied from -12° to +12° with a step size of 2° in both x and y directions with multiple experiments (5–10) performed at each angle. In both the on-axis and off-axis experiments, the scanning step size was 0.5 mm while the scanning area was 40 × 40 mm². The hydrophone voltage recordings were used to calculate the normalized intensities based on the pressures that were plotted as the mean and standard deviation of the results ($\bar{x} \pm \text{s.d.}$) and compared against the calculated values.

2.4 Ex vivo experiments

To test the ability of the array to generate lesions in non-perfused bovine tissue, the array was submerged 6 cm in water and aimed perpendicular to the surface of water. Fresh bovine tissue was obtained, placed in the water tank and held 2.5 cm in front of the array. For both on- and off-axis focusing, a single linear array was driven with an average electrical power of 1 Watt per element for six to seven minutes.

3. Results

To compare experimental and theoretical results, more than fifty exposimetry experiments were performed

throughout the desired ablation volume to determine the focusing capability of the array. As an example of a typical exposimetry result at the location (*x*, *y*, *z*) = (0, 0, 40) mm, Figure 5(a) shows a comparison plot along the *z*-axis of the calculated and experimental normalized intensities. Figure 5(b) plots similar theoretical and experimental data but instead along the *x*-axis for the same focus (0, 0, 40 mm). As can be seen for both plots, the theoretical intensity data correlated well with the experimental results. To evaluate the feasibility of the array to steer the focus, a typical three dimensional normalized intensity result from a focal point directed at 0, 0, 40 mm. The results were plotted as a mesh (Figure 6(a)) and contour (Figure 6(b)) with contour levels at 0, -1, -2, -3, -6 and -9 dB of the normalized intensity with the grating lobe levels at about -9.0 dB or less.

Ex vivo experiments were also performed to verify the ability of the array to generate lesions in bovine tissue. In one experiment, the array was turned on for about six minutes. After turning the array off, the bovine piece was cut at the position where the focal point was aimed. A lesion that has the dimensions of 1 cm × 0.3 cm was observed, as Figure 7(a) shows. An unmarked version of Figure 7(a) is shown in Figure 7(b) for better visualization of the lesion. During the experiment, thermocouples were used to monitor the temperature at two locations, the focal point and the grating lobe locations. The temperature recording, Figure 7(c), shows that the focal point temperature reached about 52°C, while the grating lobe temperature was kept below 40°C, as compared to the simulated values (using the BHTE) of 51.7°C and 40.2°C, respectively. In another experiment, the array was turned on for about seven minutes and then turned off. The observed lesion was approximately 1.3 cm × 0.38 cm in size, as shows in the marked picture of the lesion, Figure 8(a). The same picture, but without marking the lesion, is shown in Figure 8(b) for better visualization of the lesion. The temperature recordings for this experiment show that the temperature at the focal point position increased to reach about 49.5°C while the temperature at the grating lobe position was about 39°C at the end of the experiment, as shown in Figure 8(c). Although the sonication time for this experiment was seven minutes while it was six minutes for the experiment shown in Figure 8, the final temperature value at the focal point was less for the seven minute experiment as compared to the six minute one. This might be due to the uncertainty of the location of the thermocouples.

4. Discussion

Intracavitary ultrasound offers an attractive means of focused ultrasound treatment for BPH with significant advantages over other treatment methods due to the relatively short treatment time, its noninvasive nature and reduced complications. One compelling reason for using

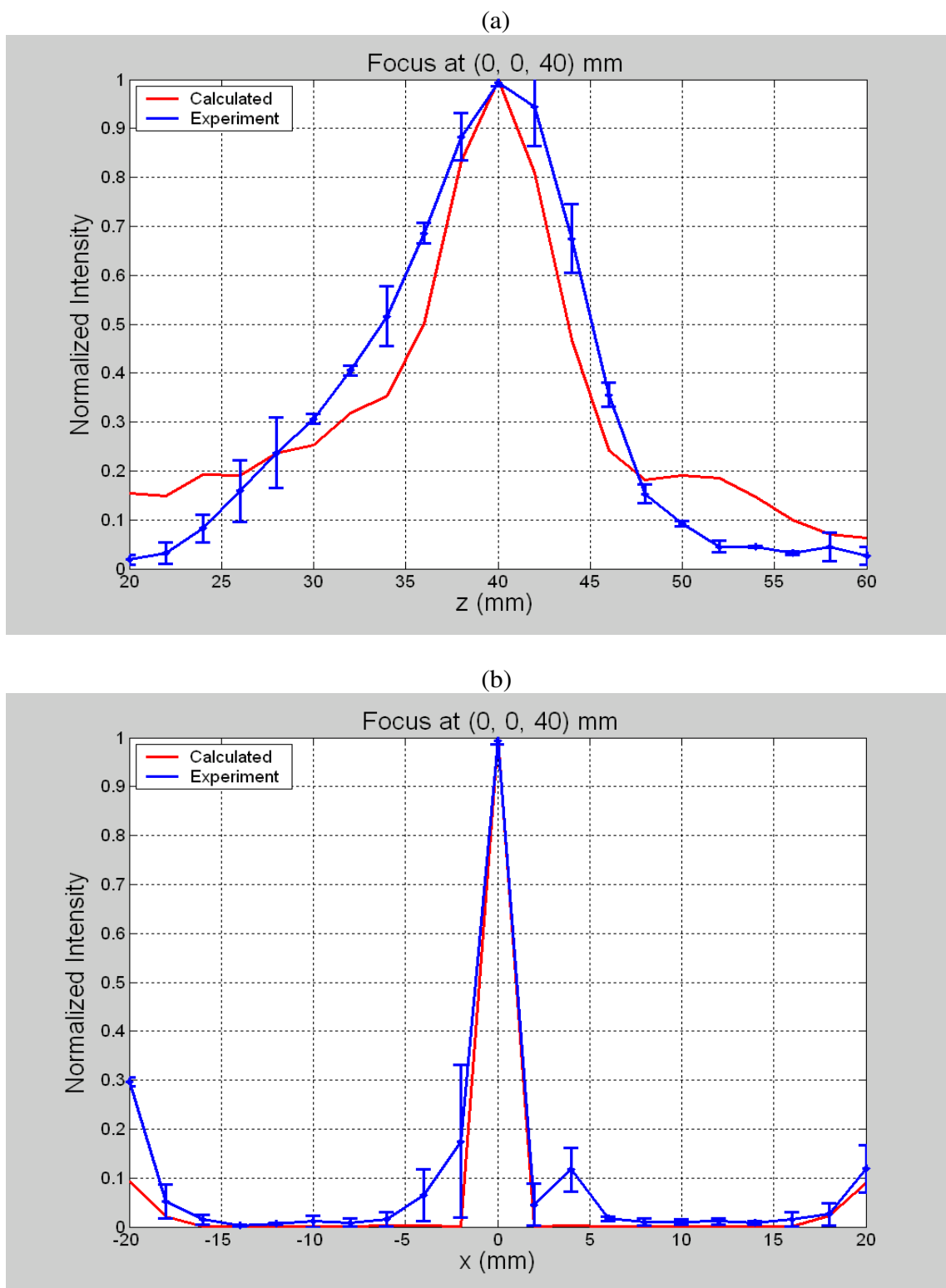
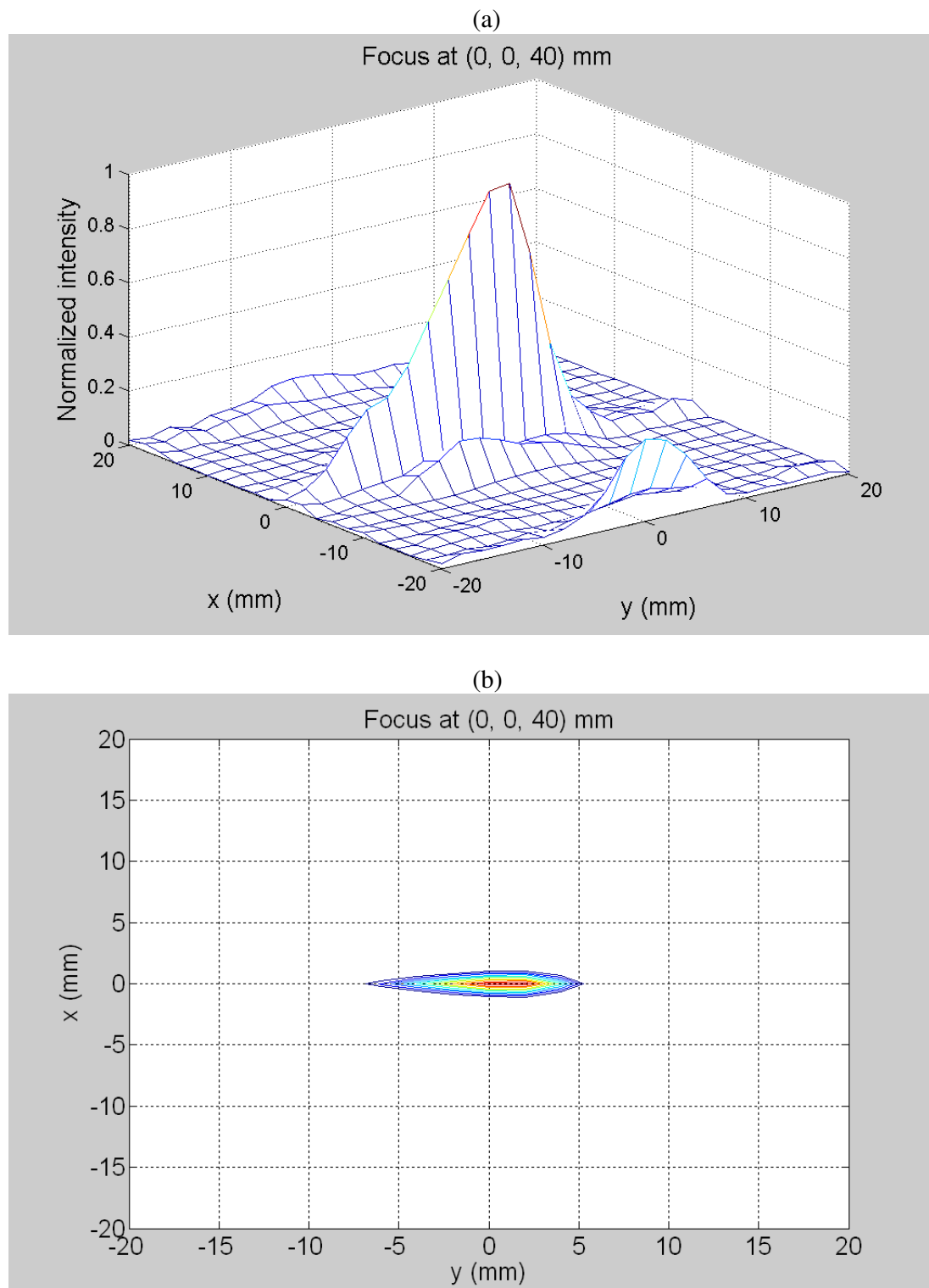


Figure 5

Comparison of calculated and experimental normalized intensities for a focus at 0, 0, 40 mm plotted along the (a) z axis and (b) x axis.

**Figure 6**

Exposimetry results of the normalized intensity for off-axis focusing with the focal point aimed at 0, 0, 40 mm plotted as a (a) mesh or (b) contour with levels indicated at 0, -1, -2, -3, -6 and -9 dB. These results indicate acceptable grating lobes of less than -9 dB.

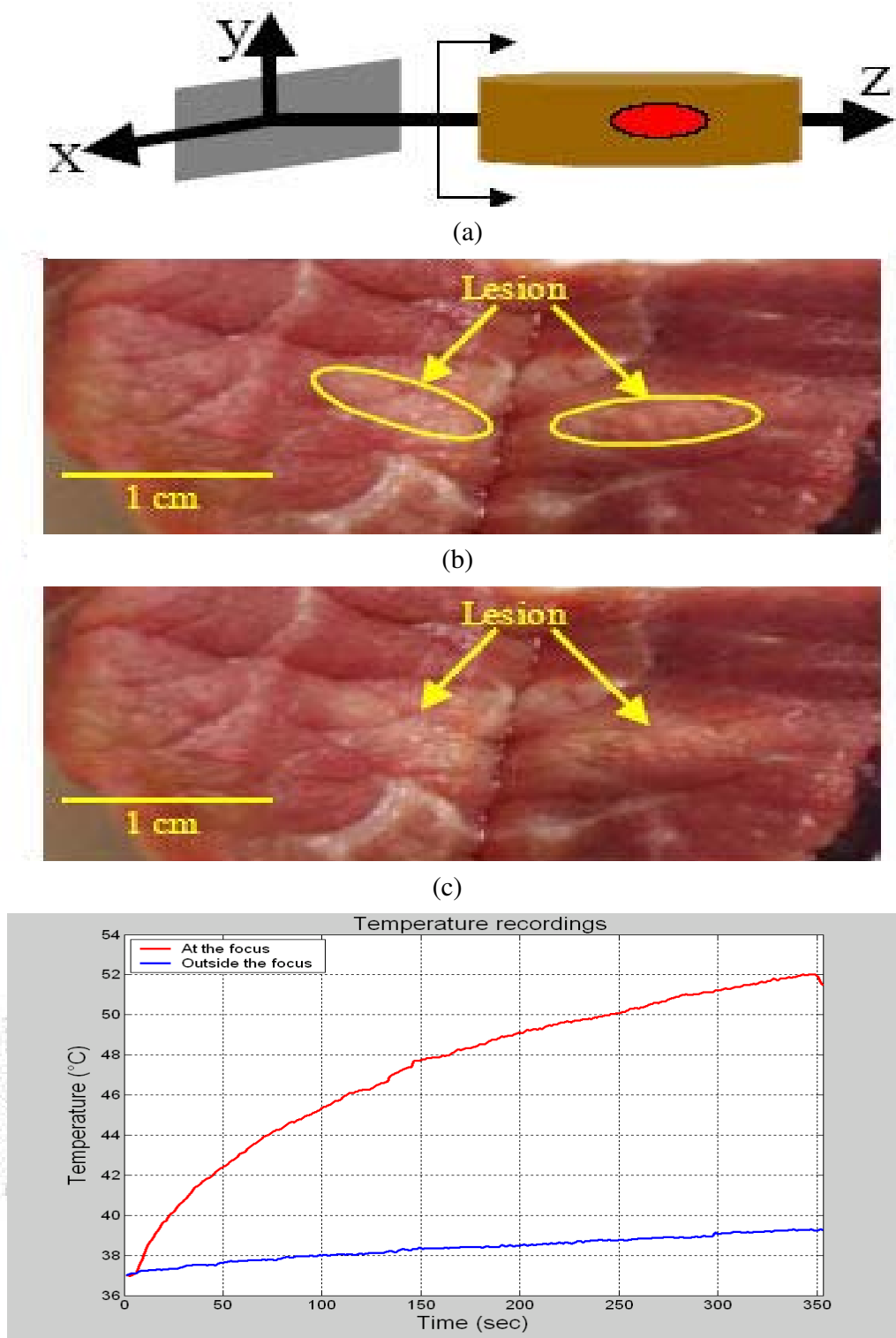
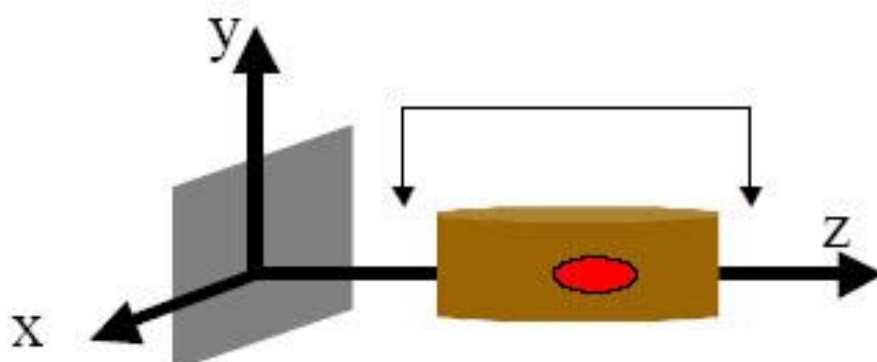


Figure 7

(a) A lesion, with dimensions of about 1 cm × 0.3 cm, generated by a six minute sonication time experiment (b) Temperature recordings at the locations of the focal point and grating lobe.



(a)



(b)



(c)

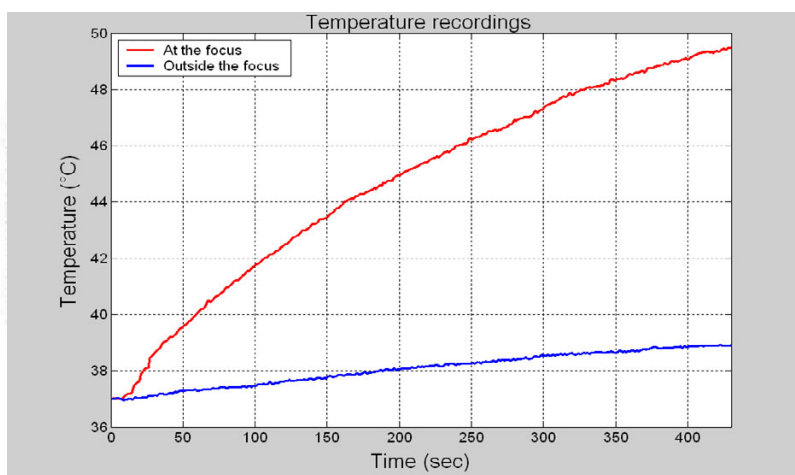


Figure 8

A marked (a) and unmarked (b) lesion, with dimensions of 1.3 cm × 0.38 cm, generated by a seven minute sonication time experiment, and the temperature recordings (c) at the locations of the focal point and grating lobe.

an intracavitary device with focused ultrasound is that the prostate is easily accessible via transrectal applicators, which allow for heating of the target volume in the prostate with minimal heating of normal tissue. Using phased arrays to electrically focus the ultrasound beam provides a controlled localized power deposition into tissue and reduces significantly the treatment time since the focus is electronically scanned instead of manually.

In designing this array, several issues were taken into account to address its application for BPH treatment. The dimensions of array were designed for an intracavitary rectal device. With appropriate housing, the array dimensions of $2.7 \times 5.3 \text{ cm}^2$ are suitable. Another issue concerning this design was the grating lobe level, which was reduced significantly by tapering the array element lengths.

To treat the prostate, the array was aimed toward the intended target volume, and the elements were driven at a calculated amplitude and phase to generate a single focal point with electrical steering.

The array can ablate a volume that lies in its steering volumes. Assuming that the volume to be ablated is $1 \times 1 \times 2 \text{ cm}^3$ and that its center is 3 cm away from the array face, two techniques can be used as a treatment plan to ablate the whole volume; the first one is using a single focal point regime in which the target volume is divided into small volumes. The size of these small volumes is chosen based on the size of the lesion and the sonication time. Assuming that the lesion was a 4 mm long cigar shape with 2 mm diameter for a 10 second sonication, dividing the $1 \times 1 \times 2 \text{ cm}^3$ volume into $5 \times 5 \times 5$ points indicates that 125 sonications are needed to ablate the target based on a single 10 second sonication that is electronically steered between the 125 positions. Starting at the center of the target volume, a single focal point is generated there and then electronically steered 125 times to cover the whole volume. To avoid uncontrolled heat buildup and pre-focal heating, the switching between the focal points is done in a way that any two focal points consecutive in time are far away from each other in distance. By doing that, enough time is given to the pre-focal positions to cool down. A second technique to ablate a large volume is by generating multi-focal points at the same time. Dividing the array into three areas, each responsible for generating a single focal point, will result in reducing the overall treatment time by a factor of three. This technique is time efficient, but the drawback behind it is that the driving electrical power per unit area should be increased.

If the maximum possible steering angle is 13.5° in the transverse direction, as the case for this array design, attempting to focus outside this volume will add a signif-

icant amount of energy to the grating lobes which will cause an unwanted heating. This puts a limitation for the array if the target volume extends beyond the 13.5° limit.

When coupled with MR temperature mapping, FUS provides an efficient way to treat BPH and at the same time gives a quick feedback about the temperature distribution inside the prostate [8]. Although ultrasound imaging for the prostate has shown to give good results [5,17], the array described here was designed to accompany an MRI.

Similar to prostate cancer treatment with focused ultrasound, benign fibroadenomas in the breast are currently treated clinically using multiple sonications from a single element transducer, which is mechanically scanned [18], in conjunction with MRI for guidance of thermotherapy of the procedure [19]. Although the treatment has been shown to be effective, the process includes an unnecessary delay due to the mechanical scanning protocol. When closely spaced locations are targeted with focused ultrasound, thermal buildup results from the accumulation of neighboring sonications and the nearfield heating. As a result, a lengthy delay between sonications (cooling time) is required to reduce thermal buildup. Investigators have shown that a cooling time of 50–60 seconds was necessary to reduce the heat from the near neighbor sonications [20] however this can add considerable time to the procedure and initiate inaccuracies to the MR thermometry through patient motion. With phased arrays a focal pattern can be arranged such that there is enough time for the heat to dissipate by sonicating non-neighboring regions within the tumor [21]. A treatment planning routine can be plotted over the entire tumor region such that the volume is ablated through distant and non-adjacent ablations to avoid thermal buildup yet destroy the volume in the least amount of time. This research demonstrates the feasibility of electrically steered arrays that can be used to ablate tissue for the intended treatment of benign prostatic hyperplasia.

5. Conclusion

A 1.75-D ultrasound phased array, that can focus and steer in a 3-D representation of the prostate without the need to physically move the array, had been successfully built and tested for the treatment of prostate cancer and BPH. Previous focused ultrasound array designs were problematic since they required complex methods to move the focus, as for the case of annular arrays, or had linear (1-D) designs that were only capable of focusing along one axis. These drawbacks were the motivation to design a new array that can be used in FUS and at the same time be systematically controlled to reposition the focus throughout a specific volume with an acceptable level of grating lobes. Further improvement over this array design seems to be feasible due to recent developments in building focused

transducers using piezocomposite technology [22]. A three-layer PZT-8 material may also be used to increase the capacitance and thus make it easier to electrically match the small elements.

6. Authors' contributions

The first author (Saleh) contributed 60% of the work done for this paper. He performed the computer simulations required for the study, participated in performing the experiments that were performed to verify the study, and participated in the drafting and revising of the article. The other Author (Smith) contributed 40% of work done. She came up with idea, participated in some of the experiments performed and participated in the drafting and revising of the article. So both authors have made substantial contributions, have been involved in writing the article and have given final approval for the final submitted version.

7. Acknowledgements

This work was supported by the Department of Defense Congressionally Directed Medical Prostate Cancer Research Program (DAMD17-0201-0124).

References

- Barrett D: **Mayo Clinic on prostate health**. 1st edition. Rochester, Minn: Mayo Clinic; New York; 2000.
- DelaRosette JJ, Zlotta AR: **Alternative Instrumental Treatments in BPH. Future Perspectives**. *European Urology* 1999, **35**:173-176.
- Diederich CJ, Hynnen K: **Induction of hyperthermia using an intracavitary multielement ultrasonic applicator**. *IEEE Trans Biomed Eng* 1989, **36**(4):432-438.
- Hutchinson E: **Intracavitary ultrasound phased arrays for thermal therapies**. In *PhD thesis* Massachusetts Institute of Technology; 1997.
- Mahoney K, Fjield T, McDannold N, Clement G, Hynnen K: **Comparison of modelled and observed in vivo temperature elevations induced by focused ultrasound: implications for treatment planning**. *Phys Med Biol* 2001, **46**(7):1785-1798.
- Sanghvi NT, Foster RS, Bihle R, Casey R, Uchida T, Phillips MH: **Noninvasive surgery of prostate tissue by high intensity focused ultrasound: an updated report**. *Eur J Ultrasound* 1999, **9**:19-29.
- Hurwitz MD, Kaplan I, Svensson GK, Hansen J, Hynnen K: **Feasibility and patient tolerance of a novel transrectal ultrasound hyperthermia system for treatment of prostate cancer**. *Int J Hyperthermia* 2001, **17**(1):31-37.
- Hutchinson EB, Hynnen K: **Intracavitary ultrasound phased arrays for noninvasive prostate surgery**. *IEEE Trans Ultrason Ferroelect Freq Control* 1996, **43**(6):1032-1042.
- Sokka S, Hynnen K: **The feasibility of MRI guided whole prostate ablation with a linear aperiodic intracavitary ultrasound phased array**. *Phys Med Biol* 2000, **45**(11):3373-3383.
- Curiel L, Chavrier F, Souchon R, Birer A, Chapelon JY: **1.5-D high intensity focused ultrasound array for non-invasive prostate cancer surgery**. *IEEE Trans Ultrason Ferroelect Freq Control* 2002, **49**(2):231-242.
- Saleh K, Smith NB: **Design and evaluation of a 3 × 21 element 1.75 dimensional tapered ultrasound phased array for the treatment of prostate disease**. *Materials Research Innovation* 2004, **8**(2):121-124.
- Saleh K, Smith NB: **Two Dimensional Ultrasound Phased Array Design for Tissue Ablation for Treatment of Benign Prostatic Hyperplasia**. *International Journal of Hyperthermia* 2004, **20**(1):7-31.
- Buchanan MT, Hynnen K: **Design and experimental evaluation of an intracavitary ultrasound phased array system for hyperthermia**. *IEEE Trans Biomed Eng* 1994, **41**(12):1178-1187.
- Zemanek J: **Beam behavior within the nearfield of a vibrating piston**. *J Acoust Soc Am* 1971, **49**:181-191.
- Pennes HH: **Analysis of tissue and arterial blood temperatures in the resting human forearm**. *J Appl Physiol* 1948, **1**:93-122.
- Nyborg WL: **Heat generation by ultrasound in a relaxing medium**. *J Acoust Soc Am* 1981, **70**:310-312.
- Chapelon J, Ribault M, Birer A, Vernier F, Souchon R, Gelet A: **Treatment of localised prostate cancer with transrectal high intensity focused ultrasound**. *Eur J Ultrasound* 1999, **9**:31-38.
- Hynnen K, Pomeroy O, Smith DN, Huber PE, McDannold NJ, Kettenbach J: **MR imaging-guided focused ultrasound surgery of fibroadenomas in the breast: a feasibility study**. *Radiology* 2001, **219**:176-185.
- Quesson B, de Zwart JA, Moonen CT: **Magnetic resonance temperature imaging for guidance of thermotherapy**. *J Magn Reson Imaging* 2000, **4**:525-533.
- McDannold NJ, Jolesz FA, Hynnen KH: **Determination of the optimal delay between sonications during focused ultrasound surgery in rabbits by using MR imaging to monitor thermal buildup in vivo**. *Radiology* 1999, **211**:419-426.
- Daum DR, Hynnen K: **Thermal dose optimization via temporal switching in ultrasound surgery**. *IEEE Trans Ultrason Ferroelect Freq Control* 1998, **45**(1):208-215.
- Fleury G, Berriet R, Le Baron O, Huguenin B: **New piezocomposite transducers for therapeutic ultrasound**. *Proceedings of the Workshop on MRI-Guided Focused Ultrasound Surgery: 19-21 June 2002; Cambridge*, 2002:39.

Publish with **BioMed Central** and every scientist can read your work free of charge

"BioMed Central will be the most significant development for disseminating the results of biomedical research in our lifetime."

Sir Paul Nurse, Cancer Research UK

Your research papers will be:

- available free of charge to the entire biomedical community
- peer reviewed and published immediately upon acceptance
- cited in PubMed and archived on PubMed Central
- yours — you keep the copyright

Submit your manuscript here:
http://www.biomedcentral.com/info/publishing_adv.asp



Utilization of the k -space method in the design of a hyperthermia phased array

Osama M. Al-Bataineh¹, T. Douglas Mast², Victor W. Sparrow³, Robert M. Keolian^{3,4}, Eun-Joo Park¹, and Nadine Barrie Smith^{1,3}

¹Department of Bioengineering, ³Graduate Program in Acoustics, ⁴Applied Research Laboratory,
The Pennsylvania State University, University Park, PA 16802

²Department of Biomedical Engineering, University of Cincinnati, Cincinnati, OH 45267

Please send correspondence to:
Eun-Joo Park, M.S.
Department of Bioengineering
The Pennsylvania State University
313 Hallowell Building
University Park, PA USA 16802
TEL: 001-814-865-8087 FAX: 001-814-863-0490
eup114@psu.edu

Abstract

This research utilizes the k -space computational method and a three-dimensional (3D), inhomogeneous, large scale, and coarse grid human prostate model to design and to fabricate an intracavitary probe for hyperthermia treatment of prostate cancer. A 3D acoustical prostate model was created utilizing photographic data from the Visible Human Project®. Ultrasound wave propagation of the designed phased array was simulated by means of the k -space computational method. Four stacked linear phased arrays composed the hyperthermia array. Good agreement between the exposimetry and the k -space simulation results was obtained. As an example, the measured -3 dB distance of the focal volume in the propagation direction deviated by only 9% compared to simulated results.

1. Introduction

Prostate cancer causes approximately 30,000 deaths among Americans every year with more than 230,000 new patients in 2004 [1]. Thermal treatment has proven effective for different kinds of tumors including prostate cancer. Hyperthermia therapy raises the temperature of the tumor and a surrounding margin of normal tissue from the normal body temperature of 37°C to 42-45°C for about 30 minutes [2;3;4]. This type of treatment has had success, in conjunction with radiation therapy, in enhancing the cytotoxic effect of the radiation [5;6;7;8;9]. Ultrasound intracavitary hyperthermia technology is an accepted treatment for prostate cancer.

Previous simulation and design studies of intracavitary ultrasound phased arrays have not considered anatomically realistic human prostate models [10;11;12;13]. Preceding intracavitary ultrasound hyperthermia phased arrays used small cylindrical radiators to conform to the natural contours of large body orifices [14;15]. Simulations of previous hyperthermia and high intensity focused ultrasound (HIFU) phased arrays were accomplished using the Rayleigh-Sommerfeld integral over a set of a geometrically superimposed point sources [16]. Homogeneous water-like media were used to simulate pressure field distributions of these arrays [10;11;12;13;14;15;17]. Such simulations, however, do not capture the interaction of ultrasound with inhomogeneous tissue structures. Accurate modeling of ultrasound wave propagation in inhomogeneous three dimensions (3D) over large length scales has become feasible using the k -space computational method [18;19]. This method solves the spatial terms of the wave equation by Fourier transformation to the spatial frequency domain; while temporal iterations are performed using a nonstandard finite difference approach using the k - t space propagator (where k represents the spatial frequency domain and t represents the time domain) [18]. In theory, this method requires only two points per wavelength (minimum sampling frequency is twice the frequency of the captured signal for better resolution in the spatial frequency domain (the spatial Nyquist criterion) [20]) for homogeneous media simulations and four points per wavelength for inhomogeneous media [18]. It provides much higher accuracy than the pseudospectral methods, in which the spatial derivatives are evaluated globally

by Fourier transformation and wavefields are advanced in time using second order accurate finite differences (leapfrog propagator) [21]. The k -space method maintains its highest accuracy up to a Courant-Friedrichs-Lewy number ($CFL = c_0\Delta t/\Delta x$, where c_0 is the sound speed; Δt is the temporal step; Δx is the spatial step) of about 0.4 [18]. However, the pseudospectral method rapidly increases in error for CFL numbers above 0.1. For weak scattering media, the k -space method provides similar accuracy for time steps two to three times larger than those required by high order pseudospectral methods [18]. Compared to finite difference computations [22], in which both spatial and temporal second order partial derivatives are solved using second order finite difference computations, the k -space method achieves higher accuracy for a much larger spatial step size. Equivalent accuracy is achieved employing only three points per minimum wavelength using the k -space method compared to 14 points per minimum wavelength for the finite difference equation using the same accuracy criterion. For 3D calculations, this increase in the spatial step reduces the storage requirements for the k -space computations compared to finite difference method by 98% [18].

Specifically, this research uses the k -space computational method to simulate ultrasound wave propagation through an acoustically accurate human prostate model. This technique aids the design and simulation of a hyperthermia planar ultrasound phased array for prostate cancer treatment. The linear phased array described here enables focusing and steering of the acoustic beam in both the propagation and azimuth directions. In the elevation direction, however, the intention is to spread the focal region in the volume that faces the length of the probe by using four stacked phased arrays. Photographic three-dimensional (3D) data from the Visible Human Project® (U.S. National Library of Medicine, Bethesda, MD) is used to build the acoustical model of the inhomogeneous medium. The anatomical measurements of the human prostate gland provide essential guide lines for optimal selection of the dimensions of the phased array, while the ultrasound wave propagation simulations predict the pressure volumetric distribution through the prostate model for better heating of both the prostate and the adjacent seminal vesicles. A

transducer consisting of four segments of planar ultrasound phased arrays is fabricated using lead zirconate titanate piezo-ceramic for hyperthermia treatment of the prostate gland. The design, simulation, fabrication, exposimetry testing and hyperthermia evaluation of this 4 x 20 element phased array are presented in this paper.

2. Materials and methods

2.1 Acoustic modeling, k -space simulation and temperature simulation

Photographic images from the Visible Human Project® library were used in constructing a 3D prostate model. Figure 1 shows a transverse (yz-plane is the transverse or axial plane; xy-plane is the coronal plane; and xz-plane is the sagittal plane) photographic slice of this model. It has 89 x 89 mm dimensions with a 0.25 mm grid size. The prostate gland and the urethral opening are marked and labeled in the figure. The rectum, the prostate gland and the seminal vesicles are surrounded by a sheath of smooth and connective tissues. Surrounding this sheath is a triangular shaped fatty tissue around the rectal wall, while skeletal muscle and connective tissues are neighboring the prostate gland and the seminal vesicles. The original 1 mm distance between adjacent transverse slices of the male subject was unsuitably coarse for simulation of acoustic propagation in the 1.2 - 1.8 MHz range. To overcome this problem, three extra slices were interpolated from the consecutive 1 mm slices to reduce the distance between neighboring slices to 0.25 mm. The photographic data permitted development of three sets of 3D acoustical data: sound speed variation, density distribution and absorption parameters. Table 1 summarizes the acoustical values from the literature of different tissue types measured at 37°C that were the basis of the model. The fractional fat, connective, glandular and muscle content of each pixel were inferred from the optical parameters [23;18]. Estimation of the sound speed depended on the fractional content of water, muscle, fat and connective tissues. Mapping the fractional content of water relied on the hue and value of each pixel, while mapping muscle and connective tissues was based on a combination of saturation and value parameters [24]. The mapping of mass density values and

absorption parameters relied on empirical linear relations between sound speed and both mass density and absorption parameters. More details are presented elsewhere [23]

Figure 2a shows the sound speed mapping of the photographic data which was previously shown in Fig. 1. The color bar relates the sound speed values in m/s to the mapped soft tissue distribution through the slice. Sound speed varies through the soft tissue from 1400 to 1600 m/s. The skeletal muscle tissue, that surrounds the prostate gland, has a sound speed of 1550 m/s. The prostate gland itself is mapped to connective tissue and some fat and muscle tissues. This mapping is consistent with descriptions of the gland consisting of tubular and alveolar tissues imbedded in smooth muscle and connective tissues [25]. The rectal wall translated to muscle (sound speed = 1580 m/s) and fat (sound speed = 1450 m/s) tissues. The connective tissue that surrounds the rectum has a sound speed of 1610 m/s. Figure 2b demonstrates density variations that depend on the empirical linear relationship between sound speed and density parameters. The color bar relates density values in kg/m^3 to the empirically related soft tissue distribution through the slice. The density varies through the slice from 900 to 1100 kg/m^3 . Compared to the sound speed map, this figure discriminates each soft tissue distinctly and corresponds well with skeletal muscle, fat, connective tissue and water. Figure 2c illustrates the absorption variations mapping of the soft tissue. The color bar relates absorption values in dB/m to the empirically related soft tissue distribution through the slice. The absorption varies from 10 to 100 dB/m for the different soft tissues. The absorption parameters of fat, connective and skeletal muscle tissues match the summarized values in Table 1. Comparing the values of sound speed, density and absorption of various tissues in Fig. 2a, 2b and 2c, respectively, to the standard values for these soft tissues, this mapping for the whole three-dimensional model provides close agreement to within 1% deviation from the standard reported values in Table 1.

To study the effect of inhomogeneity upon ultrasound waves, the k -space method was used to propagate ultrasound from a spherical source through the acoustical prostate model. The

linear acoustic wave equation was used for the simulation:

$$\nabla \cdot \left(\frac{1}{\rho(x, y, z)} \nabla p(x, y, z, t) \right) - \frac{1}{\rho(x, y, z) c^2(x, y, z)} \frac{\partial^2 p(x, y, z, t)}{\partial t^2} = \frac{\alpha(x, y, z)}{\rho(x, y, z) c^2(x, y, z)} \frac{\partial p(x, y, z, t)}{\partial t}$$

where, $\nabla \cdot ()$ is the spatial divergence operator; $\nabla ()$ is the spatial gradient operator; $\partial^2 () / \partial t^2$ is the second order temporal partial differential operator; $\partial () / \partial t$ is the temporal first order partial differential operator; $\rho(x, y, z)$ is the spatially dependent density (kg/m^3); $c(x, y, z)$ is the spatially dependent sound speed (m/s); $p(x, y, z, t)$ is the spatially and temporally dependent pressure (Pa); $\alpha(x, y, z)$ is the spatially dependent absorption coefficient (s^{-1} , the absorption in dB/m equals to $20 \times \log_{10}(e) \times \alpha(x, y, z) / (2c_0)$ [23]). All absorption effects (viscous, heat conduction and internal molecular processes losses) were represented by a single absorption coefficient which was equivalent to the inverse of a spatially dependent relaxation time [26]. The k -t propagator was used to solve for the propagation in the inhomogeneous prostate model after setting both initial and boundary conditions [18]. The dimensions of the model were $64 \times 64 \times 46$ mm with 0.25 mm spatial step size. It was composed of $257 \times 257 \times 185$ discrete points. The temporal step size was $0.082 \mu\text{s}$. A tapered absorption boundary layer, all around the model, was created to prevent wave wrapping from side to side and to prevent reflection of the waves at the boundaries. This layer is mathematically described elsewhere [23]. The spherical source was located in the rectum, five points away from the absorption boundary layer. Pressure variation results through the acoustical model were visualized using gray scale images. Three-dimensional calculations were performed; however, to reduce storage space, the middle slice was selected for image production. Figure 3 shows the log-scale, gray-scale image of spherical wave propagation in the prostate model. It shows the absorption variations through the central slice of the 3D model as a background image with the pressure variations on top of it. An identifiable incident wave leads the scattered wavefield produced from the propagation through the inhomogeneous medium. At the boundaries of the prostate a noticeable reflection and some irregularity of the shape of the wave while crossing the

urethra are labeled. This figure validates the k -space method and the acoustical model for investigation of the planar phased array.

Figure 4a shows a coronal view (xy-plane) of the 4 x 20 hyperthermia phased array. It consists of four segments of planar phased arrays; each segment consists of 20 elements with a 1 x 14 mm sub-element dimension. This arrangement enables focusing and steering of the pressure beam in the propagation and azimuth directions and enables spreading of the focal region in the volume that faces the length of the array. The description of the housing of the phased array in Fig. 4a, b, c, and d will be discussed later. The k -space computational method was used to study pressure beam formation and steering of the designed phase array through the prostate model. A single segment of the phased array was incorporated in the acoustical model for simulation purposes. Virtual elements with 1 x 14 mm dimension were integrated in the simulation. The established grid size of 0.25 mm for the model limited the effective kerf width of the array to this number. Each sub-element added to the overall virtual source that induced pressure to the surrounding media, depending on the acoustical parameters of each point of the model. All points that related to a specific element were driven temporally in a sinusoidal fashion with a 1.2 MHz frequency and a particular phase shift that compensated for its path length to a specific target. To achieve this, a slight modification to the prostate model was made to include the phased array. The modified model included a 20 mm watery region between the location of the active elements and the rectal wall to mimic the proposed water circulation system.

Temperature simulations were achieved using the bioheat transfer equation [27]:

$$\rho c_t \frac{\partial T(x,t)}{\partial t} = k \left(\frac{\partial^2 T(x,t)}{\partial x^2} \right) - w c_b (T(x,t) - T_a) + q(x)$$

where, $T(x,t)$ is the tissue temperature ($^{\circ}\text{C}$); c_t is the specific heat of the tissue ($3770 \text{ J/kg}^{\circ}\text{C}$); c_b is the specific heat of the blood ($3770 \text{ J/kg}^{\circ}\text{C}$); ρ is the density (998 kg/m^3); k is the thermal conductivity ($0.5 \text{ W/m}^{\circ}\text{C}$); T_a is the arterial blood temperature (37°C); w is the tissue perfusion rate ($8.3 \times 10^{-9} \text{ kg/m}^3\text{s}$); and $q(x)$ is the power deposited locally in the tissue (W/m^3). The square of the acoustic pressure amplitude, which is taken to be proportional to the deposited acoustic power, was

extracted along three perpendicular line scans that crossed at the focal volume of the simulated and measured acoustical pressure fields. The temperature rise after two minutes of heating was calculated from the k -space and Rayleigh-Sommerfeld simulations and exposimetry measurements along the extracted lines. The temperature was initially set to 37°C in the simulations and then the temperature of the focal point was allowed to increase to 43°C. The Rayleigh-Sommerfeld simulations computed the pressure distribution produced by a single segment of the hyperthermia phased array by summing the pressure contributions of individual simple sources along the extracted lines. The kerf width was 0.12 mm between the elements of the phased array. However, the kerf width for the k -space simulations was 0.25 mm. The Rayleigh-Sommerfeld simulations were calculated in water medium without the inclusion of the absorption term.

2.2 Phased array fabrication

Lead zirconate titanate (TRS300, TRS Ceramics, State College, PA) ferroelectric material was used for constructing the 4 x 20 ultrasound phased array. TRS300, being a hard piezo-ceramic, possesses an extremely high mechanical quality factor with the ability to withstand high levels of electrical excitations and mechanical stresses. To increase the efficiency of transmission of acoustical energy in delivering sound energy from the high acoustical impedance of the ceramic to the low acoustical impedance of water or soft tissue, two impedance matching layers were applied onto the ceramic. The choice of these matching layers was aided by design guidelines [28] that gave the desired impedance of quarter wavelength double layers. To construct the double matching layers, Parafilm was used to affix a TRS300 piece to a glass plate. An adhesive primer was poured onto the surface of the ceramic piece. It was then surrounded with an epoxy. A silver bearing, conductive matching layer was poured on top of the ceramic piece. This first layer consisted of a 2:1 epoxy-to-silver mixture of Insulcast 501 (Insulcast Inc., Roseland, NJ) and 2-3 micron silver epoxy (Aldrich Inc., Milwaukee, WI). The whole assembly was centrifuged for 10 minutes and cured overnight. The desired quarter wavelength thickness was obtained by sanding and lapping

the epoxy surface. The second matching layer was made with a similar preparation, but without centrifuging. EPO-TEK 301 part A and part B (Epoxy Technology Inc., Billerica, MA) in a 20:5 mixing ratio created a clear uncured viscous fluid. Another piece of glass spread this mixture on top of the first conductive layer, and appropriate fixtures stabilized the assembly while it cured overnight. After removing the fixtures and the second glass piece, another sanding and lapping process reduced this layer to the required quarter wavelength thickness. Heating the bonding Parafilm wax allowed the separation of the TRS300 piece with its two acoustical matching layers from the glass.

The complete array was formed by dicing the assembly into 80 elements. The dicing cuts were all the way through the thickness of the TRS300 ceramic but not through the matching layers. These cuts were made using a dicing saw (Model 780, K & S-Kulick and Soffa Industries, Willow Grove, PA) with a kerf width of 0.12 mm, the thickness of the cutting blade. Sixty, 28 American Wire Gauge (AWG) miniature magnetic resonance imaging (MRI) compatible coaxial cables (Belden Inc., St. Louis, MI), ten meters long, formed a bundle of cables that connected the elements of the array to an amplifier system. The central two segments of the hyperthermia phased array were electrically connected in parallel. Figure 4a shows a coronal view of the diced phased array placed in the specialized Delrin® plastic transrectal housing. The actual dimension of each segment is 14 x 22 mm; while the dimension of the whole array is 56 x 22 mm. RHODORSIL® V-1022 (Rhodia Inc., Cranbury, NJ) water proof insulation silicone is used to bond and seal the array to its housing. The housing includes grooves to contain O-rings that hold the water bolus in place using a latex membrane, a pair of brass tubes to circulate water in front of the array, another pair of brass tubes to circulate air in the cavity behind the array, and a 100 mm hollow cylindrical handle. The diameter of the penetrating cylindrical portion of the probe is 26 mm diameter x 100 mm length including the rounded front and rear. A smaller diameter cylindrical portion follows the penetrating section of the probe with dimensions of 18 mm diameter x 80 mm length. Figures 4b and c show sagittal and coronal views of the transrectal probe, respectively. The dotted parallel

lines show the location of the brass tubes for the water circulation system. The penetrating part, that contains the phased array, is 97 mm length x 26 mm diameter; the following un-penetrating part is 70 mm length x 18 mm diameter. The handle is 100 mm length x 26 mm diameter. Figure 4d shows the transrectal probe with its bolus inflated. The water bolus and the circulation system are essential for acoustic coupling between the probe and the tissue surrounding it, and for cooling of the piezoelectric ceramic. A water pump (Cole-Parmer Instrument Company, Barrington, IL) and a temperature controlled bath within the circulation system maintained the temperature and flow of the circulated water.

2.3 Exposimetry testing and hyperthermia evaluation

The hyperthermia phased array system was tested using an in-house automated exposimetry system based on the American Institute of Ultrasound in Medicine and National Electrical Manufacturers Association (AIUM/NEMA) guidelines [29]. The array was submerged in an anechoic tank (122 x 51 x 53 cm) filled with degassed distilled water. A needle-type hydrophone (Precision Acoustics Ltd., Dorchester, UK) was placed perpendicular to the face of the transducer to measure pressure field values at discrete points. While focusing the acoustical energy 40 mm away from the face of the transducer, seven scans were acquired for a single phased array. The average values of these scans were compared to k -space and Rayleigh-Sommerfeld simulation results.

Ex vivo hyperthermia evaluations of the probe were made using Fleuroptic® thermometry and a switching feedback controller. Figure 5 shows the setup for the hyperthermia experiments. A personal computer used as a switching temperature controller was connected via an RS 232 serial port to the digital power amplifier (UDS 2050PA, Advanced Surgical Systems, Inc., Tucson, Arizona) and to the Fleuroptic thermometer system (Luxtron 3100 Fleuroptic thermometer, Luxtron Corp., Mountain View, CA). The ultrasound transrectal probe was coupled to a bovine *ex vivo* sample using an inflated water bolus on top of the face of the array. The transducer was connected to the driving power amplifier. Water hoses were connected to a water pump via a bubble trap chamber and air hoses were connected to an air pump. A 20 gauge needle catheter

located the fiber optic thermometer probe inside the *ex vivo* tissue sample in the focal volume of the phased array. Temperature values inside the bovine tissue were read directly from the Luxtron system by the switching controller computer via the RS 232 serial port. Depending on feedback temperature values, the switching controller adjusted the driving power of each ultrasound channel by signaling the power amplifier system on and off. The temperature was made to rise from 37°C to 43°C and was maintained for 30 minutes. For two driving power levels (5 and 10 W), the results of seven experiments were averaged and were plotted including the standard deviation error bars for the period of the experiment using MATLAB® software (MathWorks Inc., Natick, MA). These hyperthermia experiments resembled the required clinical thermal dose (43°C for 30 minutes) for cancer treatment purposes.

3. Results

3.1 Simulation results using the *k*-space method

Figure 6a shows a two-layered gray-scale image of both the normalized pressure squared distribution and the absorption variations for the sagittal central slice of the modified 3D prostate model. The dimensions of this slice are 64 x 64 mm. The white colored layer surrounding the slice represents the tapered absorption boundary layer. It prevents the reflection and wrapping of the ultrasound waves at the boundaries. The phased array is located 5 mm away from the absorbing boundary layer. It is coupled to the rectal wall through the water medium. The pressure squared distribution is represented by the white colored waves on top of the absorption gray-scale distribution. Inhomogeneous tissue composition through the rectal wall causes irregularity of the focused beam. The acoustic energy is focused inside the prostate gland 40 mm away from the phased array. The phased array, the water medium, the rectal wall, the prostate gland, and the pressure focal region are labeled in the figure. Figure 6b shows the same arrangement as in Fig. 6a but with steering the focused ultrasound beam towards the boundaries of the prostate gland. The

inhomogeneous composition of the targeted region enhances the distribution of the focal region. Compared to the axial focused beam (Fig. 6a), the steered beam is covering larger area. This phenomenon improves the hyperthermia treatment by heating larger volumes at once. The grating lobe levels are -5 dB, -10 dB, -15 dB for selected steering angles of 14.5°, 7.2° and 0.0°, respectively. These angles represent Cartesian focal points of ($x = 0.0$ mm, $y = \pm 10.0$ mm, $z = 40.0$ mm), ($x = 0.0$ mm, $y = \pm 5.0$ mm, $z = 40.0$ mm), and ($x = 0.0$ mm, $y = 0.0$ mm, $z = 40$ mm), respectively.

3.2 Exposimetry results compared to simulation results

Figure 7a shows the normalized pressure distributions of a line that crosses the focal point in the y-direction. The mean exposimetry results are compared to the Rayleigh-Sommerfeld, k -space in water medium, and k -space in prostate model simulations. Compared to simulation results, the exposimetry results show elevated pressure distributions of side lobes (less than -6dB). These are due to slight misalignment of both the probe and the hydrophone during the exposimetry testing. The measured -3dB width of the focal volume in the y-direction is 2.0 ± 0.50 mm. Close agreement of exposimetry results in the y-direction compared to simulation results of Rayleigh-Sommerfeld, k -space in water medium and k -space in the prostate model are evident. Figure 7b shows another comparison of linear axial scans (z-direction) of the normalized pressure values crossing the focal volume. The k -space simulation in the prostate model shows that the inhomogeneous tissue structure of the rectal wall and the prostate gland cause focusing aberration and elevation of the pressure values (< -3 dB) within the nearfield region compared to exposimetry and other simulations. Rapid decrease in the pressure values of the k -space prostate simulation is due to the relatively high absorption values. Figure 2c shows that this axial line mostly composed of connective tissue with absorption values of 110 dB/m. Both exposimetry results and k -space water simulation results show good agreement within 9%. Rayleigh-Sommerfeld simulation show deviation of the results compared to the k -space simulations and exposimetry results. This deviation

is due to performing the calculations of the pressure values without the inclusion of absorption effects. Table 2 summarizes the -3dB widths of the focal volume of exposimetry results and the different simulation methods.

Temperature simulation results for two perpendicular lines that cross the focal volume in the y and z directions are shown in Figure 8. Fig. 8a shows temperature elevation distribution in the y-direction. Compared to the temperature at the focal point, a negligible temperature increase of the side lobes is noticed for the Rayleigh-Sommerfeld and *k*-space simulations. The simulated temperature distribution of the extracted exposimetry distribution shows only 1°C increase by the side lobes compared to 6°C at the focal point. Figure 8b shows the temperature simulation results in the z-direction line. Due to the inhomogeneous composition of the rectal wall and the prostate gland, the temperature of the rectal wall is elevated by 2°C compared to 6°C at the focal point. Homogenous simulations and measured exposimetry results show an increase of 1°C in the nearfield area.

Figure 9a shows the *ex vivo* hyperthermia results of the probe using maximum power level of 10 W per element. The temperature is raised from 37°C to 43°C in 7.3 ± 0.4 minutes and maintained steady at $43.1 \pm 0.16^\circ\text{C}$ for thirty minutes. The continuous line represents the mean value of seven hyperthermia trials, in which discrete temperature values every two seconds are read from the Luxtron® thermometer for thirty minutes. The standard deviation error bars of the hyperthermia trials are plotted on discrete points of 30 seconds intervals, for clarity purposes. Figure 9b illustrates another *ex vivo* hyperthermia results using maximum power level of 5 W per element. The rise time is 12.7 ± 1.50 minutes and the steady state temperature is $43.0 \pm 0.04^\circ\text{C}$. From the previous results, the rise time is reduced by a factor of two when the power level is increased by the same factor.

4. Discussion

The phased array design presented here is capable of focusing acoustic energy deep inside the prostate gland in the propagation direction and is capable of steering the pressure in the azimuth direction. This design intentionally spreads the focal volume in the elevation direction of the array for better uniform heating in the length of the array. Cascading four individual linear arrays together provides enhanced distribution of heat along the length of the array which in turn helps heating the prostate gland and the adjacent seminal vesicles. The dimensions of each sub-array depend on the size of the prostate gland and the rectum. The transrectal housing reduces patient discomfort by having a smaller, cylindrical-shaped non-penetrating portion that decreases the opening of the anus during the treatment. The diameter of the penetrable part of the probe (26 mm) also guarantees less damage and less discomfort. The length of the penetrable part, which is about 10 cm, can be easily reduced, if desired, by either cascading three 1D arrays together or by reducing the diameter of the spherically shaped front and rear of this part. Reducing the number of sub-arrays will not greatly affect the thermal effectiveness of the therapy since the prostate length is approximately 37 mm in the elevation direction along the axis of the probe. The inclusion of a water circulation system within a latex membrane provides effective coupling to and cooling of the rectal wall. The double-layered acoustical matching layers provide good transmission efficiency and at the same time offer an advantageous mounting method for the diced elements.

Exposimetry and simulations results were compared by measuring the -3dB widths of the produced focal volume. Table 2 summarizes these distances while focusing the energy 40 mm away from the face of the transducer for averaged exposimetry results and different simulation results. These simulations are the k -space simulation with the inhomogeneous prostate model, the k -space simulation in a watery medium, and the conventional Rayleigh-Sommerfeld simulation method in a homogenous watery medium. Good agreement between exposimetry results and k -space simulation results is evident. This agreement emphasizes the importance and the accuracy of the k -space method in predicting the pressure wavefields. Comparison of the previously described simulation

and exposimetry results is also shown in Fig. 7. This figure plots the linear normalized pressure distribution in the propagation direction through the focal point for exposimetry results and different simulation results. Due to the inhomogeneous composition of the prostate gland, the k -space results report pressure level variation at the boundary between the rectum and the glandular tissue.

Five main goals were achieved in this study. These include the creation of a three-dimensional anatomically accurate acoustical model of the human prostate gland region, the usage of the k -space computational method for ultrasound wave propagation through the created model, the design of a novel 4 x 20 element planar phased ultrasound array which relies on the k -space simulations and the acoustic model, the fabrication of an MRI compatible transrectal probe for hyperthermia treatment of prostate cancer, exposimetry testing of the probe utilizing an in-house automated exposimetry system, and *ex vivo* controlled hyperthermia evaluation. Regarding the prostate model, the acoustical conversion of the optical parameters of each pixel of the photographic data proved to be accurate for the whole three dimensional model. It discriminates each soft tissue (fat, muscle, connective and glandular tissues) in good agreement with the standard acoustical reported values. The k -space computational method is helpful in simulating ultrasound propagation through coarse-grid, large-scaled, three-dimensional acoustical models. It accounts for tissue inhomogeneity and absorption parameters, and provides a better tool than many conventional computational approaches.

Bibliography

- [1] Jemal, A., Tiwari, R. C., Murray, T., Ghafoor, A., Samuels, A., Ward, E., Feuer, E. J., and Thun, M. J., "Cancer statistics, 2004," *CA Cancer J Clin.*, vol. 54, no. 1, pp. 8-29, Jan.2004.
- [2] Seegenschmiedt, M. and Saur, R., *Interstitial and intracavitary thermoradiotherapy* Berlin: Springer-Verlag, 1993.
- [3] Seegenschmiedt, M., Fessenden, P., and Vernon, C., *Principles and practices of thermoradiotherapy and thermochemotherapy* Berlin: Springer-Verlag, 1995.
- [4] Stauffer, P., Diederich, C., and Seegenschmiedt, M., "Interstitial heating technologies," in Seegenschmiedt MH, Fessenden P, and Vernon CC (eds.) *Principles and practices of thermoradiotherapy and thermochemotherapy* Berlin: Springer-Verlag, 1995, pp. 279-320.
- [5] Dewey, W., Hopwood, L., Sapareto, S., and Gerweck, L., "Cellular Response to combinations of hyperthermia and radiation," *Radiation Biology*, vol. 123 pp. 463-479, 1976.
- [6] Sneed, P. K. and Phillips, T. L., "Combining hyperthermia and radiation: how beneficial?," *Oncology (Huntingt)*, vol. 5, no. 3, pp. 99-108, Mar.1991.
- [7] Bornstein, B. A., Zouranian, P. S., Hansen, J. L., Fraser, S. M., Gelwan, L. A., Teicher, B. A., and Svensson, G. K., "Local hyperthermia, radiation therapy, and chemotherapy in patients with local-regional recurrence of breast carcinoma," *Int J Radiat Oncol Biol Phys*, vol. 25 pp. 79-85, 1993.
- [8] Overgaard, J., Gonzalez, G. D., Hulshof, M. C., Arcangeli, G., Dahl, O., Mella, O., and Bentzen, S. M., "Hyperthermia as an adjuvant to radiation therapy of recurrent or metastatic malignant melanoma. A multicentre randomized trial by the European Society for Hyperthermic Oncology," *Int.J.Hyperthermia*, vol. 12, no. 1, pp. 3-20, Jan.1996.
- [9] van Vulpen, M., de Leeuw, A. A. C., Raaymakers, B. W., van Moorselaar, R. J. A., Hofman, P., Lagendijk, J. J. W., and Battermann, J. J., "Radiotherapy and hyperthermia in the treatment of patients with locally advanced prostate cancer: preliminary results," *Bju International*, vol. 93, no. 1, pp. 36-41, Jan.2004.
- [10] Saleh, K. Y. and Smith, N. B., "Two-dimensional ultrasound phased array design for tissue ablation for treatment of benign prostatic hyperplasia," *International Journal of Hyperthermia*, vol. 20, no. 1, pp. 7-31, Feb.2004.
- [11] Saleh, K. and Smith, N., "Design and evaluation of a 3 x 21 element 1.75 dimensional tapered ultrasound phased array for the treatment of prostate disease," *Materials Research Innovations*, 2004.
- [12] Curiel, L., Chavrier, F., Souchon, R., Birer, A., and Chapelon, J. Y., "1.5-D high intensity focused ultrasound array for non-invasive prostate cancer surgery," *Ieee Transactions on Ultrasonics Ferroelectrics and Frequency Control*, vol. 49, no. 2, pp. 231-242, Feb.2002.
- [13] Tan, J. S., Frizzell, L. A., Sanghvi, N., Wu, S. J., Seip, R., and Kouzmanoff, J. T., "Ultrasound phased arrays for prostate treatment," *J Acoust.Soc Am.*, vol. 109, no. 6, pp. 3055-3064, June2001.

- [14] Diederich, C. J. and Hynynen, K., "The feasibility of using electrically focused ultrasound arrays to induce deep hyperthermia via body cavities," *IEEE Trans Ultrason Ferroelectr Freq Contr*, vol. 38 pp. 207-219, 1991.
- [15] Buchanan, M. T. and Hynynen, K., "Design and experimental evaluation of an intracavitary ultrasound phased array system for hyperthermia," *IEEE Trans Biomed Eng*, vol. 41, no. 12, pp. 1178-1187, Dec.1994.
- [16] Zemanek, J., "Beam behavior within the nearfield of a vibrating piston," *J Acoust Soc Am*, vol. 49 pp. 181-191, 1971.
- [17] Hutchinson, E. B. and Hynynen, K., "Intracavitary phased arrays for non-invasive prostate surgery," *IEEE Trans Ultrason Ferroelectr Freq Contr*, vol. 43 pp. 1032-1042, 1996.
- [18] Mast, T. D., Souriau, L. P., Liu, D. L., Tabei, M., Nachman, A. I., and Waag, R. C., "A k-space method for large-scale models of wave propagation in tissue," *IEEE Trans.Ultrason.Ferroelectr.Freq.Control*, vol. 48, no. 2, pp. 341-354, Mar.2001.
- [19] Tabei, M., Mast, T. D., and Waag, R. C., "A k-space method for coupled first-order acoustic propagation equations," *J.Acoust.Soc.Am.*, vol. 111, no. 1 Pt 1, pp. 53-63, Jan.2002.
- [20] Oppenheim, A. V., Schafer, R. W., and Buck, J. R., *Discrete-time signal processing*, second edition ed. New Jersey: Prentice-Hall, Inc., 1998.
- [21] Witte, D. C. and Richards, P. G., "The pseudospectral method for simulating wave propagation," in Lee, D., Cakmak, A., and Vichnevetsky, R. (eds.) *Computational acoustics* New York: North-Holland, 1990, pp. 1-18.
- [22] Twizell, E. H., *Computational methods for partial differential equations* New York: Ellis Horwood Limited, 1984.
- [23] Mast T.D., "Two- and three-dimensional simulations of ultrasonic propagation through human breast tissue," *Acoustics Research Letters Online*, vol. 3, no. 2, 2001.
- [24] Mast T.D., "Empirical relationships between acoustic parameters in human soft tissues," *Acoustics Research Letters Online*, vol. 1, no. 2, pp. 37-42, 2000.
- [25] Maurieb E.N., *Human anatomy & physiology*, 5th edition ed. New York: Addison Wesley Longman, 1999.
- [26] Mast, T. D., Hinkelman, L. M., Metlay, L. A., Orr, M. J., and Waag, R. C., "Simulation of ultrasonic pulse propagation, distortion, and attenuation in the human chest wall," *J.Acoust.Soc.Am.*, vol. 106, no. 6, pp. 3665-3677, Dec.1999.
- [27] Pennes, H. H., "Analysis of tissue and arterial blood temperatures in the resting human forearm," *Journal of applied physiology*, vol. 1 pp. 93-122, 1948.
- [28] Ronald E McKeighen, "Design guidlines for medical ultrasonic arrays," *SPIE International Symposium on Medical Imaging*, 1998.
- [29] AIUM/NEMA, "Safety standard for diagnostic for ultrasound equipment," *Journal of Ultrasound in Medicine*, vol. 2 pp. S1-S50, 1983.

- [30] Pierce, A. D., *Acoustics: An Introduction to Its Physical Principles and Applications* Melville, NY: Acoustical Society of America, 1989.
- [31] ICRU, I. C. o. R. U. a. M., *Tissues Sustitutes, Pahntoms and Computation Modelling in Medical Ultrasound* Bethesda: ICRU, 1999.
- [32] ICRU, I. C. o. R. U. a. M., *Tissue Substitutes, Phantoms, and Computational Modelling in Medical Ultrasound* Bethesda: Maryland Report 61, 1998.
- [33] Kinsler, L., Frey, A., Coppins, A., and Sanders, J., *Fundemantals of Acoustics*, 4 ed. 2000.

Figure 1: From the Visible Human Project®, a photographic image of a prostate slice showing a transverse (axial, yz-plane) cross section of the prostate gland.

Figure 2: Three sets of acoustical mapping of the photographic data in Fig. 1 are generated for (b) sound speed variations, (c) density values, and (d) absorption parameters. The color bars relate the acoustical values (sound speed (m/s), density (kg/m^3), and absorption (dB/m)) to the soft tissue distribution through the selected slice.

Figure 3: A gray scaled image showing a background layer of the absorption distribution through the middle slice of the 3D prostate model. The tapered absorption boundary layer is shown at the edges with a sharp white color. A black dotted line is surrounding the image to distinguish the absorption layer. A spherically propagated wave is shown on top of this background image showing the wave propagation from left to right through the 3D prostate model. The scattered wave is shown following the three cycles wave that has a frequency of 1.2 MHz. Due to sound speed and density changes through this model the wave front is shown with an irregular shape while propagating through the urethra area.

Figure 4: Three diagrams and a photograph showing the transrectal intracavitary ultrasound probe in (a) expanded coronal view (xy-plane), (b) sagittal (xz-plane), (c) coronal (xy-plane), and (d) an actual photograph of the probe with the inflated bolus.

Figure 5: The hyperthermia setup showing the switching controller, the fleuroptic thermometer, the power amplifier, and the transrectal probe.

Figure 6: Gray scaled images showing the normalized pressure squared distribution results of a single segment of the hyperthermia phased array using the k -space computational method. These

results are shown for the central transverse plane of the 3D prostate model. Two-layered gray scale image for the central plane showing a background layer of the absorption distribution and the normalized squared pressure distribution on top of it while focusing (a) axially 40 mm away from the face of the array and (b) focusing off axis at $y = -10$ mm.

Figure 7: Normalized pressure distribution in linear scans through the focal point in the (a) y-direction and (b) z-direction for results of exposimetry averaged tests, Rayleigh-Sommerfeld simulations, k -space simulations in both water and inhomogeneous prostate media.

Figure 8: Linear temperature distributions through the focal point for exposimetry and simulation results in the (a) y-direction, (b) z-direction.

Figure 9: *Ex vivo* controlled hyperthermia results using fleuroptic thermometry for driving electrical powers of (a) 10 W per element and (b) 5 W per element.

Figure 1

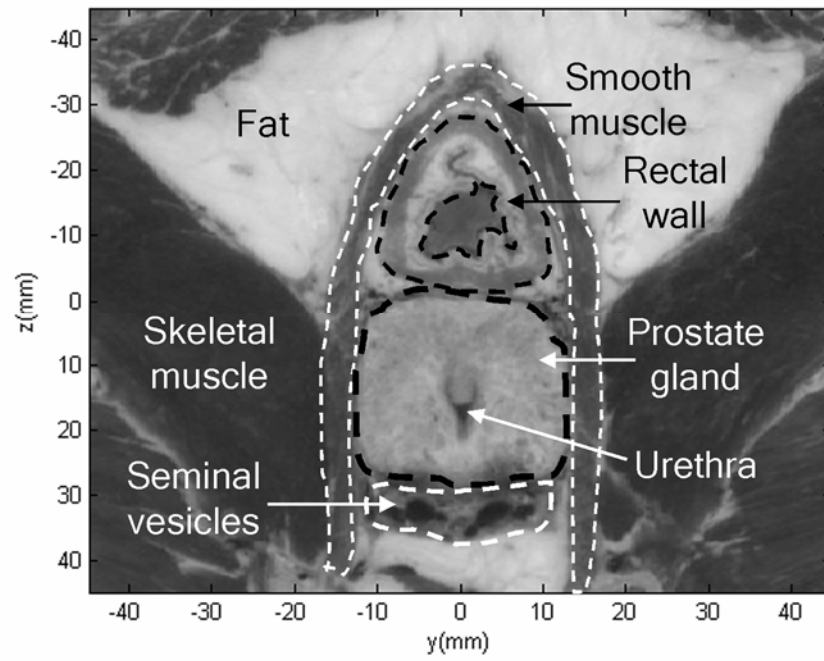


Figure 2a

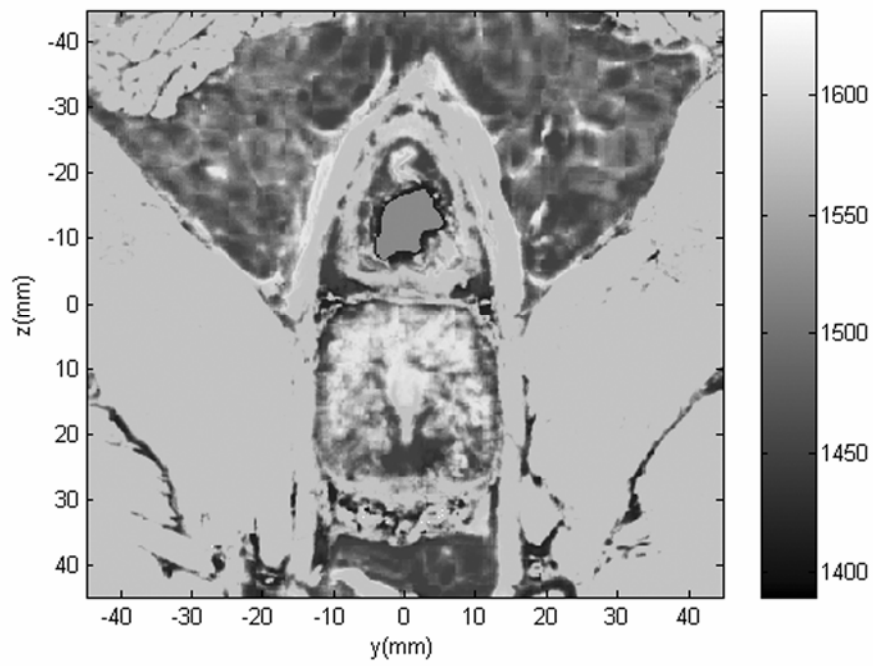


Figure 2b

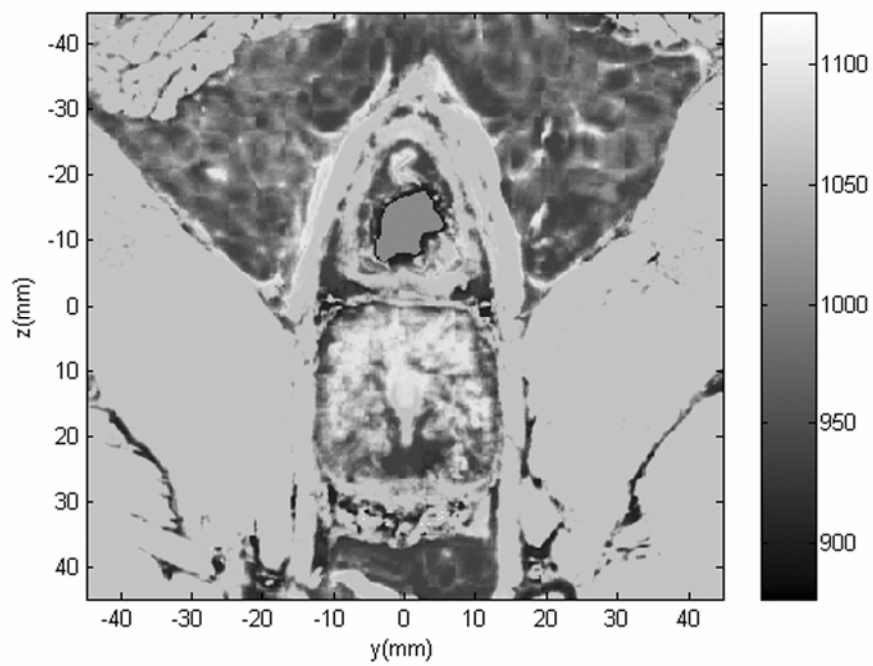


Figure 2c

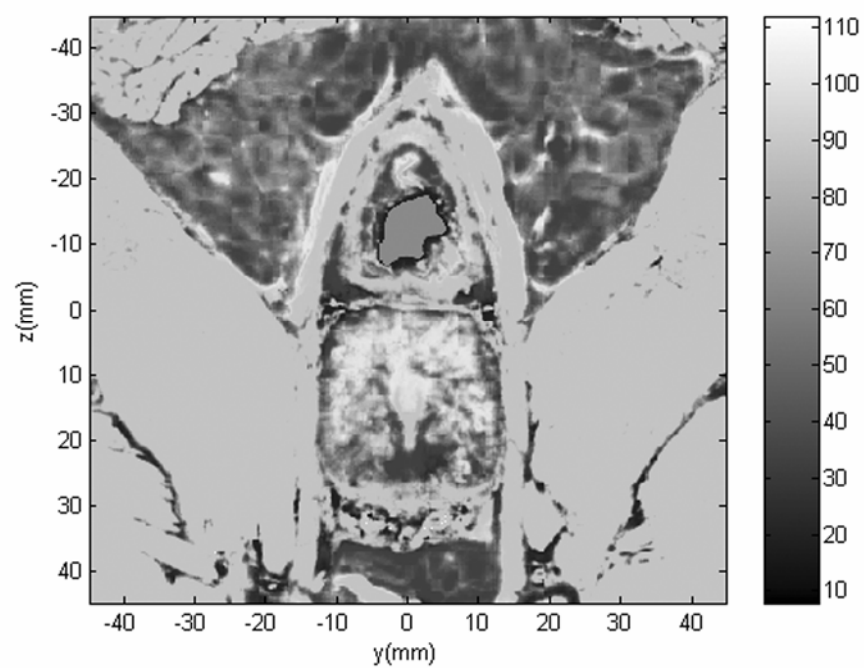


Figure 3

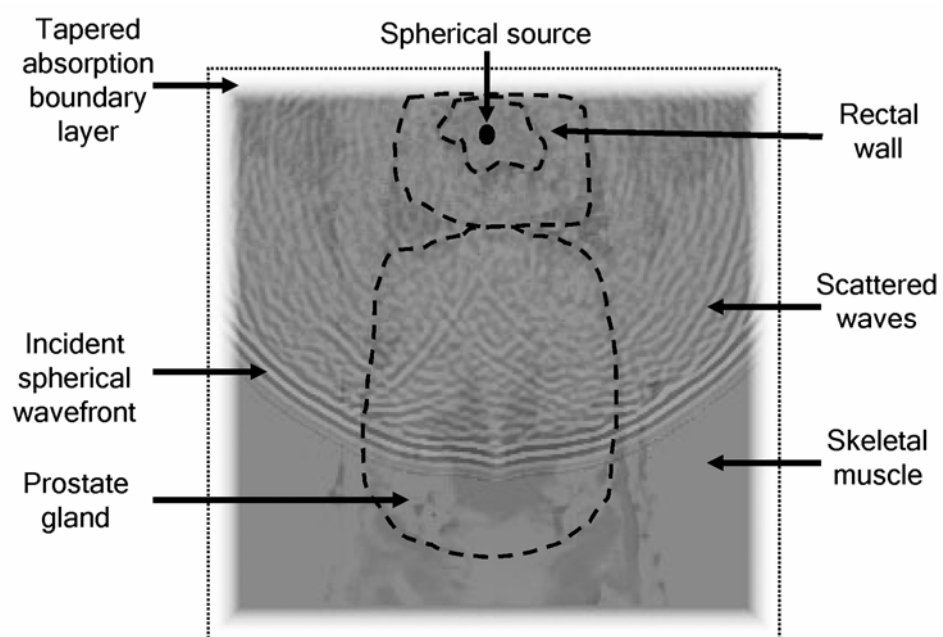


Figure 4

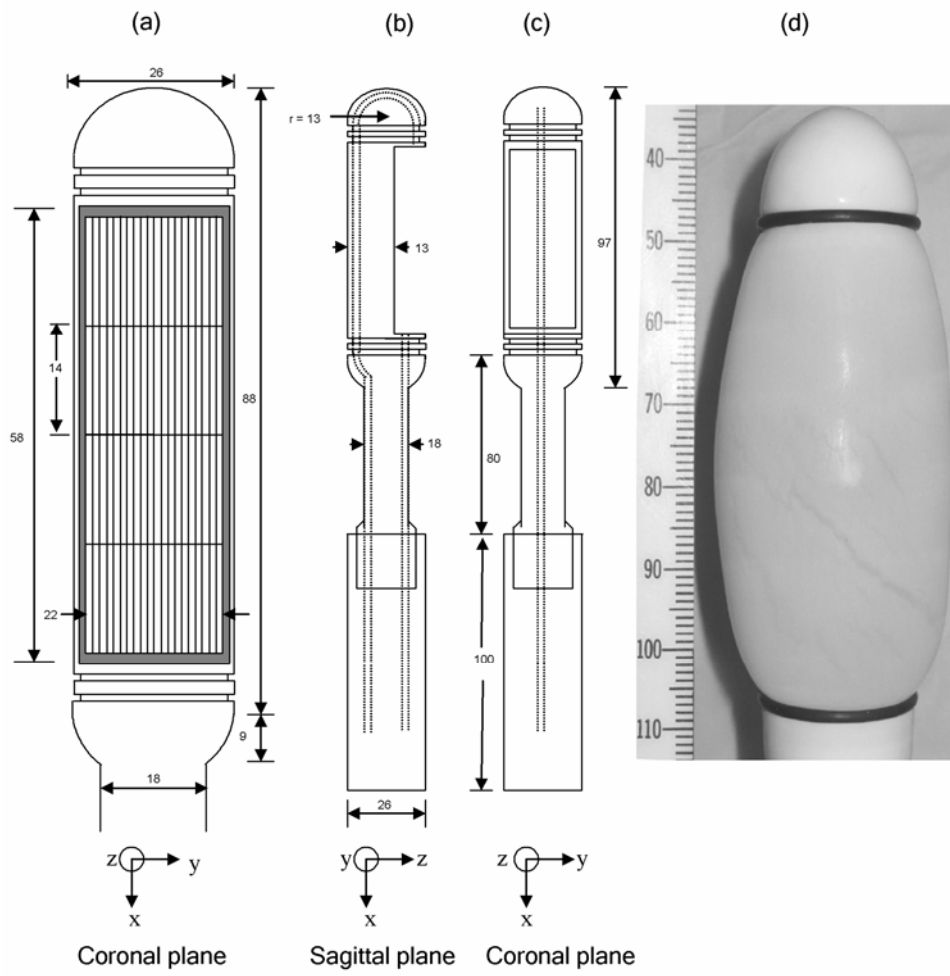


Figure 5

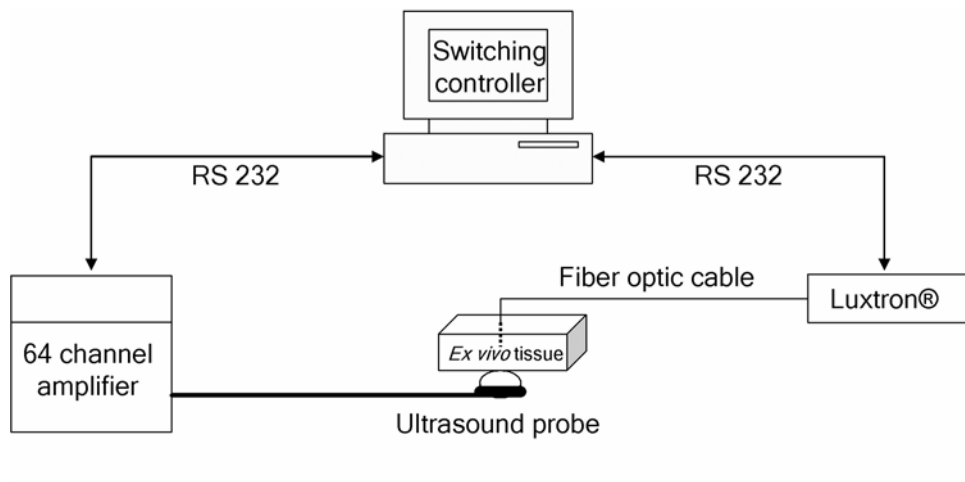


Figure 6a

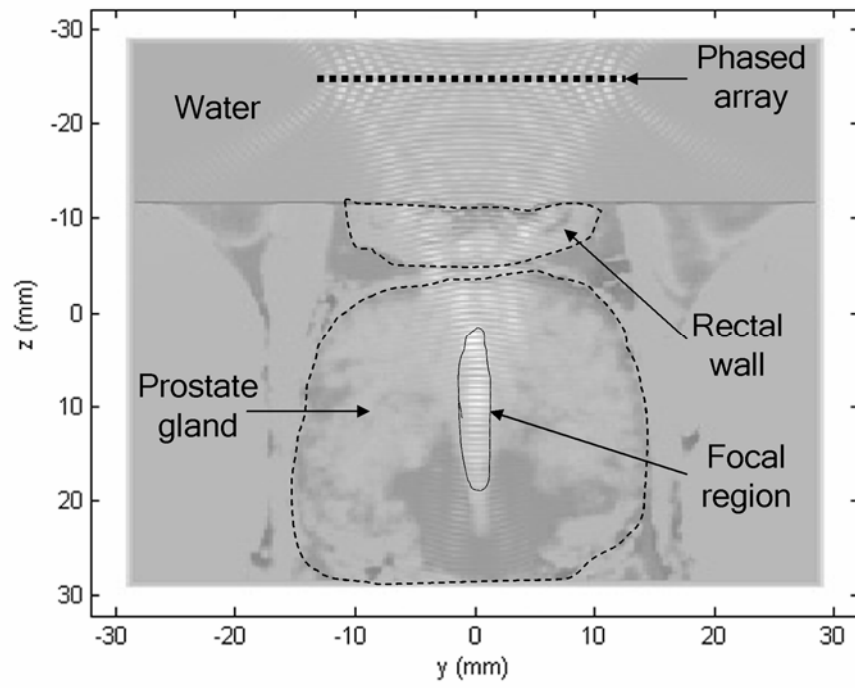


Figure 6b

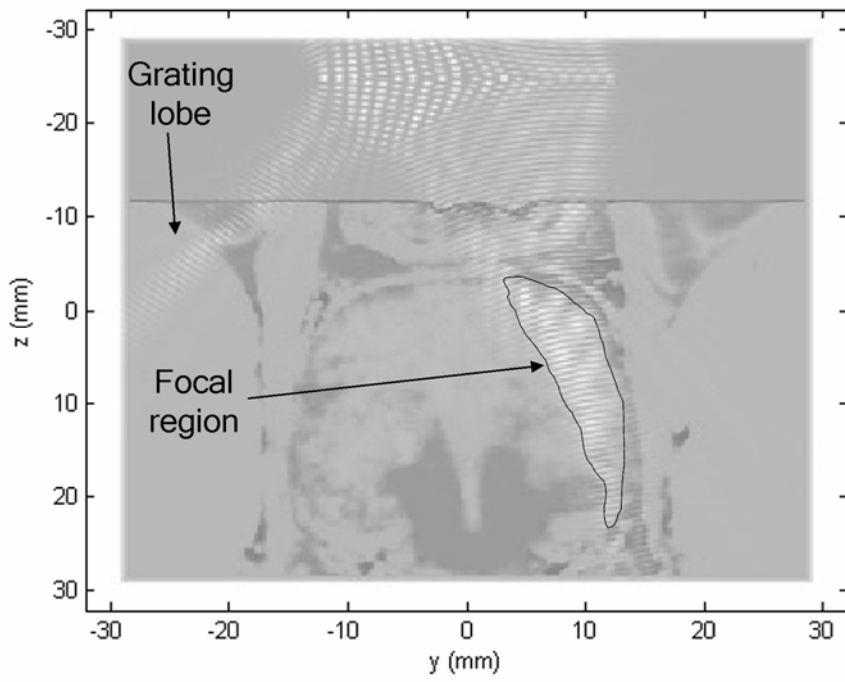


Figure 7a

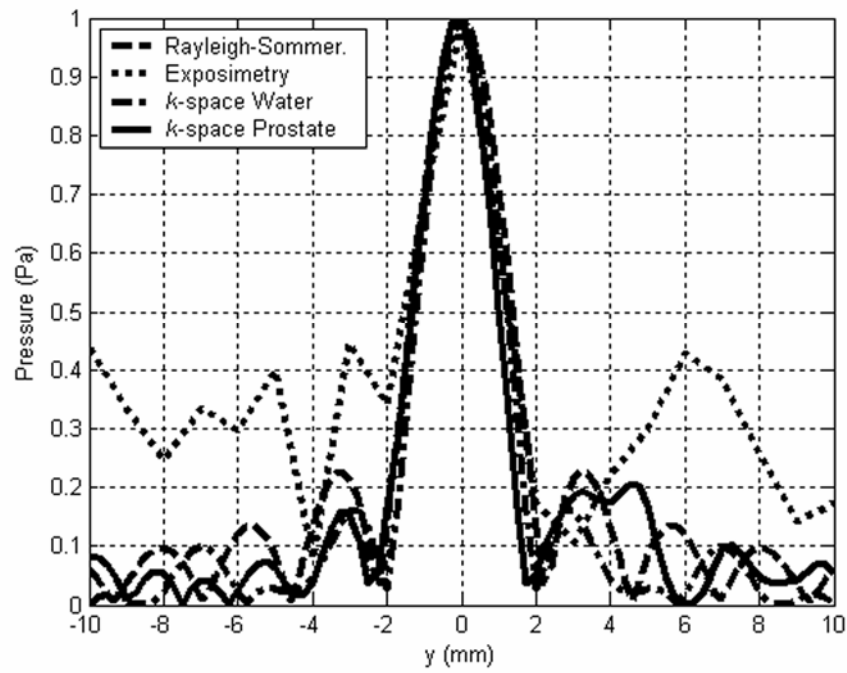


Figure 7b

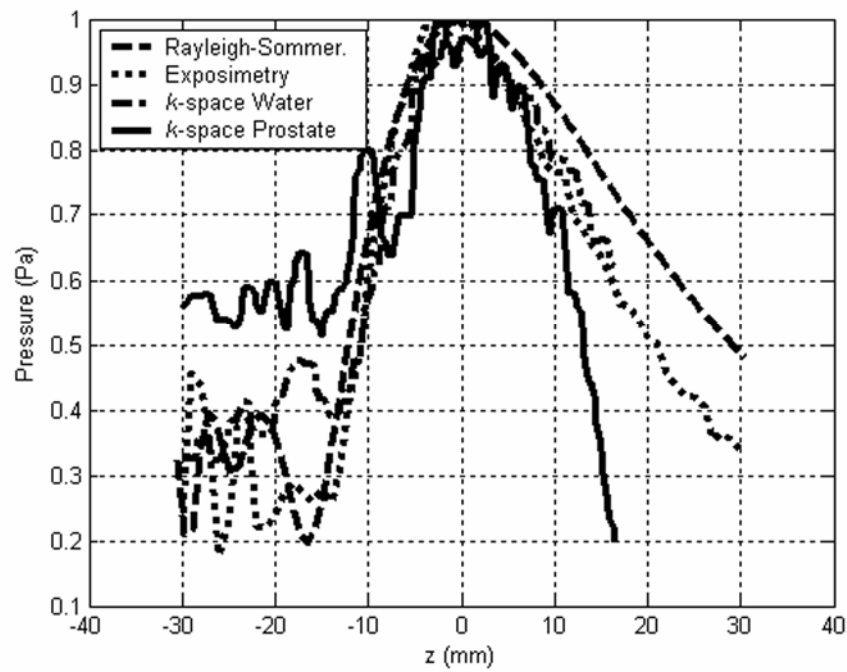


Figure 8a

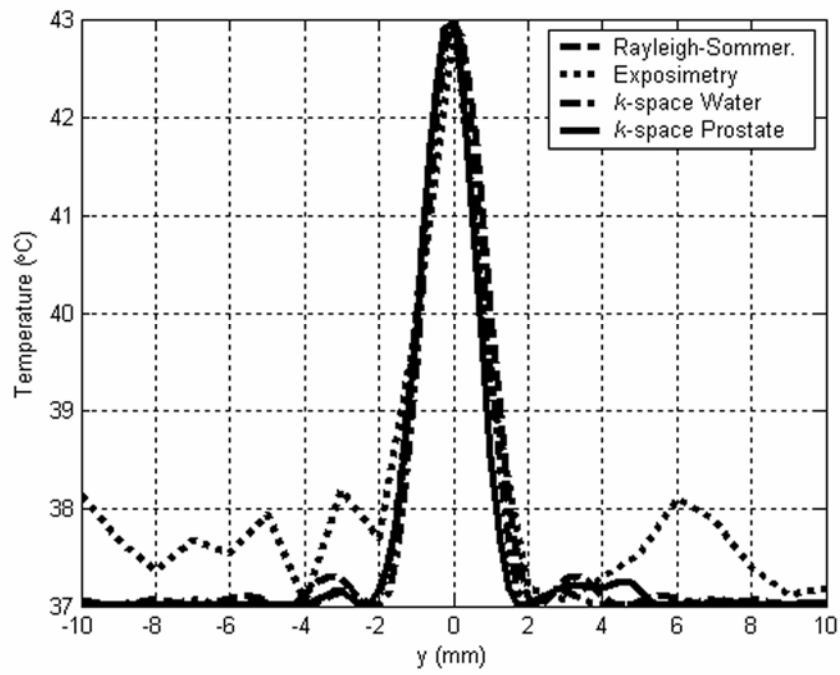


Figure 8b

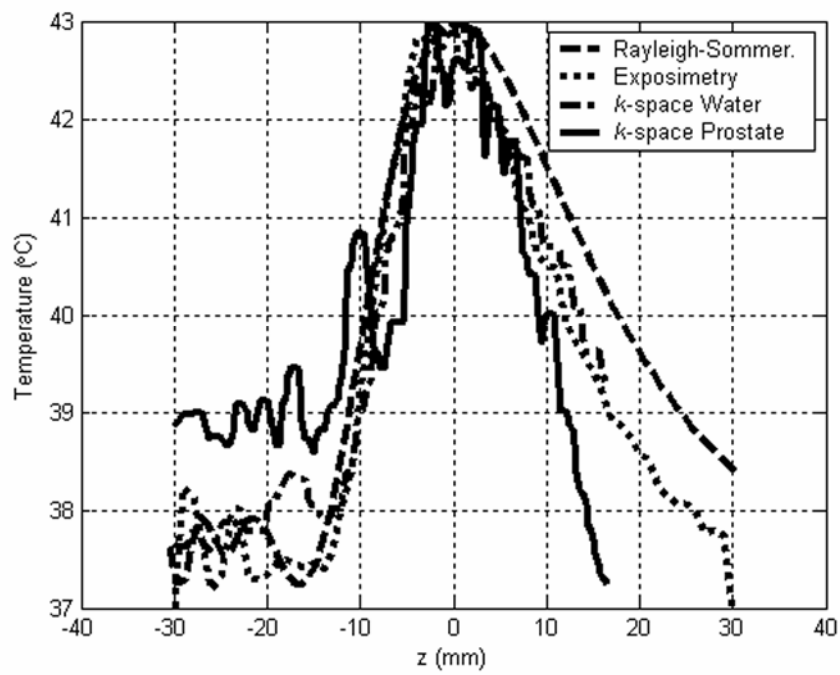


Figure 9a

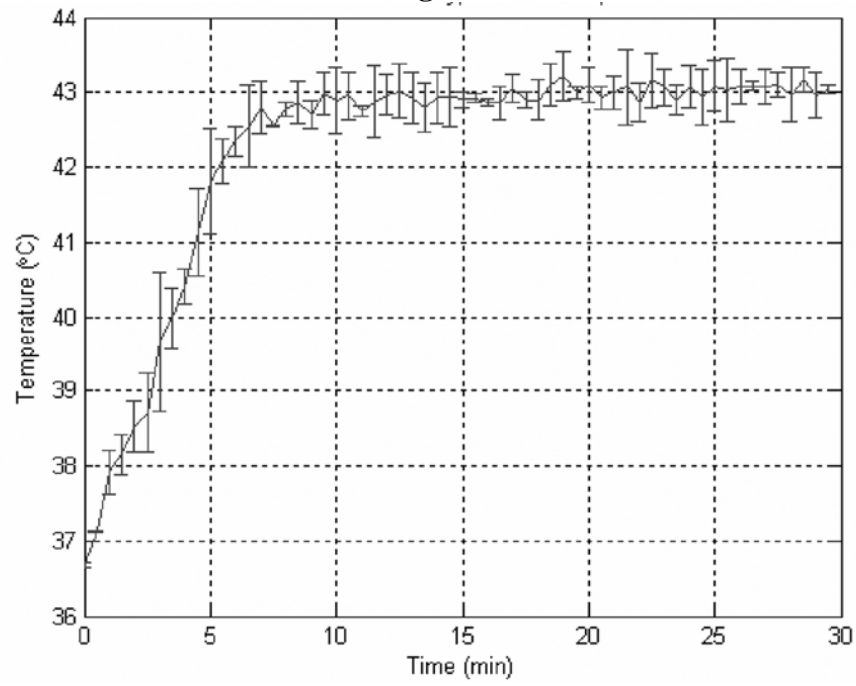


Figure 9b

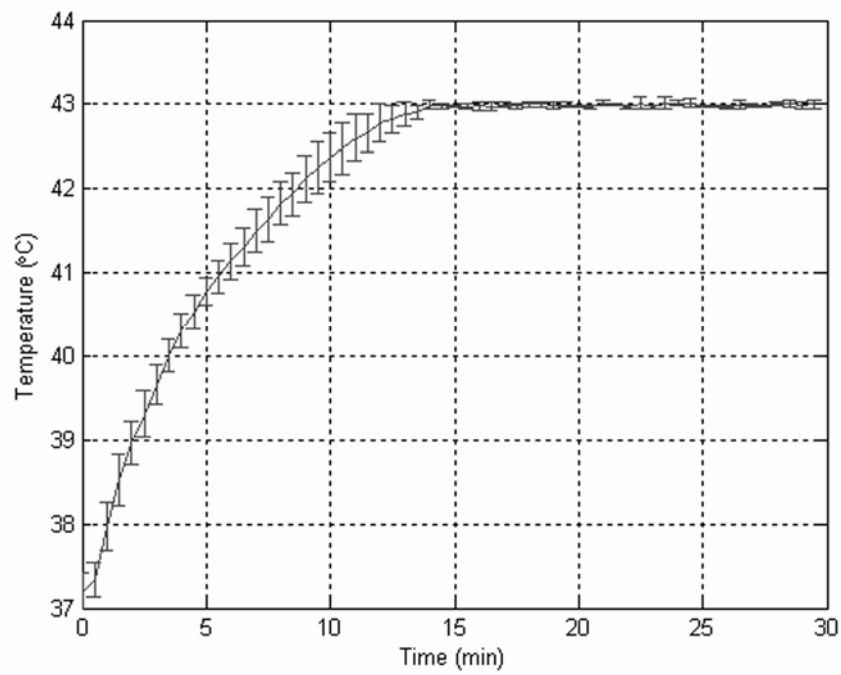


Table 1: Acoustical parameters (sound speed, density and absorption) of connective tissue, muscle, fat and water at 37°C and 1.2 MHz. Extrapolation of the absorption value of connective tissue arose from an assumed linear relation between sound speed and absorption for muscle and fat.

Tissue type	Sound speed (m/s)	Density (kg/m ³)	Absorption @ 1.2 MHz (dB/m)
Connective	1613 [*]	1120 [†]	103
Muscle	1580 [¶]	1050 [¶]	88.8 [‡]
Fat	1450 [¶]	950 [¶]	34 [‡]
Water	1524 [‡]	992 ^ψ	0.3 [‡]

^{*}[26], [†][30], [¶][31], [‡][32], [‡][33], ^ψ[30]

Table 2: Summary of the -3 dB distances of focal volume of a single segment of the hyperthermia phased array while focusing axially 40 mm away from the face of the transducer.

Type	-3 dB distances of the focal volume (mm)	
	y-direction	z-direction
Exposimetry measurement	2.0 ± 0.50	19.8 ± 0.41
<i>k</i>-space simulation in prostate model	2.0	22.0
<i>k</i>-space simulation in watery medium	2.0	20.0
Rayleigh-Sommerfeld simulation	2.0	28.0

MR thermometry verification of a hyperthermia ultrasound array designed using the *k*-space computational method

Osama M. Al-Bataineh¹, Christopher M. Collins², Eun-Joo Park^{1, §}, Hotaik Lee³ and Nadine Barrie Smith^{1,3}

¹Department of Bioengineering, The Pennsylvania State University, University Park, PA 16802, USA

²Department of Radiology, The Pennsylvania State University, Hershey PA 17033, USA

³Graduate Program in Acoustics, The Pennsylvania State University, University Park, PA 16802, USA

[§]Corresponding author

Email addresses:

OMA: omabio@engr.psu.edu

CMC: cmcollins@psu.edu

EJP: eup114@psu.edu

HL: hzl118@psu.edu

NBS: nbs@engr.psu.edu

Abstract

Background

Ultrasound induced hyperthermia is a useful adjuvant to radiation therapy in the treatment of prostate cancer. A uniform thermal dose (43°C for 30 minutes) is required within the targeted cancerous volume for effective therapy. This requires specific ultrasound phased array design and appropriate thermometry method. Inhomogeneous, acoustical, three-dimensional (3D) prostate models and economical computational methods provide necessary tools to predict the appropriate shape of hyperthermia phased arrays for better focusing and steering. This research utilizes the *k*-space computational method and a 3D human prostate model to design an intracavitary ultrasound probe for hyperthermia treatment of prostate cancer. Evaluation of the fabricated probe includes *ex vivo* and *in vivo* controlled hyperthermia experiments using the noninvasive magnetic resonance imaging (MRI) thermometry.

Methods

A 3D acoustical prostate model was created depending on photographic data from the Visible Human Project®. The *k*-space computational method was used on this coarse grid and inhomogeneous tissue model to simulate the steady state pressure wavefield of the designed phased array using the linear acoustic wave equation. To insure the uniformity and spread of the pressure in the length of the array, and the steering and focusing capability in the width of the array, the equally-sized elements of the 80 elements phased array were 1 x 14 mm. Noninvasive MRI thermometry and a switching feedback controller were used to accomplish *ex vivo* and *in vivo* hyperthermia evaluations of the fabricated probe.

Results

Both exposimetry and *k*-space simulation results demonstrated good agreement within 9%. With a desired temperature plateau of 43.0°C, *ex vivo* and *in vivo* controlled hyperthermia experiments showed that the MRI temperature at the steady state was $42.9 \pm 0.38^\circ\text{C}$ and $43.1 \pm 0.80^\circ\text{C}$, respectively, for 20 minutes of heating.

Conclusions

Unlike conventional computational methods, the *k*-space method provides powerful tool to predict pressure wavefield and temperature rise in sophisticated, large scale, 3D, inhomogeneous and coarse grid tissue models. Noninvasive MRI thermometry validated this probe and the feedback controller in an actual *in vivo* hyperthermia treatment of canine prostate.

Background

Prostate cancer causes approximately 30,000 deaths among Americans every year with more than 230,000 new patients in 2004 [1]. Most of the patients are elderly who can not withstand invasive surgical procedures to eradicate the tumor in

its early stages [2]. Radiation and hormone therapies are still the treatment of choice for these patients [3]. Thermal treatment, on the other hand, has proven effective for different kinds of tumors including prostate cancer. Hyperthermia therapy raises the temperature of the tumor and a surrounding margin of normal tissue from the normal body temperature of 37°C to 42-45°C for about 30 minutes [4;5;6]. This type of treatment has had success, in conjunction with radiation therapy, in enhancing the cytotoxic effect of the radiation therapy [7;8;9;10]. Noninvasive ultrasound intracavitary hyperthermia technology is an accepted thermal treatment for prostate cancer [11].

Many, previous simulation and design studies of intracavitary ultrasound phased arrays have not considered anatomically realistic human prostate models [12;13;14;15]. Preceding intracavitary ultrasound hyperthermia phased arrays used small cylindrical radiators to conform to the natural contours of large body orifices [16;17]. Simulations of previous hyperthermia and high intensity focused ultrasound (HIFU) phased arrays were accomplished using the Rayleigh-Sommerfeld integral over a set of a geometrically superimposed point sources [18]. Homogeneous water-like media were used to simulate pressure field distributions of these arrays [12;13;14;15;16;17]. Such simulations, however, do not capture the interaction of ultrasound with inhomogeneous tissue structures. Accurate modeling of ultrasound wave propagation in inhomogeneous three dimensions (3D) over large length scales has become feasible using the k -space computational method [19;20]. This method solves the spatial terms of the wave equation by Fourier transformation to the spatial frequency domain, while temporal iterations are performed using a nonstandard finite difference approach using the k - t space propagator (where k represents the spatial frequency domain and t represents the time domain) [19]. It provides much higher

accuracy than the pseudospectral methods, in which the spatial derivatives are evaluated globally by Fourier transformation and wavefields are advanced in time using second order accurate finite differences (leapfrog propagator) [21]. The k -space method maintains its highest accuracy up to a Courant-Friedrichs-Lewy number (CFL = $c_0\Delta t/\Delta x$, where c_0 is the sound speed; Δt is the temporal step; Δx is the spatial step) of about 0.4 [19]. However, the pseudospectral method [19] rapidly increases in error for CFL numbers above 0.1. For weak scattering media, the k -space method provides similar accuracy for time steps two to three times larger than those required by high order pseudospectral methods [19]. Compared to finite difference computations [22], in which both spatial and temporal second order partial derivatives are solved using second order finite difference computations, the k -space method achieves higher accuracy for much larger spatial step size. Equivalent accuracy is achieved employing only three points per minimum wave length using the k -space method compared to 14 points per minimum wavelength for the finite difference equation using the same accuracy criterion. For 3D calculations, this reduction in the spatial size reduces the storage requirements for the k -space computations compared to finite difference method by 98% [19].

Noninvasive magnetic resonance imaging (MRI) thermometry is helpful in monitoring and controlling hyperthermia treatment of the prostate gland [23;24;25;26]. It is important in this therapy to keep the temperature of the healthy tissue below the targeted temperature of the cancerous volume. A feedback control system is useful in maintaining the targeted tissue within the required thermal dose (43°C for 30 minutes) [27]. This research focuses on acoustical modeling of a 4 x 20 element hyperthermia phased array, exposimetry testing, and *ex vivo* and *in vivo* evaluation of the fabricated probe utilizing MRI thermometry.

Methods

The phased array design and the *k*-space acoustic modelling

Figure 1a shows a coronal view (xy-plane is the coronal plane; yz-plane is the transverse or axial plane; and xz-plane is the sagittal plane) of the 4 x 20 hyperthermia phased array in its intracavitary housing. The description of the housing of the phased array in Figs. 1a, b, and c will be discussed later. The array consists of four segments of planar phased arrays; each segment consists of 20 elements with a 1 x 14 mm sub-element dimension. This hyperthermia phased array enables focusing and steering of the pressure beam in the propagation and the azimuth directions and enables spreading of the focal region in the volume that faces the length of the array. Electronic phasing of the elements that make up each segment allows for steering of the beam in the azimuth direction and adjustment of the depth of focus in the propagation direction. The steering and focusing mechanisms permit varying the heating in the prostate gland to achieve uniform thermal dose to the targeted volume. Simulation of the exact pressure wavefield in the prostate gland requires building anatomically and acoustically accurate inhomogeneous human prostate model.

An anatomically and acoustically accurate 3D prostate model was created using actual photographic images from the Visible Human Project® library (U.S. National Library of Medicine, Bethesda, MD). Figure 2 shows a transverse (yz-plane) photographic slice of this model. It has 64 x 64 mm dimensions with a 0.25 mm grid size. The prostate gland, the rectal wall, the skeletal muscle, the fat tissue, and the added water-like medium in the rectum are marked and labeled in the figure. The optical parameters that define the fractional fat, connective, glandular and muscle soft tissues of each pixel were used to build a three-dimensional (3D) acoustical model.

The 3D photographic data permitted development of three sets of 3D acoustical data: sound speed, density and absorption parameters [19;28;29]. More details of the mapping procedure are presented elsewhere [30]. The prostate model was used to simulate the pressure distribution of the hyperthermia phased array by means of the k -space computational method.

The k -space method was used to study pressure beam formation of the designed phased array through the prostate model. The linear acoustic wave equation was used for the simulation:

$$\nabla \cdot \left(\frac{1}{\rho(x, y, z)} \nabla p(x, y, z, t) \right) - \frac{1}{\rho(x, y, z) c^2(x, y, z)} \frac{\partial^2 p(x, y, z, t)}{\partial t^2} = \frac{\alpha(x, y, z)}{\rho(x, y, z) c^2(x, y, z)} \frac{\partial p(x, y, z, t)}{\partial t}$$

where, $\nabla \cdot ()$ is the spatial divergence operator; $\nabla ()$ is the spatial gradient operator; $\rho(x, y, z)$ is the spatially dependent density (kg/m^3); $c(x, y, z)$ is the spatially dependent sound speed (m/s); $p(x, y, z, t)$ is the spatially and temporally dependent pressure (Pa); $\alpha(x, y, z)$ is the spatially dependent absorption coefficient (s^{-1} , the absorption in dB/m equals to $20 \times \log_{10}(e) \times \alpha(x, y, z)/(2c_0)$ [30]). All absorption effects (viscous, heat conduction and internal molecular processes losses) were represented by a single absorption coefficient which was equivalent to the inverse of a spatially dependent relaxation time [31]. The k -t propagator was used to solve for the propagation in the inhomogeneous prostate model after setting both initial and boundary conditions [19]. The dimensions of the model were $64 \times 64 \times 46$ mm with 0.25 mm spatial step size. It was composed of $257 \times 257 \times 185$ discrete points. The temporal step size was $0.082 \mu\text{s}$. A tapered absorption boundary layer, all around the model, was created to prevent wave wrapping from side to side and to prevent reflection of the waves at the boundaries. This layer is mathematically described elsewhere [30]. A single segment of the phased array was incorporated in the acoustical model for simulation purposes.

Virtual elements with 1 x 14 mm dimensions were integrated in the simulation. The established grid size of 0.25 mm for the model limited the effective kerf width of the array to this number. Each sub-element added to the overall virtual source that induced pressure to the surrounding media, depending on the acoustical parameters of each point of the model. All points that related to a specific element were driven temporally in a sinusoidal fashion with a 1.2 MHz frequency and a particular phase shift that compensated for its path length to a specific target.

Figure 3 shows an axial two-layered gray-scale image of both the *k*-space simulated normalized pressure squared distribution and the absorption variations of the previously shown slice in Fig. 2. The dimensions of the slice are 64 x 64 mm. The white colored boundaries of the image represent the tapered absorption layer. It prevents the reflection and wrapping of the ultrasound waves at the boundaries. The phased array is located 5 mm away from the absorbing boundary layer. It is coupled to the rectal wall through the water medium. The pressure squared distribution is represented by the white colored waves on top of the absorption gray-scale distribution. Inhomogeneous tissue composition through the rectal wall and the prostate gland causes irregularity of the focused beam. The acoustic energy is focused inside the prostate gland 40 mm away from the phased array.

Hyperthermia phased array fabrication and dosimetry testing

Figure 1a shows a coronal view of the diced phased array placed in the specialized Delrin® plastic transrectal housing. The actual dimension of each segment is 14 x 22 mm; while the dimension of the whole array is 56 x 22 mm. RHODORSIL® V-1022 (Rhodia Inc., Cranbury, NJ) water proof insulation silicone is used to bond and seal the array to its housing. The housing includes grooves to contain o-rings that hold the water bolus in place using a latex membrane, a pair of

brass tubes to circulate water in front of the array, another pair of brass tubes to circulate air in the cavity behind the array, and a 100 mm hollow cylindrical handle. The diameter of the penetrating cylindrical portion of the probe is 26 mm diameter x 100 mm length including the rounded front and rear. A smaller diameter cylindrical portion follows the penetrating section of the probe with dimensions of 18 mm diameter x 80 mm length. Figure 1b shows a sagittal view of the transrectal probe. The dotted parallel lines show the location of the brass tubes for the water circulation system. The penetrating part, that contains the phased array, is 97 mm length x 26 mm diameter; the following un-penetrating part is 70 mm length x 18 mm diameter. The handle is 100 mm length x 26 mm diameter. Figure 1c shows an actual photograph of the diced hyperthermia phased array. It was made of lead zirconate titanate (TRS300, TRS Ceramics, State College, PA) ferroelectric material. Two impedance matching layers were applied onto the ceramic to increase the acoustical transmission efficiency. The dicing cuts of the TRS300 material were all the way through its thickness but not through the matching layers. These cuts were done using a dicing saw (Model 780, K & S-Kulick and Soffa Industries, Willow Grove, PA) with a kerf width of 0.12 mm. Sixty, 28 American Wire Gauge (AWG), 32 ohm miniature magnetic resonance imaging (MRI) compatible coaxial cables (Belden Inc., St. Louis, MI), ten meters long formed a bundle that connected 60 elements of the array to the amplifier system. The central two segments of the hyperthermia phased array were electrically connected in parallel. Two brass tubes were used to circulate water in the front of the array using a latex membrane. This circulation system was essential for acoustic coupling between the probe and the tissue surrounding it, and for cooling of the TRS300 ceramic piece. A water pump (Cole-Parmer Instrument Company,

Barrington, IL) and a temperature controlled bath within the circulation system maintained the temperature and the flow of the circulated water.

The hyperthermia phased array system was tested using an in-house automated exosimetry system based on the American Institute of Ultrasound in Medicine and National Electrical Manufacturers Association (AIUM/NEMA) guidelines [32]. The array was submerged in an anechoic tank (122 x 51 x 53 cm) filled with degassed distilled water. A needle-type hydrophone (precision Acoustics Ltd., Dorchester, UK) was placed perpendicular to the face of the transducer to measure pressure field values at discrete points. While focusing the acoustical energy 40 mm axially away from the face of the transducer, seven scans were acquired in the propagation direction for a single segment of the phased array. The average values of these scans were compared to k -space and Rayleigh-Sommerfeld simulation results.

Unlike k -space computations, the Rayleigh-Sommerfeld simulations computed the pressure distribution produced by a single segment of the phased array by summing the pressure contributions of individual simple sources along the extracted lines. The kerf width was 0.12 mm and the simulations were performed in water medium without the inclusion of the absorption term.

Figure 4 shows the normalized pressure squared of a line that crosses the focal point in the z -direction. The mean exosimetry results are compared to the Rayleigh-Sommerfeld, k -space in water medium, and k -space in prostate model simulations. The k -space simulation in the prostate model shows that the inhomogeneous tissue structure of the rectal wall and the prostate gland cause focusing aberration and elevation of the pressure values ($< -3\text{dB}$) within the nearfield region compared to exosimetry and other simulations. Rapid decrease in the pressure values of the k -space prostate simulation is due to the relatively high absorption values of this axial

line which mostly composed of connective tissue with absorption values of 110 dB/m. Both exposimetry results and *k*-space water simulation results show good agreement within 9% when comparing the -3dB widths of the focal volume. Rayleigh-Sommerfeld simulation shows deviation of the results compared to the *k*-space simulations and exposimetry results. This deviation is due to performing the calculations of the pressure values without the inclusion of absorption effects.

MRI thermometry methods

Ex vivo and *in vivo* hyperthermia evaluations of the probe were made using MRI thermometry and a switching feedback controller. Figure 5 shows the setup for the hyperthermia experiments. A personal computer used as a switching temperature controller was connected via an RS 232 serial port to the digital power amplifier (UDS 2050PA, Advanced Surgical Systems, Inc. Tucson, Arizona) and to the console of the magnetic resonance imaging system (MEDSPEC S300, Bruker BioSpin, Ettlingen, Germany). The ultrasound transrectal probe was coupled to either *ex vivo* bovine samples or *in vivo* canine prostate gland using an inflated bolus of circulated water. The transducer was connected to the driving power amplifier. Water hoses were connected to a water pump (Cole-Parmer Instrument Company, Barrington, IL) via a bubble trap chamber and air hoses were connected to an air pump. Depending on feedback temperature values, the switching controller adjusted the driving power of each ultrasound channel by signaling the power amplifier system on and off. Temperature values were calculated from the phase shift of the acquired MRI images as follows [33]:

$$\Delta T = \Delta \phi / (\alpha \gamma TE B_0)$$

where, ΔT is the relative temperature (°C); $\Delta \phi$ is the phase difference (rad); α is the temperature dependent chemical shift (-0.00909 ppm/°C); γ is the gyromagnetic ratio

(rad/s.T); TE is the echo time (s), and B_0 is the magnetic field (T). A spoiled gradient echo (SPGR) sequence was used to acquire thermal images for the feedback controller. More details are presented elsewhere [26].

For *ex vivo* experiments, the transrectal probe and its bolus were held close to the bovine sample and the whole apparatus was inserted in the RF head coil and was placed in the uniform static magnetic field and gradient coils. A base line image was produced using these parameters: repetition time TR = 100 ms, echo time TE = 15 ms, flip angle = 30° , data matrix = 64 x 64, field of view (FOV) = 12 x 12 cm, and slice thickness = 4 mm. The ultrasound transducer was excited for 5 minutes before acquiring another image. Phase difference values, between base image (before driving the transducer) and an image five minutes after driving the transducer, were used to calculate temperature variations in the selected slice. The MRI-derived average temperature of a 2 x 3 pixel region was used as an input to the controller. For *in vivo* experiments, a mongrel-type canine (3 years old, 10 kg) was anesthetized with Telazol (100 mg/ml, reconstituted with Tiletamine hydrochloric acid and Zolazepam hydrochloric acid, Fort Dodge Animal Health, Fort Dodge, IA) and was placed inside the magnet. The rectum of the dog was manually cleaned and was filled with ultrasound gel using a syringe. The transrectal probe was inserted in the rectum facing the prostate gland. The vital readings of the animal were periodically checked and recorded. MRI images were acquired to help aligning both the prostate gland and the phased array perpendicularly to each other. A baseline image was produced before driving the phased array. Another image was produced five minutes after driving the transducer. These images were used to calculate thermal distribution through the prostate gland. A smaller region of interest (ROI) area inside the prostate was used to

average the temperature value and to feedback the controller system. Each controlled hyperthermia experiment was executed for 20 minutes.

Results

***Ex-vivo* results**

Hyperthermia controlled *ex vivo* experiments using MRI thermometry were conducted for 20 minutes. Figure 6a shows a transverse MRI image of the coupled transrectal probe to an *ex vivo* bovine sample with dimensions of 100 x 70 x 4 mm. Water bolus provides good coupling medium between the active elements of the array and the bovine sample. Figure 6b shows the calculated relative thermal distribution after driving the transducer for five minutes. The color bar illustrates the relative temperatures in °C. Ultrasound energy is concentrated 20 mm away from the face of the transducer and is spread axially for 30 mm. Temperature values varies from 5°C to 9°C within the focal region. The water bolus temperature is kept constant during heating period. Figure 6c shows the results of *ex vivo* controlled hyperthermia using MRI thermometry. Aiming at 6°C relative rise, the averaged temperature of the region of interest (ROI) is risen $5.9 \pm 0.38^{\circ}\text{C}$ in 9.5 ± 0.26 minutes and is kept till the end of the experiment. The solid continuous line represents averaged temperature values of seven different experiments. The standard error bars are shown at discrete points of 30 seconds intervals.

***In-vivo* results**

Figure 7a shows a transverse MRI image of the transrectal probe coupled via the pressurized water bolus to a canine prostate gland. The dimensions of this slice are 70 x 60 x 4 mm. Water bolus provides good coupling medium between the array and the prostate. Figure 7b shows the calculated relative thermal image after driving the

transducer for five minutes. The color bar illustrates the relative temperatures in °C. Ultrasound energy is spread through the prostate region. Relative temperature values vary from 3°C to 6°C within the prostate gland. Circulated water temperature within the bolus is intended to be homogeneous and close to zero. However, inhomogeneous distribution of temperature throughout the bolus is due to slower flow of the pumped water. Averaged temperature of a small ROI area of 2 x 3 pixels within the prostate gland is used as a feedback value for the controller. Figure 7c shows the results of *in vivo* controlled hyperthermia. With a desired relative temperature of 6°C, results show that the temperature of the ROI is risen $6.1 \pm 0.80^{\circ}\text{C}$ in 6.3 minutes and is maintained approximately steady till the end of the experiment. The solid line represents discrete temperature values every 7 seconds.

Discussion

The 4 x 20 element phased array provides better focusing and steering mechanism within the prostate gland. The spreading of the focal volume in the length of the array (the elevation-direction) is achieved by recruiting more segments to heat the whole prostate gland. Rayleigh-Sommerfeld and *k*-space simulations help in predicting the appropriate dimensions of the array. Good agreement between exosimetry results and the simulated *k*-space results was achieved. As an example, the -3 dB distance of the focal volume in the propagation direction (*z*-direction) is off by 9% between exosimetry and *k*-space simulations. Hyperthermia experiments of the focused probe were compared to a 16-element unfocused transducer [23]. With a desired relative temperature of 6°C, the controlled hyperthermia experiments show that the steady temperature of the ROI is maintained at $6.5 \pm 0.93^{\circ}\text{C}$ and $42.8 \pm 1.44^{\circ}\text{C}$ for *ex vivo* and *in vivo* experiments, respectively. Compared to unfocused

transducers, however, the focused transducer has the ability of focusing acoustic energy in targeted tissue and at the same time has the ability to steer the beam for better treatment. Unfocused transducer spreads the energy in a fan-shaped profile in the tissue facing the transducer without steering ability. *In-vivo* canine prostate hyperthermia trial proves the usefulness of the focused probe in prostate treatment. Blood flow is considered natural cooling system that works against temperature elevation within the prostate. The tested probes are capable of counteracting the effect of blood cooling while keeping the targeted volume within the required biological thermal dose.

Tissue-ultrasound interaction requires simulation of the ultrasound perturbations produced from phased arrays instead of summing the pressure contribution of geometrically superimposed simple sources. This requirement becomes feasible using the *k*-space computational method which provides economical and accurate simulation tool for large scale, coarse grid and inhomogeneous tissue models. Simulation results of the *k*-space are found close compared to actual exposimetry results.

The 4 x 20 phased array intentionally spreads the focal volume in the length of the array and allows for steering in the width of the array while changing the depth of the focusing in the axial direction. These variable parameters allow better thermal targeting of the whole prostate gland and the seminal vesicles. Controlling the temperature of a single point within the targeted volume helps in delivering the required clinical thermal dose into the targeted cancerous volume while maintaining surrounded healthy tissue. Compared to unfocused transducers, the 4 x 20 element phased array is capable of steering and focusing rather than spreading of the energy. Another important issue is that the unfocused transducers deposit more thermal

energy in the rectal wall compared to distant places in the prostate gland. This issue is solved using the focused transducer by focusing the energy away from the rectal wall for less damage and better treatment. Aside from that, noninvasive MRI thermometry is essential in monitoring and controlling of thermal treatment of the prostate cancer. Ultimately, this research has benefited from two non-invasive technologies to help treating prostate cancer in conjunction with classical therapeutic modalities.

Acknowledgements

This work was supported by the Department of Defense Congressionally Directed Medical Prostate Cancer Research Program (DAMD17-0201-0124).

References

1. Jemal, A., Tiwari, R. C., Murray, T., Ghafoor, A., Samuels, A., Ward, E., Feuer, E. J., and Thun, M. J.: **Cancer statistics, 2004**. *CA Cancer J Clin.*, vol. 54, no. 1, pp. 8-29, Jan.2004.
2. Jemal, A., Murray, T., Ward, E., Samuels, A., Tiwari, R. C., Ghafoor, A., Feuer, E. J., and Thun, M. J.: **Cancer statistics, 2005**. *CA Cancer J Clin.*, vol. 55, no. 1, pp. 10-30, Jan.2005.
3. Stanford J.L., Stephenson R.A., Cerhan J., Correa R., Eley J.W., Gilliland F., Hankey B., Kolonel L.N., Kosary C., Ross R., Severson R., and West D.: *Prostate Cancer Trends 1973-1995*. NIH Pub. No. 99-4543. 1999. Bethesda, MD, SEER Program, National Cancer Institute.
4. Seegenschmiedt, M. and Saur, R., *Interstitial and intracavitary thermoradiotherapy* Berlin: Springer-Verlag, 1993.
5. Seegenschmiedt, M., Fessenden, P., and Vernon, C., *Principles and practices of thermoradiotherapy and thermochemotherapy* Berlin: Springer-Verlag, 1995.
6. Stauffer, P., Diederich, C., and Seegenschmiedt, M.: **Interstitial heating technologies**. in Seegenschmiedt MH, Fessenden P, and Ernon CC (eds.) *Principles and practices of thermoradiotherapy and thermochemotherapy* Berlin: Springer-Verlag, 1995, pp. 279-320.
7. Sneed, P. K. and Phillips, T. L.: **Combining hyperthermia and radiation: how beneficial?**. *Oncology (Huntingt)*, vol. 5, no. 3, pp. 99-108, Mar.1991.
8. Bornstein, B. A., Zouranjian, P. S., Hansen, J. L., Fraser, S. M., Gelwan, L. A., Teicher, B. A., and Svensson, G. K.: **Local hyperthermia, radiation therapy, and chemotherapy in patients with local-regional recurrence of breast carcinoma**. *Int J Radiat Oncol Biol Phys*, vol. 25 pp. 79-85, 1993.
9. Overgaard, J., Gonzalez, G. D., Hulshof, M. C., Arcangeli, G., Dahl, O., Mella, O., and Bentzen, S. M.: **Hyperthermia as an adjuvant to radiation therapy of recurrent or metastatic malignant melanoma. A multicentre randomized trial by the European Society for Hyperthermic Oncology**. *Int.J.Hyperthermia*, vol. 12, no. 1, pp. 3-20, Jan.1996.
10. Van Vulpen, M., de Leeuw, A. A. C., Raaymakers, B. W., van Moorselaar, R. J. A., Hofman, P., Lagendijk, J. J. W., and Battermann, J. J.: **Radiotherapy and hyperthermia in the treatment of patients with locally advanced prostate cancer: preliminary results**. *Bju International*, vol. 93, no. 1, pp. 36-41, Jan.2004.
11. Diederich, C. J. and Hynynen, K.: **Ultrasound technology for hyperthermia**. *Ultrasound in Medicine and Biology*, vol. 25, no. 6, pp. 871-887, July1999.
12. Saleh, K. Y. and Smith, N. B.: **Two-dimensional ultrasound phased array design for tissue ablation for treatment of benign prostatic hyperplasia**. *International Journal of Hyperthermia*, vol. 20, no. 1, pp. 7-31, Feb.2004.
13. Saleh, K. and Smith, N.: **Design and evaluation of a 3 x 21 element 1.75 dimensional tapered ultrasound phased array for the treatment of prostate disease**. *Materials Research Innovations*, 2004.
14. Curiel, L., Chavrier, F., Souchon, R., Birer, A., and Chapelon, J. Y.: **1.5-D high intensity focused ultrasound array for non-invasive prostate cancer surgery**. *IEEE Transactions on Ultrasonics Ferroelectrics and Frequency Control*, vol. 49, no. 2, pp. 231-242, Feb.2002.

15. Tan, J. S., Frizzell, L. A., Sanghvi, N., Wu, S. J., Seip, R., and Kouzmanoff, J. T.: **Ultrasound phased arrays for prostate treatment.** *J Acoust.Soc Am.*, vol. 109, no. 6, pp. 3055-3064, June2001.
16. Diederich, C. J. and Hynynen, K.: **The feasibility of using electrically focused ultrasound arrays to induce deep hyperthermia via body cavities.** *IEEE Trans Ultrason Ferroelectr Freq Contr*, vol. 38 pp. 207-219, 1991.
17. Buchanan, M. T. and Hynynen, K.: **Design and experimental evaluation of an intracavitary ultrasound phased array system for hyperthermia.** *IEEE Trans Biomed Eng*, vol. 41, no. 12, pp. 1178-1187, Dec.1994.
18. Zemanek, J.: **Beam behavior within the nearfield of a vibrating piston.** *J Acoust Soc Am*, vol. 49 pp. 181-191, 1971.
19. Mast, T. D., Souriau, L. P., Liu, D. L., Tabei, M., Nachman, A. I., and Waag, R. C.: **A k-space method for large-scale models of wave propagation in tissue.** *IEEE Trans.Ultrason.Ferroelectr.Freq.Control*, vol. 48, no. 2, pp. 341-354, Mar.2001.
20. Tabei, M., Mast, T. D., and Waag, R. C.: **A k-space method for coupled first-order acoustic propagation equations.** *J.Acoust.Soc.Am.*, vol. 111, no. 1 Pt 1, pp. 53-63, Jan.2002.
21. Witte, D. C. and Richards, P. G.: **The pseudospectral method for simulating wave propagation.** in Lee, D., Cakmak, A., and Vichnevetsky, R. (eds.) *Computational acoustics* New York: North-Holland, 1990, pp. 1-18.
22. Twizell, E. H.: *Computational methods for partial differential equations* New York: Ellis Horwood Limited, 1984.
23. Smith, N. B., Buchanan, M. T., and Hynynen, K.: **Transrectal ultrasound applicator for prostate heating monitored using MRI thermometry.** *Int.J.Radiat.Oncol.Biol.Phys.*, vol. 43, no. 1, pp. 217-225, Jan.1999.
24. Sokka, S. D. and Hynynen, K. H.: **The feasibility of MRI-guided whole prostate ablation with a linear aperiodic intracavitary ultrasound phased array.** *Physics in Medicine and Biology*, vol. 45, no. 11, pp. 3373-3383, Nov.2000.
25. Hazle, J. D., Diederich, C. J., Kangasniemi, M., Price, R. E., Olsson, L. E., and Stafford, R. J.: **MRI-guided thermal therapy of transplanted tumors in the canine prostate using a directional transurethral ultrasound applicator.** *Journal of Magnetic Resonance Imaging*, vol. 15, no. 4, pp. 409-417, Apr.2002.
26. Sun, L., Collins, C. M., Schiano, J. L., Smith, M. B., and Smith, N. B.: **Adaptive real-time closed-loop temperature control for ultrasound hyperthermia using magnetic resonance thermometry.** *Magnetic Resonance Engineering*, vol. 27B, no. 1, pp. 51-63, 2005.
27. Sapareto, S. A. and Dewey, W. C.: **Thermal dose determination in cancer therapy.** *Int J Radiat Oncol Biol Phys*, vol. 10 pp. 787-800, 1984.
28. Mast, T. D.: **Empirical relationships between acoustic parameters in human soft tissues.** *Acoustics Research Letters Online*, vol. 1, no. 2, pp. 37-42, 2000.
29. Mast T.D.: **Empirical relationships between acoustic parameters in human soft tissues.** *Acoustics Research Letters Online*, vol. 1, no. 2, pp. 37-42, 2000.
30. Mast T.D.: **Two- and three-dimensional simulations of ultrasonic propagation through human breast tissue.** *Acoustics Research Letters Online*, vol. 3, no. 2, 2001.

31. Mast, T. D., Hinkelman, L. M., Metlay, L. A., Orr, M. J., and Waag, R. C.: **Simulation of ultrasonic pulse propagation, distortion, and attenuation in the human chest wall.** *J.Acoust.Soc.Am.*, vol. 106, no. 6, pp. 3665-3677, Dec.1999.
32. AIUM/NEMA: **Safety standard for diagnostic for ultrasound equipment.** *Journal of Ultrasound in Medicine*, vol. 2 pp. S1-S50, 1983.
33. Chung, A. H., Hynynen, K., Colucci, V., Oshio, K., Cline, H. E., and Jolesz, F. A.: **Optimization of spoiled gradient-echo phase imaging for in vivo localization of a focused ultrasound beam.** *Magn Reson.Med.*, vol. 36, no. 5, pp. 745-752, Nov.1996.

Figures

Figure 1 - Hyperthermia phased array

Two diagrams and a photograph showing the transrectal intracavitary ultrasound probe in (a) sagittal view (xz-plane), (b) expanded coronal view (xy-plane), and (c) an actual photograph of the diced hyperthermia array.

Figure 2 - The prostate model

From the Visible Human Project®, a photographic image of a prostate slice shows a transverse (axial, yz-plane) cross section of the prostate gland.

Figure 3 - The *k*-space simulation

A gray scaled image showing the simulated normalized pressure squared distribution of a single segment of the hyperthermia phased array using the *k*-space computational method. The results are shown for the central transverse plane of the 3D prostate model. The image shows a two-layered gray scale photograph for the central plane showing a background layer of the absorption distribution and the normalized squared pressure distribution on top of it while focusing axially 40 mm away from the face of the array.

Figure 4 - Exposimetry results

Normalized pressure squared distribution in linear scans through the focal point in the propagation direction showing the averaged exposimetry results compared to conventional Rayleigh-Sommerfeld and *k*-space simulation results.

Figure 5 - Hyperthermia setup

A sketch shows the setup of hyperthermia experiments using MRI thermometry.

Figure 6 - *Ex-vivo* MRI hyperthermia

(a) An MRI image of a selected bovine slice showing the focused transducer cross sectional view. (b) The thermal image after driving the transducer for five minutes. The color bar relates relative temperature values in °C. (c) *Ex vivo* controlled hyperthermia results using MRI thermometry and the switching controller.

Figure 7 - *In-vivo* MRI hyperthermia

In vivo canine prostate hyperthermia results. (a) MRI image of a canine prostate gland showing the focused transducer and the water bolus. (b) Relative thermal distribution image produced after driving the transducer for five minutes. The color bar shows the temperature values in °C. (c) Controlled hyperthermia results for 20 minutes.

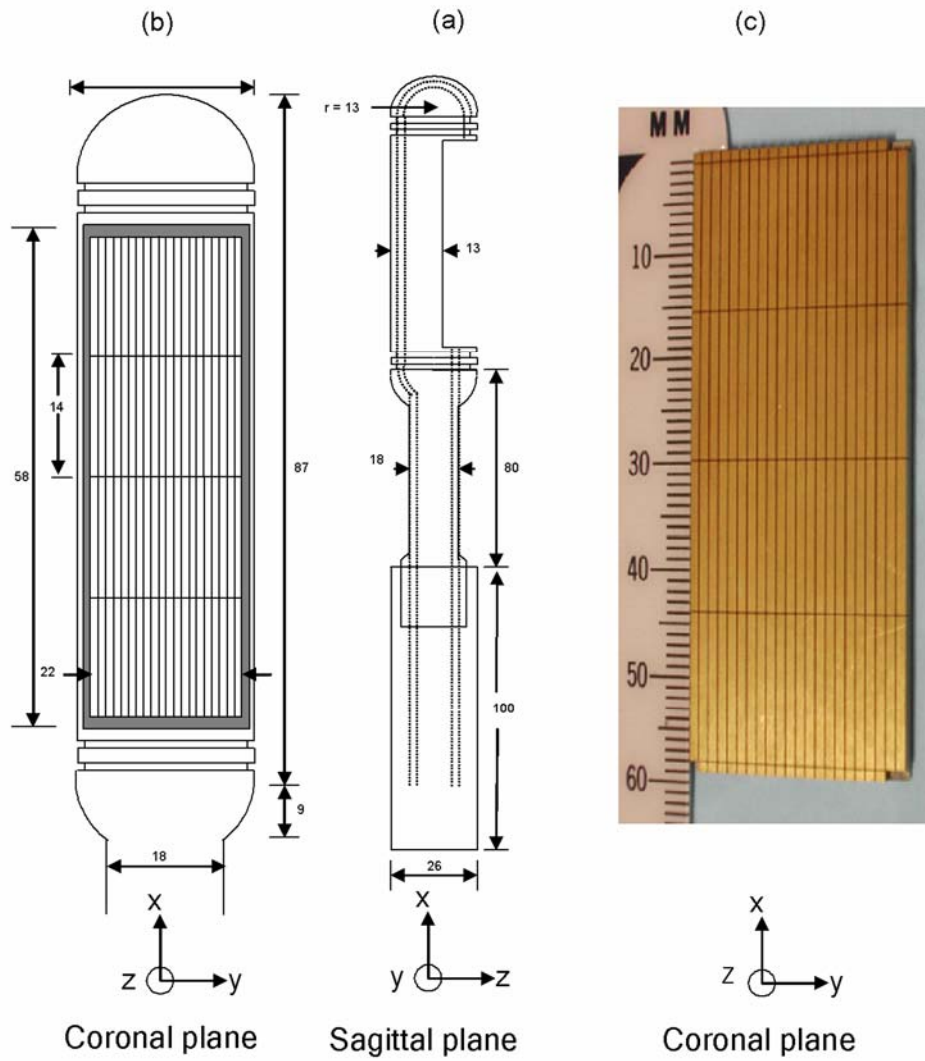


Figure 1: Two diagrams and a photograph showing the transrectal intracavitary ultrasound probe in (a) sagittal view (xz-plane), (b) expanded coronal view (xy-plane), and (c) an actual photograph of the diced hyperthermia array.

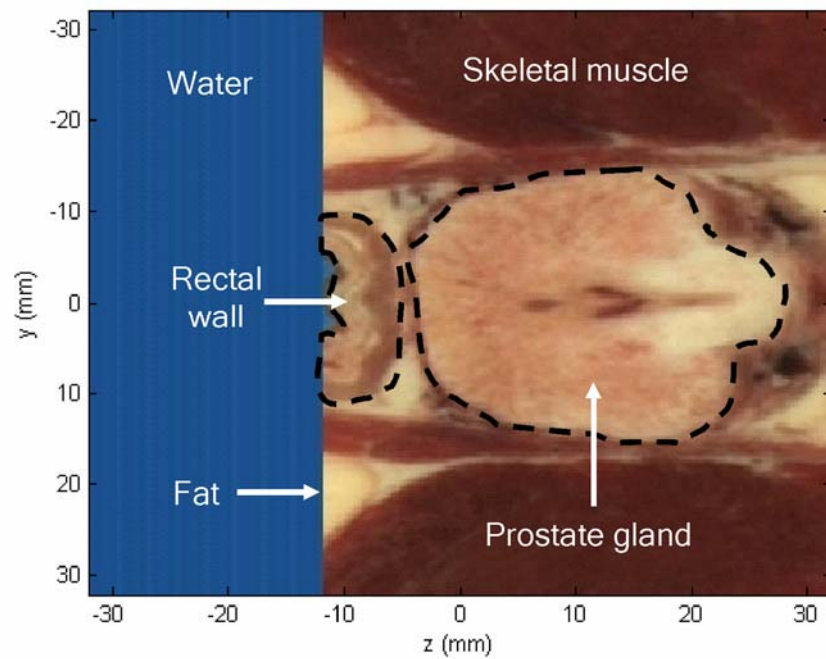


Figure 2: From the Visible Human Project®, a photographic image of a prostate slice showing a transverse (axial, yz-plane) cross section of the prostate gland.

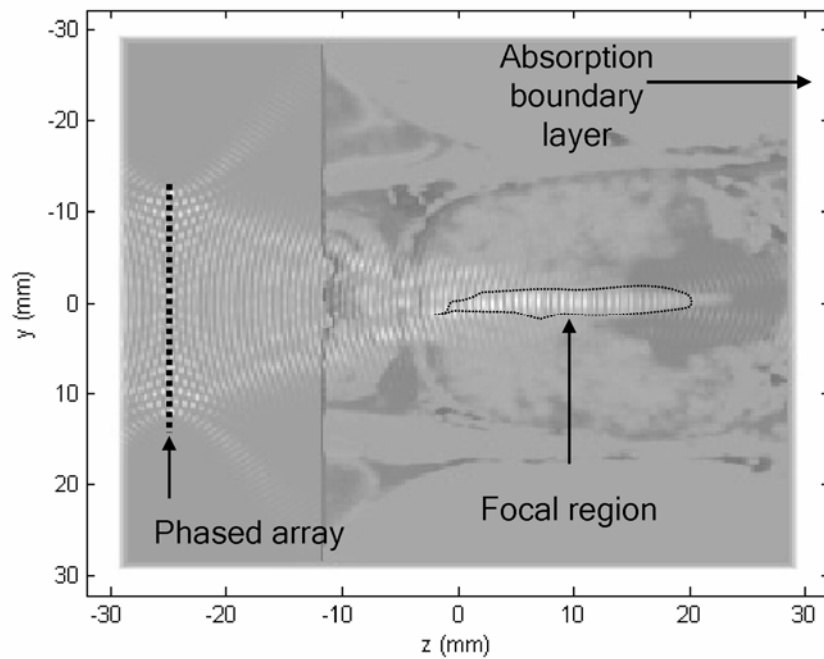


Figure 3: A gray scaled image showing the simulated normalized pressure squared distribution of a single segment of the hyperthermia phased array using the k-space computational method. The results are shown for the central transverse plane of the 3D prostate model. The image shows a two-layered gray scale photograph for the central plane showing a background layer of the absorption distribution and the normalized squared pressure distribution on top of it while focusing axially 40 mm away from the face of the array.

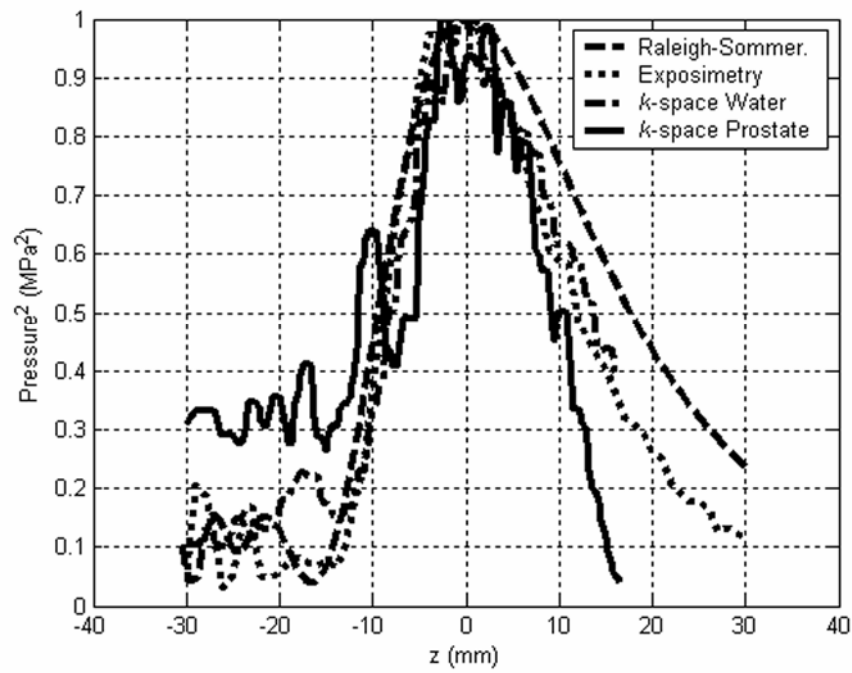


Figure 4: Normalized pressure squared distribution in linear scans through the focal point in the propagation direction showing the averaged exposimetry results compared to conventional Rayleigh-Sommerfeld and k -space simulation results.

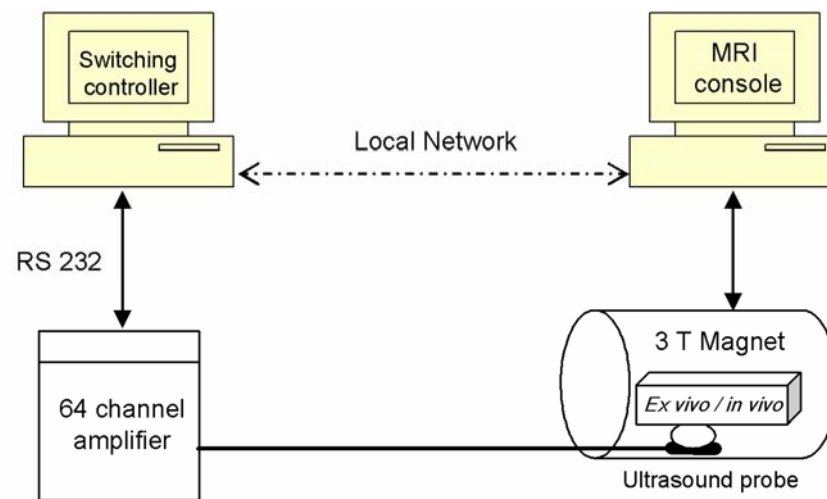


Figure 5: A sketch showing the setup of the hyperthermia experiments using MRI thermometry.

Figure 6(a)

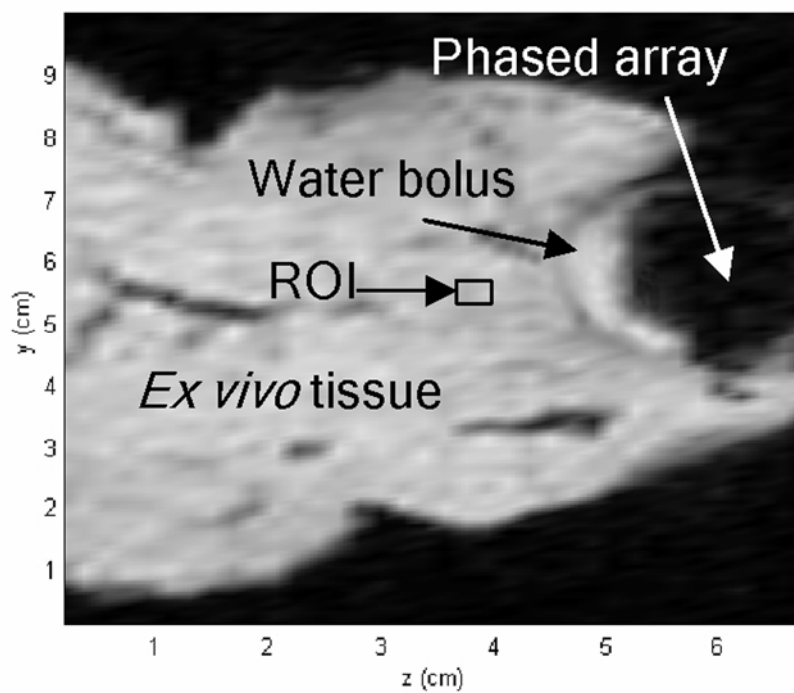


Figure 6(b)

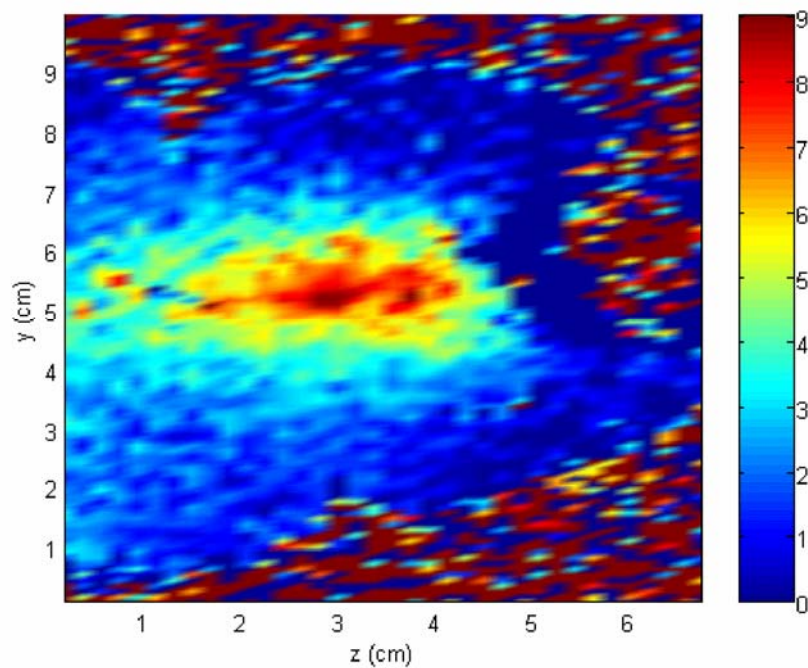


Figure 6(c)

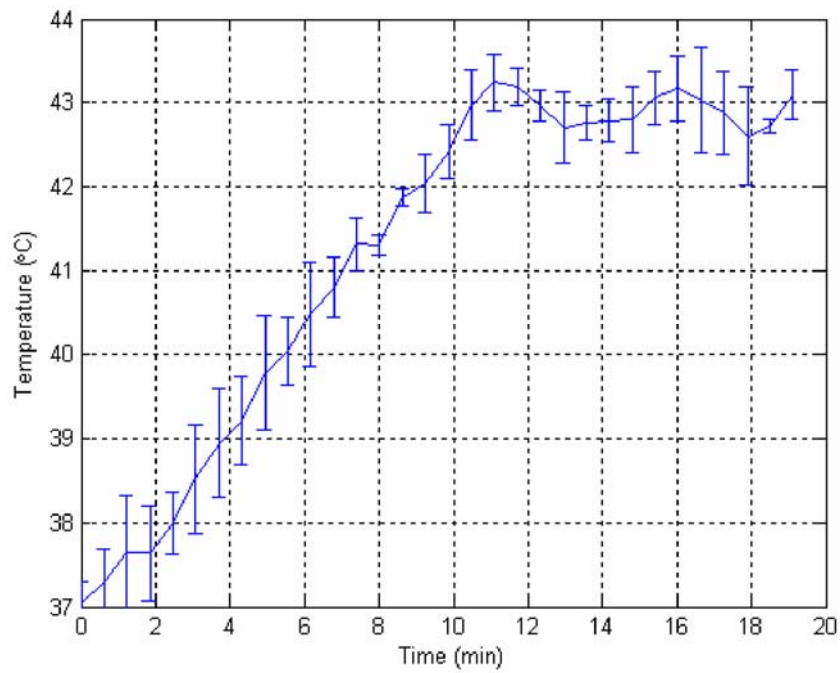


Figure 6: (a) An MRI image of a selected bovine slice showing the focused transducer cross sectional view. (b) The thermal image after driving the transducer for five minutes. The color bar relates relative temperature values in °C. (c) *Ex vivo* controlled hyperthermia results using MRI thermometry and the switching controller.

Figure 7(a)

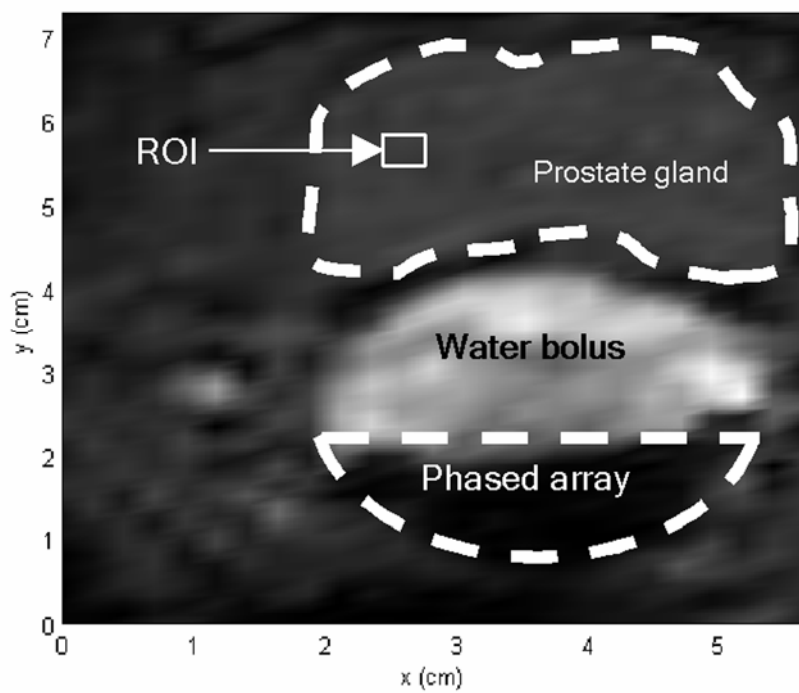


Figure 7(b)

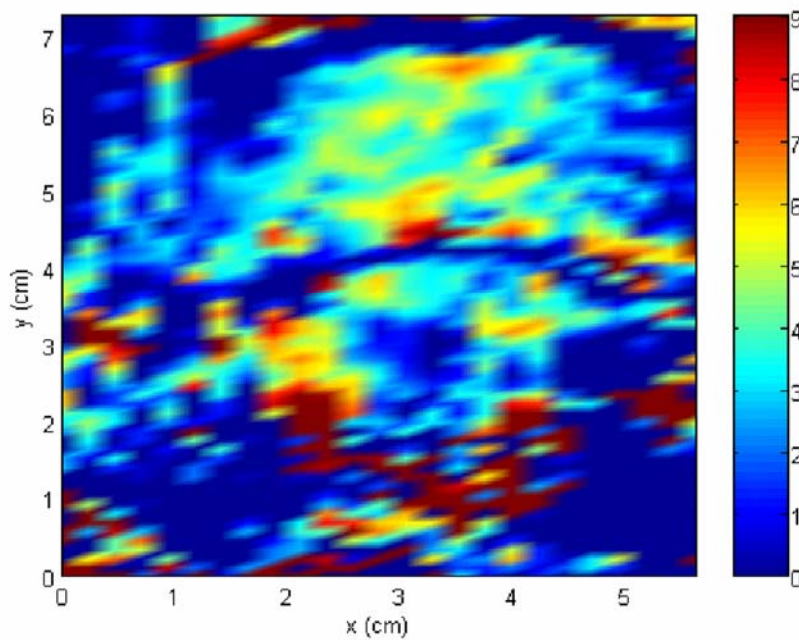


Figure 7(c)

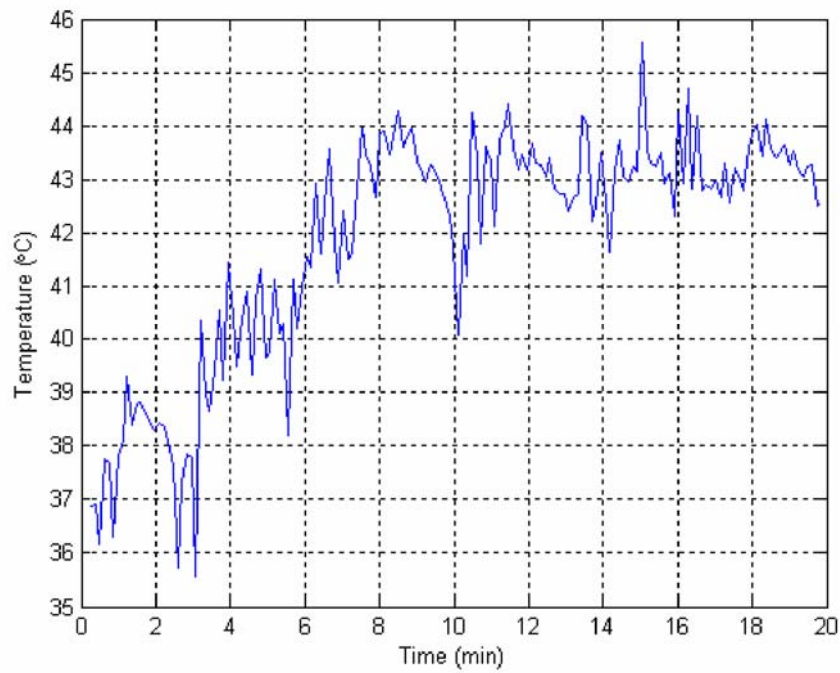


Figure 7: *In vivo* canine prostate hyperthermia results. (a) MRI image of a canine prostate gland showing the focused transducer and the water bolus. (b) Relative thermal distribution image produced after driving the transducer for five minutes. The color bar shows the temperature values in °C. (c) Controlled hyperthermia results for 20 minutes.

Bibliography

- [1] Jemal, A., Tiwari, R. C., Murray, T., Ghafoor, A., Samuels, A., Ward, E., Feuer, E. J., and Thun, M. J., "Cancer statistics, 2004," *CA Cancer J Clin.*, vol. 54, no. 1, pp. 8-29, Jan.2004.
 - [2] Jemal, A., Murray, T., Ward, E., Samuels, A., Tiwari, R. C., Ghafoor, A., Feuer, E. J., and Thun, M. J., "Cancer statistics, 2005," *CA Cancer J Clin.*, vol. 55, no. 1, pp. 10-30, Jan.2005.
 - [3] Stanford JL, Stephenson RA, , C. L., Cerhan J, Correa R, Eley JW, Gilliland F, Hankey B, Kolonel LN, Kosary C, Ross R, Severson R, and West D. Prostate Cancer Trends 1973-1995. NIH Pub. No. 99-4543. 1999. Bethesda, MD, SEER Program, National Cancer Institute.
- Ref Type: Report
- [4] Seegenschmiedt, M. and Saur, R., *Interstitial and intracavitary thermoradiotherapy* Berlin: Springer-Verlag, 1993.
 - [5] Seegenschmiedt, M., Fessenden, P., and Vernon, C., *Principles and practices of thermoradiotherapy and thermochemotherapy* Berlin: Springer-Verlag, 1995.
 - [6] Stauffer, P., Diederich, C., and eegenschmiedt, M., "Interstitial heating technologies," in Seegenschmiedt MH, Fessenden P, and erson CC (eds.) *Principles and practices of thermoradiotherapy and thermochemotherapy* Berlin: Springer-Verlag, 1995, pp. 279-320.
 - [7] Sneed, P. K. and Phillips, T. L., "Combining hyperthermia and radiation: how beneficial?," *Oncology (Huntingt)*, vol. 5, no. 3, pp. 99-108, Mar.1991.
 - [8] Bornstein, B. A., Zouranjian, P. S., Hansen, J. L., Fraser, S. M., Gelwan, L. A., Teicher, B. A., and Svensson, G. K., "Local hyperthermia, radiation therapy, and chemotherapy in patients with local-regional recurrence of breast carcinoma," *Int J Radiat Oncol Biol Phys*, vol. 25 pp. 79-85, 1993.
 - [9] Overgaard, J., Gonzalez, G. D., Hulshof, M. C., Arcangeli, G., Dahl, O., Mella, O., and Bentzen, S. M., "Hyperthermia as an adjuvant to radiation therapy of recurrent or metastatic malignant melanoma. A multicentre randomized trial by the European Society for Hyperthermic Oncology," *Int.J.Hyperthermia*, vol. 12, no. 1, pp. 3-20, Jan.1996.
 - [10] van Vulpen, M., de Leeuw, A. A. C., Raaymakers, B. W., van Moorselaar, R. J. A., Hofman, P., Lagendijk, J. J. W., and Battermann, J. J., "Radiotherapy and hyperthermia in the treatment of patients with locally advanced prostate cancer: preliminary results," *Bju International*, vol. 93, no. 1, pp. 36-41, Jan.2004.
 - [11] Diederich, C. J. and Hynynen, K., "Ultrasound technology for hyperthermia," *Ultrasound in Medicine and Biology*, vol. 25, no. 6, pp. 871-887, July1999.

- [12] Saleh, K. Y. and Smith, N. B., "Two-dimensional ultrasound phased array design for tissue ablation for treatment of benign prostatic hyperplasia," *International Journal of Hyperthermia*, vol. 20, no. 1, pp. 7-31, Feb.2004.
- [13] Saleh, K. and Smith, N., "Design and evaluation of a 3 x 21 element 1.75 dimensional tapered ultrasound phased array for the treatment of prostate disease," *Materials Research Innovations*, 2004.
- [14] Curiel, L., Chavrier, F., Souchon, R., Birer, A., and Chapelon, J. Y., "1.5-D high intensity focused ultrasound array for non-invasive prostate cancer surgery," *Ieee Transactions on Ultrasonics Ferroelectrics and Frequency Control*, vol. 49, no. 2, pp. 231-242, Feb.2002.
- [15] Tan, J. S., Frizzell, L. A., Sanghvi, N., Wu, S. J., Seip, R., and Kouzmanoff, J. T., "Ultrasound phased arrays for prostate treatment," *J Acoust.Soc Am.*, vol. 109, no. 6, pp. 3055-3064, June2001.
- [16] Diederich, C. J. and Hynynen, K., "The feasibility of using electrically focused ultrasound arrays to induce deep hyperthermia via body cavities," *IEEE Trans Ultrason Ferroelectr Freq Contr*, vol. 38 pp. 207-219, 1991.
- [17] Buchanan, M. T. and Hynynen, K., "Design and experimental evaluation of an intracavitary ultrasound phased array system for hyperthermia," *IEEE Trans Biomed Eng*, vol. 41, no. 12, pp. 1178-1187, Dec.1994.
- [18] Zemanek, J., "Beam behavior within the nearfield of a vibrating piston," *J Acoust Soc Am*, vol. 49 pp. 181-191, 1971.
- [19] Mast, T. D., Souriau, L. P., Liu, D. L., Tabei, M., Nachman, A. I., and Waag, R. C., "A k-space method for large-scale models of wave propagation in tissue," *IEEE Trans.Ultrason.Ferroelectr.Freq.Control*, vol. 48, no. 2, pp. 341-354, Mar.2001.
- [20] Tabei, M., Mast, T. D., and Waag, R. C., "A k-space method for coupled first-order acoustic propagation equations," *J.Acoust.Soc.Am.*, vol. 111, no. 1 Pt 1, pp. 53-63, Jan.2002.
- [21] Witte, D. C. and Richards, P. G., "The pseudospectral method for simulating wave propagation," in Lee, D., Cakmak, A., and Vichnevetsky, R. (eds.) *Computational acoustics* New York: North-Holland, 1990, pp. 1-18.
- [22] Twizell, E. H., *Computational methods for partial differential equations* New York: Ellis Horwood Limited, 1984.
- [23] Smith, N. B., Buchanan, M. T., and Hynynen, K., "Transrectal ultrasound applicator for prostate heating monitored using MRI thermometry," *Int.J.Radiat.Oncol.Biol.Phys.*, vol. 43, no. 1, pp. 217-225, Jan.1999.
- [24] Sokka, S. D. and Hynynen, K. H., "The feasibility of MRI-guided whole prostate ablation with a linear aperiodic intracavitary ultrasound phased array," *Physics in Medicine and Biology*, vol. 45, no. 11, pp. 3373-3383, Nov.2000.

- [25] Hazle, J. D., Diederich, C. J., Kangasniemi, M., Price, R. E., Olsson, L. E., and Stafford, R. J., "MRI-guided thermal therapy of transplanted tumors in the canine prostate using a directional transurethral ultrasound applicator," *Journal of Magnetic Resonance Imaging*, vol. 15, no. 4, pp. 409-417, Apr.2002.
- [26] Sun, L., Collins, C. M., Schiano, J. L., Smith, M. B., and Smith, N. B., "Adaptive real-time closed-loop temperature control for ultrasound hyperthermia using magnetic resonance thermometry," *Magnetic Resonance Engineering*, vol. 27B, no. 1, pp. 51-63, 2005.
- [27] Sapareto, S. A. and Dewey, W. C., "Thermal dose determination in cancer therapy," *Int J Radiat Oncol Biol Phys*, vol. 10 pp. 787-800, 1984.
- [28] Mast, T. D., "Empirical relationships between acoustic parameters in human soft tissues," *Acoustics Research Letters Online*, vol. 1, no. 2, pp. 37-42, 2000.
- [29] Mast T.D., "Empirical relationships between acoustic parameters in human soft tissues," *Acoustics Research Letters Online*, vol. 1, no. 2, pp. 37-42, 2000.
- [30] Mast T.D., "Two- and three-dimensional simulations of ultrasonic propagation through human breast tissue," *Acoustics Research Letters Online*, vol. 3, no. 2, 2001.
- [31] Mast, T. D., Hinkelman, L. M., Metlay, L. A., Orr, M. J., and Waag, R. C., "Simulation of ultrasonic pulse propagation, distortion, and attenuation in the human chest wall," *J.Acoust.Soc.Am.*, vol. 106, no. 6, pp. 3665-3677, Dec.1999.
- [32] AIUM/NEMA, "Safety standard for diagnostic for ultrasound equipment," *Journal of Ultrasound in Medicine*, vol. 2 pp. S1-S50, 1983.
- [33] Chung, A. H., Hynynen, K., Colucci, V., Oshio, K., Cline, H. E., and Jolesz, F. A., "Optimization of spoiled gradient-echo phase imaging for in vivo localization of a focused ultrasound beam," *Magn Reson.Med.*, vol. 36, no. 5, pp. 745-752, Nov.1996.

INTERNATIONAL SOCIETY FOR MAGNETIC RESONANCE IN MEDICINE

Workshop on

MRI-Guided: Focused Ultrasound Surgery

SYLLABUS

19-21 June 2002

Cambridge, Massachusetts, USA

ORGANIZING COMMITTEE:

Ferenc A. Jolesz, M.D.

Kullervo Hynynen, Ph.D.

Two Dimensional Array Design for Tissue Ablation for Treatment of Benign Prosthetic Hyperplasia

¹Khaldon Y. Saleh and ²Nadine Barrie Smith

Department of Bioengineering, The Pennsylvania State University, University Park, PA 16802

¹kysbio@engr.psu.edu (presenter), ²nbs@engr.psu.edu
814-865-8087(office) 814-863-0490 (fax)

Abstract

For treating prostate disease such as benign prosthetic hyperplasia, a two dimensional ultrasound array has been designed and constructed. Intracavitary ablation of tissue requires an array be small in size and be able to electrically steer the focus within the prostate volume without physically moving the device. The goal of this research was to design and construct an ultrasound array that will be capable of focusing and steering in a three dimensional volume. After theoretically designing the array using the calculated pressure field and the bioheat transfer equation, a small two dimensional array was cut 70% through the ceramic (PZT-8) using a dicing saw into an eight by eight aperiodic design (total size, 2 x 2 cm²). The structural integrity of the array face was fortified with a unique matching layer for maximum acoustic power transfer to tissue. With regards to the cabling of a multi element device, analysis of the transducer ceramic and cable impedance has been designed for maximum power transfer with minimal capacitance and diameter. For this initial prototype, the final construction used MRI compatible housing and cabling. From the numerical analysis, array has the capability of focusing and steering in a three dimensional volume with a steering angle of $\pm 14^\circ$ and has the ability to necrose tissue.

key words: transducer design, two dimensional array, beamsteering, matching layer

Introduction

Focused ultrasound has been shown to give promising results in treating benign prosthetic hyperplasia (BPH). Although BPH is not life threatening, treatment is necessary since normal urine flow can be blocked as a result of prostate pushing against the urethra and the bladder. The goal of this research is to construct, computationally and experimentally, a two-dimensional intracavitary phased array suitable for tissue ablation in the prostate. Part of the design criteria is that a specific region in a target volume will be ablated by focusing the ultrasound beam at that region using short high temperature sonications. A magnetic resonance imaging (MRI) compatible, ultrasound phased array will be presented for the treatment of BPH.

Previous one dimensional prostate array transducer geometries include a 64 x 1 aperiodic, linear array which reduced grating lobes and could electrically adjust the focus at distal and proximal locations along the urethra [1], and a 60 x 1, linear array with a mechanical rotation which could electrically steer the focus along the urethra and mechanically steer left and right of the mid-sagittal urethra [2]. The drawbacks behind these prostate arrays are that they can only focus at distal or proximal locations along the urethra or complex mechanics which move the focus. The advantage with a two dimensional array is that it can electrically focus at distal and proximal locations along the urethra and left and right of the mid-sagittal line by changing the phase to the elements. The difficulty with designing a two dimensional array is the dicing of the ceramic while maintaining a structural grounding plane for the individual elements. To overcome this problem, the elements of the ceramic can be partially diced and the structural integrity of the transducer face can be maintained with an acoustic matching layer. An additional problem is the impedance matching to 50 ohms for a ceramic diced into small elements. This research presents a small, eight by eight two dimensional ultrasound array designed to ablate tissue while overcoming many problems involved with transducer fabrication.

Materials and Methods

Array Design:

A two dimensional ultrasound phase array has been designed to be able to focus, and thus ablate tissue, and steer inside a volume of interest. The array was designed to heat the entire prostate from the limited confines of the rectum. As with previous array designs, Huygen's principle, which models each surface element as a grid of simple sources and then sums the contribution from the field, was used to

model the pressure field [3]. From the pressure field, the temperature increase in the tissue volume was determined using the bioheat transfer equation [4]. Based on the computational results, a two dimensional (8 x 8) design using 64 elements was chosen (Fig. 1). The size was a 2 x 2 cm² array, with individual elements with equal lengths and widths of 2.00, 2.33, 2.66, 3.00, 3.00, 2.66, 2.33, 2.00 mm for elements 1, 2, ..., 8, respectively. All ceramics were cut using a dicing saw at (Model 780, K & S-Kulick and Soffa Industries, Willow Grove, PA) the NIH Medical Ultrasonic Transducer Technology Resource Center (University Park, PA, USA).

From the analysis, this array was capable of focusing and steering with a steering angle of 14° with maximum focal depth of 4 cm. For off-axis focusing, Figure 2a shows the normalized pressure field in the x, z plane (x = transverse, z = radial) locations of 5, 30 mm, respectively, while Figure 2b shows the temperature distribution at the same location. In the y, z plane (x = transverse, y = longitudinal), Figure 2c shown the pressures at -5, 30 mm, respectively, with the temperature rise at this locations also plotted (Fig. 2d).

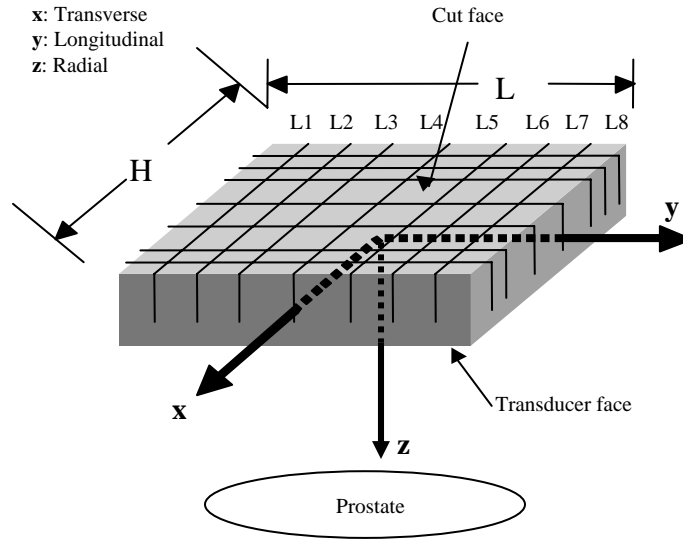


Fig. 1. The upper face is the cut face of the transducer in which the 70% cut through is made, in this face, the 64 elements are visible. The other side of the array is the transducer face, which radiates the ultrasound wave into the prostate.

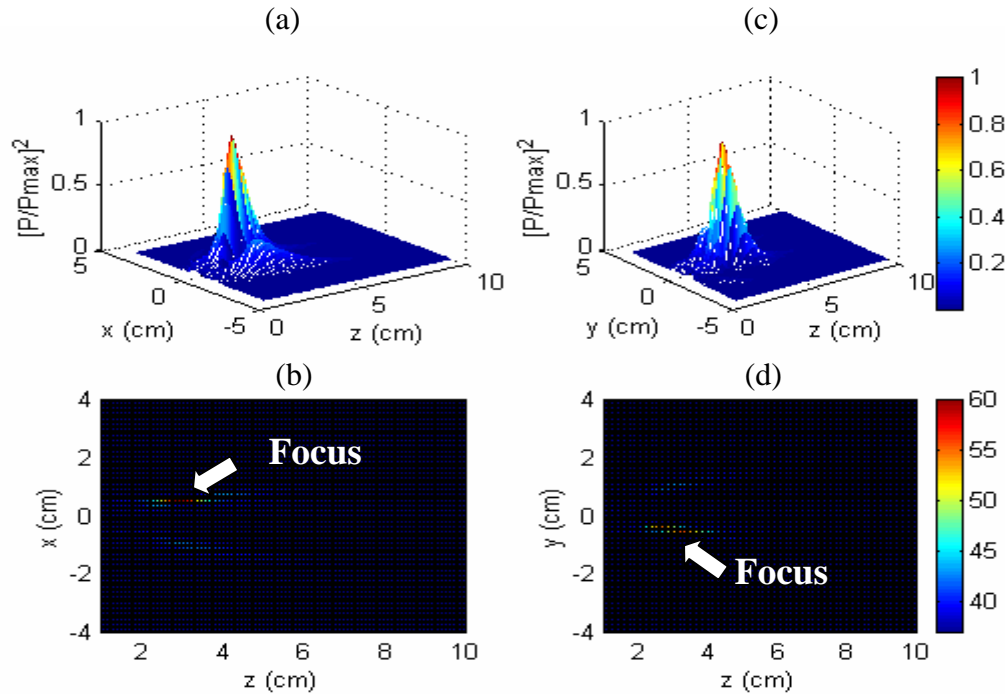


Fig. 2. Pressure field distribution was calculated using Rayleigh-Sommerfeld equation for a focus at (5, -5, 30) mm in the (a) x, z plane (c) y, z plane, and the temperature distribution

Matching layer:

The piezoelectric material has an acoustic impedance of about 33 MPa·s/m and the human tissue (also water) has an acoustic impedance of about 1.48 MPa·s/m [5]. Based on the maximum power transfer, the load (human tissue) must have the same acoustic impedance as the input impedance (piezoelectric impedance). Since the input and the load impedances are not the same, an intermediate layer (matching layer) must be put between the piezoelectric material and the human tissue thereby becoming a three layer problem to be solved. Applying the continuity of normal specific acoustic impedance at $z = 0$ and $z = L$ with some algebraic manipulation yields that the maximum intensity transmission coefficient, T , (and thus the power transmission coefficient since the surface area is the same at both the transmitting and receiving sides) occurs when the thickness of the matching layer equals an integer multiple of quarter a wavelength [$L = (2n - 1)\lambda / 4$ $n = 1, 2, 3, \dots$].

To construct the matching layer, parafilm was used to wax the ceramic to a glass plate. Adhesive primer was poured into the surface of the transducer face. The transducer was surrounded with a rubber dam and the silver conducting matching layer was poured onto the transducer surface. The matching layer (mixed in-house) was a 2:1, epoxy to silver mixture of Insulcast 501 (Insulcast, Roseland, NJ, USA) and 2-3 micron silver epoxy (Aldrich, Milwaukee, WI, USA). The whole assembly was centrifuged for 10 minutes and cured overnight. After the rubber assemble was removed, the surface was sanded and lapped to the designed thickness.

Cable impedance:

Permittivity is an important factor in determining the electrical performance of a lead zirconate titanate (PZT) ceramics. The effect of permittivity becomes more evident when the surface area of the individual elements of the array are small, which is exactly the case in this design. For a PZT-8 material, element with dimensions of 2 mm x 2 mm² dimensions and resonance frequency of 1.5 MHz, the element capacitance was found to be 20.63 pF, which means an element impedance of 5.14 k Ω magnitude. Since the load impedance (element impedance) was high, the cable has to be a low capacitance cable which effectively means high cable impedance, so a cable with high characteristic impedance is necessary for our requirement. It has been found that a cable with a characteristic impedance of 75 Ω was suitable. A 75 Ω , 15 pF/ft and 42 AWG was used. The electrical connection to the amplifier side was done using loose crimp contacts (PEI Genesis, Philadelphia, PA), while the connection to the PZT was using Indalloy # 1E (Indium Corporation of America, Utica, NY), which is a low temperature soldering material that was used to be sure that the temperature during soldering did not exceed the curie temperature for PZT-8 material.

Results

Based on the design criteria, lead zirconate titanate type 8 (PZT-8) ceramic was chosen for the final design based its efficiency as a high power device. The PZT-8 material (TRS Ceramics, State College, PA, USA) was cut 70% through the ceramic with a kerf width of 98 μ m on the dicing saw (Fig. 3). Although many computational transducer designs account for element size, very few take into account the final effect of the kerf size between each element. For this design, total of kerfs would be about 0.7 mm from the original array layout which can potentially effect the ability to properly steer the

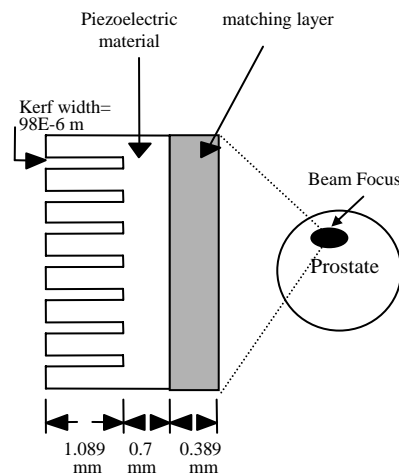


Fig. 3. Side view of the piezoelectric material and the matching layer, which shows the 70% cut through ceramic. The layer acoustically matches the high characteristic impedance piezoelectric material to the low characteristic impedance human tissue.

beam.

To give maximum acoustic transmission from the ceramic to the tissue and maintain the integrity of the two dimensional design, a matching layer was placed onto the transducer surface with a thickness of $L = 0.389$ mm (Fig. 3). The matching layer was found to firmly hold the array together while attaching the electrodes (Fig. 4a) to the individual element and be submerged for in indefinite length underwater without any leakage problems at the array face.

As an early phase prototype and not a clinical device, a water tight magnet compatible assembly for the 64 element phased array is shown in Fig. 4b. The array is shown connected to a 2.3 m long DL cable connector cable. The DL connector can easily be attached to a specially built amplifier driving system (Advanced Surgical Systems, Inc, Tucson, AZ). With this design, each element of the transducer was match to the 50 ohm impedance of the amplifier.

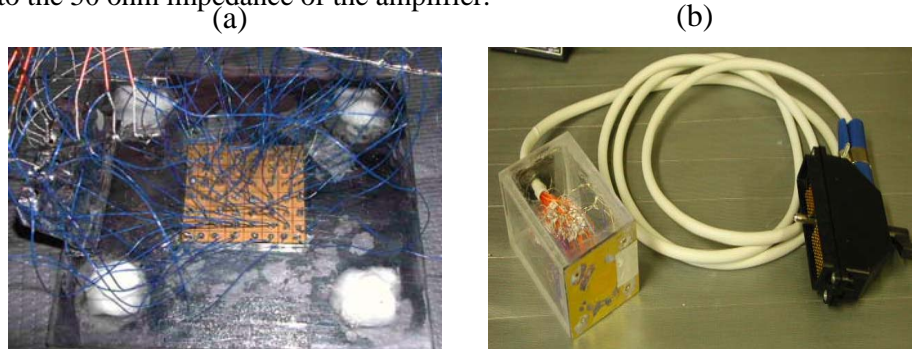


Fig. 4. The actual array (a) after finishing soldering the coaxial cable to the array (b) the final array that includes a 2.3 m coaxial cable and a water proof housing to be used in water.

Discussion

Exposimetry of a previously constructed four by five array had very good agreement between the theoretical and experimental results [6]. Unfortunately the earlier array suffered from power mismatch between the transducer elements and the cabling. Greater care was taken with this new 64 element, eight by eight array to account for capacitance issues between the ceramic and cables by modeling the system and impedance testing with various cables. Moreover, earlier array designs also had problems with water leakage into the interior housing of the array however the matching layer has solved this situation.

To choose an appropriate PZT material to be used in such an application is an issue of great importance, Although PZT-5H has a better performance if compared to PZT-4 and PZT-8, from a capacitance point of view, it cannot handle the large power that is used in tissue ablation. PZT-4 and PZT-8 are good candidates concerning power, with an advantage for PZT-8 over PZT-4. Following designs may use three layer PZT-8 material to increase the capacitance, and thus make it easier to electrically match. The matching layer helped to mechanically match the PZT material to the load, while the impedance matching circuits helped to electrically match the electrical impedance of the cable and load to the amplifier.

Acknowledgments: This research was sponsored by the Department of Defense Congressionally Directed Medical Prostate Cancer Research Program (DAMD17-0201-0124).

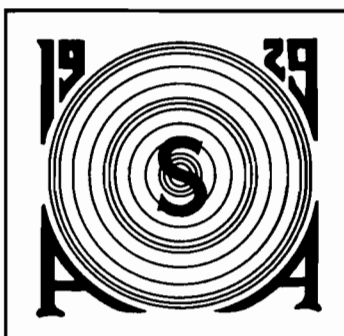
References

- [1] Hutchinson, E. B., Buchanan, M. T., and Hynynen, K., "Design and optimization of an aperiodic ultrasound phased array for intracavitary prostate thermal therapies," *Med.Phys.*, vol. 23, no. 5, pp. 767-776, May1996.
- [2] Sokka, S. and Hynynen, K. "The feasibility of MRI guided whole prostate ablation with a linear aperiodic intracavitary ultrasound phased array" *Phys. Med. Biol.*, 45 (11), 3373-3383, 2000.
- [3] Zemanek, J., "Beam behavior within the nearfield of a vibrating piston," *J Acoust Soc Am*, vol. 49 pp. 181-191, 1971.
- [4] Pennes, H. H., "Analysis of tissue and arterial blood temperatures in the resting human forearm.," *Journal of Applied Physiology*, vol. 1, no. 2, pp. 93-122, 1948.
- [5] Kinsler, L. E., Frey, A. R., Coppers, A. B., and Sanders, J. V., *Fundamentals of Acoustics*, 3rd ed. New York: John Wiley & Sons, 1982.
- [6] Helser, J. L., Sparrow, V. W., and Smith, N. B., "Two-dimensional ultrasound phased array for treatment of benign prostatic hyperplasia," *J Acoust Soc Am*, vol. 5 pp. 2546, 2000.

The Journal of the Acoustical Society of America

Vol. 114, No. 4, Pt. 2 of 2, October 2003

<http://asa.aip.org>



**146th Meeting
Acoustical Society of America**

**Renaissance Austin Hotel
Austin, Texas
10–14 November 2003**

Table of Contents on p. A5

nature of this problem. It is shown that a large number of samples is often required to optimally resolve surface orientation using the optimality criteria of the MLE derived in Naftali and Makris [J. Acoust. Soc. Am. **110**, 1917-1930 (2001)].

4:45

2pAO15. Geocorrection and filtering of 3D bottom images from multi-beam sonar records. Jerzy Demkowicz, Krzysztof Bikonis, Andrzej Stepnowski, and Marek Moszynski (Gdansk Univ. of Technol., Narutowicza 11/12, 80-952 Gdansk, Poland)

For the last decade multibeam sonars have been increasingly used for mapping and visualization of the seafloor to provide the "physical bases" for environmental studies. Increasing amount of digital (raster) echo

records of high resolution from a multibeam sonar have enhanced the potential of computer modeling of the marine environment to improve our understanding of the bottom processes. However, the 3D bottom images as the result of merging different sonar transects do not comply exact geographical positions and should be corrected. Additionally, the raw sonar records are subject to systematic errors, random noise and outliers. In this paper, Kalman filtering technique to generating optimal estimates of bottom surface from a noisy raw sonar records is proposed. The experiment on the surface indicates that after applying the Kalman filtering the outliers of raw records can be efficiently removed. Moreover, the two-step Kalman filtering method enables 3D seabed visualization in real time. The paper proposes the geographical corrections applied to the merged multi-beam sonar transects records. The 3D bottom relief before, and after the filtering method are presented.

TUESDAY AFTERNOON, 11 NOVEMBER 2003

TRINITY A ROOM, 1:00 TO 3:30 P.M.

Session 2pBB

Biomedical Ultrasound/Bioresponse to Vibration: HIFU and Scattering

Ibrahim M. Hallaj, Chair

Wolf, Greenfield and Sacks, PC, Federal Reserve Plaza, 600 Atlantic Avenue, Boston, Massachusetts 02210

Contributed Papers

1:00

2pBB1. Synchronization of HIFU therapy system with an arbitrary ultrasound imager. Neil Owen, Michael Bailey, James Hossack, and Lawrence Crum (Ctr. for Industrial and Medical Ultrasound, 1013 NE 40th St., Seattle, WA 98105)

Synchronization for image guided therapy using high intensity focused ultrasound (HIFU) and imaging ultrasound is achieved with a new technique that uses the focused transducer as a receiver that can detect the acoustic pulses created by the imaging probe. Without synchronization, interference from the high intensity source occludes the imager's display unpredictably, degrading the quality of the system. An imaging probe (Sonosite 180) is registered with a HIFU transducer ($d=33$ mm, $roc=55$ mm, $f=3.5$ MHz) such that the scan line bisects the single element focus. When acoustically coupled through a scattering medium, imaging pulses are passively detected with the HIFU transducer and electronically conditioned into a TTL level trigger. A LabVIEW program uses the trigger to create a pulse width modulated signal that controls the timing of HIFU excitation during treatment. Detection takes less than 1% of the time between displayed images when the imager is running at 20 frames per second. HIFU excitations are programmed to occur such that the single element focus is free of interference when viewed with the imager during treatment. With no electrical connections for this new, simple technique, an arbitrary imager can be selected for synchronized image guided therapy. [Work supported by NSBRI.]

1:15

2pBB2. Rapid continuous-wave pressure field calculations for spherically focused radiators. Robert McGough (Dept. of Elec. and Computer Eng., Michigan State Univ., 2120 Eng. Bldg., East Lansing, MI 48824, mcgough@egr.msu.edu)

A new accelerated expression for the continuous-wave pressure field generated by a spherically focused radiator is obtained when the impulse response formulation is transformed and optimized for numerical evaluations. The resulting integral expression converges much more quickly than the impulse response approach, resulting in far fewer function evaluations for the same numerical error. The optimized integral expression is between

two and seven times as fast as the impulse response approach, where the increase in speed depends on the peak value of the specified error. In addition, this new result completely eliminates the cone-shaped regions required for impulse response calculations, so the resulting computer code for the accelerated expression is less complicated than the corresponding code for the impulse response. Results also show that the new expression eliminates the numerical artifact that is encountered near the boundary between regions defined for impulse response calculations. All of these features are useful in thermal therapy computer simulations that employ spherically focused transducer geometries.

1:30

2pBB3. Design and evaluation of a 63 element 1.75-dimensional ultrasound phased array for treating benign prostatic hyperplasia. Khaldon Y. Saleh and Nadine B. Smith (Dept. of Bioengineering, 205 Hallowell Bldg., The Penn State Univ., University Park, PA 16802)

Focused ultrasound surgery (FUS) is a clinical method for treating benign prostatic hyperplasia (BPH) in which tissue is noninvasively necrosed by elevating the temperature at the focal point above 60 °C using short sonications. With 1.75-dimensional (1.75-D) arrays, the power and phase to the individual elements can be controlled electronically for focusing and steering. This research describes the design, construction and evaluation of a 1.75-D ultrasound phased array to be used in the treatment of benign prostatic hyperplasia. The array was designed with a steering angle of ± 13.5 deg in the transverse direction, and can move the focus in three parallel planes in the longitudinal direction with a relatively large focus size. A piezoelectric ceramic (PZT-8) was used as the material of the transducer and two matching layers were built for maximum acoustic power transmission to tissue. To verify the capability of the transducer for focusing and steering, exosimetry was performed and the results correlated well with the calculated fields. *In vivo* experiments were performed to verify the capability of the transducer to ablate tissue using short sonications. [Work supported by the Whitaker Foundation and the Department of Defense Congressionally Directed Medical Prostate Cancer Research Program.]

2pBB4. Optimized hyperthermia treatment of prostate cancer using a novel intravaginal ultrasound array. Osama M. Al-Bataineh, Nadine B. Smith (Dept. of Bioengineering, The Penn State Univ., University Park, PA 16802), Robert M. Keolian, Victor W. Sparrow (The Penn State Univ., University Park, PA 16802), and Lewis E. Harpster (Penn State Milton S. Hershey Medical Ctr., Hershey, PA 17033)

Localized uniformly distributed ultrasound-induced hyperthermia is a useful adjuvant to radiotherapy in the treatment of prostate cancer. A two-dimensional, 20×4 element, transrectal phased-array probe was designed to deliver a uniform and controllable amount of heat directly to the prostate without damaging the rectal wall or surrounding tissue. A three-dimensional prostate model was created using anatomical markers from the Visible Human Project to optimize the array. Sound speed, density, and absorption parameters were mapped to hue, saturation and value of the photographic data to simulate sound propagation through inhomogeneous tissue using the k -space method. To satisfy the requirements of this method from 1.2 to 1.8 MHz, the grid was adjusted to have 5 points per millimeter in each Cartesian direction. A spherical wave pulse was propagated through the model using tapered absorption boundary conditions. The expected temperature rise due to sound was obtained using the bio-heat transfer equation. Optimalinsonication parameters that uniformly heat the prostate to 43°C for 40–60 minutes were determined for use in the construction of a clinical hyperthermia array. [Research supported by the Department of Defense Congressionally Directed Medical Prostate Cancer Research Program.]

2:00

2pBB5. Separating thermal coagulation and cavitation effects in HIFU attenuation measurements. Justin Reed, Michael Bailey, Ajay Anand, and Peter Kaczkowski (Appl. Phys. Lab., Univ. of Washington, 1013 NE 40th St., Box 355640, Seattle, WA 98105-6698)

HIFU can be used to destroy tumors. The conversion of acoustic energy into heat causes protein coagulation (Lesion) in tissue. Attenuation measurements have been proposed to monitor the progression of thermal therapy. The goal of this work is to study and separate the effects of cavitation and thermal coagulation in attenuation measurements. A HIFU transducer was used to treat Bovine liver. A receiving transducer mounted across from the transmitting HIFU transducer measured attenuation during the treatment. A pressure chamber provided static pressure greater than the pressure amplitude of the HIFU wave, which suppressed cavitation. rf data from a commercial ultrasound scanner was also obtained. A large increase in attenuation was observed with cavitation present, while a subtle increase in attenuation was observed with cavitation suppressed. Attenuation estimated from the RF data showed an increase in attenuation downstream of the location of the lesion with cavitation present, while a subtle increase in attenuation was observed at the location of the lesion with cavitation suppressed. It has been found that attenuation measurements are greatly affected by the presence of cavitation, and the actual effect of thermal coagulation on attenuation is quite small. [Work supported by NIH, NSF, NSBRI.]

2:15

2pBB6. Numerical investigation of dual-frequency HIFU pulsing for lithotripsy. Wayne Kreider, Michael Bailey, and Lawrence Crum (Ctr. for Industrial and Medical Ultrasound, APL, Univ. of Washington, 1013 NE 40th St., Seattle, WA 98105, wkreider@u.washington.edu)

As an alternative to traditional shock-wave lithotripsy, high-intensity focused ultrasound (HIFU) is currently being investigated for its capability to comminute renal calculi. Because current data indicate that cavitation plays a role in both stone comminution as well as collateral tissue damage, the cavitation effects of HIFU treatment strategies are investigated numerically. In particular, numerical simulations are designed to model the response of bubbles to acoustic excitations generated by a prototype, dual-

frequency HIFU transducer for lithotripsy. The prototype transducer is capable of producing both high- ($\sim 4\text{-MHz}$) and low-frequency ($\sim 100\text{-kHz}$) outputs, while the bubble dynamics are modeled by the Gilmore equation for a single spherical bubble subject to diffusion. Numerical simulations are currently ongoing to investigate the effects of the relative phase between high and low-frequency pulses. Initial results demonstrate that the simultaneous application of high and low-frequency pulses can generate maximum pressures several orders of magnitude higher than high-frequency pulses alone.

2:30

2pBB7. The characterization of the lesion growth in time. Marie Nakazawa, Justin A. Reed, Michael R. Bailey, and Yongmin Kim (Dept. of Elec. Eng., Univ. of Washington, 1400 NE Campus Pkwy., Seattle, WA, nakazawa@ns.cradle.titech.ac.jp)

Thermal heating effects of high intensity focused ultrasound (HIFU) on the dynamics of lesion formation were characterized automatically to assess the role of vapor bubbles in distorting the shape. Tissue mimicking phantom was used in experiments by a 4.2 MHz curve-linear transducer with 44 mm diameter and 44 mm radius of curvature. A variety of HIFU intensities were produced by different amplitudes. Images were acquired by a CCD camera and HDI-1000 ultrasound imager, recorded to VHS, and digitized to measure lesion size and shape. Each image was subtracted with noise reduction in order to detect the HIFU on time and to segment the boundaries of the lesions performed by Matlab programming. Area, length, width, and ratio of lesion area proximal to center line over area distal to center line were calculated along HIFU exposure time. Slight increase in HIFU intensity, means hyperecho forms earlier, and lesion shape change. The data supported the hypothesis that lesion dramatically distorts well after hyperecho with only small increase in HIFU intensity. [Work supported by National Space and Biomedical Research Institute.]

2:45

2pBB8. Optimization of angular compounding in scatterer size estimation. Anthony L. Gerig, Quan Chen, and James A. Zagzebski (Dept. of Medical Phys., Univ. of Wisconsin-Madison, 1300 Univ. Ave., Rm. 1530, Madison, WI 53706, algerig@wisc.edu)

Ultrasonic scatterer size estimates generally have large variances due to the inherent noise of the spectral estimates used to calculate size. Compounding partially correlated size estimates associated with the same tissue, but produced with data acquired from different angles of incidence, is an effective way to reduce the variance without making dramatic sacrifices in spatial resolution. This work derives theoretical approximations for the correlation between these size estimates, and between their associated spectral estimates, as functions of data acquisition and processing parameters, where a Gaussian spatial autocorrelation function is assumed to adequately model scatterer shape. Size results exhibit a fair degree of agreement with those of simulation experiments, while spectral results compare favorably with simulation outcomes. Utilization of the theoretical correlation expressions for data acquisition and processing optimization is discussed. Further simplifying approximations, such as the invariance of phase and amplitude terms with rotation angle, are made in order to obtain closed-form solutions to the derived spectral correlation, and permit an analytical optimization analysis. Results indicate that recommended parameter adjustments for performance improvement depend upon whether, for the system under consideration, the primary source of estimate decorrelation with rotation is scatterer phase change or field separation. [Work supported by NIH T32CA09206.]

2p TUE. PM

on principles of the acoustic characterization of bone quality, fracture risk evaluation, and monitoring of therapeutic interventions. New approaches are based on the use of the ultrasound radiation pressure for the remote generation of acoustic waves in bones, on the use of various modes of guided acoustic waves having a propagation speed dependent on both the elasticity modulus and the bone thickness, on the use of geometrical dispersion of sound velocity for bone characterization, and the use of principles of nonlinear acoustic spectroscopy for remote bone testing. [Work supported by NIH.]

Contributed Papers

9:20

3aBB4. A "Fresnel-transducer" for prostate hyperthermia treatment. Robert M. Keolian (Penn State Appl. Res. Lab., P.O. Box 30, State College, PA 16804-0030, bonzo@sabine.acs.psu.edu), Osama M. Al-Bataineh, Nadine B. Smith, Victor W. Sparrow (Penn State, University Park, PA 16802), and Lewis E. Harpster (Penn State Milton S. Hershey Medical Ctr., Hershey, PA 17033)

Simulations and construction methods will be described for a novel "Fresnel-transducer." The transducer is designed for transrectal hyperthermia treatment of prostate cancer as an adjuvant to radiotherapy or chemotherapy. Forty nine 6.3 mm diameter 1.5 MHz PZT elements are arranged in a 3 by 7 cm honeycomb-like pattern. They are individually aimed so that their beams partially converge behind the prostate. The increased beam density away from the transducer compensates for the loss of acoustic intensity due to attenuation. The aiming of the beams is additionally biased toward the periphery of the heated region to compensate for cooling from lateral heat conduction. The elements are divided into three interspersed sets, each driven at a slightly different frequency, to minimize stationary Moire interference bands between the beams. The combined effect is to uniformly raise the prostate temperature to 43 °C without overheating the rectal wall. [Research supported by the Department of Defense Congressionally Directed Medical Prostate Cancer Research Program.]

9:35

3aBB5. Vibration characteristics of implants. Ahmed M. Al-Jumaily (Diagnostics and Control Res. Ctr., Auckland Univ. of Technol., Auckland, New Zealand, ahmed.al-jumaily@aut.ac.nz), Mostafa Fatemi, and James F. Greenleaf (Ultrasound Res. Lab., Mayo Clinic and Foundation, Rochester, MN 55905)

Vibro-acoustography is a technique that uses the radiation force of amplitude-modulated ultrasound to evaluate the dynamic response of an object at the modulation frequency. One potential application of this technique is to assess the reaction of the host tissue to the implant material by evaluating the mechanical properties of the tissue surrounding the implant. To do this, we use vibro-acoustography to measure the frequency response of the implant, and use this information to evaluate the mechanical parameters of the surrounding. Two theoretical models are developed to study the dynamic response of an implant in tissue. The first model is for an implant (1 × 25-mm steel beam) fully embedded in a viscoelastic medium (tissue). The second model is for a partially embedded implant with one part exposed to the open environment. The exposed end is rigidly connected to a base, and the other end is freely embedded in the viscoelastic medium. At the interface between the two media matching of boundary conditions is achieved to determine the force response. For both models eigenvalues and eigenfunctions are determined and transfer functions are evaluated. The first two natural frequencies compare well with available experimental and finite-element data.

9:50

3aBB6. Sector array transducers for vibro-acoustography. Glauber Silva, Shigao Chen, Randall Kinnick, James Greenleaf, and Mostafa Fatemi (Mayo Clinic and Foundation, Rochester, MN 55905)

Vibro-acoustography is an imaging technique that maps the acoustic response of an object to a localized harmonic radiation force. This force is generated by two interfering continuous-wave ultrasound beams at slightly different frequencies f_1 and f_2 . The system point-spread function (PSF) is related to the radiation force on a point-target. Imaging artifacts depend on the PSF sidelobes, which can be reduced by mismatching the sidelobes of each ultrasound beam. Here, we propose a beamforming approach based

on an 8-element sector transducer with consecutive elements alternately driven at f_1 and f_2 . The transducer generates two ultrasound beams skewed by 22.5° with respect to each other. The system PSF is analytically derived. The theory is validated by experiments using a small steel sphere (radius = 0.2 mm) as a point-target. A laser vibrometer is used to measure the vibration of the sphere and evaluate the PSF of the system. Theoretically, the PSF sidelobes are under -15.8 dB in eight spots circularly distributed and separated by 22.5°, which agrees with the experimental results. Simulation shows that with 16 elements sidelobes are under -35.2 dB. In conclusion, sector transducers for vibro-acoustography may have lower sidelobes as the number of array elements is increased. [Work supported by Grant Nos. EB00535-01, EB2640, and IMG0100744.]

10:05–10:15 Break

10:15

3aBB7. Radiation force produced by time reversal acoustic focusing system. Armen Sarvazyan and Alexander Sutin (Artann Labs., Inc., 1753 Linvale-Harbourton Rd., Lambertville, NJ 08530)

An ultrasonic induced radiation force is an efficient tool for remote probing of internal anatomical structures and evaluating tissue viscoelastic properties, which are closely related to tissue functional state and abnormalities. Time Reversal Acoustic Focusing System (TRA FS) can provide efficient ultrasound focusing in highly inhomogeneous media. Furthermore, numerous reflections from boundaries, which distort focusing in conventional ultrasound focusing systems and are viewed as a significant technical hurdle, lead to an improvement of the focusing ability of the TRA system. In this work the TRA FS field structure and radiation force in a transcranial phantom were investigated. A simple TRA FS comprising a plane piezoceramic transducer attached to an external resonator such as an aluminum block was acoustically coupled to the tested transcranial phantom. A custom-designed compact electronic unit for TRA FS provided receiving, digitizing, storing, time reversing and transmitting of acoustic signals in a wide frequency range from 0.01 to 10 MHz. The radiation force produced by ultrasonic pulses was investigated as a function of the transmitted ultrasound temporal parameters. The simplest TRA FS provided focusing of 500 kHz ultrasound pulses and the generation of a radiation force with an efficacy hardly achievable using conventional sophisticated phased array transmitters. [Work supported by NIH.]

10:30

3aBB8. Effects of transducer and tissue parameters on motion induced by radiation force during ultrasonic lesion monitoring. Samuel Mikaelian and Frederic L. Lizzi (Riverside Res. Inst., 156 William St., 9th Fl., New York, NY 10038, mikaelian@rrinyc.org)

Tissue motion induced by acoustic radiation force is studied as a means of monitoring the formation of therapeutic lesions with increased stiffness produced by high-intensity focused ultrasound (HIFU). Our analyses and simulations examine the role and interplay of various tissue and system parameters to assist in designing practical systems and interpreting results. The radiation force is generated by a therapeutic transducer excited at levels below lesion-production threshold, while the magnitude and time-course of the induced motion is monitored via a confocal and collinear diagnostic transducer. Lesions are detected by comparing pre- and post-treatment motion patterns. Parameters characterizing properties of the motion-inducing beam, such as its intensity and spatial profile, and tissue parameters signifying its viscoelastic properties, acoustic attenuation, and geometry, are the focus of this investigation. Acoustic attenuation, which can increase significantly during lesion production and directly

NOVEL ADAPTIVE CONTROL SYSTEM FOR ULTRASOUND HYPERTHERMIA TREATMENT OF PROSTATE DISEASE

L. Sun¹, J. Schiano², and N. B. Smith^{1,3}

¹Department of Bioengineering, ²Department of Electrical Engineering, ³Graduate Program in Acoustics, Pennsylvania State University, University Park, USA, 16802

Abstract: A novel model reference adaptive control (MRAC) method was proposed and tested with a transrectal intracavitary applicator for thermal treatment of prostate disease using ultrasound hyperthermia. Two significant advantages of this innovative adaptive control method are: 1) there is no need of *a priori* knowledge of the tissue properties and 2) the controller could adaptively change the amplitudes and phases of the array's driving signal according to the perfusion rate and other dynamic tissue properties. Computer simulations, *ex vivo* and *in vivo* experimental results all showed that with this adaptive controller the tissue was heated up to $43 \pm 0.2^\circ\text{C}$ within 7 ± 2 minutes, and adaptively maintained 43°C with dynamic blood flow for the rest period of the hyperthermia.

I. INTRODUCTION

Diseases associated with the prostate gland include benign prostate hyperplasia (BPH) and prostate cancer. Although surgery is the current treatment, older men often have additional health problems, which rule out surgery as a viable option. One promising alternative is ultrasound hyperthermia treatment, which is to increase the tissue temperature to $43\text{-}45^\circ\text{C}$ for 30-60 minutes. Ultrasound hyperthermia has been used clinically and has shown effectiveness for the prostate treatment when it is associated with radiotherapy or chemotherapy [1]. Hyperthermia can enhance radiotherapy by preventing cellular repair mechanisms from radiation induced injury and is effective in killing hypoxic cells, which are resistant to radiation therapy [2].

Despite the advantages, the treatment provides various challenges to design a control system satisfying hyperthermia requirements: low overshoot, small oscillation, and fast rising time. Previously, various control strategies have been designed for controlling temperature in either actual or simulated

physiological systems [3]. However, adaptive control system is specially appreciated because the response of the tissues to ultrasound varies in type, size, location, shape, stage of growth, and proximity to significant organs. Also the blood flow changes as a function of time and as a function of tissue temperature.

The goal of this research is to design and evaluate adaptive feedback control methods for ultrasound hyperthermia treatment of prostate cancer with minimal overshoots, rapid rising time, and small oscillations. Simulations were used to determine the proper initial settings for the adaptive controllers. *In vivo* and *ex vivo* experiments were performed to evaluate different combinations of control parameters for the optimal adaptive control performance.

II. MATERIALS AND METHODS

2.1 Hyperthermia System Setup

For adaptive control experiments, the ultrasound hyperthermia system primarily consists of ultrasound applicator, multi-channel programmable ultrasound phased array driving system, multi-channel fiber optic thermometer, and adaptive control algorithms (Figure 1). The ultrasound applicator was designed for transrectal intracavitary use with PZT-8 material (lead zirconate-titanate, EDO, Salt Lake City, Utah), which resonates at 1.5 MHz with 16 elements in a 4×4 pattern. Detailed design and operation of this applicator can be referred to somewhere else [4]. The adaptive control process was performed through an interactive Visual Basic program installed in adaptive control unit, which implemented data communications with the amplifier and the fiber optic thermometer through RS-232 protocol.

2.2 Adaptive Controllers and Simulations

For simplicity, an assumption was made that the hyperthermia system satisfied an auto-regressive

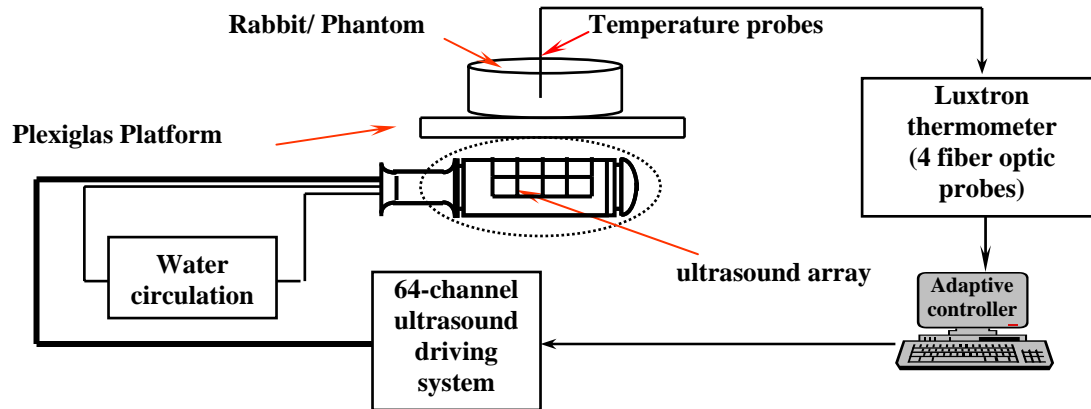


Figure 1. Schematic diagram showing the setup of the adaptive control system for an intracavitary ultrasound hyperthermia system used for *in vivo* and *ex vivo* experiments

moving average (ARMA) model with unknown orders and coefficients [5]. Based on this discovery, model reference adaptive control method was proposed and evaluated, since it can perform suitably well without exactly knowing the system parameters. The diagram of a model reference adaptive system is shown in Figure 2.

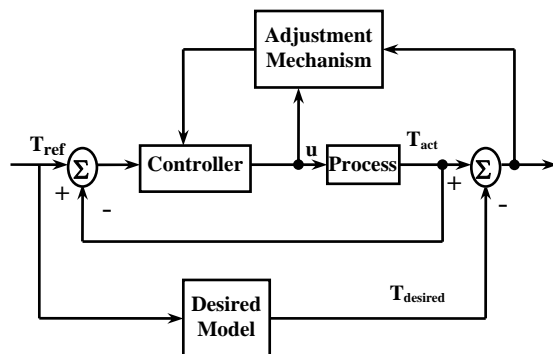


Figure 2. The block diagram of a model reference adaptive control.

The system has an ordinary feedback loop composed of the hyperthermia process, and another feedback loop that changes the controller parameters. The mechanism for adjusting the parameters in a model reference adaptive system can be obtained in gradient method such as “the MIT rule” or applying stability theory such as Lyapunov stability theory [6]. Detailed derivation of the MRAC based on both “the MIT rule” and Lyapunov theory can be referred to somewhere else [7].

Computer simulations were initially performed to determine the control variables and to evaluate the

performance of the controller. The acoustical pressure field of the applicator was calculated using the Rayleigh-Sommerfeld equation. The heat transfer in tissue was determined by applying Pennes’ bioheat transfer equation (BHTE). The adaptive controlled hyperthermia process was solved using a 3-D numerical finite difference equation and all boundary and initial conditions were set to 36.8°C. A time step of 1 second and a grid spacing of $1 \times 1 \times 1 \text{ mm}^3$ were used for the temporal and spatial resolution of the simulation implementation.

2.3 Ex vivo and in vivo Experiment

Ten *ex vivo* experiments were conducted with bovine muscle using the intracavitary applicator. The bovine muscle as well as the degassed water circulated through the bolus was kept at room temperature to allow the constant boundary conditions. One fiber optic probe was inserted into the tissue by $2.1 \times 133 \text{ mm}$ catheter to monitor the tissue temperature at the hot spot. Two other fiber optic probes were placed at the surface of the muscle facing the applicator to monitor the burning of the rectal wall. The temperature increase of 8°C in the hot spot simulated the temperature rise from 37°C to 45°C. Exponential function with time constant $4\tau = 10\text{min}$ was applied as reference input. Adaptation gain optimized by the computer simulations was set to 0.005. The sonication time was 30 minutes, with the initial power set to 0.1 W/channel. The tissue was allowed to return to the room temperature before each experiment. The temperature at the hot spot and surface of the tissue and electrical energy to each

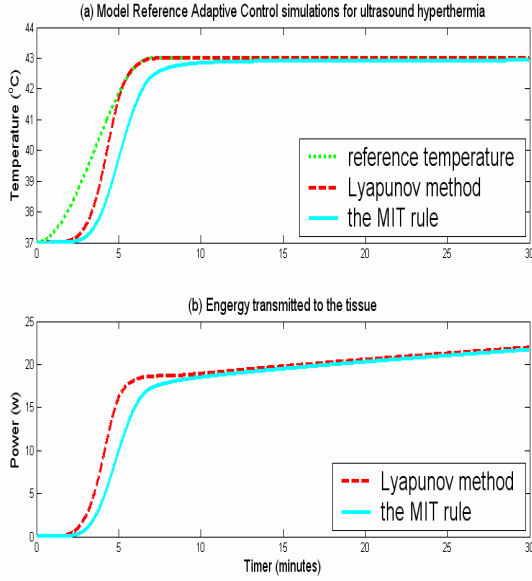


Figure 3. Adaptive control computer simulations using Lyapunov MRAC and “the MIT rule” MRAC with blood perfusion rate from $2\text{kg/m}^3\text{s}$ to $10\text{kg/m}^3\text{s}$. (a) Temperature elevation and reference temperature trajectory. (b) Electrical energy transmitted to the tissues.

channel were recorded.

In vivo experiments were conducted by procedures approved by the Penn State Institutional Animal Care and Use Committee (IACUC). Three New Zealand white rabbits (3-4 kg, male) were used for 10 separate adaptive experiments. The rabbits were anaesthetized with a combination of ketamine (40mg/kg intramuscularly, Fort Dodge Animal Health, Fort Dodge, IA) and xylazine (10mg/kg intramuscularly, Phoenix Scientific, Inc., St. Joseph, MO). After shaving the thigh, hair removal cream was applied to the skin to eliminate any remaining hair. The fiber optic probe was inserted about 2 cm deep into the thigh muscle. The rabbit’s vital signs (ECG, SpO_2 , HR) were monitored by SurgiVet monitoring system (SurgiVet, Inc., Waukesha, WI). The *in vivo* experiments were performed in the same manner as the *ex vivo* experiments except that the adaptation gain was 0.002 and the time constant was $4\tau = 7\text{min}$, and the therapy time was 25 minutes.

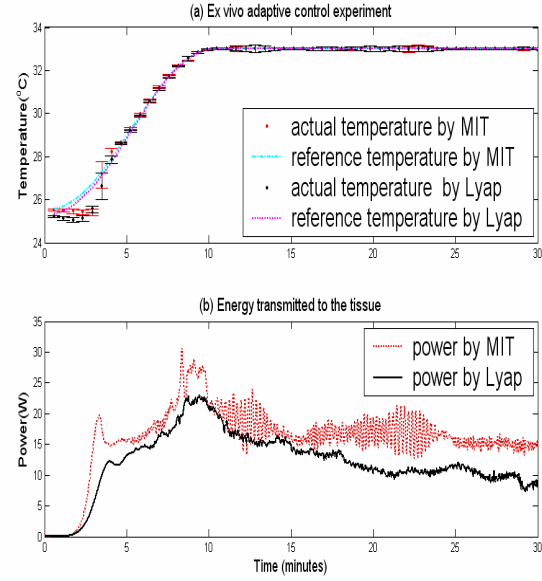


Figure 4. *Ex vivo* adaptive hyperthermia control experiment using bovine muscles with Lyapunov MRAC and “the MIT rule” MRAC. (a) Average temperature elevation with standard deviation. (b) Electrical energy transmitted to the tissue.

III. RESULTS

3.1. Simulation Results

Model reference adaptive control simulations using Lyapunov stability theorem and “the MIT rule” were performed, respectively. With proper setting of adaptation gains ($\gamma = 0.005$), both MRAC methods performed similarly well with the temperature elevations closely followed the reference with fast rising time and without overshoot and oscillation (Fig 3(a)). The time constant was set to $4\tau = 7\text{min}$. During simulations, the blood perfusion rate was increasing linearly from $2.0\text{ kg/m}^3\text{s}$ to $10\text{ kg/m}^3\text{s}$ for 30 minutes therapy time. However, the steady state responses of both MRAC were maintained stably at 43°C . The loss of energy due to the increased blood flow was compensated by the increasing energy transmitted to the tissue (Fig 3(b)). This result clearly demonstrated one advantage of adaptive control that was able to adjust the input energy according to the dynamic properties of the tissue.

3.2. Ex vivo results

Using the experimental setup shown in Figure 1, five pieces of bovine muscles were used to conduct ten

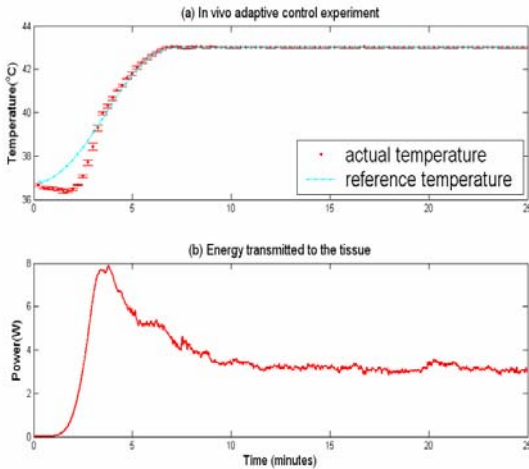


Figure 5. *In vivo* adaptive hyperthermia control experiment using rabbit with Lyapunov MRAC. (a) Temperature elevation and reference temperature trajectory. (b) Electrical power transmitted to the applicator.

adaptive control experiments. Each piece of muscle was applied by Lyapunov method and “the MIT rule” method, respectively. During *ex vivo* experiments, the tissue was heated from room temperature ($\sim 25^{\circ}\text{C}$) to 33°C (8°C above room temperature). The time constant was chosen to be $4\tau = 10$ min. The adaptation gain was 0.005. Figure 4(a) shows the mean temperature elevations averaging each 5 experiments for Lyapunov MRAC and “the MIT rule” MRAC, respectively. Standard deviations represented by the error bars show that very close results were obtained for each one of the ten experiments. No overshoot, little oscillation, and fast rising time were also achieved by these experiments. The maximum temperature rise at the surface of the tissue did not exceed 4.5°C . No sign of any burning of the surface tissue was observed as well.

3.3. *In vivo* results

Three rabbits experienced ten experiments with Lyapunov MRAC method with the rabbits’ thigh muscle was heated from 37°C to 43°C for 25 minutes. Time constants were chosen to be $4\tau = 7$ min. The adaptation gain was 0.002. Temperature elevation of the average of 10 experiments is shown in Figure 5(a). The results indicate the steady state temperature were within $\pm 0.2^{\circ}\text{C}$ of their target temperatures. Also

the maximum temperature rise at the surface of the skin was less than 7.5°C , and post-experimental examination showed no sign of any burning.

IV. CONCLUSIONS

This research investigated adaptive control design for ultrasound hyperthermia system. With the adaptive controller, the dynamic tissue properties such as blood perfusion rate can be compensated by adjusting the electrical energy inputting to the system. With a transrectal intracavitary ultrasound applicator, adaptive control methods was evaluated with computer simulations, phantom and animal experiments. Both experiment and simulations results show that adaptive control system especially with model reference adaptive control methods is able to elevate tissue temperature to clinically therapeutic level with no oscillations, no overshoots, and fast rising times.

V. ACKNOWLEDGEMENT

The support provided by Department of Defense Congressionally Directed Medical Prostate Cancer Research Program (DAMD17-0201-0124) to this work is gratefully acknowledged.

VI. REFERENCE

- [1] M. D. Hurwitz, *et al.*, “Feasibility and patient tolerance of a novel transrectal ultrasound hyperthermia system for treatment of prostate cancer,” *Int. J. Hyperthermia*, vol. 17, no. 1, pp. 31-37, 2001.
- [2] J. Overgaard, and M. Overgaard, “Hyperthermia as an adjuvant to radiotherapy in the treatment of malignant melanoma,” *Int. J. Hyperthermia*, vol. 3, no. 6, pp. 483-501, 1987.
- [3] N. B. Smith, *et al.*, “An MRI compatible intracavitary ultrasound array for thermal treatment of prostate disease,” *Int. J. Hyperthermia*, vol. 17, no. 3, pp. 271-282, 2001.
- [4] N. B. Smith, *et al.*, “Transrectal ultrasound applicator for prostate heating monitored using MRI thermometry,” *Int J Radiation Oncol Biol Phys* vol. 43, pp. 217-25, 1999.
- [5] L. Sun, J. Schiano, and N. B. Smith, “An adaptive control method for ultrasound prostate hyperthermia,” *Proceedings of the IASTED international conference on applied modeling and simulation (AMS 2002)*, Cambridge, Massachusetts, 4-6 November 2002, pp 347-352.
- [6] K. J. Astrom and B. Wittenmark, *Adaptive Control*, Boston: Addison Wesley, 1995.
- [7] L. Sun, J. Schiano, and N.B. Smith, “Novel adaptive control for ultrasound hyperthermia”, submitted to *Int. J. Hyperthermia*.

Fast adaptive control for MRI-guided ultrasound hyperthermia treatment for prostate disease: *in vitro* and *in vivo* results

L. Sun¹, C. M. Collins², M. B. Smith², N. B. Smith^{1,3}

¹Bioengineering, The Pennsylvania State University, University Park, PA, United States, ²Radiology, The Pennsylvania State University College of Medicine, Hershey, PA, United States, ³Graduate Program in Acoustics, The Pennsylvania State University, University Park, PA, United States

INTRODUCTION

Previous researchers have successfully demonstrated the application of temperature feedback control for thermal treatment of disease using MR thermometry (1-4). Using the temperature-dependent proton resonance frequency (PRF) shift, ultrasound heating for hyperthermia to a target organ (such as the prostate) can be tightly controlled. However, the response of the target to ultrasound heating varies in type, size, location, shape, stage of growth, and proximity to other vulnerable organs. To adjust for clinical variables, a novel adaptive feedback control system has been designed utilizing real-time, on-line MR thermometry by adjusting the output power to an ultrasound array to quickly reach the hyperthermia target temperatures. The advantages of this fast adaptive control method are that there is no need of *a priori* knowledge of the initial tissue properties and it can quickly reach the steady state target temperature by adaptively changing the output power according to the dynamic tissue properties (e.g. thermal conductivity, blood perfusion). To rapidly achieve and manage therapeutic temperatures from an ultrasound array, this research was conducted to utilize closed loop MRI guided temperature control using a novel adaptive feedback system with *in vitro* and *in vivo* experiments.

MATERIALS AND METHODS

Fast adaptive MRI control system: To shorten hyperthermia treatment time, previous researchers have evaluated several control schemes (1, 4, 5). Although the controllers initially operated well, some controllers had undesirable overshoots and oscillations (1, 5). The rapid adaptive control approach used here was designed to track an exponential target temperature with a very fast time constant and to avoid overshoots and oscillations. This robust control system had an ordinary feedback loop composed of the hyperthermia process and a second feedback loop that adjusted the controller parameters (Fig. 1). The mechanism for adjusting the parameters in a model reference adaptive system can be obtained in gradient method by applying Lyapunov stability theory (6). Three dimensional finite difference time domain computer simulations based on Pennes' bioheat transfer equation were conducted to determine the initial values of the control parameters.

Ultrasound hyperthermia system: For treatment of prostate disease, the ultrasound hyperthermia system consisted of a transrectal intracavitary array with 16 elements operating at 1.5 MHz. To drive the array, a multi-channel programmable ultrasound phased array driving system operating between 1-2 MHz and capable of 60W per channel was used. Verification of the temperature change within the target used a multi-channel fiber optic (Luxtron®) thermometer probe to provide a reference for the MR temperature map results.

In vitro and in vivo experiments: Nine *in vitro* adaptive control experiments were conducted using bovine muscle phantom within the Nine *in vitro* adaptive control experiments were conducted using bovine muscle phantom within the 3 Tesla Bruker S-300 MRI scanner using the ultrasound array. The tissue was coupled to the ultrasound through a circulating water filled bolus surrounding the applicator. MR temperatures in a region of interest (ROI) were selected from the tissue from pre-treatment images were used as feedback thermometry data to the controller. Using rabbit thigh muscle (New Zealand white), *in vivo* animal experiments were conducted using a similar procedure as the phantom experiments with the animal anesthetized using ketamine (40 mg/kg) and xylazine (10 mg/kg). Both the animal and phantom experiments used a 26 cm diameter birdcage coil. For rapid hyperthermia heating, the time constant (target temperature) was selected to be less than 2 minutes for a total experiment of 25 minutes.

MR temperature imaging: The proton resonant frequency shift was evaluated by using a spoiled gradient echo (SPGR) sequence with the following imaging parameters: TR = 100 ms, TE = 15 ms, flip angle = 30°, data matrix 64 x 64, field of view (FOV) = 14 x 14 cm, slice thickness = 8 mm and bandwidth = 61.7 kHz. These parameters were chosen to maximize the temperature dependent phase shift, while maintaining a high temporal resolution. A baseline scan was acquired before ultrasound heating and subsequent temperature measurement scans were obtained every 19.7 seconds. Phase subtraction was conducted on-line in real-time to calculate the PRF shift (7). The temperature elevation was obtained using the temperature dependence for muscle $\alpha(t) = -0.00909$ ppm/°C by averaging temperatures within a 4 x 3 pixel region located at least 1 cm above the bolus-tissue interface.

RESULTS

Robust adaptive MR temperature control has been demonstrated for both the *in vitro* and *in vivo* experiments. A temperature map (Fig. 2) using phase subtraction images from an *in vivo* rabbit experiment can be seen with a color bar indicating the temperature change within the selected heating ROI from the array below. Since the desired target temperature profile was 38°C for all nine *in vitro* experiments, Fig. 3(a) plots nine averaged MR temperature results (mean \pm s.d.) which were consistent with the controller target temperature (solid line) and comparable with the Luxtron® results (x-marks). Consistently starting with an initial phantom

temperature of 28°C, the controller achieved the steady state temperature within 6 minutes and deviation from the target profile was no greater than $\pm 1.37^\circ\text{C}$. Similar to the *in vitro* results, *in vivo* temperature control can be seen in Fig. 3(b) where the rabbit thigh muscle was heated initially from about 36.5°C for 25 minutes. For this experiment, the target temperature was 44.5°C and was achieved in 8 minutes. From other *in vivo* experiments, the maximum variation from the desired temperature profile was -3.9°C; after reaching steady state, tissue temperature was maintained at $44.5^\circ\text{C} \pm 1.2^\circ\text{C}$.

DISCUSSION AND CONCLUSION

Dynamic MR temperature control for hyperthermia is necessary for fast effective thermal treatments while eliminating the risk of permanently damaging healthy tissue due to overheating. Integration of ultrasound hyperthermia and MR thermometry with robust adaptive control between the modalities has clinical applications. Considering that the accuracy of PRF technique is approximately $\pm 1^\circ\text{C}$, the adaptive control system works well to effectively track the reference by adjusting the transducer power according to dynamic tissue properties such as blood perfusion rate. This work was supported by the Whitaker Foundation (RG-00-0042).

REFERENCES

- (1) F. Vimeux et al, *Invest Rad*, 34,3,1999; (2) N. B. Smith et al, *Proc. ISMRM* 1999; (3) B. Behnia et al, *MRE*, 15:101-110, 2002; (4) R. Salomir et al, *MRM*, 43: 342-347, 2000; (5) A. Hartov et al, *Int. J Hyperthermia*, 9, 4, 1993; (6) L. Sun et al, *Proc IEEE Ultrasonics Symposium*, 2003; (7) A. H. Chung et al, *MRM*, 36: 745-752, 1996

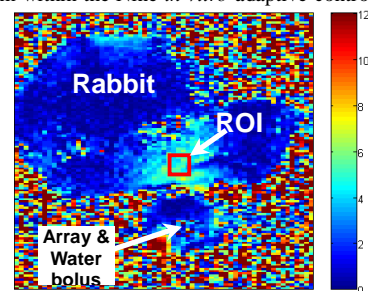
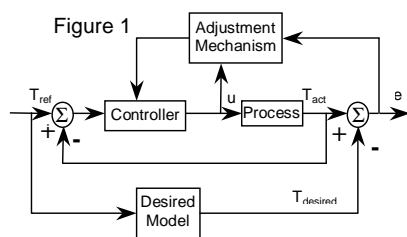
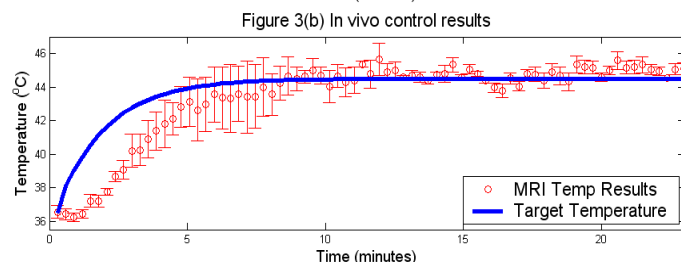
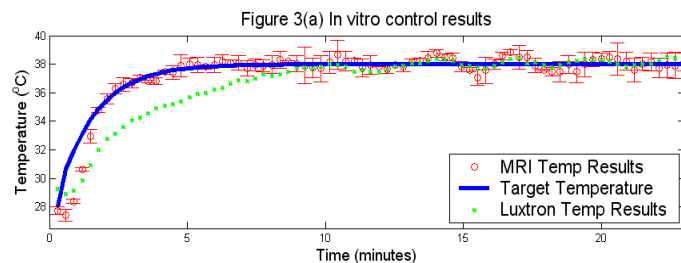


Figure 2



AN ADAPTIVE CONTROL METHOD FOR ULTRASOUND PROSTATE HYPERTHERMIA

Lei Sun¹, Jeffery Schiano², and Nadine Barrie Smith^{1,3}

¹Department of Bioengineering, ²Department of Electrical Engineering, ³Acoustics Program, Pennsylvania State University, University Park, USA, 16802

Abstract

For thermal treatment of prostate diseases, an ultrasound phased array was designed and operated with a computer controlled amplifier system which adjusted the power and phase of each transducer element. The clinical application of such a system is to increase the temperature in the prostate to 43-45°C and maintain the temperature for 30-60 minutes for a hyperthermia therapy treatment. In this paper, an adaptive self-tuning regulator (STR) controller has been designed and implemented with this hyperthermia system using a negative feedback transfer operator and a feedforward transfer operator. The transfer operators' parameters were obtained directly from plant input and output with recursive least square estimation (RLSE). The advantage of this controller was that it did not need *a priori* knowledge of the tissue properties and could adaptively change its control variables according to the perfusion rate or other dynamic properties. Simulations indicated that the prostate reached the target temperature without overshoots and oscillations within 100 seconds. The system also successfully adapted to the dynamic tissue properties. Phantom experiments showed that the measured temperature tracked the reference temperature closely and reached the target temperature with a little oscillations and without overshoots within 150 seconds, which was consistent with the computer simulations.

Key Words: self-tuning regulator, ultrasound hyperthermia, prostate disease

1. Introduction

Diseases associated with the prostate gland include benign prostate hyperplasia (BPH) and prostate cancer. Although surgery is the current treatment, older men often have additional health problems, which rule out surgery as a viable option. Ultrasound hyperthermia treatment, which is to increase the tissue temperature to 43-45°C for 30-60 minutes, has been used clinically and have shown effectiveness for the prostate treatment when it is associated with radiotherapy or chemotherapy [1-4]. Hyperthermia can enhance radiotherapy by preventing cellular repair mechanisms from radiation induced injury and is effective in killing hypoxic cells, which are resistant to radiation therapy [5].

However, in the clinical treatments, the temperature distribution is controlled by a clinician's intervention and judgment through adjusting the power to the array elements based on temperature information from thermocouples placed in the prostate. Previously, various control strategies have been designed for controlling temperature in either actual or simulated hyperthermia treatment, such as proportional-integral (PI) bang-bang control [6], reduced-order multi-input multi-output (MIMO) control [7], adaptive MIMO control [8], multipoint adaptive control [9], linear quadratic regulator (LQR) [10], magnetic resonance imaging (MRI) compatible single input single output (SISO) PI control [11]. The purpose of this research is to introduce an adaptive feedback control method for ultrasound hyperthermia treatment to achieve the desired prostate temperature with minimal overshoots, rapid rise time, fast settle time, and small oscillations.

2. Materials and Methods

2.1 The Ultrasound Hyperthermia System

The ultrasound hyperthermia system consisted of an ultrasound phased array driven by a computer controlled amplifier system (Fig. 1) [4;10-15]. *In vitro* prostate phantom experiments used a 16-element ultrasound unfocused array immersed in a Plexiglas[®] tank (25 x 38 x 53 cm³) filled with distilled degassed water. The array was driven by a programmable 64-channel radio frequency (RF) amplifier (Advanced Surgical System Incorporated, Tucson, AZ) connected to the computer through a RS-232 port [16;17]. Temperatures change within the *in vitro* phantom was determined by a multi-element fiber optic thermometer (Luxtron Corporation, Mountain View, CA) inserted in the prostate phantom. Each probe was shielded with copper tube to prevent heat absorption of the ultrasound by the probe [18]. The prostate phantom was made of agar powder simulating the response of human tissue to capture the temperature of the heated tissue [19]. The adaptive feedback control algorithm was used to maintain a desired temperature evolution by controlling the electrical power of the individual phased array element.

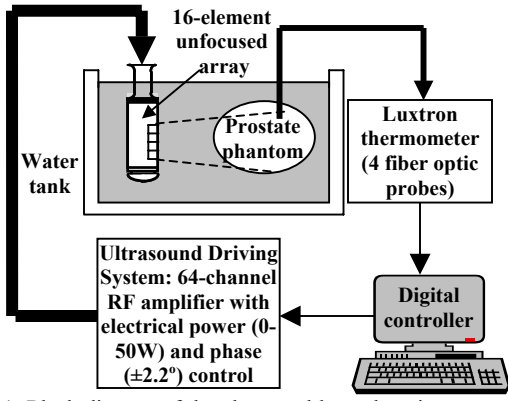


Figure 1. Block diagram of the ultrasound hyperthermia system. A 16-element ultrasound array driven by a computer controlled amplifier generates acoustic energy to heat the tissue phantom. The heating in the prostate phantom is monitored by a fiber optic thermometer which sends temperature information to digital controller.

2.2 Control Simulations

2.2.1 Pressure Field Calculation

Simulations were initially performed before *in vitro* experiments to determine the control variables such as the reference model parameters and tissue thermal response to heat from the ultrasound wave by a 64-element phased array [20]. The acoustical pressure of the array was calculated by modeling every element of the array as an independent simple source and summing the contribution of each simple source at each point in the field. The acoustic pressure $p(x,y,z)$ at a specific point (x,y,z) in the field due to a simple source was calculated using the Rayleigh-Sommerfeld equation [21]:

$$p_i(x,y,z) = \sqrt{\frac{2W\rho}{cA}} \left(\frac{fS}{d} \right) e^{\{(\phi - \frac{2\pi d}{\lambda})i - d\alpha\}} \quad (1)$$

where W is total acoustical power output from the array, ρ is density of the medium (998 kg/m^3), c is speed of sound in the medium (1500 m/s), A is total transducer surface area, f is frequency (1.2 MHz), S is area represented by the simple source, d is distance from the source to the point (x,y,z) , ϕ is phase of the simple source, λ is wavelength and α is attenuation in the medium (10 Np/(m·MHz)).

The net pressure due to all the elements was determined by summing the effects of each simple source:

$$P_{net}(x,y,z) = \sum_{i=1}^n p_i(x,y,z) \quad (2)$$

and net power deposition at point (x,y,z) was the result of the attenuation [22]:

$$q(x,y,z) = \frac{\alpha P_{net}^2(x,y,z)}{\rho c} \quad (3)$$

Two pressure fields were calculated by Matlab[®] program (Mathworks Incorporated, Natick, MA) in an $8 \times 8 \times 4 \text{ cm}^3$ three-dimensional (3-D) volume 1.5 cm away from the array surface. The first was a single focus pattern where the focal point was at $(0, 0, 2.5 \text{ cm})$ given that the center of the array was the origin and z -axis was

perpendicular to the array surface. The other was a four foci pattern with all the foci at $(0.3, 0.3, 3 \text{ cm})$. Each focus was generated by a quarter of the array on a symmetric way. The phase of each element of the array was determined by:

$$\phi_i = \frac{360^\circ}{\lambda} (d_i - d_0) - 360^\circ n \quad (4)$$

where ϕ_i is phase of element i in degrees, d_i is distance from the center of element i to the focus, d_0 is the focus depth, n is an integer used to maintain $0 \leq \phi_i \leq 360^\circ$.

2.2.2 Thermal Model of Tissue

The nature of heat transfer in tissue field was determined by applying Pennes' bioheat transfer equation (BHTE) [23;24]. The three dimensional representation of this equation in Cartesian coordinates is:

$$\rho c_t \frac{dT}{dt} = \kappa \left(\frac{d^2 T}{dx^2} + \frac{d^2 T}{dy^2} + \frac{d^2 T}{dz^2} \right) - w c_b (T - T_a) + q(x,y,z) \quad (5)$$

where ρ is density (998 kg/m^3), c_t is specific heat of the tissue ($3770 \text{ J/(kg } ^\circ\text{C)}$), κ is thermal conductivity ($0.5 \text{ W/(m } ^\circ\text{C)}$), T is temperature at time t and point (x,y,z) , T_a is arterial blood temperature (37°C), w is perfusion rate (in $\text{kg/m}^3\text{s}$), c_b is specific heat of the blood ($3770 \text{ J/(kg } ^\circ\text{C)}$) and $q(x,y,z)$ is the power deposited (Equ. 3) at the point (x,y,z) in the tissue. Although it is widely used, this implementation neither accounts for variations in tissue, such as the presence of blood vessels, nor for any spatial or temporal variation in perfusion levels. Therefore, it does not provide a "perfect" model for the behavior of tissue targeted with the acoustical power of an ultrasound array. However, it is adequate to estimate the effectiveness of the different controllers.

The BHTE was solved using a 3-D numerical finite difference equation with Compaq Fortran 6.0 (Compaq Computer Corporation, Houston, TX) programming language and all boundary and initial conditions were set to 36.8°C . A time step of 1 second and a grid spacing of $1 \times 1 \times 1 \text{ mm}^3$ were used for the temporal and spatial resolution of the BHTE implementation. The 1 second sampling period was the fast period the system can achieve.

2.2.3 The Self-Tuning Regulator Method

The BHTE (Equ. 5) indicates a nonlinear relationship between the power and the temperature, and therefore, it is difficult to apply the existing control theories. For simplicity, an assumption was made such that the power and the temperature satisfied an autoregressive moving average (ARMA) model with unknown orders and coefficients. The assumed ARMA model is:

$$A(q)y(k) = B(q)u(k) \quad (6)$$

where $y(k)$ is the temperature output and $u(k)$ is the command power input. A and B are polynomials in the forward shift operator q . The system transfer function is $B(z)/A(z)$. The polynomials A and B have the degrees:

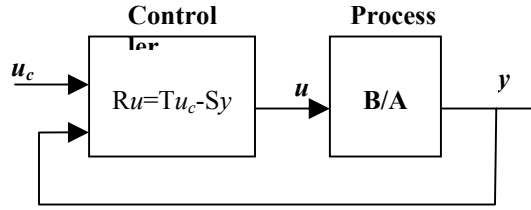


Figure 2. A general linear controller with two degrees of freedom. B/A is the transfer function of the process. A and B are relative prime and A is also assumed monic. R, S and T are control polynomials to achieve desired performance of the closed-loop system.

$$\deg A = n \quad (7)$$

$$\deg B = \deg A - d_0 = n - d_0 \quad (8)$$

where parameter n denotes the order of polynomial A and parameter d_0 represents the integer part of ratio of time delay and sampling period. Further assumptions were that A and B were relatively prime and A was monic, that was, the coefficient of the highest power in A was unity.

An adaptive self-tuning regulator control method was proposed based on the ARMA model assumption. This control method could converge the measured temperature to the reference temperature. An interesting result is that this could happen even if the model structure is incorrect.

A general linear controller can be described by:

$$Ru(k) = Tu_c(k) - Sy(k) \quad (9)$$

where R, S and T are polynomials. This control law represents a negative feedback with the transfer operator equal to $-S/R$ and a feedforward with the transfer operator equal to T/R . With the feedback and feedforward, this model has two degrees of freedom (Fig. 2).

Elimination of $u_c(k)$ between Equ. 6 and 9 gives the following equations for the closed-loop system:

$$y(k) = \frac{BT}{AR + BS} u_c(k) \quad (10)$$

$$u(k) = \frac{AT}{AR + BS} u_c(k) \quad (11)$$

The close-loop characteristic polynomial A_c is thus,

$$AR + BS = A_c \quad (12)$$

The key idea of the design method was to specify the desired closed-loop characteristic polynomial A_c . The polynomials R and S could then be solved from Equ. 12. The significance of the design procedure for polynomial A_c was that it was considered to be a design parameter that was chosen to give the desired properties to the closed-loop system. Equ. 12 played a fundamental role in algebra, which is called *Diophantine* equation, and always has solutions if the polynomials A and B do not have

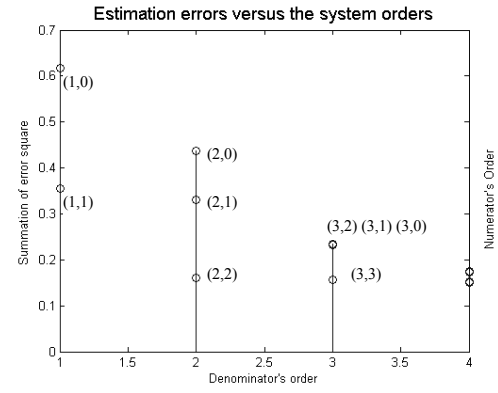


Figure 3. The system estimation errors versus the system order. The first number in parenthesis is the denominator's order, the second number is the numerator's.

common factors. With direct self-tuning regulators, the model parameters A and B did not need to be solved. The controller polynomials R, T and S could be obtained directly from plant input $u(k)$ and output $y(k)$ using recursive least square estimation (RLSE).

2.2.4 Control Simulations and Experiments

For the simulations, the first 20 seconds of the hyperthermia treatment was used to estimate the initial STR control parameters. The excitation signal for estimation was a square wave with period of 4 seconds switching between 0 and 1 Watt to guarantee the persistency of the excitation. After 20 seconds, the control parameters were updated every 1 second with new $u(k)$ and $y(k)$ data using RLSE, then the controller calculated the power level of the array and outputted it to each array element at the same rate. The reference temperature was an exponential signal with a time constant of 15 seconds.

The control experiments followed the same procedure as the simulations. Since the 64-element array was not available yet, another 16-element unfocused array was applied. The SISO STR experiments were conducted with one element of the array and one fiber optic probe. The STR control algorithm coded in Microsoft Visual Basic 6.0 (Microsoft Corporation, Redmond, WA) manipulated the real time heating process. The sampling period was also chosen to be 1 second to make the control as fast as possible.

3. Results

3.1 The Second Order ARMA Model Assumption

Figure 3 plots the system estimation errors versus the system orders using experimental data. The numbers in parenthesis represent the transfer function denominator and numerator's order, respectively. Figure 3 shows that at orders larger than (2,2) increasing the order number can not decrease the estimation errors, which means the system was a second order system.

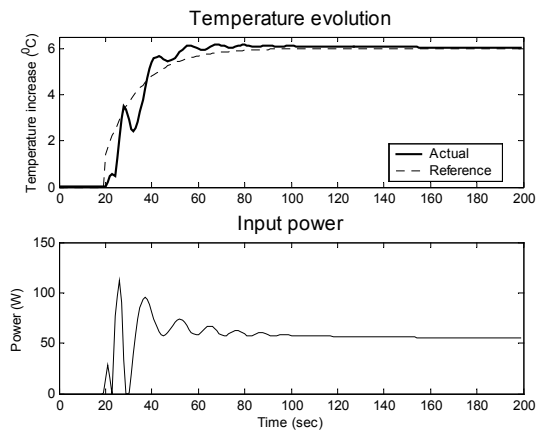


Figure 4. Temperature evolution (top) and input power (bottom) for SISO STR control with constant perfusion rate 2.0 kg/m³s.

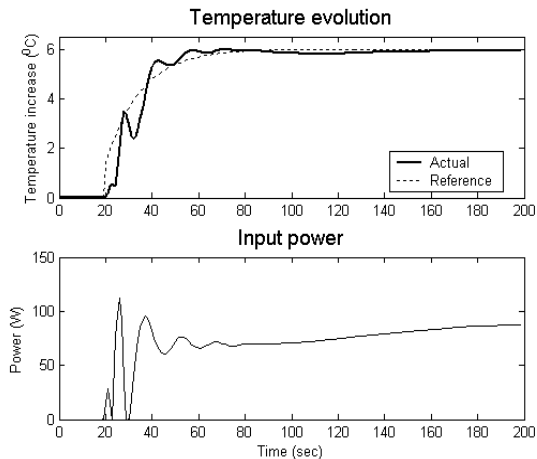


Figure 5. Temperature evolution (top) and input power (bottom) for SISO STR control with linearly changing perfusion rate.

3.2 Single Input Single Output Control Simulations

The SISO STR control simulations were conducted under two control conditions. One was at constant perfusion rate of 2.0 kg/m³s, and the other was at linearly increasing perfusion rate changing from 2.0 kg/m³s at 20 seconds to 20.0 kg/m³s at 180 seconds. Figure 4 shows the measured temperature change from 0 to 200 seconds (top graph) and the array's input power level from 0 to 200 seconds (bottom graph) at constant perfusion rate. From 20 to 80 seconds, the measured temperature approached the reference temperature quickly. At 100 seconds the temperature reached its steady state point, and maintained it for the last 100 seconds without oscillations. The input power ranged from 0 to about 100 Watts (W) and after 100 seconds it reached a constant value of 55 W. This was reasonable because when the temperature reached its equilibrium point, the input power compensated the heat loss of the tissue to its surrounding environments.

Figure 5 shows the measured temperature evolution (top) and input power (bottom) at linearly increasing perfusion rate. The temperature evolution in Fig. 5 is similar with that in Fig. 4 during the first 80

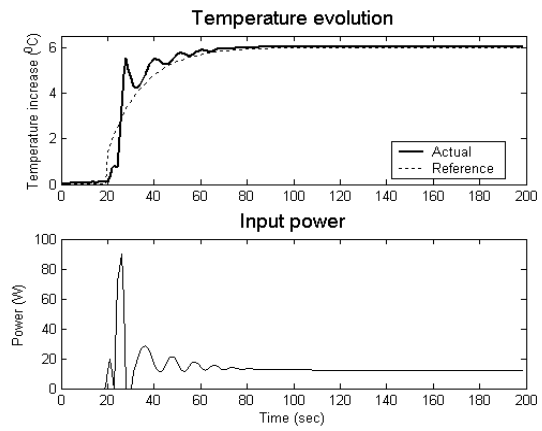


Figure 6. Average temperature evolution (top) and input power (bottom) for MIMO STR control with constant perfusion rate 2.0 kg/m³s.

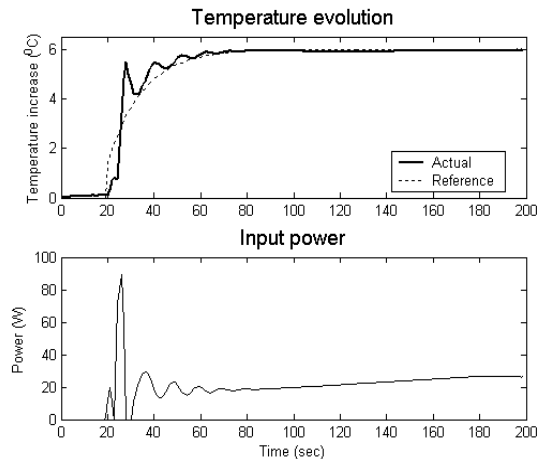


Figure 7. Average temperature evolution (top) and input power (bottom) for MIMO STR control with linearly changing perfusion rate.

seconds when the perfusion rate was small. From 100 to 160 seconds, a concave curve was present due to the fact that the large perfusion rate was not compensated enough by the input power. After 160 seconds, the temperature reached the steady state when the input power balanced the heat loss completely. The steady state values difference between Fig. 4 and 5 could be explained by the fact that more energy was needed when blood removed more energy from the hot spot at larger perfusion rate.

3.3 Multiple Input Multiple Output Control Simulations

In the four foci pattern hyperthermia, the controller was multi-input multi-output (MIMO). To avoid complex matrix operation, one temperature was obtained by averaging the 4 foci's temperatures. As a result, the MIMO control was transformed to a single input multiple output (SIMO) control. Furthermore, the SIMO was simplified to a SISO control because the 4 output power levels were identical due to the symmetry. Without any modification, the SISO STR control method could be applied to this MIMO control.

Figure 6 shows the average temperature evolution (top) and input power (bottom) at constant

- [2]Strohmaier, W. L., Bichler, K. H., Bokcing, A., and Fluchter, S. H., Histological effects of local microwave hyperthermia in prostatic cancer, *Int. J. Hyperthermia*, vol. 7(1), 1991, 27-33.
- [3]Fosmire, H., Hynynen, K., Drach, G. W., Stea, B., Swift, P., and Cassady, R., Feasibility and toxicity of transrectal ultrasound hyperthermia treatment of locally advanced adenocarcinoma of the prostate, *Int. J. Rad. Onc., Biol., Phys.*, vol. 26, 1993, 253-259.
- [4]Hurwitz, M. D., Kaplan, I. D., Svensson, G. K., Hanson, J. L., and Hynynen, K., Feasibility and patient tolerance of a novel transrectal ultrasound hyperthermia system for treatment of prostate cancer," *Int. J. Hyperthermia*, vol. 17(1), 2001, 31-37.
- [5]Overgaard, J. and Overgaard, M., Hyperthermia as an adjuvant to radiotherapy in the treatment of malignant melanoma, *Int. J. Hyperthermia*, vol. 3(6), 1987, 483-501.
- [6]Lin, W., Roemer, R. B., and Hynynen, K., Theoretical and experimental evaluation of a temperature controller for scanned focused ultrasound hyperthermia, *Med. Phys.*, vol. 17(4), 1990, 615-625.
- [7]Potocki, J. K. and Tharp, H. S., Reduced-order modeling for hyperthermia control, *IEEE Transactions on Biomedical Engineering*, vol. 39(12), 1992, 1265-1273.
- [8]Hartov, A., T.A.Colacchio, J.W.Strohbehn, T.P.Ryan, and P.J.Hoopes, Performance of an adaptive MIMO controller for a multiple-element ultrasound hyperthermia, *Int. J. Hyperthermia*, vol. 9(4), 1993, 563-579.
- [9]VanBaren, P. and Ebbini, E., Multipoint Temperature Control During Hyperthermia Treatments: Theory and Simulation, *IEEE Transactions on Biomedical Engineering*, vol. 42(8), 1995, 818-827.
- [10]Hutchinson, E., Dahleh, M., and Hynynen, K., The feasibility of MRI feedback control for intracavitary phased array hyperthermia treatments, *Int. J. Hyperthermia*, vol. 14(1), 1998, 39-56.
- [11]Smith, N. B., Merrilees, N. K., Dahleh, M., and Hynynen, K., An MRI compatible intracavitary ultrasound array for thermal treatment of prostate disease, *Int. J. Hyperthermia*, vol. 17(3), 2001, 271-282.
- [12]C. J. Diederich and E. C. Burdette, Transurethral ultrasound array for prostate thermal therapy: initial studies, *IEEE Transactions on Ultrasonics, Ferroelectrics, and Frequency Control*, vol. 43(6), 1996, 1011-1022.
- [13]Douglas R.Daum and Kullervo Hynynen, A 256-Element Ultrasonic Phased Array for the Treatment of Large Volume of Deep Seated Tissue, *IEEE Transactions on Ultrasound, Ferroelectrics and Frequency Control*, vol. 46(5), 1999, 1254-1268.
- [14]Smith, N. B., Buchanan, M., and Hynynen, K., Transrectal ultrasound applicator for prostate heating monitored using MRI thermometry, *Int. J. Radiat. Oncol., Biol., Phys.*, vol. 43(1), 1999, 217-225.
- [15]Sokka, S. D. and Hynynen, K., The feasibility of MRI-guided whole prostate ablation with a linear aperiodic intracavitary ultrasound phased array, *Phys. Med. Biol.*, vol. 45(11), 2000, 3373-3383.
- [16]Buchanan, M. and Hynynen, K., Design and experimental evaluation of an intracavitary ultrasound phased array for hyperthermia, *IEEE Transactions on Biomedical Engineering*, vol. 41(12), 1994, 1178-1187.
- [17]Daum, D. R., Buchanan, M. T., Fjield, T., and Hynynen, K., Design and Evaluation of a Feedback Based Phased Array for Ultrasound Surgery, *IEEE Transactions on Ultrasound, Ferroelectrics and Frequency Control*, vol. 45(2), 1998, 431-438.
- [18]Hynynen, K. and Edwards, D. K., Temperature measurements during ultrasound hyperthermia, *Med. Phys.*, vol. 16(4), 1989, 618-626.
- [19]Payne, A., Mattingly, M., Shelkey, J., Scott, E., and Roemer, R. B., A Dynamic two-dimensional Phantom for Ultrasound Hyperthermia Controller Testing," *Int. J. Hyperthermia*, vol. 17(2), 2001, 143-159.
- [20]Saleh, K. and Smith, N. B. Two dimensional ultrasound phased array for thermal treatment of prostate cancer, *Proc. Ultrasonic Transducer Engineering Conference 2001 of NIH Resource on Medical Ultrasonic Transducer Technology*, University Park, USA, 2001.
- [21]Goodman, J. W., *Introduction to Fourier Optics*, (New York: McGraw-Hill, 1968).
- [22]Seip, R., VanBaren, P., Cain, C. A., and Ebbini, E. S., Noninvasive Real-Time Multipoint Temperature Control for Ultrasound Phased Array Treatments, *IEEE Transactions on Ultrasonics, Ferroelectrics, and Frequency Control*, vol. 43(6), 1996, 1063-1073.
- [23]Pennes, H. H., Analysis of tissue and arterial blood temperatures in the resting human forearm, *Journal of Applied Physiology*, vol. 1(2), 1948, 93-122.
- [24]Sapareto, S. A. and Dewey, W. C., Thermal dose determination in cancer therapy, *International Journal of Radiation Oncology-Biology and Physics*, vol. 10, 1984, 787-800.